

**A METHODOLOGY FOR MODULATING THE INTENSIFICATION RATES
OF FORECAST MID-LATITUDE CYCLONES WITH IMPLICATIONS FOR
PREDICTABILITY**

By

Alexander M. Goldstein

A dissertation submitted in partial fulfillment of the requirements for the degree of

Doctor of Philosophy

(Atmospheric and Oceanic Sciences)

at the

UNIVERSITY OF WISCONSIN – MADISON

2018

Date of final oral examination: 14 August 2018

The dissertation is approved by the following members of the Final Oral Committee:

Michael C. Morgan, Professor, Atmospheric and Oceanic Sciences

Brett T. Hoover, Research Associate, SSEC-CIMSS

Jonathan E. Martin, Professor, Atmospheric and Oceanic Sciences

Gregory Tripoli, Professor, Atmospheric and Oceanic Sciences

Grace Wahba, Professor, Statistics

Daniel Holdaway, Research Associate, NASA-GMAO

© Copyright by Alexander M. Goldstein

2018 All Rights Reserved

The University of Wisconsin-Madison

The Graduate School

Candidate for the degree of PHD

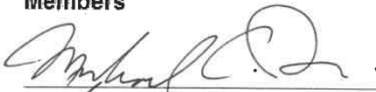
Goldstein, Alexander M

9064864052 - 0004736483

Major: Atmospheric & Oceanic Sciences - G675
Subplan:
Minor: GMIN254 - Distributed
Second Minor:

We, the undersigned, report that as a committee we have examined **Alexander M Goldstein** on _____ and upon the work done in the subjects named and upon the dissertation presented by the candidate we find that the candidate may properly be admitted to the degree of Doctor of Philosophy.

(By signing this warrant I am confirming that I have also approved this student's UMI abstract.)

Committee Member Names	Signatures of Committee Members	
Morgan, Michael Cottman	Advisor	 Reader
Hoover, Brett		 Reader
Martin, Jonathan		 Reader
Tripoli, Greg		 Reader
WAHBA, GRACE G		 Reader
Holdaway, Daniel		 Reader
		<hr/> <hr/>

I dissent from the following report.

Dissertation approved by the Graduate School on:

Acknowledgements

It's pretty incredible how fast this journey has flown by. It feels like just yesterday I was walking into AOS for the first time. I won't soon forget that first visit; I took the freight elevator because I couldn't find the main ones (anyone familiar with AOS knows how silly this is) and sprayed myself in the face at the water fountain on the eighth floor in front of an open classroom door (the class was full). From that day until this one, there have been two people who have guided, mentored, consoled, boosted, humbled and taught me, and to them I am so thankful. My advisors, Drs. Michael Morgan and Brett Hoover have seen me through what's been a tumultuous journey through graduate school, all the while shaping me into the scientist I am today. There were many times throughout this experience that they have shown so much more faith, patience and confidence in me than I think I ever deserved. I am eternally grateful to not only be able to call them both my advisors and colleagues, but also my friends. Thank you both for never giving up on me, even when I wanted to give up myself.

It goes without saying of course that there were plenty of other people who helped me in getting to this point and making sure my work is of a caliber worthy of a PhD from our esteemed department. Dr. Jonathan Martin, thank you for all of the rich conversations about everything from politics to the history of meteorology to our shared disdain for the Yankees. It's been an absolute pleasure since the moment I met you at AMS 2014. Thank you Dr. Gregory Tripoli for daring me to question the very framework of our understanding of modern meteorology. You've challenged me to think critically in a way I'm not sure I did before I came to AOS. Thank you Dr. Grace Wahba for believing in me and seeing me through to this point. Thank you Dr. Daniel Holdaway. Without you, *none*

of this would be possible. Since day one, you've helped solve every problem we could possibly run into. I couldn't possibly ask for a better collaborator. My understanding of numerical models is exponentially better having worked with you. Finally, there will never be enough thank you's to adequately express my gratitude to Pete Pokrandt. You solved every technical problem I faced without complaint, afforded me with all of the data and tools I could possibly need to be successful and provided me with the phrase, "the problem is between the keyboard and the chair". I'm not going to soon forget that one.

I'd be remiss in not mentioning the countless graduate and undergraduate students who I've been fortunate enough to befriend along the way. To my Morgan groupmates; Becky Schultz, Craig Oswald and Zoë Brooke-Zibton, it's been such an honor to work so closely with such a great group of people. I'm so glad I had the opportunity to learn alongside you all. You've enriched this experience beyond measure. To my pseudo-groupmates in the Martin group; especially Zak Handlos, Andrew Winters, Kyle Griffin, Melissa Breeden, Maria Madsen and Jessica Taheri, between top cuts and mugball to the weird horse calendar on your lab door to the 14th floor-wide discussions about characteristic sandwich geometry (sorry Melissa, a Hot Dog *is* a sandwich), I'm not quite sure how I would've made it through grad school without you all. Thank you. To David Loveless, Luke "George" Gloege, Sean Ridge, Kate Sauter, Keiko Yamamoto, Elliot Shiben, Kelton Halbert, Sarah Larson, Ken Dixon and the multitude of others with whom I've developed friendships while in Madison, thank you so much for all of the discussions, ideas and support you've given me.

To all of my friends who've stuck with me over the years while I made my back and forth trips between Maplewood, Miami and Madison, you mean the world to me. Mike Glassman, Chris Mancuso, Adam Wortman, Sarah Hoffman, Evie Swirski, Ray Agüero, Adam Steinbauer, Dario Lambkin, Lee Picard, Claire Waxenberg, Samantha Camposano and Caitlin Orlando, you've made this all possible. I love you all. To my fearless storm chasing partners Adam Penney, Kevin "Chief" Bente and Travis Farncombe, I don't think I'd be half the meteorologist I am today if not for the conversations and adventures we've had. We've had some hairy moments, but I can't wait to chase with you all for the next 50-100 years. Additionally, I owe a huge debt of gratitude to Roger Hill and Dr. David Gold, without whom I never would've even begun this journey. I learned so much about storm chasing and convective meteorology from Roger, knowledge that undoubtedly aided in my understanding of the dynamics of the atmosphere in the classroom.

To Kat Ternus, you believed in me when I almost gave up meteorology freshman year of undergrad. You told me I could do this when I cried on my dorm room bed, fearful that I would never pass calculus and physics and live my dream as a meteorologist. You have such a huge hand in this accomplishment. To Karly Spillane, you've been with me through it all. You've seen me at my lowest, my highest and everywhere in between. You've built me up and humbled me. You've given me a shoulder to cry on and provided me with endless support. You've even spent 20 consecutive hours in airports and on planes with me while helping me pursue my goal of you seeing a tornado. I don't know what I'd do without you. I also hope you enjoyed

your Wawa sandwich tonight¹. To Bailey Howington, you and Rhae are two of the most wonderful souls I've ever encountered. You've done more for me than you'll ever know.

I owe a special thanks to a few educators from my past who were so instrumental in getting me here. First, my eighth grade science teacher (and current fellow Friday floor hockey player) Roger Johnson. I won't ever forget the giant hurricane tracking whiteboard on the wall of your classroom. You've inspired so much of this. To Mrs. Norma Agras, my freshman year calculus instructor at the University of Miami, you singlehandedly led me to believe that I could do math again. You instilled a sense of academic confidence in me that few before you had. Without you this wouldn't be possible. Thank you. To Professors Sharan Majumdar, Paquita Zuidema, Brian Mapes, Shuyi Chen, Chidong Zhang, Bruce Albrecht and David Nolan, my meteorology professors at the University of Miami, you helped me live my dream. I am eternally grateful. Finally, Professor Daniel Vimont here at AOS, thank you for giving me the opportunity to explore my love for teaching. Working alongside you was a privilege and gave me invaluable insight into the life of a professor.

Most importantly, my family. To my parents, Lisa and Danny. You are the single reason that I am writing this today. You've fostered my love for science from a young age, from taking me to see Apollo 13 (and unfortunately Mars Attacks) and encouraging my dream of working for NASA (I did it!) to bringing me storm chasing every year since I was 16. You've afforded me every opportunity to succeed as a scientist and as a man, and not a day goes by that I'm not infinitely thankful that I have the privilege of being your son. I love you both so much, thank you for everything. To my brother Jake and my

¹ I think it's really funny to include a footnote about a sandwich in the acknowledgements section so I'm going to do it. Tonight (July 26, 2018), Karly enjoyed a Wawa sandwich but her belly hurts. So that should clear up the confusion 50 years from now.

sister Olivia. It's been a bumpy ride, but I'm so proud to call myself your brother. I'm so proud of all that you've both accomplished, and look forward to continuing to watch you both grow. Without your love and support, none of this would be possible.

Don't knock the weather; nine-tenths of the people couldn't start a conversation if it didn't change once in a while. – Kin Hubbard

Abstract

For a particular aspect of interest (defined by a “response function”) within a numerical weather prediction (NWP) forecast trajectory, one may use the adjoint of the NWP model to calculate the sensitivity of the response function to small changes to the model state at a previous time. These adjoint-derived sensitivities, expressed as gradients of the response function with respect to the forecast trajectory, yield powerful insight into the dynamics that govern the meteorological phenomena of interest described by that response function. It is possible to use this sensitivity gradient information to compute and apply perturbations to the initial model state, optimized for a prescribed impact on the response function, in order to gain an explicit understanding of the dynamics and evolution of the response of the forecast to initial perturbation.

Within the traditional adjoint framework however, the examination of highly non-linear processes such as mid-latitude cyclone *intensification rate* is challenged by: 1) the adjoint model’s reliance upon the assumption of linearity; and 2) response functions typically being defined at a single point within the forecast trajectory rather than for the time-rate-of-change of a forecast aspect over a period of time. In order to remedy these two issues, two new methods for adjoint analysis are proposed and explored. First, the calculation of *quasi-optimal iterative perturbations* (QOIP), an iterative, incremental perturbation method inspired by incremental four dimensional variational data assimilation (4DVAR) that seeks to minimize the constraint of linearity is introduced and discussed. Second, a response function for cyclone intensification rate is derived by taking the difference between the sensitivity of cyclone intensity at two times within the forecast trajectory. In using these two methods, the impact of small changes to the initial

model state on the intensification rate of three mid-latitude cyclones is investigated, with implications for predictability of these kinds of events. Additionally, piecewise potential vorticity inversion is used to diagnose the evolution of these perturbations. The adjoint-derived, perturbation quasi-geostrophic potential vorticity (QGPV) is calculated and inverted in a piecewise manner relative to the instantaneous basic state supplied by the control forecast, allowing for a direct attribution of discrete QGPV perturbations to the balanced, perturbation mass and momentum fields.

Within the above framework, three case studies were performed on mid-latitude cyclones that varied based upon qualitative measures of predictability. For the cases characterized by lower (higher) levels of predictability, QOIP prescribed at the analysis time were more successful (unsuccessful) in modulating the cyclone intensification rate over a chosen response period. It is argued that those perturbations that successfully augment the larger-scale synoptic environment in a manner that promotes enhanced baroclinic growth of the cyclone results in the largest change to the response function, while perturbations that largely impact the thermodynamic fields result in a small to moderate change. This result is further shown within the context of vertical profiles of perturbation energy, in which the cases characterized by larger changes to the response function largely see an augmentation to the perturbation kinetic energy in the upper-troposphere/lower-stratosphere, versus those characterized by smaller changes experiencing larger augmentation to the perturbation available potential energy in the lower-levels.

TABLE OF CONTENTS

ACKNOWLEDGEMENTS	i
ABSTRACT	vii
TABLE OF CONTENTS	ix
LIST OF FIGURES	xi
LIST OF TABLES	xxii
1. INTRODUCTION	1
1.1. BAROCLINIC GROWTH OF MID-LATITUDE CYCLONES	1
1.2. A BRIEF HISTORY OF OUR UNDERSTANDING OF MID-LATITUDE CYCLOGENESIS	3
1.3. EXPLOSIVE CYCLOGENESIS	6
1.4. MOTIVATION	11
2. METHODOLOGY AND TOOLS	18
2.1. DYNAMICAL SENSITIVITY ANALYSIS.....	18
2.1.1. FORWARD AND ADJOINT MODELS.....	20
2.1.2. RESPONSE FUNCTIONS	23
2.1.3. OPTIMAL PERTURBATIONS	25
2.1.4. GENERATING <i>QUASI-OPTIMAL ITERATIVE PERTURBATIONS</i>	28
2.2. NASA GEOS-5 FORWARD AND ADJOINT MODEL SPECIFICATIONS	32
2.2.1. NONLINEAR FORWARD MODEL	32
2.2.2. LINEAR ADJOINT MODEL.....	32
2.2.3. MERRA-2 ANALYSES	33
2.3. STANDARDIZED UNCERTAINTY ANOMALIES.....	34
2.3.1. GLOBAL ENSEMBLE FORECAST SYSTEM REFORECAST DATASET	37
2.4. PIECEWISE POTENTIAL VORTICITY INVERSION	38
3. MODULATING THE INTENSIFICATION RATE OF THE 24-26 JANUARY 2000 “SURPRISE SNOW STORM” THROUGH THE USE OF ADJOINT-DERIVED <i>QUASI-OPTIMAL</i> ITERATIVE PERTURBATIONS.....	46
3.1. ABSTRACT	46
3.2. BACKGROUND	47
3.3. SYNOPTIC OVERVIEW – THE 24-25 JANUARY 2000 MID-ATLANTIC “SURPRISE SNOW STORM”	49
3.4. PRIOR SENSITIVITY ANALYSES	53
3.5. BAROTROPIC PRECONDITIONING	57
3.6. QOIP ANALYSIS	61
3.6a. <i>EXPERIMENT DESIGN</i>	61
3.6b. <i>IIR EXPERIMENT</i>	64
3.6c. <i>RIIR EXPERIMENT</i>	69
3.6.1. A NOTE ON THE LINEAR RELATIONSHIP BETWEEN THE IIR AND DIR CASES ...	71

3.7. QOIP AUGMENTATION OF BAROCLINIC DEVELOPMENT.....	72
3.6a. IIR EXPERIMENT.	75
3.6b. RIIR EXPERIMENT.....	79
3.6c. DIR AND RDIR EXPERIMENTS.....	81
3.8. SUMMARY AND CONCLUSIONS	82
4. A COMPARISON OF <i>QUASI-OPTIMAL ITERATIVE PERTURBATION</i> STRUCTURE AND EVOLUTION FOR TWO NORTHEAST SNOWSTORMS WITH DIFFERENT PREDICTABILITY	115
4.1. ABSTRACT	115
4.2. BACKGROUND	116
4.3. SYNOPTIC OVERVIEWS	118
4.3.1. 11-14 MARCH 1993 “STORM OF THE CENTURY”	118
4.3.2. 25-28 JANUARY 2015 NORTHEAST SNOW EVENT.....	122
4.4. PRIOR SENSITIVITY ANALYSES	126
4.4.1. COMMENTS ON LINEARITY AND “FORECAST ELASTICITY”	126
4.4.2. VERTICAL PERTURBATION ENERGY PROFILES.....	131
4.4.3. BAROTROPIC PRECONDITIONING.....	135
4.4.4. QGPV ANALYSIS	136
4.4.4a. 11-13 MARCH 1993 “ <i>STORM OF THE CENTURY</i> ”	136
4.4.4b. 25-28 JANUARY 2015 NORTHEAST SNOW EVENT	138
4.5. SUMMARY AND CONCLUSIONS	145
5. CONCLUSIONS AND DIRECTIONS FOR FUTURE WORK	177
5.1. BACKGROUND	177
5.2. INTRODUCTION OF NEW METHODOLOGIES.....	178
5.2.1. A TIME-RATE-OF-CHANGE OF SURFACE PRESSURE RESPONSE FUNCTION.....	178
5.2.2. “PERTURBATION-RESPONSE” AND THE QOIP	179
5.2.3. PIECEWISE INVERSION OF QOIP QUASI-GEOSTROPHIC POTENTIAL VORTICITY	
.....	180
5.3. SUMMARY OF RESULTS	182
5.3.1. BROADER CONTEXT.....	184
5.4. FUTURE DIRECTIONS FOR RESEARCH	186
5.4.1. STANDARDIZED UNCERTAINTY ANOMALIES.....	186
5.4.2. QOIP PIECEWISE TENDENCY DIAGNOSIS	188
5.4.3. INVESTIGATION OF TROPICAL CYCLONE RAPID INTENSIFICATION USING THE	
QOIP.....	189
5.4.4. SENSITIVITY TO POTENTIAL VORTICITY	190
6. REFERENCES.....	202

List of Figures

Chapter 1.

Figure 1.1. Properties of the most unstable Eady wave. (a) Phase variations: Above p , φ ; below v_z , $\text{div}_H v$. (b) Amplitude variations: left p , φ ; Right v_z , $\text{div}_H v$. (Eady 1949)

Figure 1.2. The Norwegian Cyclone Model life-cycle evolution with lower tropospheric geopotential height and fronts (top) and lower tropospheric potential temperature (bottom). (Schultz 1998; adapted from Bjerknes and Solberg 1922)

Figure 1.3. The Shapiro-Keyser Cyclone Model life-cycle evolution with lower tropospheric geopotential height and fronts (top) and lower tropospheric potential temperature (bottom). (Schultz 1998; adapted from Shapiro and Keyser 1990)

Figure 1.4. Distribution of 24 h deepening rates for all Northern Hemisphere surface cyclones in one year. The dark line indicates the sum of two normal curves while the gray lines and shading represent the separate distributions (light shading for the “ordinary and “darker” for the explosive). (Martin 2006; adapted from Roebber 1984)

Chapter 2.

Figure 2.1. A schematic diagram of the differences between NWP, TLM and Adjoint models in terms of their inputs and outputs as well as directions of propagation in time. Arrows facing to the right indicate a forward propagation in time; arrows facing left indicate a backwards propagation in time. Model state variables are denoted as \mathbf{x} , prime terms indicate perturbation variables, and the response function is denoted as R .

Figure 2.2. A schematic diagram of the algorithm used in computing quasi-optimal iterative perturbations. Courtesy Hoover (2017)

Figure 2.3. 500 hPa stream function standardized uncertainty anomaly (fill; $\text{m}^2 \text{s}$) and stream function (contour; $\text{m}^2 \text{s}$) valid (a) 0000 UTC 2000 January 24 (Analysis) and (b) 0000 UTC 2000 January 25. Warm colors indicate higher than climatological uncertainty, cool colors indicate lower than average uncertainty.

Figure 2.4. 500 hPa stream function standardized uncertainty anomaly (fill; $\text{m}^2 \text{s}$) and stream function (contour; $\text{m}^2 \text{s}$) valid (a) 0000 UTC 1993 March 12 (Analysis) and (b) 0000 UTC 1993 March 13. Warm colors indicate higher than climatological uncertainty, cool colors indicate lower than average uncertainty.

Chapter 3.

Figure 3.1. MERRA-2 analyses of surface pressure (black contours; hPa); and six-hourly snow (blue circles); mixed precipitation (magenta circles); freezing rain (red circles) and severe weather (green circles) reports. Circle size indicates amount of reports at the time of the observation. valid at (a) 0000 UTC 24 January 2000; (b) 1200 UTC 25 January 2000; (c) 0000 UTC 25 January 2000 and (d) 1200 UTC 25 January 2000. Code used to generate these panels courtesy Dr. Brett Hoover.

Figure 3.2. MERRA-2 analyses of the 250 hPa wind (fill and vectors; m s^{-1}); height (red contours; m) and divergence (cyan contours; s^{-1} ; contoured from 2×10^{-5} to 10×10^{-5} by 2×10^{-5}) valid at (a) 0000 UTC 24 January 2000; (b) 1200 UTC 25 January 2000; (c) 0000 UTC 25 January 2000 and (d) 1200 UTC 25 January 2000

Figure 3.3. MERRA-2 analyses of the 500 hPa vorticity (fill; 10^5 s^{-1}); and height (black contours; m) valid at (a) 0000 UTC 24 January 2000; (b) 1200 UTC 25 January 2000; (c) 0000 UTC 25 January 2000 and (d) 1200 UTC 25 January 2000

Figure 3.4. NWS subjective surface analyses valid at (a) 0000 UTC 24 January 2000; (b) 1200 UTC 25 January 2000; (c) 0000 UTC 25 January 2000 and (d) 1200 UTC 25 January 2000. The boundaries highlighted in panel (b) are the wavy remnant wind-shift baroclinic zone east of the synoptic frontal boundaries (green); (c) the wind-shift cold-front (green); the synoptic cold-front (blue); and the stationary-/warm-front (magenta); and (d) the wind-shift cold-front (green); the synoptic cold front (blue) and the warm-front (red)

Figure 3.5. Conceptual diagram of barotropic signature in zonal wind sensitivities around a zonal jet. Gray lines are isotachs, with a “J” indicating the jet core. Vectors indicate relatively stronger zonal flow within the jet core. Sensitivity with respect to zonal flow is indicated with shaded regions representing areas of positive (red) and negative (blue) sensitivity. From Hoover (2015)

Figure 3.6. Cyclone-following time series of the 9° by 9° box-mean sea level pressure for the increased intensification rate perturbation simulation (IIR; dark blue); reversed sign intensification rate perturbation simulation (RIIR; light blue); decreased intensification rate perturbation simulation (DIR; red); and reversed sign decreased intensification rate perturbation simulation (RDIR; pink). The control simulation is seen as the black curve. The magenta, vertical bars at 17- and 24-hrs indicate the response period over which changes to the intensification rate by the QOIP to the analysis are intended.

Figure 3.7. (a) Analysis time, IIR simulation upper-level (400 hPa to 150 hPa) quasi-geostrophic potential vorticity (QGPV) perturbations (fill; $5 \times 10^5 \text{ s}^{-1}$); control simulation height (magenta contour; m); and stretching deformation (black contour; s^{-1}). Stretching deformation is contoured from 10^{-4} to 4×10^{-4} by 5×10^{-5} ; (b) cross-sectional view along the green line of (a) with control integrations isentropes (grey dash; K). Deformation is not plotted in (b).

Figure 3.8. Analysis time 400 hPa to 150 hPa average barotropic energy conversion (BEC; fill; $\text{m}^2 \text{s}^3$); axes of contraction (vectors; s^{-1}); control simulation height (magenta, dashed contour; m); and perturbed simulation height (dark blue, solid contour; m); and total deformation (light magenta, solid contour; s^{-1}). Heights are contoured every 120 m; deformation is contoured from 10^{-4} to 4×10^{-4} . BEC rates shown are (a) total; (b) BEC by the stretching deformation; and (c) BEC by the shearing deformation.

Figure 3.9. Cross section of the analysis time zonal-mean BEC from 60°W to 100°W longitude and 20°N to 55°N latitude (fill; $\text{m}^2 \text{s}^3$) for the increased intensification rate (IIR) case. Predominant BEC occurs between the 400 hPa and 150 hPa layer. The analysis time zonal-mean BEC for the RIIR case is identical to that of the IIR case, and therefore is not shown.

Figure 3.10. Time series of the 400 hPa to 150 hPa BEC normalized by the total KE (s^{-1}) over the course of the full, 48-hr forecast integration for the increased intensification rate perturbation simulation (IIR; dark blue); reversed sign intensification rate perturbation simulation (RIR; light blue); decreased intensification rate perturbation simulation (DIR; red); and reversed sign decreased intensification rate perturbation simulation (RDIR; pink). BEC rates in shown are (a) total; (b) BEC by the stretching deformation; and (c) BEC by the shearing deformation. The magenta, dashed vertical bars at 17- and 24-hrs indicate the response period over which changes to the intensification rate by the QOIP to the analysis are intended.

Figure 3.11. Increased intensification rate (IIR) 400 hPa to 150 hPa average BEC (fill; $\text{m}^2 \text{s}^3$); axes of contraction (vectors; s^{-1}); control simulation height (magenta, dashed contour; m); perturbed simulation height (dark blue, solid contour; m); and total deformation (light magenta, solid contour; s^{-1}). Heights are contoured every 120 m; deformation is contoured from 10^{-4} to 4×10^{-4} by 5×10^{-5} . Times shown are (a) 0-hrs; (b) 3-hrs; (c) 6-hrs; (d) 9-hrs; (e) 12-hrs; and (f) 15-hrs into the simulation). Note that the color bars are not consistent across all times, as BEC increases (decreases) non-linearly.

Figure 3.12. Increased intensification rate (IIR) 400 hPa to 150 hPa average local time rate of change of perturbation kinetic energy (fill; $\text{m}^2 \text{s}^3$); BEC (orange, solid contours indicate positive BEC, cyan, dashed contours indicate negative BEC; $\text{m}^2 \text{s}^3$); control simulation height (magenta, dashed contour; m); perturbed simulation height (dark blue, solid contour; m); Heights are contoured every 120 m; BEC is contoured as in Fig. 3.10. Times shown are (a) 0-hrs; (b) 3-hrs; (c) 6-hrs; (d) 9-hrs; (e) 12-hrs; and (f) 15-hrs into the simulation). Note that the color bars are not consistent across all times, as perturbation kinetic energy increases (decreases) non-linearly.

Figure 3.13. Increased intensification rate (IIR) 400 hPa to 150 hPa average local time-rate-of-change of perturbation kinetic energy (fill; $\text{m}^2 \text{s}^3$) with the component of the perturbation kinetic energy due to advection subtracted from the total; BEC (orange, solid contours indicate positive BEC, cyan, dashed contours indicate negative BEC; $\text{m}^2 \text{s}^3$); control simulation height (magenta, dashed contour; m); perturbed simulation height (dark blue, solid contour; m); Heights are contoured every 120 m; BEC is contoured as in Fig. 3.10. Times shown are (a) 0-hrs; (b) 3-hrs; (c) 6-hrs; (d) 9-hrs; (e) 12-hrs; and (f) 15-

hrs into the simulation). Note that the color bars are not consistent across all times, as perturbation kinetic energy increases (decreases) non-linearly.

Figure 3.14. Reversed sign increased intensification rate (RIIR) 400 hPa to 150 hPa average BEC (fill; $\text{m}^2 \text{s}^3$); axes of contraction (vectors; s^{-1}); control simulation height (magenta, dashed contour; m); perturbed simulation height (dark blue, solid contour; m); and total deformation (light magenta, solid contour; s^{-1}). Heights are contoured every 120 m; deformation is contoured from 10^{-4} to 4×10^{-4} by 5×10^{-5} . Times shown are (a) 0-hrs; (b) 3-hrs; (c) 6-hrs; (d) 9-hrs; (e) 12-hrs; and (f) 15-hrs into the simulation). Note that the color bars are not consistent across all times, as BEC increases (decreases) non-linearly.

Figure 3.15. Reversed sign increased intensification rate of the RIIR experiment between 400 hPa and 150 hPa average local time-rate-of-change of perturbation kinetic energy (fill; $\text{m}^2 \text{s}^3$) with the component of the perturbation kinetic energy due to advection subtracted from the total; BEC (orange, solid contours indicate positive BEC, cyan, dashed contours indicate negative BEC; $\text{m}^2 \text{s}^3$); control simulation height (magenta, dashed contour; m); perturbed simulation height (dark blue, solid contour; m); Heights are contoured every 120 m; BEC is contoured as in Fig. 3.10. Times shown are (a) 0-hrs; (b) 3-hrs; (c) 6-hrs; (d) 9-hrs; (e) 12-hrs; and (f) 15-hrs into the simulation). Note that the color bars are not consistent across all times, as perturbation kinetic energy increases (decreases) non-linearly.

Figure 3.16. Analysis time 350 hPa quasi-geostrophic potential vorticity (QGPV) perturbations (fill; $2.5 \times 10^5 \text{ s}^{-1}$); control simulation height (magenta, dashed contour; m); and perturbed simulation height (dark blue, solid contour; m) for (a) IIR simulation at iteration two; (b) DIR simulation and 400 hPa to 150 hPa average BEC (fill; $\text{m}^2 \text{s}^3$); axes of contraction (vectors; s^{-1}); control simulation height (magenta, dashed contour; m); perturbed simulation height (dark blue, solid contour; m); and total deformation (light magenta, solid contour; s^{-1}) for (c) IIR simulation at iteration two and (d) the DIR simulation. Heights are contoured every 120m.

Figure 3.17. Control-simulation-cyclone-following summed 900 hPa inverted height perturbations for the (a) IIR; (b) RIIR; (c) DIR; and (d) RDIR cases. The solid lines colored as labeled represent the sum of the perturbations within a 9° by 9° box. The lines are bound within traces of summed 7° by 7° and 11° by 11° boxes. The observed contour is computed as the 900 hPa perturbation height difference between the perturbed and control simulations. The integration time is found on the x-axis with the gray, dashed lines representing the goal-post times of the response period. The summed perturbation values are found along the y-axis.

Figure 3.18. 24-hr IIR simulation upper-level QGPV 900 hPa inverted height perturbations (fill; m); inverted wind (vectors; m s^{-1}); control simulation height (magenta, dashed contour; m); and perturbed simulation height (dark blue, solid contour; m). Even at a forecast time that features an intense lower-level circulation, the upper-level QGPV has only a minimal impact on the lower-level (i.e., 900 hPa) height field, yielding height perturbations on the order of 10 - 20 m. Wind less than 5 m s^{-1} is masked.

Figure 3.19. IIR simulation, layer average quasi-geostrophic potential vorticity (QGPV) perturbations (fill; 10^5 s^{-1}); inverted perturbation wind (vectors; m s^{-1}); control simulation height (magenta, dashed contour; m); and perturbed simulation height (dark blue, solid contour; m) for (a) upper-level at (a) 12-hrs; (b) 17-hrs; (c) 24-hrs; mid-level at; (d) 12-hrs; (e) 17-hrs simulations; (f) 24-hrs; and lower-level at (g) 12-hrs; (h) 17-hrs; and (i) 24-hrs. All quantities described are layer averaged. Wind less than 5 m s^{-1} is masked.

Figure 3.20. 900 hPa control simulation temperature advection by the IIR simulation inverted wind (fill; K day^{-1}); inverted wind (vectors; m s^{-1}); control simulation height (magenta, solid contour; m); and control simulation potential temperature (gray, dashed contours; K) for mid-level at (a) 12-hrs; (b) 17-hrs; (c) 24-hrs; and lower-level at (d) 12-hrs; (e) 17-hrs; and (f) 24-hrs. Wind less than 5 m s^{-1} is masked.

Figure 3.21. Mid-level layer average perturbation QGPV as in Fig. 3.20 valid at (a) 12-hrs and (b) 17-hrs; cross-sectional view of QGPV (fill; 10^5 s^{-1}); perturbed simulation potential temperature (gray, dashed contours, K) and perturbed simulation omega (blue solid contour is indicative of positive values and blue dashed contour is indicative of negative values; Pa s^{-1}) valid at (c) 12-hrs and (d) 17-hrs; and cross sectional view of static stability (fill; K Pa^{-1}); and perturbed simulation potential temperature (gray, dashed contours, K) valid at (e) 12-hrs and (f) 17-hrs. Wind less than 5 m s^{-1} is masked.

Figure 3.22. IIR simulation 900 hPa inverted height perturbations (fill; m); inverted wind (vectors; m s^{-1}); control simulation height (magenta, dashed contour; m); and perturbed simulation height (dark blue, solid contour; m) for mid-level at (a) 12-hrs; (b) 17-hrs; (c) 24-hrs; and lower-level at (d) 12-hrs; (e) 17-hrs; and (f) 24-hrs. Wind less than 5 m s^{-1} is masked.

Figure 3.23. RIIR simulation, layer average quasi-geostrophic potential vorticity (QGPV) perturbations (fill; 10^5 s^{-1}); inverted perturbation wind (vectors; m s^{-1}); control simulation height (magenta, dashed contour; m); and perturbed simulation height (dark blue, solid contour; m) for (a) upper-level at (a) 12-hrs; (b) 17-hrs; (c) 24-hrs; mid-level at; (d) 12-hrs; (e) 17-hrs simulations; (f) 24-hrs; and lower-level at (g) 12-hrs; (h) 17-hrs; and (i) 24-hrs. All quantities described are layer averaged. Wind less than 5 m s^{-1} is masked.

Figure 3.24. RIIR simulation 900 hPa inverted height perturbations (fill; m); inverted wind (vectors; m s^{-1}); control simulation height (magenta, dashed contour; m); and perturbed simulation height (dark blue, solid contour; m) for mid-level at (a) 12-hrs; (b) 17-hrs; (c) 24-hrs; and lower-level at (d) 12-hrs; (e) 17-hrs; and (f) 24-hrs. Wind less than 5 m s^{-1} is masked.

Figure 3.25. 900 hPa control simulation temperature advection by the RIIR simulation inverted wind (fill; K day^{-1}); inverted wind (vectors; m s^{-1}); control simulation height (magenta, solid contour; m); and control simulation potential temperature (gray, dashed contours; K) for mid-level at (a) 12-hrs; (b) 17-hrs; (c) 24-hrs; and lower-level at (d) 12-hrs; (e) 17-hrs; and (f) 24-hrs. Wind less than 5 m s^{-1} is masked.

Chapter 4.

Figure 4.1. NWS subjective surface analyses valid at (a) 1200 UTC 12 March 1993, (b) 0000 UTC 13 March 1993, (c) 1200 UTC 13 March 1993, and (d) 0000 UTC 14 March 1993

Figure 4.2. MERRA-2 analyses of the 500 hPa vorticity (fill; 10^5 s^{-1}); and height (black contours; m) valid at (a) 1200 UTC 12 March, (b) 0000 UTC 13 March 1993, (c) 1200 UTC 13 March 1993, and (d) 0000 UTC 14 March 1993

Figure 4.3. MERRA-2 analyses of the 250 hPa wind (fill and vectors; m s^{-1}); height (red contours; m) and divergence (cyan contours; s^{-1} ; contoured from 2×10^{-5} to 10×10^{-5} by 2×10^{-5}) valid at (a) 1200 UTC 12 March, (b) 0000 UTC 13 March 1993, (c) 1200 UTC 13 March 1993, and (d) 0000 UTC 14 March 1993

Figure 4.4. Snow forecast maps as issued by the National Weather Service (NWS) offices in (a) Philadelphia/Mt. Holly; and (b) New York City/Upton issued mid-morning January 25. Verifying snow totals can be seen in panel (c) and display a significant disparity from forecasted totals, especially over inland regions.

Figure 4.5. MERRA-2 analyses of the 500 hPa vorticity (fill; 10^5 s^{-1}); and height (black contours; m) valid at (a) 1200 UTC 2015 January 25; (b) 0000 UTC 2015 January 26; (c) 1200 UTC 2015 January 26; (d) 0000 UTC 2015 January 27; (e) 1200 UTC 2015 January 27 and (f) 0000 UTC 2015 January 28

Figure 4.6. MERRA-2 analyses of the 250 hPa wind (fill and vectors; m s^{-1}); height (red contours; m) and divergence (cyan contours; s^{-1} ; contoured from 2×10^{-5} to 10×10^{-5} by 2×10^{-5}) valid at (a) 1200 UTC 2015 January 25; (b) 0000 UTC 2015 January 26; (c) 1200 UTC 2015 January 26; (d) 0000 UTC 2015 January 27; (e) 1200 UTC 2015 January 27 and (f) 0000 UTC 2015 January 28

Figure 4.7. NWS subjective surface analyses valid at (a) 1200 UTC 2015 January 25; (b) 0000 UTC 2015 January 26; (c) 1200 UTC 2015 January 26; (d) 0000 UTC 2015 January 27; (e) 1200 UTC 2015 January 27 and (f) 0000 UTC 2015 January 28

Figure 4.8. WSR-88d base reflectivity valid at the specified (Eastern Standard) times. Banded precipitation structures are found within regions of deformation.

Figure 4.9. Cyclone-following time series of the 9° by 9° box-mean sea level pressure for the increased intensification rate perturbation simulation (Final IIR denoted by dark blue line; individual IIR iterations denoted by the light blue lines); decreased intensification rate perturbation simulation (Final DIR denoted by dark red line; individual IIR iterations denoted by the pink line). The control simulation is seen as the black curve. The black, vertical bars at 17- and 24-hrs indicate the response period over which changes to the intensification rate by the QOIP to the analysis are intended.

Figure 4.10. Cyclone-following time series of the 9° by 9° box-mean sea level pressure for the increased intensification rate perturbation simulation (IIR; dark blue); reversed sign intensification rate perturbation simulation (RIIR; light blue); decreased intensification rate perturbation simulation (DIR; red); and reversed sign decreased intensification rate perturbation simulation (RDIR; pink). The control simulation is seen as the black curve. The magenta, vertical bars indicate the response period over which changes to the intensification rate by the QOIP to the analysis are intended. The cases plotted are seen as (a) SSS; (b) SOTC; and (c) j15 simulations.

Figure 4.11. Cyclone-following time series of the 9° by 9° box-mean sea level pressure difference between the control simulation and the increased intensification rate perturbation simulation (IIR; dark blue); reversed sign intensification rate perturbation simulation (RIIR; light blue); decreased intensification rate perturbation simulation (DIR; red); and reversed sign decreased intensification rate perturbation simulation (RDIR; pink). The magenta, vertical bars indicate the response period over which changes to the intensification rate by the QOIP to the analysis are intended. The cases plotted are seen as (a) SSS; (b) SOTC; and (c) j15 simulations

Figure 4.12. Non-normalized vertical perturbation profiles for the SSS-IIR case valid at (a) F000; (c) F006; (e) F012; (g) F017 – beginning of the response period; (i) F024 – end of response period. Vertical perturbation profiles normalized by the sum of the total energy (e.g., the sum of the components) valid at (b) F000; (d) F006; (f) F012; (h) F017 – beginning of the response period; (j) F024 – end of response period. The components of the energy are colored as blue – kinetic energy; red – available potential energy; black – elastic energy; cyan – moist energy. Energy components are computed by taking the mean of the component values on every level.

Figure 4.13. Non-normalized vertical perturbation profiles for the SOTC-IIR case valid at (a) F000; (c) F006; (e) F012; (g) F017 – beginning of the response period; (i) F024 – end of response period. Vertical perturbation profiles normalized by the sum of the total energy (e.g., the sum of the components) valid at (b) F000; (d) F006; (f) F012; (h) F018 – beginning of the response period; (j) F027 – end of response period. The components of the energy are colored as blue – kinetic energy; red – available potential energy; black – elastic energy; cyan – moist energy. Energy components are computed by taking the mean of the component values on every level.

Figure 4.14. Non-normalized vertical perturbation profiles for the j15-IIR case valid at (a) F000; (c) F006; (e) F012; (g) F016 – beginning of the response period; (i) F021 – end of response period. Vertical perturbation profiles normalized by the sum of the total energy (e.g., the sum of the components) valid at (b) F000; (d) F006; (f) F012; (h) F017 – beginning of the response period; (j) F024 – end of response period. The components of the energy are colored as blue – kinetic energy; red – available potential energy; black – elastic energy; cyan – moist energy. Energy components are computed by taking the mean of the component values on every level.

Figure 4.15. Non-normalized vertical perturbation profiles for the j15-DIR case valid at (a) F000; (c) F006; (e) F012; (g) F016 – beginning of the response period; (i) F021 – end of response period. Vertical perturbation profiles normalized by the sum of the total energy (e.g., the sum of the components) valid at (b) F000; (d) F006; (f) F012; (h) F017 – beginning of the response period; (j) F024 – end of response period. The components of the energy are colored as blue – kinetic energy; red – available potential energy; black – elastic energy; cyan – moist energy. Energy components are computed by taking the mean of the component values on every level.

Figure 4.16. Non-normalized vertical perturbation profiles for the SOTC-DIR case valid at (a) F000; (c) F006; (e) F012; (g) F018 – beginning of the response period; (i) F027 – end of response period. Vertical perturbation profiles normalized by the sum of the total energy (e.g., the sum of the components) valid at (b) F000; (d) F006; (f) F012; (h) F017 – beginning of the response period; (j) F024 – end of response period. The components of the energy are colored as blue – kinetic energy; red – available potential energy; black – elastic energy; cyan – moist energy. Energy components are computed by taking the mean of the component values on every level.

Figure 4.17. Non-normalized vertical perturbation profiles for the SSS-DIR case valid at (a) F000; (c) F006; (e) F012; (g) F017 – beginning of the response period; (i) F024 – end of response period. Vertical perturbation profiles normalized by the sum of the total energy (e.g., the sum of the components) valid at (b) F000; (d) F006; (f) F012; (h) F017 – beginning of the response period; (j) F024 – end of response period. The components of the energy are colored as blue – kinetic energy; red – available potential energy; black – elastic energy; cyan – moist energy. Energy components are computed by taking the mean of the component values on every level.

Figure 4.18. Cross section of the analysis time zonal-mean BEC from 60°W to 100°W longitude and 20°N to 55°N latitude (fill; $\text{m}^2 \text{s}^3$) for the (a) SSS-IIR; and (b) SOTC-IIR and (c) j15-IIR. Initial time BEC rates for IIR and RIIR (DIR and RDIR) are similar, and therefore not shown.

Figure 4.19. Time series of BEC normalized by the total kinetic energy (s^{-1}) over the course of the forecast integrations for the reversed sign intensification rate perturbation simulation (IIR; dark blue); reversed sign intensification rate perturbation simulation (RIIR; light blue); decreased intensification rate perturbation simulation (DIR; red); and reversed sign decreased intensification rate perturbation simulation (RDIR; pink). BEC rates in shown are (a) SSS (calculated and summed over a 400 hPa to 150 hPa layer); (b) SOTC (calculated and summed over a 600 hPa to 150 hPa layer); and (c) j15 (calculated and summed over a 400 hPa to 150 hPa layer). The magenta, dashed vertical bars indicate the response period over which changes to the intensification rate by the QOIP to the analysis are intended. Note that SOTC failed the linearity test within the QOIP algorithm after the first iteration for each case, resulting in only one iteration for both the IIR and DIR simulations. Therefore, no additional RIIR and DIIR simulations were performed.

Figure 4.20. SOTC-IIR upper level QGPV perturbations (red to blue fill; s^{-1}); control simulation height (magenta, dashed contour; m); perturbed simulation height (dark blue, solid contour; m); and inverted wind (vectors; $m s^{-1}$); valid at (a) F012; (b) F18; and (c) F27 and large-scale precipitation perturbations (brown to green fill; in hr^{-1}); control simulation height (dark green solid contours, dashed contour; m); and control simulation theta (red, dashed contour; m) valid at (d) F012; (e) F18; and (f) F27. QGPV perturbations are largely coincident with large-scale precipitation perturbations, indicating the important on diabatic effects on the QGPV perturbations. Wind less than $5 m s^{-1}$ is masked.

Figure 4.21. j15 layer averaged QGPV perturbations (fill; s^{-1}); control simulation height (magenta, dashed contour; m); perturbed simulation height (dark blue, solid contour; m); and inverted wind (vectors; $m s^{-1}$); valid at 16 hours into the simulation for (left) the IIR experiment, and (right) the RIIR experiment, for (top) the upper-troposphere, (middle) the middle-troposphere, and (bottom) the lower-troposphere. Note that lower-tropospheric contours in panels (c) and (f) intersect high terrain. Wind less than $5 m s^{-1}$ is masked.

Figure 4.22. j15 large-scale (fill; in hr^{-1}); control simulation height (magenta, dashed contour; m); and perturbed simulation height (dark blue, solid contour; m) precipitation perturbations valid for (a) F016 – IIR; (b) F016 – DIR; (c) F021 – IIR; (d) F021 – DIR.

Figure 4.23. j15 layer averaged QGPV perturbations (fill; s^{-1}); control simulation height (magenta, dashed contour; m); perturbed simulation height (dark blue, solid contour; m); and inverted wind (vectors; $m s^{-1}$); valid at 21 hours into the simulation for (left) the IIR experiment, and (right) the RIIR experiment, for (top) the upper-troposphere, (middle) the middle-troposphere, and (bottom) the lower-troposphere. Note that lower-tropospheric contours in panels (c) and (f) intersect high terrain. Wind less than $5 m s^{-1}$ is masked.

Figure 4.24: j15 control-simulation-cyclone-following summed 900 hPa inverted height perturbations for the (a) IIR; (b) RIIR; (c) DIR; and (d) RDIR cases. The solid lines colored as labeled represent the sum of the perturbations within a 9° by 9° box. The lines are bound within traces of summed 7° by 7° and 11° by 11° boxes. The observed contour is computed as the 900 hPa perturbation height difference between the perturbed and control simulations. The integration time is found on the x-axis with the gray, dashed lines representing the goal-post times of the response period. The summed perturbation values are found along the y-axis.

Figure 4.25. j15 – IIR piecewise 16-hr 900 hPa inverted height perturbations (fill; m); inverted wind (vectors; $m s^{-1}$); control simulation height (magenta, dashed contour; m); and perturbed simulation height (dark blue, solid contour; m) for (a) upper-level; (b) mid-level; (c) lower-level; (d) surface QGPV; and (e) total inversions. Wind less than $5 m s^{-1}$ is masked.

Figure 4.26. j15 – IIR piecewise 21-hr 900 hPa inverted height perturbations (fill; m); inverted wind (vectors; m s^{-1}); control simulation height (magenta, dashed contour; m); and perturbed simulation height (dark blue, solid contour; m) for (a) upper-level; (b) mid-level; (c) lower-level; (d) surface QGPV; and (e) total inversions. Wind less than 5 m s^{-1} is masked.

Figure 4.27. j15 – DIR piecewise 16-hr 900 hPa inverted height perturbations (fill; m); inverted wind (vectors; m s^{-1}); control simulation height (magenta, dashed contour; m); and perturbed simulation height (dark blue, solid contour; m) for (a) upper-level; (b) mid-level; (c) lower-level; (d) surface QGPV; and (e) total inversions. Wind less than 5 m s^{-1} is masked.

Figure 4.28. j15 – DIR piecewise 21-hr 900 hPa inverted height perturbations (fill; m); inverted wind (vectors; m s^{-1}); control simulation height (magenta, dashed contour; m); and perturbed simulation height (dark blue, solid contour; m) for (a) upper-level; (b) mid-level; (c) lower-level; (d) surface QGPV; and (e) total inversions. Wind less than 5 m s^{-1} is masked.

Chapter 5.

Figure 5.1. 500 hPa (a) GEFS stream function standardized uncertainty anomaly (fill; $\text{m}^2 \text{ s}$) and mean stream function (contour; $10^{-7} \text{ m}^2 \text{ s}$); and (b) 24-hr sensitivity of cyclone intensity into the forecast to the analysis time 500 hPa stream function (fill; 10^8 Pa s m^{-2}) and the deterministic GEOS-5 500 hPa stream function (contour; $10^{-7} \text{ m}^2 \text{ s}$), valid 2000 January 24 0000 UTC. Significant overlap between positive SUA and non-zero sensitivity indicates anomalously low levels of predictability are likely with respect to the intensity of the cyclone 24-hrs into the forecast. When assessing overlap between the two quantities, it is only the magnitude of the sensitivity that need be considered.

Figure 5.2. 500 hPa (a) GEFS stream function standardized uncertainty anomaly (fill; $\text{m}^2 \text{ s}$) and mean stream function (contour; $10^{-7} \text{ m}^2 \text{ s}$); and (b) 60-hr sensitivity of cyclone intensity into the forecast to the 36-hr forecast state 500 hPa stream function (fill; 10^8 Pa s m^{-2}) and the deterministic GEOS-5 500 hPa stream function (contour; $10^{-7} \text{ m}^2 \text{ s}$), valid 2000 January 25 1200 UTC. Lessened overlap between *positive* SUA and *non-zero* sensitivity as compared to 36-hrs previous indicates higher levels of predictability are likely with respect to the intensity of the cyclone 60-hrs into the forecast. When assessing overlap between the two quantities, it is only the magnitude of the sensitivity that need be considered.

Figure 5.3. 500 hPa (a) GEFS stream function standardized uncertainty anomaly (fill; $\text{m}^2 \text{ s}$) and mean stream function (contour; $10^{-7} \text{ m}^2 \text{ s}$); and (b) 24-hr sensitivity of cyclone intensity into the forecast to the analysis time 500 hPa stream function (fill; 10^8 Pa s m^{-2}) and the deterministic GEOS-5 500 hPa stream function (contour; $10^{-7} \text{ m}^2 \text{ s}$), valid 1993 March 0000 UTC. Negligible overlap between *positive* SUA and *non-zero* sensitivity indicates anomalously high levels of predictability are likely with respect to the intensity

of the cyclone 24-hrs into the forecast. When assessing overlap between the two quantities, it is only the magnitude of the sensitivity that need be considered.

Figure 5.4. 500 hPa (a) GEFS stream function standardized uncertainty anomaly (fill; $\text{m}^2 \text{s}$) and mean stream function (contour; $10^{-7} \text{m}^2 \text{s}$); and (b) 60-hr sensitivity of cyclone intensity into the forecast to the 36-hr forecast state 500 hPa stream function (fill; 10^8Pa s m^{-2}) and the deterministic GEOS-5 500 hPa stream function (contour; $10^{-7} \text{m}^2 \text{s}$), valid 1993 March 12 1200 UTC. Non-negligible overlap between positive SUA and non-zero sensitivity indicates a small but non-negligible level of unpredictability for the 60-hr forecast of intensity. When assessing overlap between the two quantities, it is only the magnitude of the sensitivity that need be considered.

Figure 5.5. A schematic diagram indicating how equivalently timed SUA and forecast-state sensitivity gradients are calculated. The GEFS and GEOS-5 are initialized at the same analysis time, with the GEOS-5 integrated 24-hrs longer than the GEFS integration. The GEOS-5 adjoint is then integrated backwards in time 24-hrs, resulting in SUA and sensitivity gradients valid at equivalent times.

List of Tables

Table 3.1. Isobaric layers over which experimental quantities are averaged.

Table 4.1. GEOS-5 hybrid-sigma coordinate and equivalent isobaric levels in hPa.

Chapter 1: Introduction

1.1 Baroclinic Growth of Mid-Latitude Cyclones

The fundamental dynamics of mid-latitude cyclogenesis can be explained through the process of baroclinic conversion of available potential energy (APE) to eddy kinetic energy manifest as growth of a wave disturbance (e.g., Eady 1949; Lindzen and Farrell 1980; Farrell 1982a; Farrell 1985; Farrell and Ioannou 1996). Within the atmosphere, this process is consistent with what Petterssen and Smebye (1971) termed “Type-B” cyclogenesis, and typically occurs as an upper-tropospheric potential vorticity (PV) anomaly approaches a lower tropospheric frontal wave (baroclinic zone). As this upper level wave approaches the surface baroclinic zone, barotropic deformation by the horizontal shear may cause the disturbance to become increasingly isotropic, (Simmons and Hoskins 1980; Kucharski and Thorpe 2001) helping to impart a cyclonic circulation upon the surface baroclinicity and allow for the development of a surface thermal ridge (downstream of the upper level vorticity maximum), which Bretherton (1966) demonstrated as being equivalent to a near-surface cyclonic quasi-geostrophic (QG) PV anomaly. This near surface QGPV anomaly likewise imparts a circulation onto the wave aloft, and helps to amplify and develop the upper-tropospheric disturbance in a process known as “mutual amplification” (Petterssen 1956; Hoskins et al. 1985). This mutual amplification process results in an amplifying baroclinic wave characterized by an upshear tilt with height of the stream function/geopotential and an downshear tilt with height of the temperature field (Fig. 1.1; Eady 1949).

In his seminal paper, Eady describes parametric dependence of the rate of this baroclinic growth, σ , as a function of the baroclinic shear (\bar{u}_z), Coriolis parameter (f), and stratification (N), which can be expressed as

$$\sigma \propto \frac{f\bar{u}_z}{N}. \quad (1.1)$$

It can therefore be surmised that the baroclinic growth rate at a given latitude will be greatest within environments characterized by strong baroclinic shear (equivalent to a large horizontal thermal gradient) and weak stratification.

The importance of stratification can further be seen within the QG framework. It can be shown through PV invertibility (Davis and Emanuel 1991; Davis 1992a) that the non-divergent and irrotational components of the QG balanced wind field are strongly dependent upon stratification as well, which implies stratification plays an important role in the low-level convergence and vortex column stretching that controls cyclogenesis. Additionally, it is well-understood that cyclogenesis is associated with upward vertical motion (i.e., vortex stretching) near the surface. The Q-vector form of the QG-omega equation² can be expressed as:

$$N \left(\nabla^2 + \frac{f_0^2}{N} \frac{\partial^2}{\partial p^2} \right) \omega = -2\nabla \cdot \bar{\mathbf{Q}}, \quad (1.2)$$

where N represents a measure of the stratification, ω represents vertical motion, and $\bar{\mathbf{Q}}$ represents the Q-vector, The divergence of the Q-vector represents an alternative form of the right hand side forcing terms (vertical derivative of vorticity advection and the horizontal Laplacian of temperature advection) of the classical (adiabatic, inviscid) QG-omega equation, and whose convergence results in the spin-up of cyclonic vorticity

² Traditionally, the stratification term is expressed as σ , however to be consistent across both expressions (1.1) and (1.2), σ will refer to the Eady growth rate and N the stratification.

(Hoskins et al. 1978). Given two identical situations in which the right hand side (RHS) forcing remains the same, the only modulator of the vertical motion, and the associated deepening of a cyclone, is the stratification – a variable that is strongly controlled by multiple types of diabatic processes (e.g., condensational heating by convection; cloud development and precipitation; and surface moisture and temperature flux variations). This dependence upon moisture in determining stratification was convincingly shown in Emanuel et al. (1987), who demonstrated through numerical simulations that condensation processes increase the growth rate of baroclinic waves where saturated air renders effective stratification to be zero.

1.2 A Brief History of Our Understanding of Mid-latitude Cyclogenesis

The first model of the life-cycle of a mid-latitude cyclone can be attributed to scientists at the Bergen School of Meteorology (e.g., Bjerknes 1919; Bjerknes and Solberg 1922). The accuracy and contemporary relevance of what was discovered at Bergen is remarkable given the dearth of real-time observational coverage at the time. The scientists at Bergen were not only able to postulate the horizontal and vertical structure of the evolution of a mid-latitude cyclone and the energetics associated with each stage, but also that there existed two main types of occlusions (warm- and cold-type). The latter discovery is particularly impressive considering that observations were limited to platforms such as kite soundings and visual observation of clouds (Shapiro and Keyser 1990). The resulting conceptual model for cyclogenesis came to be known as the Norwegian Cyclone Model (NCM) and is comprised of four main periods of development: (I) incipient frontal cyclone, (II) open wave phase (III) narrowing warm

sector and seclusion, (IV) occlusion. A conceptual diagram of the NCM can be seen in Fig. 1.2.

In the 40 years following the initial work at Bergen, several further refinements and advances of note were made to the framework laid out within the NCM. Rossby and Weightman (1926) first applied the NCM to North America, identifying the origins of the air masses that drive mid-latitude cyclones, as well as pointing out that the uniform character of the precipitation shields (especially within the warm-frontal region) was oversimplified and that warm, moist air overrunning colder air resulted in convective instability and deep, moist convection. Bjerknes and Palmén (1937) asserted that the vertical structure of the frontal boundaries associated with mid-latitude cyclones was continuous from the surface to the tropopause. Later studies went on to reveal the character of the vertical structure of fronts as being often discontinuous, with separated upper and lower level fronts governed by differing dynamics (e.g., Reed and Sanders 1953, Sanders 1955; Shapiro 1970; Bosart 1970). Bjerknes (1937; 1939) developed a better understanding of the vertical structure of the mid-latitude cyclone, outline of the vertical motion field associated with mid-latitude cyclones by deriving the divergence field in the upper-troposphere from the gradient wind equation and explaining the role of conservation of vorticity in the development of long-waves in the atmosphere, respectively. Bjerknes and Holmboe (1944) would go on to clarify further the divergence patterns associated with the vertical coupling of upper- and lower-level waves, explaining that cyclones are characterized by a westward tilt with height due to the necessity of upper-level divergence downstream of an upper trough. The advancements by Bjerknes and Holmboe marked a significant advancement in the theory of mid-latitude cyclone

dynamics, explaining the important relationship between the vertical shear (baroclinicity) and the intensity of the three-dimensional divergence field³.

As computational capacity increased by the middle of the 20th century, it became possible to create quasi-realistic numerical simulations of amplifying baroclinic waves such as those seen in the real atmosphere. Simulations of three-dimensional Eady waves (e.g., Hoskins 1976; Hoskins and West 1979; Heckley and Hoskins 1982) displayed frontal evolutions unlike those consistent with the NCM, seemingly much to the surprise of the authors⁴, such as frontolysis near the cyclone center during the early stages of development, a warm frontal structure that migrated westward into the northerly flow west of the intensifying cyclone (similar to the bent-back front theorized by Godske et al. 1957), and a warm-core seclusion well into the cold air region of a fully developed cyclone (Shapiro and Keyser 1990). As a result of these inconsistencies between simulation and the NCM, Shapiro and Keyser (1990) devised a new model for cyclogenesis based upon both numerical simulations and observations. The Shapiro-Keyser (S-K) model is also comprised of four periods of development; (I) incipient frontal cyclone, (II) frontal fracture (due to decreased baroclinicity and resulting cold-frontolysis near the low center), (III) frontal T-bone and bent-back front, (IV) frontal T-bone and warm seclusion. The conceptual model of the S-K model can be seen in Fig. 1.3.⁵

³ For a general history on the research advancements of extratropical cyclones, the reader is referred to *The Life Cycles of Extratropical Cyclones* edited by Sigbjørn Grønås and Melvyn Shapiro (1994), which discusses these and other articles on the subject in great detail.

⁴ Heckley and Hoskins (1982) even went so far as to note that a mathematically simplified tropopause lid perhaps undermined the realism of the results shown in Hoskins (1976) and Hoskins and West (1979)

⁵ For a succinct summary of the evolution of the cyclone model paradigm over the intervening period between the advent of the Norwegian cyclone and S-K models, the reader is referred to Shapiro and Keyser (1990), which discusses these and other articles on the subject in great detail.

Several studies have attempted to show the relationship between the large-scale atmospheric flow and the model of cyclogenesis (NCM vs S-K). Idealized numerical simulations (e.g. Davies et al. 1991; Schultz et al. 1998; Wernli et al. 1998) have shown that those cyclones that move into diffluent, high-amplitude downstream ridges are more likely to become meridionally elongated, possessing a strong cold front and weak, “stubby” warm front. The cyclone eventually develops a NCM type classical occlusion, as the cold front rotates into and undercuts the warm front. By contrast, cyclones that move into confluent, low-amplitude zonal flow patterns however are more likely to become more zonally elongated and possess strong, zonally oriented warm and bent-back fronts and weaker cold fronts (Schultz et al. 1998). Since these types of flow patterns are highly idealized, they are rarely representative of the real atmosphere in which the large-scale flow pattern is constantly evolving. Therefore, cyclones transitioning between large-scale flow patterns may exhibit behavior characteristic of either or both models at varying points in their lifecycles.

1.3 Explosive Cyclogenesis

The propensity for rapidly intensifying, or *explosive* cyclones, to occur along the highly populated urban corridor of the eastern seaboard of the United States characterizes these storms as events of high socio-economic impact that pose a tremendous forecasting challenge with respect to public safety and the successful carriage of commerce. The dynamics and phenomenology of explosive cyclones have been subject to a multitude of studies within the past 40 years (e.g., Sanders and Gyakum 1980; Sanders 1986; Anthes et al. 1983; Reed and Albright 1986; Chen et al. 1992; Huo et al. 1995; Wang and Rogers

2001; Boettcher and Wernli 2011; Heo et al. 2015), with two major field campaigns taking place in the late 1980s to provide *in situ* observations: The Experiment on Rapidly Intensifying Cyclones in the Atlantic (Hadlock and Kreitzberg 1988; Kuo et al. 1996; ERICA) and the Genesis of Atlantic Lows Experiment (Dirks et al. 1988; GALE).

Explosive cyclogenesis events typically occur during the cold season along the warm, western boundary currents of the Atlantic (The Gulf Stream) and Pacific (Kuroshio current) basins where strong sea surface baroclinicity associated with strong sea surface temperature (SST) gradients is present (Sanders and Gyakum 1980; Kuo et al. 1990). Eastward moving, continental cold-air outbreaks act to lessen static stability and encourage transfer of latent and sensible heat as well as moisture from the ocean surface (the latter demonstrated by Emanuel et al. (1987) to be another method by which to lower the effective stratification). It is not uncommon along the eastern United States for the development of a semi-stationary surface boundary known as the *coastal front*, a boundary rich in surface vorticity from which explosive cyclones can form (Miller 1946; Bosart 1981). In the mid- and upper-troposphere, explosive development is typically found downstream of a mobile 500 hPa trough or poleward of maximum westerlies and ahead or within planetary scale troughs (Sanders and Gyakum 1980; Reed 1990). These explosively deepening cyclones, also known as “bombs”, are defined as extratropical cyclones whose central minimum pressure falls at an average rate of no less than one Bergeron, defined as the 24-hr pressure decrease multiplied by a factor based on latitude (typically normalized to 60° latitude) such that one Bergeron represents a 24-hr pressure drop of between 12-28 hPa depending on latitude (Sanders and Gyakum 1980). Roebber (1984) showed that a histogram of 24-hour deepening rates of Northern Hemisphere

surface cyclones was bimodal (Fig 1.4 from Martin (2006), adapted from Roebber 1984), where the primary peak is centered on cyclones that undergo a more “ordinary” deepening and a smaller, secondary peak is centered on bombs. This bimodal distribution suggests that explosively deepening cyclones are likely a separate class of cyclones modulated by processes distinct from cyclones that deepen less rapidly.

While bombs, like ordinary cyclones, are fundamentally manifestations of baroclinic growth processes (Sanders 1986; Anthes et al. 1983; Orlanski and Sheldon 1995), they are undoubtedly more complex atmospheric phenomena which, from a synoptic perspective, are likely influenced by a confluence of multiple diabatic effects that separate their development from that of “ordinary” cyclones. Identifying the specific impacts of those diabatic effects is not an easy task. Within explosively deepening cyclones, it is not uncommon for intense moist convection to develop (Gyakum 1983a, b; Reed and Albright 1986; Rogers and Bosart 1986; Huo et al. 1995). To first order, this convection can act to a) reduce static stability, N , in saturated updrafts; and b) diabatically generate an upper-level shortwave ridge downstream (via latent heat release associated with clouds and precipitation) of the cyclone center, thus increasing advection of cyclonic PV by the thermal wind and further helping to develop the cyclone through enhanced vertical motion near the surface by virtue of self-development (Kocin and Uccellini 1990). Both of these effects are consistent with traditional development perspectives of mid-latitude cyclones.

Perhaps even more importantly, the intense latent heating release in vigorous convection may tip the scale from “ordinary” to “explosive” cyclogenesis for some storms. Although practically all mid-latitude cyclones are influenced by latent heat

release, many studies assert that cyclones undergoing explosive deepening often experience higher rates of latent heat release through the aforementioned deep convection than is observed in more ordinary cyclones. Reed and Albright (1986) discuss a plume of convective instability (and resultant condensational heating by vigorous thunderstorm development) found near the center of a cyclone that soon thereafter underwent a period of explosive deepening. Reed et al. (1988) demonstrated that within a poorly forecast bomb near the Nova Scotia, models inadequately simulated the convection resulting from what was observed to be a very unstable air mass characterized by lifted indices of approximately -6° within the cyclone's inflow region.

In addition to the effects of upright convection, Reed and Albright (1986) suggested that symmetric instability (Emanuel 1983) found within frontal cloud bands is an important factor in explosive cyclogenesis, an idea that Kuo and Reed (1988) confirmed through a numerical simulation of an explosive cyclone initialized at the onset of the explosive deepening period. During this period, it was shown that a symmetrically neutral to slightly unstable state existed within a region of low-level inflow ahead of the storm, a region also characterized by strong vertical velocities and enhanced spin-up of vertical vorticity. This suggests that a key feature of explosive development is the magnitude of the slantwise ascent found above warm fronts, a result further described and confirmed by Huo et al. (1995) in their exploration of the dynamics of the 1993 "Storm of the Century".

Finally, there may exist difficult to simulate, non-linear interactions on small spatio-temporal scales that contribute to distinguishing between ordinary and explosive cyclones (Anthes et al. 1983; Uccellini 1990; Kuo et al. 1991; Wang and Rogers 2001;

Heo et al. 2015). Even within a dry-dynamics adjoint model framework, Langland (1995) further supports this consideration in a study of an idealized extratropical cyclone, pointing to lower tropospheric thermodynamics (e.g., sensitivity to lower tropospheric baroclinicity and thermal advection) as well as surface heat flux and surface momentum stress as being important to intensification of cyclones. Although it is hard to appropriately address difficult to simulate, non-linear processes within an adjoint framework, Langland is able to approximate the generalized expressions for both the sensible heat flux and surface momentum stress in order to calculate the sensitivity of near surface kinetic energy (per unit mass) to both quantities respectively. Another adjoint study on severe extratropical cyclone Xynthia was performed by Doyle et al. (2014) and showed similar results within a real-world case, in which the inclusion of the adjoints of sophisticated boundary layer and surface flux schemes provided for the ability to calculate the sensitivity to SST (and the implied importance of sea surface temperature and moisture flux into the atmosphere), and thereby allowed for an objective example of the importance of small-scale non-linear processes within the rapid growth of cyclones.

Additionally, it was shown that the sensitivity maxima to low- and mid- level temperature and moisture perturbations had a greater impact on the intensity of Xynthia than did perturbations to the wind field, further indicating the relative importance of diabatic impacts on cyclogenesis. Finally, it should be noted that the sensitivity maxima appeared to be oriented along a sloping, warm-frontal boundary in the low- and mid-levels as within the warm-conveyor belt region, a result consistent with the idea that processes attendant to the the warm front are likely a key contributors to the explosive development process.

1.4 Motivation

To adequately motivate this study, the methodology is summarized here and how it differs from previous studies of explosive cyclogenesis is described. In prior studies (Atlas 1987; Chen and Dell’Osso 1987; Mullen and Baumhefner 1988; Mailhot and Chouinard 1989; Sanders et al. 1999; Ludwig et al. 2013; Heo et al. 2015), the dynamics of explosive cyclones have been explored through an intuition-based exploration of the sensitivity of numerical weather prediction model simulations of these events to model initial conditions and forcing. In these prior studies, unperturbed, control simulations were compared to simulations in which the parameterizations or initial conditions of a model were altered based on intuition about what parameterized processes or synoptic scale features were perceived as being the most important. As a result, these studies are highly subjective in nature and do not represent a full sampling of all of the possible initial-time perturbations to which that a cyclone could be sensitive. In this study, the use of an adjoint model will be employed to define the sensitivity of a cyclone’s intensity to the initial model state, a method that not only calculates *objective*, dynamical sensitivity of specific aspects of the forecast state to earlier model states, but also allows for the calculation of optimal perturbations to the earlier model state (most often the analysis state) based upon those sensitivities.

Although there *have* been previous adjoint-based sensitivity studies of explosive cyclones (e.g., Doyle et al. 2014; Chu et al 2016), these studies focus on sensitivities of cyclone *intensity* at particular times within the evolution of a forecast trajectory. The new methodology proposed in this work defines the time-tendency of cyclone intensity as the

forecast field of interest (i.e., the response function), thus allowing for the calculation of the sensitivities (and resultant perturbations) to the *rate* of intensification of the cyclone over a prescribed period in the forecast to perturbations of the model state at an earlier time. This difference in methodology allows for an objective evaluation of how perturbations to model state variables (as well as derived variables, see Section 2.1.2) influence the actual *deepening process*, rather than what leads to a *final, deepened state* of a cyclone. Within this context, a *perturbation-response* framework is introduced, which seeks to evaluate how small initial perturbations to a cyclone simulation change the future intensification rate of that cyclone. With this in mind, several motivating research questions (RQs) are posed:

RQ1: *What are the fundamental processes that can modulate the forecast of rapid intensification (weakening) through small perturbations to the model initial state, and where do these processes appear most important?*

RQ2: *Given the inherent non-linearity within the processes that govern the intensification rates of cyclones, is there a methodology that allows for the relaxation of the tangent-linear assumption (further described in Section 2.1.4) in order to create perturbations which modulate the intensification rates of mid-latitude cyclones?*

RQ3: *Does the character of the perturbations aimed at increasing the intensification rate of cyclones differ greatly from perturbations*

aimed at decreasing the intensification rate of cyclones within a framework of relaxed linearity?

RQ4: *What is the link between sensitivity of cyclone intensification to small perturbations to the initial forecast state and forecast uncertainty/predictability?*

These research questions will be explored through the examination of several case studies of cyclones chosen semi-quantitatively as having had varying levels of predictability. Chapter 2 provides a more in depth explanation of the tools and methodology as well as the data to be used throughout the study. Chapter 3 presents a proof-of-concept case study that displays the efficacy of both the time-tendency of intensity response function as well as the algorithm used as a means by which to introduce non-linearity into adjoint-derived optimal perturbations. In Chapter 4, additional case studies are performed and compared to the results in chapter 3, and implications on predictability discussed in greater detail. Chapter 5 will summarize key findings and discuss future applications of the research techniques described, developed, and applied in this study.

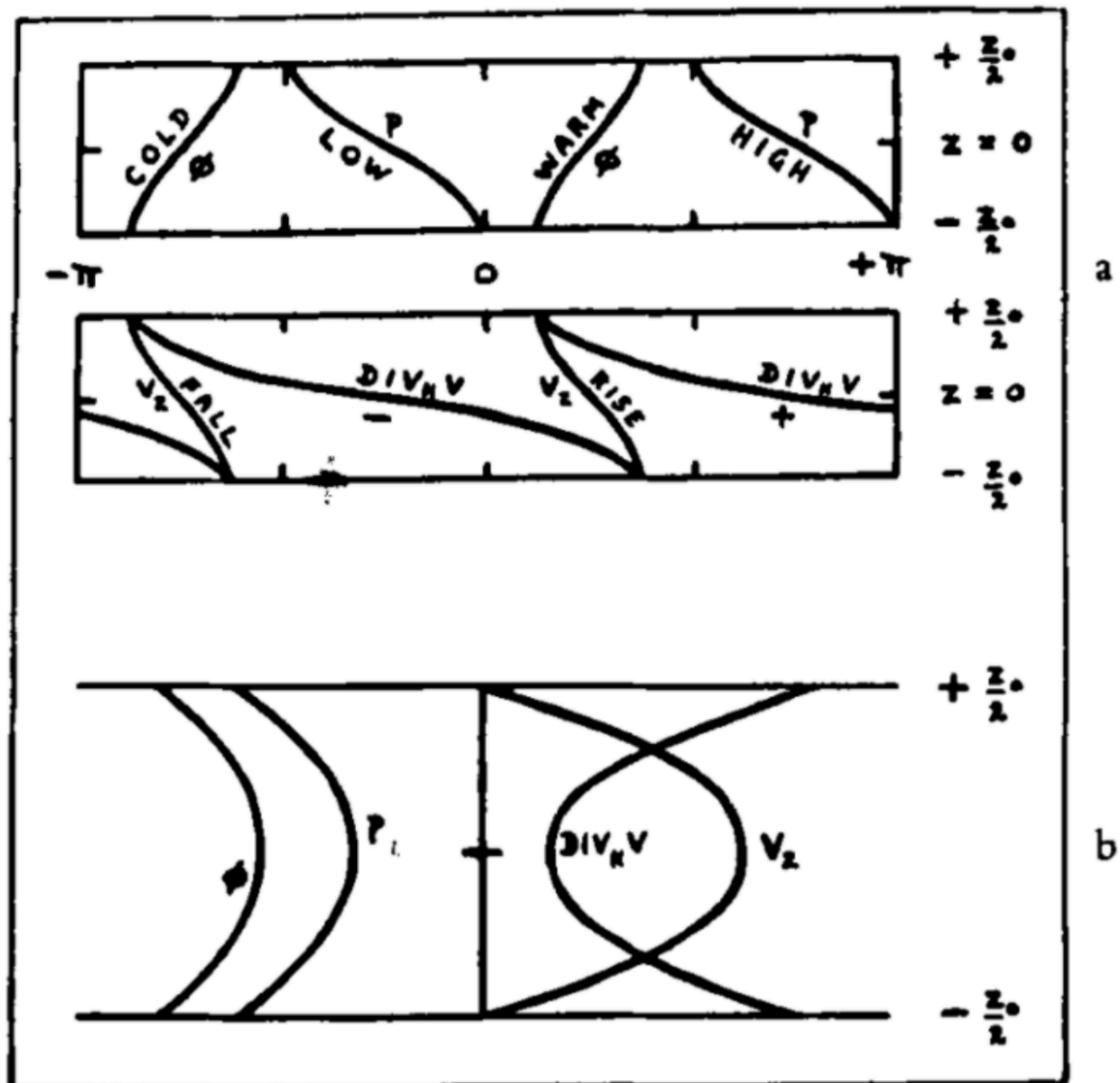


Figure 1.1. Properties of the most unstable Eady wave. (a) Phase variations: Above p , φ ; below v_z , div_{HV} . (b) Amplitude variations: left p , φ ; Right v_z , div_{HV} . (Eady 1949)

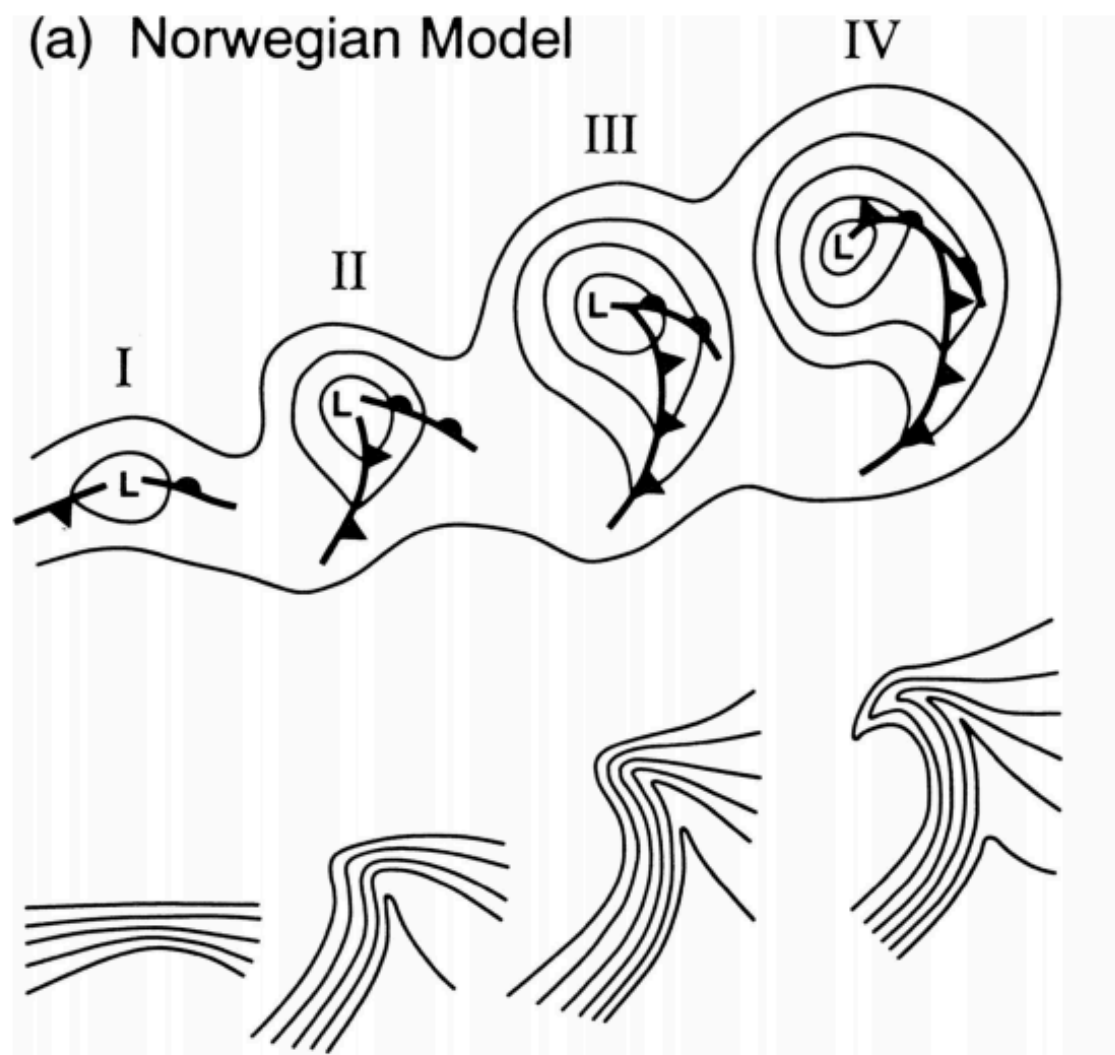


Figure 1.2. The Norwegian Cyclone Model life-cycle evolution with lower tropospheric geopotential height and fronts (top) and lower tropospheric potential temperature (bottom) (Schultz 1998; adapted from Bjerknes and Solberg 1922)

(b) Shapiro–Keyser Model

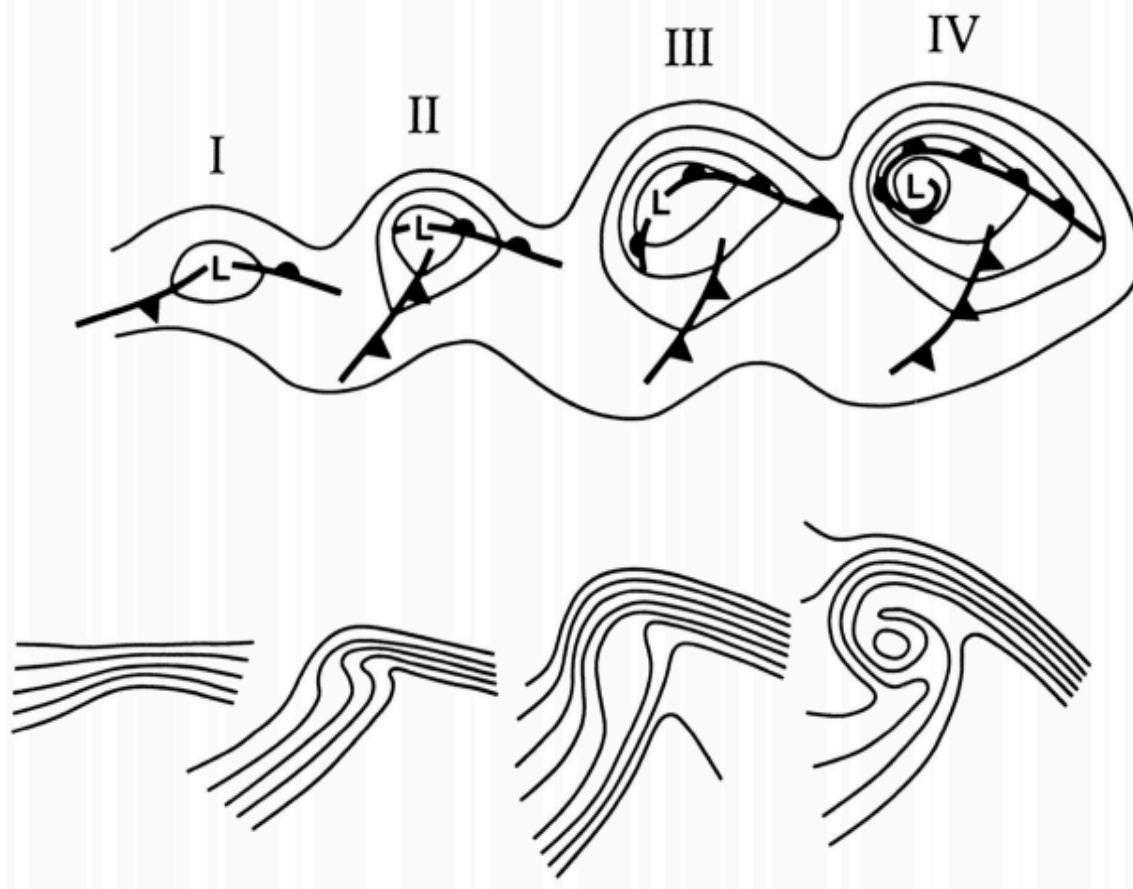


Figure 1.3. The Shapiro–Keyser Cyclone Model life-cycle evolution with lower tropospheric geopotential height and fronts (top) and lower tropospheric potential temperature (bottom) (Schultz 1998; adapted from Shapiro and Keyser 1990)

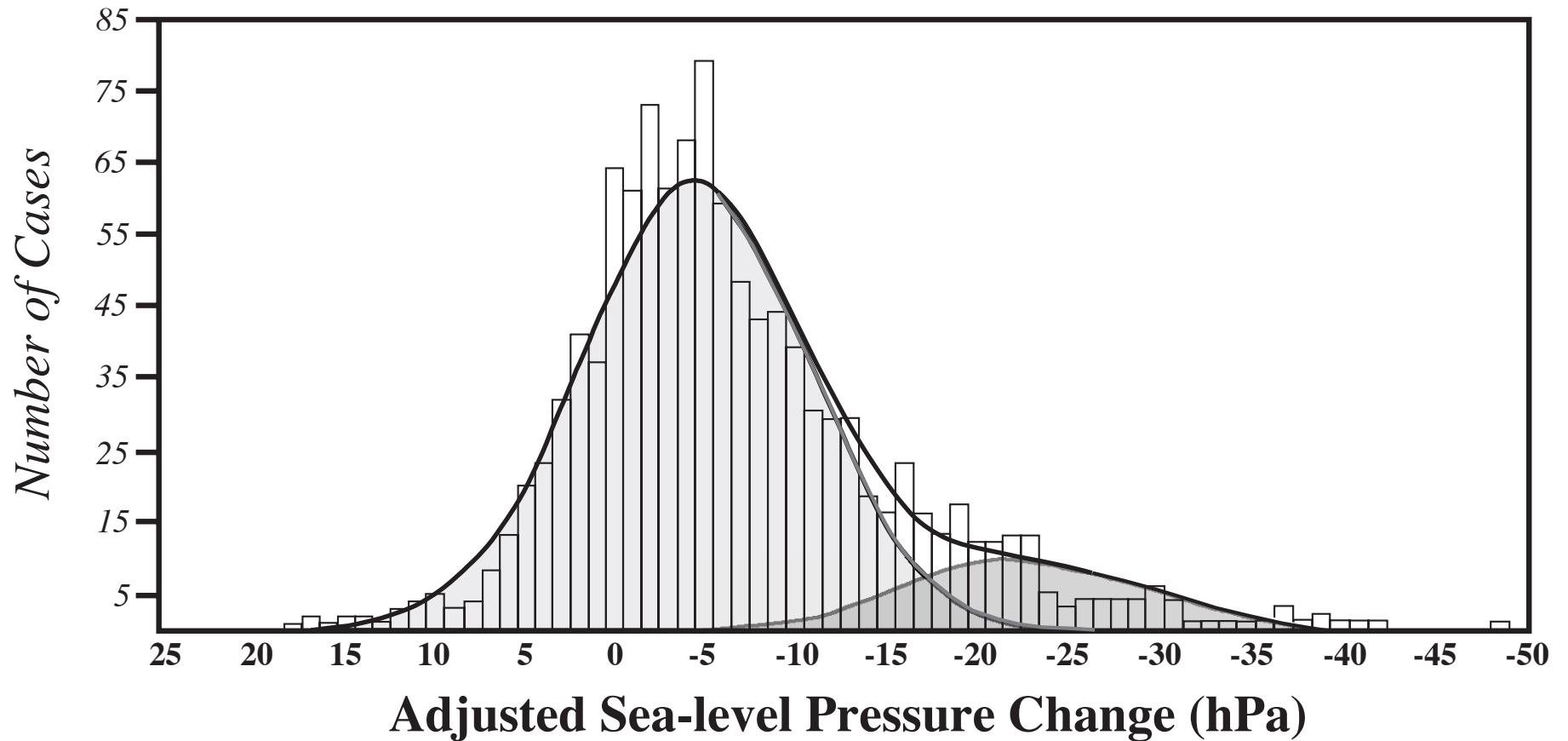


Figure 1.4. Distribution of 24 h deepening rates for all Northern Hemisphere surface cyclones in one year. The dark line indicates the sum of two normal curves while the gray lines and shading represent the separate distributions (light shading for the “ordinary and “darker” for the explosive). Martin (2006); adapted from Roebber (1984)

Chapter 2: Methodology and Tools

2.1 Dynamical Sensitivity Analysis

Dynamical sensitivity analysis is a powerful method for gaining insight into the dynamics of weather systems. This method is a tool to discern the dynamical processes most important to changing some aspect of a numerical weather prediction (NWP) forecast by using the model's adjoint (see Section 2.1.1) to comprehensively and succinctly estimate the change in some function of the model forecast state to perturbations of prior model states. This analysis method is distinctly different from other forms of sensitivity analysis in which a particular parameter of the model, such as the convective parameterization (Ratnam and Kumar 2005), or a presumed feature of importance in the model initial state, such as an upper-tropospheric potential vorticity feature (Fehlmann and Davies 1997), are altered *a priori* to observe their impact on a forecast. These kinds of sensitivity analysis can probe the nonlinear sensitivity of a wide range of forecast aspects at any desired forecast lead time, at the cost of examining the forecast impact of only one prescribed change to the model or initial state. Even sensitivity analysis employing an ensemble of perturbations to model parameterization (Bassill 2015) or initial state (e.g. Brown and Hakim 2015) only samples a narrow range of the possible perturbations. By contrast, adjoint-based dynamical sensitivity analysis samples the full range of possible perturbations subject to limiting assumptions (see Section 2.1.1).

In the context of adjoint-derived sensitivities, a sensitivity is defined as the gradient of some function of the model output state (referred to as a response function,

denoted by R) to the model state at some time, $\frac{\partial R}{\partial \mathbf{x}_\tau}$. Examples of response functions are provided in section 2.1.2.

Adjoint-based dynamical sensitivity analysis has been used to study a wide range of atmospheric phenomena on scales from individual convective storms (Park and Droegemeier 2000) to the global circulation (Blessing et al. 2008). Experiments using adjoints have been performed both within an idealized framework (Langland et al. 1995; Langland et al. 1996) and in full-physics NWP applications such as the dynamics of tropical cyclone steering (Hoover and Morgan 2011) and tropical cyclogenesis (Doyle et al. 2012; Hoover 2015; Holdaway 2015, 2016). Adjoint experiments have also been used to help diagnose error growth within extratropical cyclogenesis (Kleist and Morgan 2005a), the predictability of rapidly deepening extratropical cyclones (Doyle et al. 2014), and the dynamics of sudden stratospheric warming events via troposphere-stratosphere coupling (Holdaway 2016).

For this study, this powerful tool will be employed to gain insight into the dynamics that govern the intensification rates of extratropical cyclones by identifying the lowest energy initial perturbations that change the intensification rate of simulated cyclones by a prescribed amount. The character of those perturbations, their evolution in the NWP model, and their impact on the cyclone and its environment are analyzed using diagnostic tools including piecewise potential vorticity inversion (Davis and Emanuel, 1991; see Section 2.4) to interpret the processes by which they influence the intensification rate of the cyclone at specific periods in the forecast.

2.1.1 Forward and Adjoint Models

A numerical weather prediction (NWP) model can be regarded as a solver of system of non-linear partial differential equations (the dynamical core of the model) that evolve the atmospheric state forward in time from a prescribed initial state to yield a future forecast state. The NWP model M can be represented as a function of the model state (\mathbf{x}_{in}): $M(\mathbf{x}_{\text{in}})$. The model which takes as input \mathbf{x}_{in} , a vector containing the initial and boundary conditions and propagates forward in time to calculate a future state of the system, \mathbf{x}_{out} , where

$$\mathbf{x}_{\text{out}} = M(\mathbf{x}_{\text{in}}) \quad (2.1).$$

Adding to the complexity of these non-linear NWP models, is the inclusion of parameterized physical and moisture schemes that are switched on and off by the dynamical core depending upon the spatial and temporal evolution of the forecast state. These parameterization schemes serve to resolve highly non-linear, small-scale processes on a sub-grid scale through the use of physical approximations and/or closure assumptions.

The tangent linear model (TLM) is a linearization of the dynamical core and physical parameterizations about a *basic* state defined from the trajectory of the nonlinear NWP model. The TLM propagates perturbations to the initial state (\mathbf{x}'_{in}) forward in time to yield perturbations to the final state (\mathbf{x}'_{out}) *as defined by the full physics trajectory of the NWP model* (Hoover 2010). Because the TLM is, in fact, a linear operator, it may be expressed as a matrix, \mathbf{L} , called the “propagator matrix.” The final time state vector of evolved perturbations, \mathbf{x}'_{out} , is then:

$$\mathbf{x}'_{\text{out}} = \mathbf{L}\mathbf{x}'_{\text{in}} \quad (2.2).$$

The adjoint of a linear operator represented by a matrix is the transpose of that matrix, thus the adjoint of the TLM is the matrix \mathbf{L}^T . An adjoint model is a tool to calculate efficiently, sensitivity gradients (Errico 1997). The adjoint propagates sensitivities to the final state, $\frac{\partial R}{\partial \mathbf{x}_{out}}$ backward in time to yield sensitivities to the initial state state $(\frac{\partial R}{\partial \mathbf{x}_{in}})$:

$$\frac{\partial R}{\partial \mathbf{x}_{in}} = \mathbf{L}^T \frac{\partial R}{\partial \mathbf{x}_{out}} \quad (2.3)$$

The resulting initial time *sensitivity gradient* concisely describes how the response function is sensitive to perturbations to the model state initial state. The accuracy of this calculation is limited by the assumptions of linearity and the simplifications to highly nonlinear processes in the model, including those associated with moisture processes, which are often greatly simplified or ignored entirely in the TLM and adjoint. Adjoint models that include linearized moist processes are better capable of resolving the dynamics that drive tropical and extratropical cyclones, but even adjoint models only including dry (adiabatic) dynamics are able to derive useful information about moist processes by being linearized around a trajectory defined by a nonlinear NWP model that includes moist processes (Kleist and Morgan 2005a).

The gradient of the response function can either be computed with respect to a model state variable (Errico 1997) or a variable derived from the state variables (Kleist and Morgan 2005a), allowing for a straightforward and explicit understanding of how small changes made to a prior model state or derived variable may impact the response function at a later forecast state, thus making the technique effective for physical

interpretation. For an NWP forecast initialized from an analysis state, the adjoint sensitivity to an analysis is relevant to the potential impact of analysis errors (which can be treated as perturbations to a perfect analysis or truth-state) on the aspect of the forecast state described by R (e.g. Rabier et al. 1996, Klinker et al. 1998, Kim et al. 2004).

Since the adjoint sensitivity method relies on a linear approximation, the sensitivity gradients are only meaningful over the time which the evolution of perturbations in the TLM is an appropriate approximation to the evolution of perturbations in the nonlinear NWP model. Typically, the linear approximation is accurate over time scales as long as 48-72 hours (Errico et al. 1993) and within processes in which highly nonlinear moist convection does not dominate (Errico and Raeder 1999). Within these constraints, subject to the availability of sophisticated linearized parameterizations for nonlinear model processes (e.g. Mahfouf 1999), the adjoint model gives robust insight into the processes that govern the evolution of the forecast response function. Unlike subjective sensitivity studies where perturbations to initial conditions of the model are made based upon *a priori* expectations about their importance (e.g. Fehlmann and Davies 1997, McTaggart-Cowan et al. 2004), the adjoint technique is able to provide comprehensive, objective information about where perturbations to the initial state will influence the response function of the forecast. It is noted that since the TLM is a linear approximation, sensitivity gradients will not be perfect representations of how small perturbations to the initial state will evolve. However, a simple test can be performed to evaluate the accuracy of the linear approximation by comparing the observed change in the response function, ΔR , between a perturbed and unperturbed nonlinear NWP forecast with the expected change from the adjoint $\delta R = \langle \frac{\partial R}{\partial \mathbf{x}_0}, \mathbf{x}'_0 \rangle$,

where the angle-brackets represent an inner-product. It can be assumed that the TLM is an appropriate approximation to the nonlinear NWP model for the chosen perturbations when $\delta R \cong \Delta R$, providing a check for the appropriateness of the TLM approximation over the chosen forecast, which is often case-dependent. Fig. 2.1 shows schematically the difference between the NWP, TLM and Adjoint models.

2.1.2 Response Functions

As previously stated, a response function R can be defined as some aspect of interest of the model forecast that is differentiable with respect to the model state, \mathbf{x} . There are a number of possible choices of response function that may be used to adequately quantify cyclone intensity. Hoover (2010) provides a careful examination of several response functions aimed at describing intensity of a tropical cyclone with hybrid tropical/extratropical features, and asserts that a surface- or terrain-level pressure (SLP) based response function is most appropriate. In Hoover (2015), an analogous intensity response function describing the integrated bottom-(sigma) level perturbation pressure in a box centered on the minimum sea level pressure of a forecast tropical storm was used to analyze the sensitivity of tropical cyclogenesis to the initial state for simulations of east Pacific tropical cyclogenesis. For the present study, a response function is proposed that describes the time-rate-of-change of intensity based on an SLP-like representation of instantaneous storm intensity. First, an instantaneous intensity response function, R_p , can be defined at a particular forecast time as the average perturbation pressure within a box surrounding a cyclone at the lowest (hybrid-sigma) model level, and can be expressed as:

$$R_p = \frac{\sum_{i,j \in D} p_s}{\sum_{i,j \in D} 1} \quad (2.4),$$

for every grid-point indexed zonally by i and meridionally by j in a 2-dimensional region D defined as a $9^\circ \times 9^\circ$ box centered on the minimum sea-level pressure of a cyclone in the forecast state. The denominator in (4) is the number of points in region D .

Equation 4 is a useful response function that defines the intensity of a cyclone at a specific time (Hoover 2015). By defining the intensity as an average perturbation pressure over a region encompassing the minimum sea level pressure, R_p is relatively insensitive to small displacements of the location of the minimum, while response functions defining the intensity at a single grid-point (e.g. Langland et al. 1995, Ancell and Hakim 2007) would interpret any deflection of the storm track by an initial perturbation as a change in storm intensity. Unlike a storm intensity response function based on the average lower-tropospheric vorticity within the region defined by D (e.g. Kleist and Morgan 2005b), R_p is composed of a smooth and slowly-evolving field with a defined minimum. This response function is preferable to an average-vorticity-based response function as it reduces the influence on R_p from highly nonlinear interactions as individual vorticity minima/maxima near the boundaries of D migrate into and out of the region as a result of initial perturbation. Finally, the value of R_p is strongly controlled by features within the region D , unlike, for example, a response function defined by the average kinetic energy in D (e.g. Doyle et al. 2014), in which R is also strongly controlled by the strength of the geopotential gradient within D , adding ambiguity to whether an increase in the function comes from an intensification of the cyclone or an intensification of a nearby anticyclone.

In order to define a response function for the time-rate-of-change of intensity, it is necessary to define a second response function, R_{dp} , expressed as:

$$R_{dp} = \frac{\partial R_p}{\partial t} \approx \frac{R_p|_{t_2} - R_p|_{t_1}}{\Delta t} \quad (2.5),$$

which describes the difference in the instantaneous intensity (described by R_p) evaluated at two forecast times $t = t_1$ and $t = t_2$, separated in time by Δt . Since the adjoint is linear, it can easily be shown from the above expression that when calculating sensitivity gradients for R_{dp} , the adjoint model can be initialized at two different forecast times $t = t_1$ and $t = t_2$ and each initialization evolved backward along the same nonlinear model trajectory, to define $\frac{\partial R_p}{\partial t}$ at $t=t_0$ from the difference in sensitivity at $t = t_0$ computed from each adjoint integration:

$$\frac{\partial R_{dp}}{\partial \mathbf{x}_0} = \frac{\partial}{\partial \mathbf{x}_0} \left(\frac{R_p|_{t_2} - R_p|_{t_1}}{\Delta t} \right) = \frac{1}{\Delta t} \left(\frac{\partial R_p|_{t_2}}{\partial \mathbf{x}_0} - \frac{\partial R_p|_{t_1}}{\partial \mathbf{x}_0} \right) \quad (2.6).$$

Equation 6 provides a means to compute the sensitivity of the time-rate-of-change of intensity between times t_1 and t_2 , by computing the sensitivity of the instantaneous intensity at those times individually and then performing a finite-difference approximation to the time derivative across the period, $\Delta t = t_2 - t_1$.

2.1.3 Optimal Perturbations

Given an adjoint-derived sensitivity gradient $\frac{\partial R}{\partial \mathbf{x}_0}$, the impact of any initial condition perturbation \mathbf{x}'_0 on the response function can be estimated by the inner-product of the sensitivity gradient with respect to the initial state and the perturbation: $\Delta R \approx \delta R = \langle \frac{\partial R}{\partial \mathbf{x}_0}, \mathbf{x}'_0 \rangle$. The sensitivity gradient itself can be used to construct perturbations designed to change the response function by a specific amount in an optimal fashion. These ‘‘optimal perturbation’’ are optimal in this sense: *they represent initial condition*

perturbations with the smallest initial energy designed to change the response function by a specific amount.

For a cost-function representing the total initial perturbation energy e :

$$e = \frac{1}{2} \left[u'^2 + v'^2 + \frac{c_p}{T_0} T'^2 + RT_0 \left(\frac{p'}{p_0} \right)^2 + \varepsilon \frac{L^2}{c_p T_0} q'^2 \right] \quad (2.7),$$

the cost-function represents a moist static energy norm (Ehrendorfer et al. 1999, Holdaway et al. 2014), where u' , v' , p' , and q' are the perturbed zonal flow, meridional flow, perturbation (i.e. non-static) pressure, and specific humidity, respectively. T_0 and p_0 are reference state temperature (270.00 K) and pressure (1000.00 hPa), respectively, c_p is the specific heat at a constant pressure, R is the dry gas constant, and L is the latent heat of condensation per unit mass. The scalar coefficient ε controls the relative weighting of the moist static energy term, $\frac{L^2}{c_p T_0} q'^2$, within the norm. For the purposes of this study, the moist static energy norm is used to define perturbations optimized for smallest initial “size” by converting each of the perturbed fields into an equivalent energy (kinetic, available potential, elastic, and latent heat energies), which allows for simple comparisons of the relative cost of each of the perturbed fields in the function e .

The coefficients of each perturbed variable represent the diagonal terms in the weighting matrix \mathbf{W} where $e = \frac{1}{2} \langle \mathbf{x}'_0, \mathbf{W} \mathbf{x}'_0 \rangle$. The perturbation to the initial state estimated to yield a prescribed change to the forecast of ΔR while minimizing the cost function $e = \frac{1}{2} \langle \mathbf{x}'_0, \mathbf{W} \mathbf{x}'_0 \rangle$, is solvable as a Lagrange multiplier problem minimizing the Lagrangian:

$$L = e + \lambda \left(\Delta R - \left\langle \frac{\partial R}{\partial \mathbf{x}_0}, \mathbf{x}'_0 \right\rangle \right) = \frac{1}{2} \langle \mathbf{x}'_0, \mathbf{W} \mathbf{x}'_0 \rangle + \lambda \left(\Delta R - \left\langle \frac{\partial R}{\partial \mathbf{x}_0}, \mathbf{x}'_0 \right\rangle \right) \quad (2.8).$$

Differentiation of L with respect to the Lagrange multiplier λ yields:

$$\Delta R = \lambda \frac{\partial R}{\partial \mathbf{x}_0} \mathbf{W}^{-1} \frac{\partial R}{\partial \mathbf{x}_0} \quad (2.9),$$

which can alternatively be expressed as a solution for λ of the form:

$$\lambda = \frac{\Delta R}{\langle \frac{\partial R}{\partial \mathbf{x}_0}, \mathbf{W}^{-1} \frac{\partial R}{\partial \mathbf{x}_0} \rangle} \quad (2.10).$$

Optimal perturbations can be obtained by differentiation of L in (8) with respect to \mathbf{x}'_0 and

by solving given $\frac{\partial L}{\partial \mathbf{x}_0} = 0$:

$$\frac{\partial L}{\partial \mathbf{x}_0} = 0 = \mathbf{W} \mathbf{x}'_0 - \lambda \frac{\partial R}{\partial \mathbf{x}_0} \quad (2.11),$$

which yields:

$$\mathbf{x}'_0 = \lambda \mathbf{W}^{-1} \frac{\partial R}{\partial \mathbf{x}_0} \quad (2.12).$$

The term $\mathbf{x}'_0 = \{u', v', T', p', q'\}$ defines the initial perturbation to the state vector, that will yield a specified change to R , ΔR , while minimizing the initial perturbation energy defined by e in (2.7). This is defined as the *optimal perturbation* for the purposes of the text. The optimal perturbation found in Eqn. 2.12 is informed by the initial time sensitivity gradient as calculated by the adjoint model, therefore providing a relationship between the perturbation itself and the sensitivity gradient. The choice of the moist static energy norm is a subjective choice for an optimization norm, and other choices for norm that defines the weighting coefficients in \mathbf{W} will yield different perturbations defined as optimal that express different growth rates (Snyder and Joly 1998). Similar energy norms have been employed with adjoint models to identify total energy singular vectors, defined as orthogonal sets of perturbations that express the maximum growth over a prescribed verifying area and forecast lead-time, used for

(among other things) investigation of the dynamics of tropical cyclones (Peng and Reynolds 2006, Chen et al. 2009, Kim and Jung 2009, Reynolds et al. 2009, Kim et al. 2011).

2.1.4 Generating *Quasi-Optimal Iterative Perturbations*

Although the adjoint technique is powerful in its ability to calculate objective sensitivity gradients, the linearity assumption it relies upon is a shortcoming that can make it difficult to justify the sensitivity gradients as appropriate estimates of the true sensitivity. This issue may be especially problematic when trying to model a highly nonlinear phenomenon such as rapid-intensification of mid-latitude cyclones. Chu and Yi (2016) studied the appropriateness of the linearity assumption by comparing perturbations evolved through the forecast using the nonlinear model and the TLM in an idealized explosive cyclogenesis simulation. They found that similarity between the linearly-evolved and nonlinearly-evolved perturbations drops off rapidly much earlier in simulations with high relative humidity in the basic-state than for drier simulations. Errico and Raeder (1999) demonstrated that perturbation growth rates varied dramatically between singular vector perturbations defined using dry-physics versus careful inclusion of moist processes in the TLM and adjoint. Zhang et al. (2007) and Selz and Craig (2015) demonstrated that forecast errors grow quickly from small-scale errors in regions of precipitation before transitioning to slowly growing, large-scale errors of the balanced flow. These studies suggest that the quantitative value of adjoint-derived sensitivity gradients is always limited by assumptions of linearity and the simplified (or non-existent) moist physics in the TLM and adjoint, and these limitations need to be carefully

addressed when investigating the dynamics of weather systems in non-idealized conditions.

For this reason, an iterative, inner-/outer-loop technique inspired by incremental four-dimensional variational data assimilation (4DVAR; Courtier et al. 1994) has been developed in order to relax the tangent linear assumption and allow for more exploration of nonlinear evolution of perturbations along the forecast trajectory while using the adjoint-technique to incrementally compose an initial condition perturbation through several iterations. Within this method, a total perturbation is defined through iteratively applying small, optimal perturbations defined to produce small ΔR values, and each incremental perturbation is tested for linearity before it is allowed to be committed to the initial conditions and establish a new nonlinear trajectory around which to linearize for the next incremental perturbation. In this way, what is termed a “*quasi-optimal* total perturbation” is calculated through small steps which each prescribe to optimization.

This technique offers several advantages over producing an optimal perturbation produced from one sensitivity gradient computed along the control (unperturbed) trajectory. First, by iteratively applying small perturbations to the initial conditions and then allowing them to evolve through the nonlinear model to produce a new trajectory around which to linearize for computing the next perturbation, the limitation of linearity in traditional adjoint-based optimal perturbation is relaxed, and since the iterative procedure is not seeking convergence to a minimum as in incremental 4DVAR, there is no concern about failing to converge to a solution (e.g. Tremolet 2005). Second, the accumulation of nonlinear impacts from the iteratively composed perturbation allows for asymmetric solutions between, for example, an iteratively composed optimal perturbation

designed to increase R and a perturbation designed to decrease R , while the traditional optimal perturbation approach automatically assumes via linearity that any perturbation designed to increase R will decrease R by an equal amount if it is reversed in sign. Finally, since the response function region D can be defined for each iteration independently, the effect of a change in cyclone track on a response function (e.g. Hoover 2009) is minimized by allowing each iteration to re-center the response function on the cyclone's new forecast position.

Each individual optimal perturbation contributing to the total, iteratively composed perturbation is computed like a regular optimal perturbation and then tested through a series of “inner-loop” iterations to test the effective linearity of the perturbation evolution, with an “outer-loop” to commit the perturbation to the initial conditions and establish a new nonlinear trajectory once the perturbation is deemed to evolve sufficiently linearly. The algorithm for the nested loops is as follows:

1. (Outer-Loop) The non-linear model is run forward to define a forecast trajectory.
2. (Outer-Loop) Adjoint model integrations are initialized with the gradient $\frac{\partial R_p}{\partial \mathbf{x}_t}$ at $t=t_1$ and $t=t_2$, the gradient $\frac{\partial R_{dp}}{\partial \mathbf{x}_0}$ is computed from (2.6), and an optimal perturbation is computed to either increase or decrease the intensification rate by a prescribed amount ΔR_{dp} over a specific time interval using (2.12).
3. (Inner-Loop) The optimal perturbation calculated in Step-2 is applied to the initial model state as a trial, and the non-linear model is integrated forward in time yielding a new, perturbed model forecast state.
4. (Inner-Loop) The linearity of the perturbation is calculated by comparing the target ΔR_{dp} to the actual ΔR_{dp} achieved by the non-linear model.

5. (Inner-Loop) If the calculated linearity $1 - \frac{|\Delta R_{dp}|_{\text{observed}} - \Delta R_{dp}|_{\text{target}}|}{|\Delta R_{dp}|_{\text{target}}|}$

achieves at least a threshold minimum value (specified for all experiments within this dissertation as 50%), the inner loop stops, the perturbation is committed to the initial conditions, and the outer-loop starts again to define the next perturbation (Step-1). If the linearity falls below the threshold acceptable level, the inner-loop is repeated at step-3 with the perturbation reduced in size (based on the moist static energy norm) by 10% of its current value, and the linearity test is repeated (Step-3).

6. The stopping criteria of the algorithm is evaluated within the inner-loop. If the perturbation attempting to be committed to the initial state either: (i) fails the linearity test in Step-3 three consecutive times, or (ii) achieves ten total outer-loops, the algorithm completes.

Once these arbitrary stopping criteria are met, an iteratively composed perturbation has been computed as a sum of the perturbations committed on each outer-loop: $\mathbf{x}'_0|_{\text{tot}} = \sum_{i=1}^N \mathbf{x}'_0|_i$ for N outer-loops. A schematic diagram of the algorithm is shown in Figure 2.2. It should be noted that unlike incremental 4DVAR, the “inner-loop” presented in the above method does not seek to minimize a cost-function but rather seeks to maximize the impact of a perturbation on R in a quasi-optimal way by composing the perturbation through iterative steps, each of which is optimized and scaled to achieve an acceptable threshold of linear evolution in the nonlinear model.

2.2 NASA GEOS-5 Forward and Adjoint Model Specifications

2.2.1 Nonlinear Forward Model

The NASA Goddard Earth Observing System model, version five (GEOS-5) and its adjoint are employed for this study. The GEOS-5 is a global, hydrostatic numerical weather prediction (NWP) model that employs the FV3 dynamical core to solve the finite volume equations of motion (Lin and Rood 1996; Lin 2004) on a cube sphere grid (Putnam and Lin 2007). The model is run at 0.625° longitudinal resolution by 0.5° latitudinal resolution on 72 vertical levels from the surface to the model top at 0.01 hPa, and employs a hybrid sigma-pressure vertical coordinate which is terrain following below 180 hPa and pressure following above 180 hPa (McGrath-Spangler and Molod 2014). The forward model is run using a 7.5-minute time step. The model uses a relaxed Arakawa-Schubert (RAS; Arakawa and Schubert 1974) cumulus parameterization scheme and two different PBL schemes; the Louis scheme (Louis et al. 1982) for stable flows characterized by a positive Richardson number and the Lock scheme (Lock et al. 2000) for unstable, negative Richardson number flows (Holdaway, personal communication). The model is initialized from the Modern-Era Retrospective analysis for Research and Applications, Version 2 (MERRA-2) analyses, as described in section 2.2.3.

2.2.2 Adjoint Model

The adjoint of the GEOS-5 is defined as the line-by-line transpose of the tangent linear approximation to the nonlinear forward model. The GEOS-5 TLM and adjoint models include sophisticated moist physics routines that make the adjoint model

attractive for this study. The adjoint includes a nearly exact linearization of the RAS convection scheme (Holdaway et al. 2014). This is made possible because it is found through evaluation of the scheme's Jacobian, based on prescribed perturbations, to contain stable eigenmodes; the scheme is weakly sensitive to perturbations in deep convection and a simple smoothing is performed for the more sensitive shallow convection in order to make a direct linearization feasible under both deep and shallow convective conditions (Holdaway and Errico 2013). In addition, a linearized prognostic cloud scheme is included for clouds produced through large-scale condensation (Holdaway et al. 2015). The inclusion of sophisticated moist physics in the GEOS-5 adjoint makes it more applicable to investigation of problems where moist processes play a major role, such as evaluating the impact of observations on global forecast error using a forecast error-norm including moist energy, or computing sensitivity of mid-latitude cyclogenesis to the model initial conditions (Holdaway et al. 2014). The adjoint is integrated along the trajectory defined by the nonlinear forward model with model state updates at 15-minute intervals.

2.2.3 MERRA-2 Analyses

The GEOS-5 model is initialized with data from the second edition of the Modern Era Retrospective Analysis for Research and Applications (MERRA-2). MERRA-2 is a NASA reanalysis product that contains data from 1980 to present and is produced by completing full (re-)analysis cycles of the GEOS-5. This allows for a seamless interface between the MERRA-2 analyses and the GEOS-5 NWP model. MERRA-2 assimilates

the most state of the art earth observations currently available and replaces the original MERRA reanalysis dataset (Rienecker et al. 2011).

All data provided within the MERRA-2 dataset are available on uniform latitude-longitude grids with a horizontal grid resolution of $0.625^\circ \times 0.5^\circ$, identical to the GEOS-5 configuration used for all experiments herein. Three-dimensional fields are available on either 42 pressure levels or 72 hybrid sigma-pressure levels with an analysis top pressure fixed to $P_{TOP} = 0.01$ hPa. The MERRA-2 dataset contains variables that are either instantaneous in three dimensions or time averaged. Instantaneous fields are collected at *synoptic times* (0000 UTC, 0600 UTC, 1200 UTC and 1800 UTC) in addition to intermediate *mid-synoptic times* (0300 UTC, 0900 UTC, 1500 UTC and 2100 UTC). Time averaged fields contain hourly, three-hourly, monthly or monthly-diurnal mean values, as well as a daily average field for near surface maximum and minimum air surface temperatures. These time averaged fields are collected continuously with time-stamps centered over the range of the temporal average taken (e.g. hourly fields would be time-stamped at half-hours). Monthly averages represent averages taken over a calendar month, and each file that is output pertains to a single calendar month (Bosilovich et al. 2016). MERRA-2 analyses are publicly available for download through NASA Earth Data⁶.

2.3. Standardized Uncertainty Anomalies

There are two main methods by which NWP forecasts can be created: via *deterministic* prediction and *probabilistic* prediction. A single NWP model operating with a particular dynamical core and physical parameterizations, and initialized with a

⁶ <https://disc.gsfc.nasa.gov/>

single realization of initial and boundary conditions, produces a *deterministic* prediction. A deterministic prediction represents a single (possible) realization of the model forecast state, but provides no information about the certainty of the model in predicting that particular realization. An NWP model, representing the solution of a dynamical system of equations, is susceptible to numerical chaos (Lorenz 1963), and so exploring only one trajectory through the possible range of solutions in the model phase-space, knowing that errors exist in both the model physics and in initial/boundary conditions, may be insufficient as other trajectories originating from nearly identical initial/boundary conditions or model formulations may be equally likely.

In order to explore more possible solutions, an *ensemble* of model simulations can be performed. Ensemble (probabilistic) predictions are comprised of multiple deterministic predictions using several realizations of initial/boundary conditions and/or different models, and create a range of possible outcomes based on uncertainties in the model physics and initial/boundary conditions, in which the true future state should appear if the ensemble were properly configured. By evaluating an ensemble forecast as a probabilistic prediction, it is possible to draw both qualitative and quantitative conclusions about the uncertainty characteristics of the forecast.

The variance of the ensemble solutions can be used as a measure of uncertainty in the model forecast state. While this ensemble information is useful, it requires an uncertainty reference state with which to compare how uncertain a particular aspect of the forecast is relative to the baseline uncertainty in the forecast for a particular variable, 3-dimensional location, and forecast length. For example, the uncertainty in the 500 hPa geopotential height forecast should be expected to be higher within the mid-latitude storm

track where forecast variance is typically high, than it would be in the subtropics where forecast variance is much lower. Thus, it is insufficient to observe merely that ensemble forecast variance of 500 hPa geopotential height is large within the mid-latitude storm track, but rather it is necessary to know whether the uncertainty represented by that ensemble forecast variance is larger or smaller than what is typical climatologically for that variable, in that location, and for that forecast lead time. To appropriately compare a forecast's ensemble-based uncertainty to a climatological baseline, a methodology has been developed for computing *standardized uncertainty anomalies* (SUA). The SUA technique allows for the quantification of the predictability of a particular aspect of an ensemble forecast by comparing the variance found within an individual ensemble forecast to a climatology of ensemble variance corresponding to the variable, location, time of year, and length of the forecast. For this study, the forecast uncertainty is defined as the standard deviation among ensemble forecast members.

In order to compute uncertainty and SUA for a given forecast variable, vertical (pressure) level, and forecast length, two main steps are necessary: First, the uncertainty from the ensemble-forecast is calculated as the standard deviation among ensemble members (σ_f^x). For the same date, a climatology of uncertainty ($\bar{\sigma}_c^x$) is created by calculating and averaging the uncertainties over a 30 day window centered on that date over the course of 30 years, using an available ensemble-(re)forecast archive:

$$\bar{\sigma}_c^x = \frac{1}{M} \sum_M \frac{1}{N} \sum_{N-15}^{N+15} \sigma_{f,N,M}^x \quad (2.13),$$

where M represents the number of years comprising the climatology, N represents the day of the year, $\sigma_{f,N,M}^x$ represents the standard deviation of the ensemble members from the (re)forecast archive for day- N and year- M . Thus, for a given day $\bar{\sigma}_c^x$ comprises the

climatological uncertainty averaged over 961 individual ensemble forecasts. The 31-day total period was chosen to be long enough to form a sufficiently large climatological dataset, but short enough such that averaging over the period will likely filter out significant seasonal signals. Once σ_f^x and $\bar{\sigma}_c^x$ are calculated, a standard anomaly is calculated, yielding the SUA:

$$SUA = \frac{\sigma_f^x - \bar{\sigma}_c^x}{std(\bar{\sigma}_c^x)} \quad (2.14).$$

Assuming a sufficiently long averaging interval, use of the SUA method rather than relying on uncertainty derived solely from the model forecast poses the significant advantage that SUA can describe the *anomalous* uncertainty within a forecast *relative to the climatological uncertainty*. Examples of SUA both at the analysis time and 24-hrs into a forecast trajectory can be seen in Figs. 2.3a, b-2.4a, b.

2.3.1 Global Ensemble Forecast System Reforecast Dataset

In order to calculate the aforementioned SUA, the second-generation NOAA Global Ensemble Forecast System (GEFS) reforecast dataset (Hamill 2011; Hamill 2013) is employed. The most current configuration is calculated on a Gaussian grid which during the first eight days of a reforecast integration is run at an equivalent latitude-longitude grid spacing of 40 km at 40° latitude. The data used in this study is interpolated to a coarser 1° x 1° resolution grid via a bilinear interpolation scheme.

Control initial conditions are produced using a hybrid ensemble Kalman filter-variational analysis system (Hamill et al., 2011). The perturbed initial conditions for the reforecast data set are consistent with the operational GEFS, and are produced using the ensemble transform technique with rescaling (Wei et al. 2008). Unlike the operational

GEFS, in which the leading 20 perturbations plus the control (out of a possible 81 perturbations created during the model cycling process) are retained at every synoptic time (Hamill 2013), the reforecast data is comprised of only the ten ranked perturbed members with the largest perturbation growth plus the control forecast. The reforecast data is only initialized at 0000 UTC only and is available over a period from December 1984 to present. Given that this is a reforecast dataset, all of the data is consistent with respect to model formulation.

2.4 Piecewise Potential Vorticity Inversion

Though much of the early work on the physical mechanisms of cyclogenesis (e.g., Petterssen 1956) remains largely valid to this day, it is perhaps more concise to appreciate cyclogenesis through a “PV thinking” (Hoskins et al. 1985) framework. By adopting this framework, one can cleanly and succinctly diagnose the dynamics of particular features of the atmospheric mass and momentum fields through the inversion of a three-dimensional PV distribution. Furthermore, as first demonstrated by Davis and Emanuel (1991), it is possible to perform a *piecewise* PV inversion (e.g., Hakim et al. 1996; Morgan 1999; Korner and Martin 2000) wherein the full PV (q) is divided into a mean and perturbation (\bar{q} and q' , respectively) and N discrete PV anomalies ($q'_k, k = 1, N$) are inverted in order to recover and attribute the balanced perturbation geopotential height (φ'_k) and streamfunction (ψ'_k).

When performing a piecewise PV inversion, an appropriate formulation for PV as well as an associated balance condition (a diagnostic relationship between the stream function ψ and the geopotential φ) and boundary conditions must first be established.

Early applications of piecewise potential vorticity inversion (e.g., Davis and Emanuel 1991; Davis 1992; Hakim et al. 1996) discuss in relative detail the strengths and weaknesses of two typical formulations of PV; Ertel's PV (EPV) and quasi-geostrophic PV (QGPV). Although inversions performed throughout the course of this study will exclusively employ QGPV, an understanding of the drawbacks and benefits of both inversions techniques is helpful.

For baroclinic, compressible (three-dimensional) flow EPV is conserved following three-dimensional, adiabatic inviscid motion (Rossby 1940; Ertel 1942). EPV can be expressed as

$$q_E \equiv \frac{1}{\rho} \eta_a \cdot \nabla \theta, \quad (2.15)$$

where η_a is the absolute vorticity vector, $\nabla \theta$ the *three*-dimensional gradient of potential temperature and ρ the density. Unlike that used within the inversion of QGPV, the balance conditions used to invert EPV are recognized as highly accurate even for flows with Rossby numbers much larger than unity. A common balance definition, known as non-linear balance (also known as the Charney balance condition; Charney 1955), is expressed below as in Morgan (1999):

$$\nabla^2 \varphi = \nabla \cdot (f \nabla \psi) + 2m^2 \left(\frac{\partial^2 \psi}{\partial x^2} \frac{\partial^2 \psi}{\partial y^2} - \frac{\partial^2 \psi}{\partial x \partial y} \frac{\partial^2 \psi}{\partial x \partial y} \right), \quad (2.16)$$

where m is a map factor and f is the Coriolis parameter. Inversion of EPV using the non-linear balance condition is in principle advantageous within flows characterized by large ageostrophic motion, given the similarity between the balance condition and gradient wind balance (Davis and Emanuel 1991). A significant drawback to this method however is a lack of uniqueness in the solution of the non-linear balance equation, a symptom of

the non-linearity therein. For this reason, piecewise inversion of EPV introduces ambiguity into the solution in a manner in which inversion of QGPV does not.

Unlike the inversion of EPV, the inversion of QGPV is performed using a linear operator, thus eliminating the ambiguity found in its solution. Additionally, the QGPV inversion employs a far simpler balance condition, geostrophy, than does the EPV inversion. QGPV is defined in pressure coordinates as in Nielsen-Gammon and Lefevre (1996) and Hakim et al. (1996) as:

$$q' \equiv \frac{1}{f_0} \nabla^2 \varphi' + f + f_0 \frac{\partial}{\partial p} \left(\frac{1}{\sigma_r} \frac{\partial \varphi'}{\partial p} \right) = f + \mathcal{L}(\varphi'), \quad (2.17)$$

where ∇^2 is the *two*-dimensional Laplacian operator, φ is the geopotential, f is the Coriolis parameter ($f_0 = 10^{-4} s^{-1}$) and σ_r is a layer-averaged static stability parameter. Prime terms represent deviations (perturbations) from a reference geopotential field. The full QGPV field can be inverted by substituting the full geopotential field, φ , in place of the prime terms. \mathcal{L} , a Laplacian-like operator, can be inverted linearly to obtain the geopotential field,

$$\varphi' = \mathcal{L}^{-1}(q - f). \quad (2.18)$$

It should be noted that in principle, the QG system loses validity within flows that are not characterized by small Rossby numbers, however Davis (1992) and Hakim et al. (1996) showed that QGPV and EPV in flows characterized by higher Rossby numbers often correlate well, and can still be effectively inverted in order to recover the geopotential distribution of higher-ordered Rossby number flows. For the experiment undertaken herein, inversions will be performed using QGPV, subject to the geostrophic balance condition and lateral boundary conditions set to zero and top and bottom boundaries

defined by potential temperature perturbations and the hypsometric equation to derive geopotential perturbations at the boundaries.

A novel aspect of the research presented here however lies within the procedure by which the perturbation and mean QGPV quantities are derived. Unlike previous studies in which the perturbation QGPV quantities are defined as the deviation from a time-mean basic-state (e.g., Breeden and Martin 2018), the basic-state in this study is defined by the control (unperturbed) simulation, and the difference between the perturbed model state and the control model state defines the perturbation QGPV as it evolves forward in time along an NWP trajectory. In this way, the piecewise QGPV inversion that is performed allows for an explicit understanding of the impact of portions of the quasi-optimal perturbation on the evolution of the case in a piecewise sense.

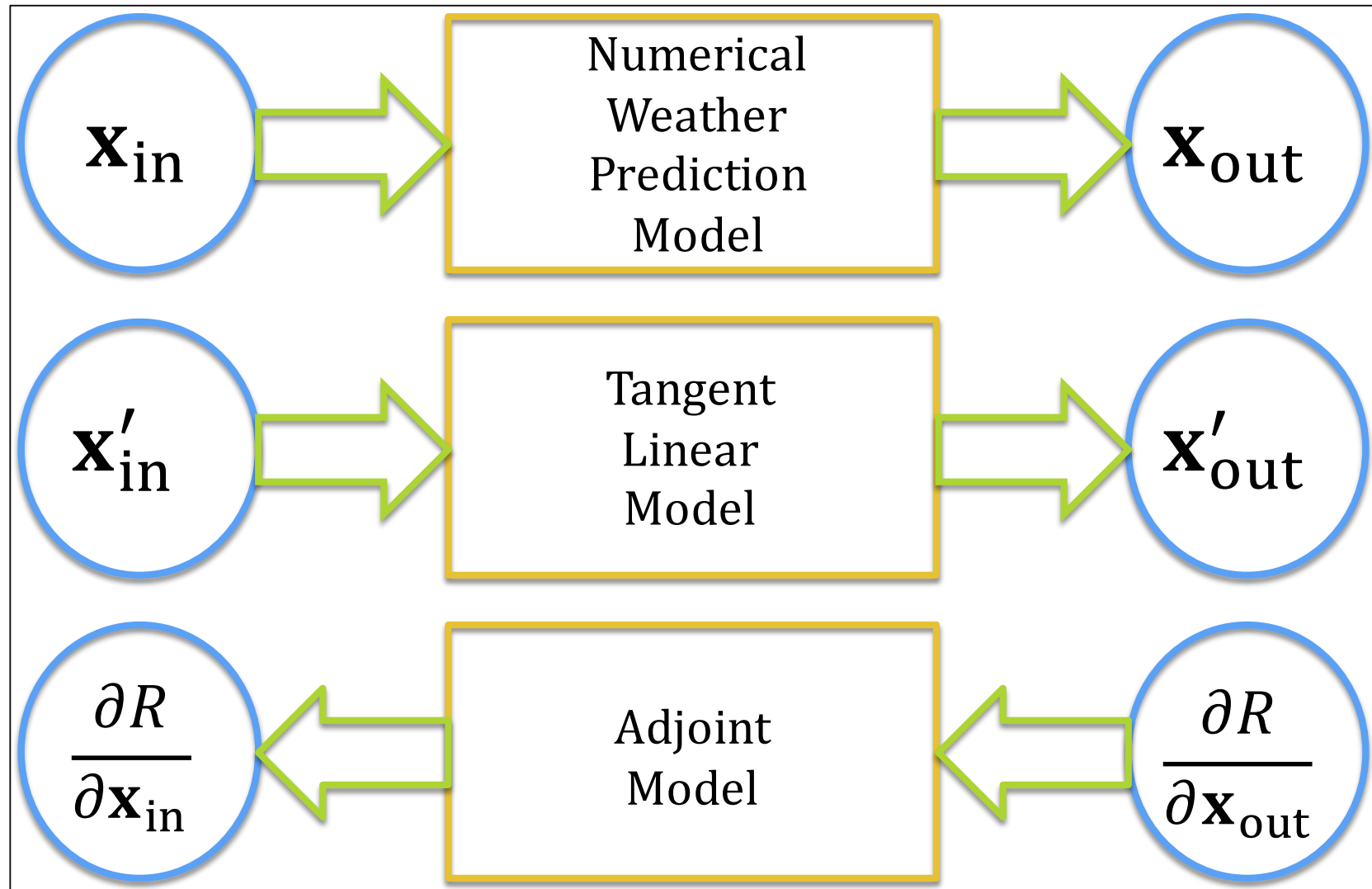


Figure 2.1. A schematic diagram of the differences between NWP, TLM and Adjoint models in terms of their inputs and outputs as well as directions of propagation in time. Arrows facing to the right indicate a forward propagation in time; arrows facing left indicate a backwards propagation in time. Model state variables are denoted as \mathbf{x} , prime terms indicate perturbation variables, and the response function is denoted as R .

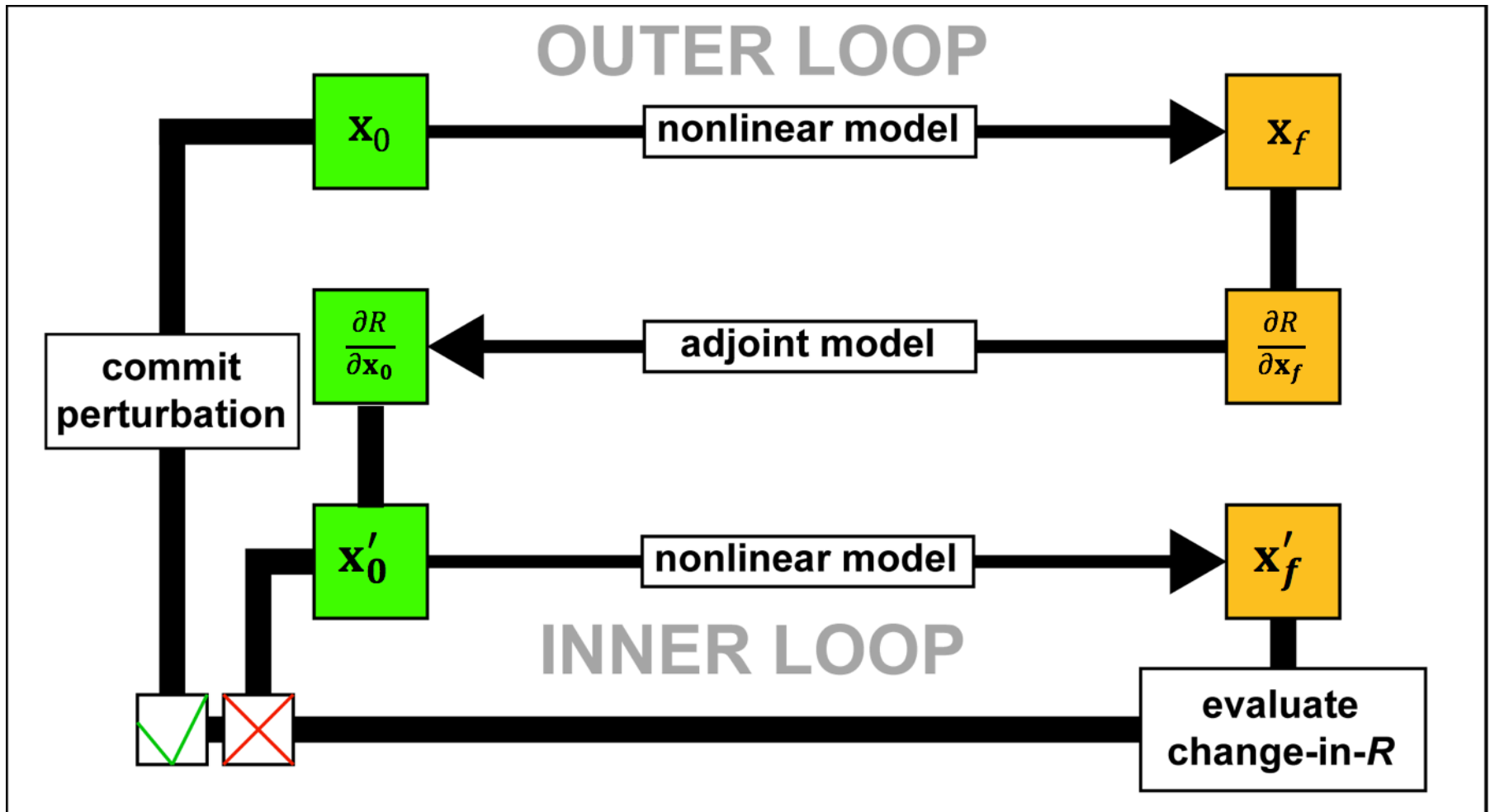


Figure 2.2. A schematic diagram of the algorithm used in computing *quasi-optimal iterative perturbations*. Courtesy Hoover (2017)⁷

⁷ Adapted with permission from Hoover (2017): Adjoint Models Beyond 4DVAR: Forecast uncertainty, impact of assimilated observations, and east coast snowstorms. Colloquium Presentation, University of Wisconsin - Madison, Department of Atmospheric and Oceanic Sciences. November 29, 2017.

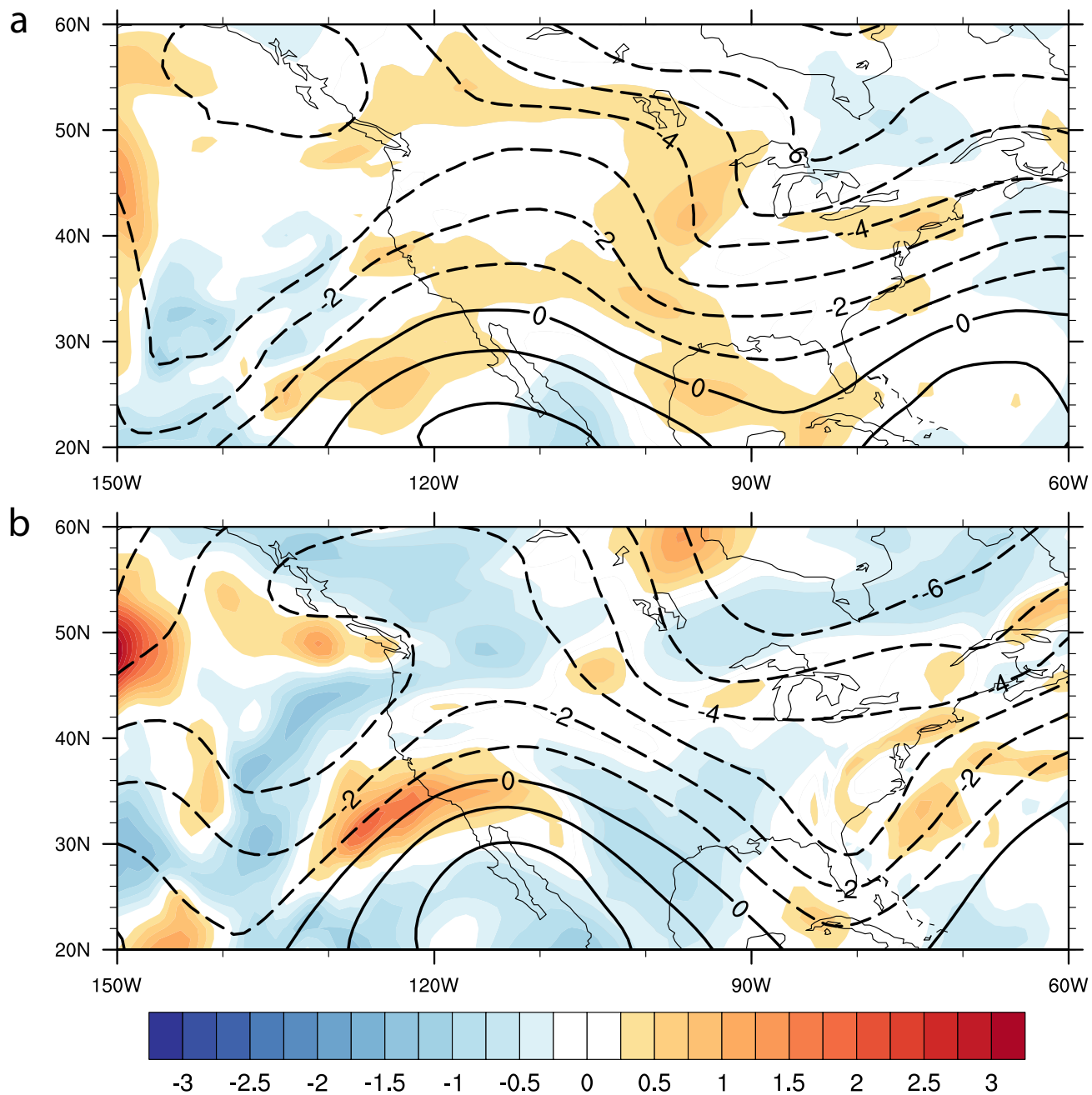


Figure 2.3. 500 hPa stream function standardized uncertainty anomaly (fill; $\text{m}^2 \text{s}$) and stream function (contour; $\text{m}^2 \text{s}$) valid (a) 0000 UTC 2000 January 24 (Analysis) and (b) 0000 UTC 2000 January 25. Warm colors indicate higher than climatological uncertainty, cool colors indicate lower than average uncertainty.

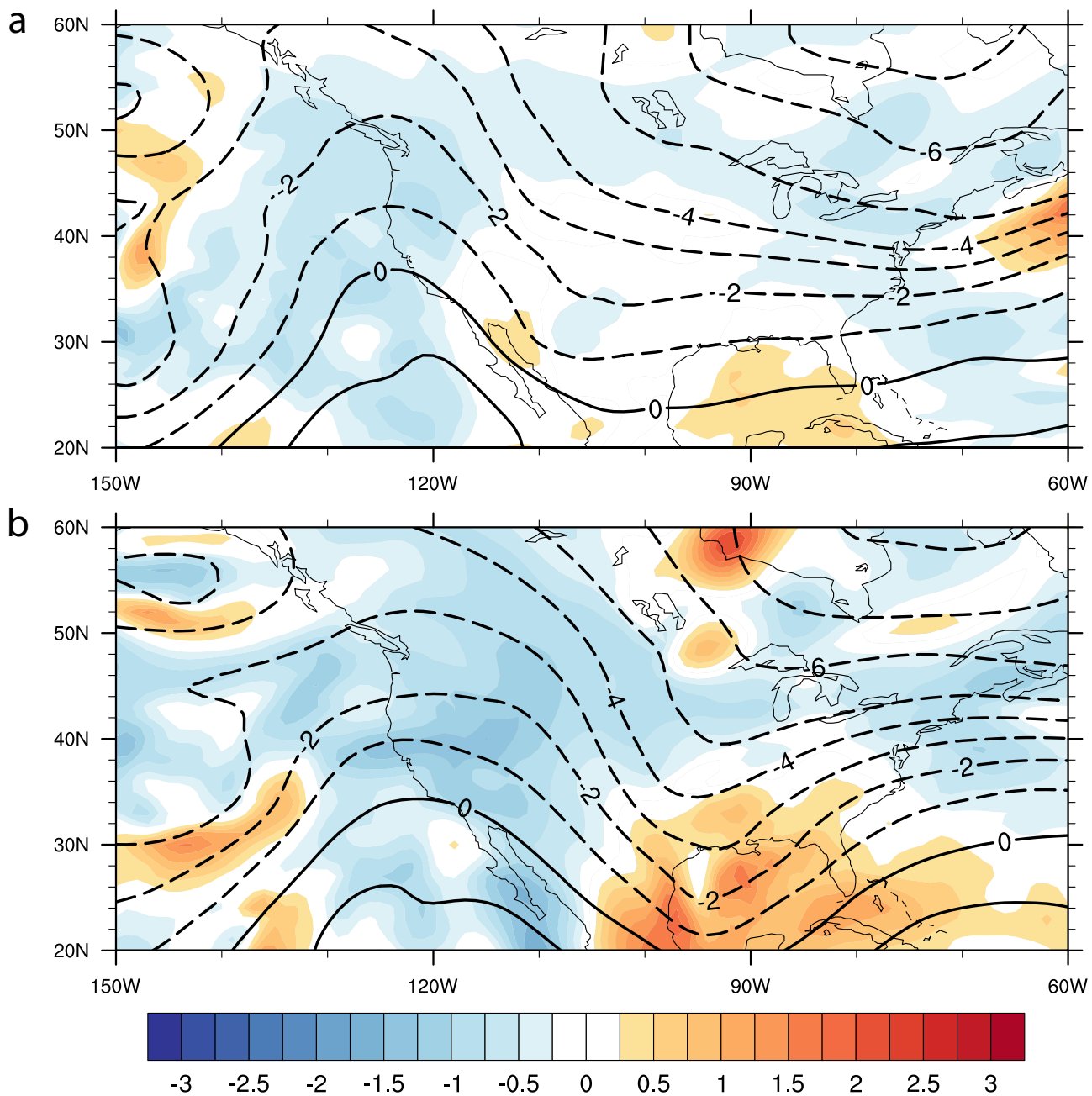


Figure 2.4. 500 hPa stream function standardized uncertainty anomaly (fill; $\text{m}^2 \text{s}$) and stream function (contour; $\text{m}^2 \text{s}$) valid (a) 0000 UTC 1993 March 12 (Analysis) and (b) 0000 UTC 1993 March 13. Warm colors indicate higher than climatological uncertainty, cool colors indicate lower than average uncertainty.

Chapter 3: Modulating the Intensification Rate of the 24-26 January 2000 “Surprise Snow Storm” Through the Use of Adjoint-Derived *Quasi-Optimal* Iterative Perturbations

3.1 Abstract

A new response function that defines the sensitivity gradients of mid-latitude cyclone intensification *rate*, along with a method for iteratively perturbing the model analysis state in order to make changes to that response function are defined and tested. Termed the *quasi-optimal iterative perturbation* (QOIP) method, analysis-time perturbations are computed that are proportional to the sensitivity gradients (Errico 1997), while minimizing the expense of the total, moist energy (Ehrendorfer et al. 1999; Holdaway et al. 2014). The linear behavior of these perturbations is quantified for successive NWP simulations, with those perturbations that satisfy a “target” linearity value then summed and re-applied to the analysis state before integrating the model forward. Those perturbations that do not meet the linearity criterion are re-calculated based upon a lower target threshold and re-integrated forward in time successively.

The case that serves to test the intensification rate response function as well as the QOIP method is the 24-26 January 2000 “Surprise Snow Storm”, a case that represented a significant forecast challenge. It is shown that the QOIP method is successful in modulating the intensification rate of the surprise snow storm over a finite period in its evolution, as simulated in the NASA GEOS-5 NWP model. Perturbations aimed at increasing (decreasing) the intensification rate of the cyclone, as well as their inverses

(e.g., identical perturbation magnitudes and spatial structures multiplied by negative one) are simulated and evaluated. It is shown that the linearity and behavior of the perturbations to all four cases has significant implications on the evolution of the cyclone, where perturbations aimed at increasing (decreasing) the intensification rate of the cyclone behave more (less) linearly, therefore achieving more (fewer) iterations within the QOIP algorithm resulting in larger (smaller) perturbation magnitudes. As a result, the perturbations aimed at increasing the intensification rate have a much greater impact on the response function than those that are aimed at decreasing the intensification rate. Additionally, it can be seen that the total, quantified impact of the perturbations are greater in the increased intensification rate direction than in the decreased intensification rate direction, a result that has significant implications for the predictability of the cyclone.

The cases are evaluated using both energy and quasi-geostrophic potential vorticity (QGPV) diagnostics. A new application for the use of a piecewise QGPV inversion is also introduced, in which the QGPV of the QOIP perturbations is calculated and inverted. This method differs from previous instances of piecewise QGPV inversion, where QGPV perturbations are calculated as deviations from a time-mean QGPV state rather than from an adjoint-derived perturbation perspective.

3.2 Background

The 24-26 January 2000 mid-Atlantic snowstorm was a significant numerical weather prediction (NWP) forecast bust that impacted highly populated areas along the eastern seaboard of the United States (Fig. 3.1). Even at short lead times, NWP guidance

was poor, indicating an intrinsic lack of predictability within the system. Previous studies (Zhang 2002; 2003; Brennan and Lackmann 2005; Kleist and Morgan 2005a) have shown that significant error growth in NWP forecasts for the event were likely sourced from initial condition errors.

The potentially large impact of initial errors on the forecast make the adjoint of an NWP model a useful tool for assessing the sensitivity of the forecast to changes to the initial state. Using an adjoint model, it is possible to calculate sensitivity of some forecast aspect of interest, known as a *response function* (R) to perturbations to the model initial conditions. Given a model forecast state at some final time ($\mathbf{x}_f = \mathbf{x}(t_f)$), and a response function that is differentiable with respect to the model state, one can calculate the explicit sensitivity gradient with respect to the model forecast state, $\frac{\partial R}{\partial \mathbf{x}_f}$. The adjoint model integrates this sensitivity gradient *backward* in time along a model state trajectory defined by the NWP model (called the *basic-state*) to yield the sensitivity gradient with respect to the model initial state $\frac{\partial R}{\partial \mathbf{x}_0}$, ($\mathbf{x}_0 = \mathbf{x}(t_0)$). The sensitivity gradient describes how small perturbations to the model initial state \mathbf{x}_0 will result in a change to the response function at the final time $t=t_f$. Within this framework, it is possible to gain useful insight into how small initial condition perturbations, such as prescribed initial errors, influence the response function.

Using the *quasi-optimal iterative perturbation* (QOIP) method outlined in section 2.1.4, initial-time perturbations are iteratively generated and applied to the analysis and the perturbed initial state is integrated forward in the fully nonlinear NWP model to produce a perturbed forecast. These perturbations are designed to modulate the *intensification rate* of the cyclone over a *specified period* in the unperturbed (control)

forecast, as opposed to previous similar studies that use response functions defining the intensity of a cyclone at a particular forecast time (e.g., Kleist and Morgan 2005; Doyle et al. 2014). The perturbations are evolved in the nonlinear NWP model and analyzed to identify key processes responsible for changing the response function; termed the “perturbation-response” framework, this method allows for an objective, dynamically informed investigation of the dynamics that govern the intensification rates of the cyclone, helping to elucidate how seemingly innocuous initial state perturbations may have significant influence on the forecast.

3.3 Synoptic Overview - The 24-25 January 2000 “Surprise Snow Storm”

Over the two-day period 24-25 January 2000, a significant winter storm impacted a large portion of the eastern seaboard of the United States, with significant accumulating snow occurring throughout portions of the Carolinas, Mid-Atlantic and New England. Forecasts for this event were unusually poor for lead times as short as 24-h, where the heaviest bands of precipitation as depicted by NWP guidance remained too far east, resulting in significant under-forecasting of total snowfall over the region. Remarkably, NWP model guidance for this event was poor, with some of the most contemporarily sophisticated deterministic and (ensemble) probabilistic NWP systems failing to accurately depict the event and its resulting impact (Kleist and Morgan 2005a). Due to its poor forecast, the event has been termed the “surprise snow storm”, hereafter “SSS”.

The second edition of the Modern Era Retrospective Analysis for Research and Applications (MERRA-2; Rienecker et al. 2011) analysis data are used for the upper- and mid-tropospheric portions of this this synoptic overview. MERRA-2 data are available on

36 pressure levels at $0.625^\circ \times 0.5^\circ$, horizontal resolution. NOAA/NWS/NCEP/WPC subjective surface analyses retrieved from the University of Washington archive⁸ are also used. Analyses are displayed at 12-hr increments from 2000 January 24 0000 UTC (24/00) through 2000 January 25 1200 UTC (25/12), a period that encompasses the development of the cyclone from an incipient surface wave along a baroclinic zone through its post-bomb phase.

At the initial time 0000 UTC 24 January, a broad, positively-tilted 250 hPa shortwave trough is evident over the central US (Fig. 3.2a). Two main jet streak maxima are present associated with the trough portion of the wave: 1) an upstream, quasi-zonal jet extending from the California coast southeastward into the Gulf of Mexico (GOM) characterized by a 70 ms^{-1} jet core found over northern New Mexico and the Texas panhandle; and 2) a downstream, slightly more amplified jet streak characterized by an 85 ms^{-1} jet core, associated with a departing surface cyclone just east of the southeastern coast of maritime Canada. It is this upper-level precursor wave that will be shown in subsequent sections to be augmented by the intensifying (weakening) QOIP in a manner that allows for a more (less) favorable configuration for mutual amplification of the surface cyclone, and as such a greater (lessened) rate of intensification. Broad divergence is also seen in Fig. 3.2a associated with the left exit region of the upstream jet streak, with a more concentrated region of divergence found to the east as consequence of QG ascent associated with both jet streaks. By 1200 UTC 24 January, the trough had deepened into the southern Tennessee Valley (Fig. 3.2b); while a 75 m s^{-1} wind maximum associated with the upstream jet began to round the base of the trough off the Texas coast and into

⁸ Data access available at: <https://atmos.washington.edu/data/vmaproom/varchive.cgi>

the northern GOM, drawing the exit region of the upstream jet closer to the entrance region of the downstream jet. As the upstream jet streak approaches the eastern wind maximum, enhanced divergence is evident over the eastern GOM north and east over Northern Florida and off the Georgia coast resulting from enhanced QG ascent by the now-developed “double jet” structure (Bell and Bosart 1993; Huo et al. 1994). By 0000 UTC 25 January (Fig 3.2c), downstream ridging is evident over North Carolina and Virginia north through New England coincident with robust surface cyclogenesis as the trough to the west becomes negatively (eastward) tilted. Strong divergence is noted to the east of Florida over the Bahamas, also aiding in the process of surface cyclogenesis. Finally, by 1200 UTC on January 25 the eastern side of the trough takes on a strongly meridional orientation with divergence downstream of the trough axis (Fig. 3.2d). By this time, enhanced wind speeds are also noted in response to the upper-level outflow of the surface cyclone, with strong divergence noted in both the left exit and right entrance regions of the enhanced jet streak associated with this outflow. The evolution of the 500 hPa vorticity (and heights) over the same 36h period in Fig. 3.2 is presented in Fig. 3.3). The vorticity associated with the trough is an initially elongated structure (Fig 3.3a) that becomes concentrated at the trough base (Fig. 3.3b) and compacted into an isotropic, cutoff structure as the downstream ridge amplifies (Figs. 3.3 c and d).

Figure 3.4 displays a sequence of subjectively-analyzed surface analyses depicting the evolution of the surface cyclone. At 0000 UTC 24 January, a stationary front associated with a departing cyclone off the Mid-Atlantic coast was draped across the Gulf Stream, running southwest-to-northeast and intersecting another stationary front connected to an incipient surface low-pressure over southern Louisiana, and running

parallel to the Gulf Coast and west over southern Texas. To the north, a sprawling anticyclone was centered over the Great Plains extending eastward into the Midwest. By 1200 UTC 24 January (Fig. 3.4b), in response to the increased upper-level divergence, the incipient cyclone that had been present 12 hours earlier moved eastward and developed into a 1005 hPa surface cyclone over northern Florida. Warm frontogenesis characterized by a strengthening temperature gradient began to the northeast of the low in association with the remnant baroclinic zone, while a trailing cold-front had developed to its southwest and pushed southeastward across the central and eastern GOM. By 0000 UTC 25 January, the cyclone moved northeast to the Gulf Stream waters off the coast of South Carolina, undergoing a period of rapid-intensification with its minimum sea level pressure (SLP) dropping from 1005 hPa to 992 hPa in 12 hours (Fig. 3.4c). This period of intensification technically qualified the storm as a bomb (Sanders and Gyakum 1980). To the north, a stationary/warm-frontal structure extends to the northeast, while a subtle offshore wind-shift along the Carolina coast is indicative of the beginning of coastal-frontogenesis in association with the sharp temperature gradient between the land-surface and the warmer ocean water. QOIP perturbations to this warm-frontal region are in later sections shown to be a pivotal region for the generation and aggregation of near surface vorticity that is ingested into the core of the cyclone during its development stages. By 1200 UTC 25 January, the surface low had further deepened to 981 hPa off the North Carolina and Virginia coast (Fig. 3.4d).

3.4 Prior Sensitivity Analyses

By performing sensitivity studies, one can evaluate the impact of potential analysis errors on the model forecast. In regions where a potential analysis error projects strongly onto large sensitivity, the evolved error in the NWP forecast will have a substantial impact on the forecast aspect defined by the response function; since initial errors can grow rapidly over the length of the forecast trajectory, even seemingly small and innocuous initial errors can create substantial forecast challenges. Previous studies have shown that high sensitivity of the forecast of this event to initial conditions defined by the National Center for Environmental Prediction (NCEP) final analysis likely allowed existing initial condition errors to contribute to the poor forecast (Langland et al. 2002; Zhang et al. 2002, 2003; Kleist and Morgan 2005). In regions where sensitivity is high, the projection of small perturbations onto the sensitivity is able to create large changes to the response function at the final forecast time, thus introducing potential error into the forecast aspect of interest.

In particular, Zhang et al. (2002) showed that 1) by initializing the MM5 model with a number of equally plausible analyses, synoptic-scale aspects of the forecast such as cyclone position were adjusted by small amounts; and 2) increased model resolution drastically improved the representation of moist processes within the forecast, noted to be a source of large error growth. Zupanski et al. (2002) demonstrated that while the operational three-dimensional variational data assimilation system used by NCEP (3DVAR; Parrish et al. 1996) struggled to produce an accurate analysis on 0000 UTC and 1200 UTC 24 January 2000, while implementing a four-dimensional variational data assimilation system (4DVAR; Courtier et al. 1994; Tremolet 2005) produced a much improved analysis. The 4DVAR generated analysis resulted in a nearly perfect forecast of

precipitation distribution, particularly over Georgia, owing to an improved depiction of surface convergence with an increase in precipitable water (relative to the 3DVAR analysis) in the Mid-Atlantic region. From a potential vorticity (PV) perspective, Brennan and Lackmann (2005) noted the importance of moist processes early on in the evolution of the forecast, showing that incipient precipitation and resulting diabatic generation of PV was misdiagnosed within the analysis, resulting in a poor representation the associated wind field and resultant onshore moisture flux and quasi-geostrophic forcing for ascent.

Perhaps most directly relevant to this study, Kleist and Morgan (2005; henceforth KM05) performed an adjoint-derived sensitivity study of the SSS for 36- and 48-hr forecasts using the PSU-NCAR MM5 NWP and adjoint models (Zou et al. 1997). Four response functions were considered, describing the forecast error of the mean sea-level pressure forecast relative to a verifying analysis as well as several functions describing dynamical aspects of the cyclone forecast including the lower tropospheric mean vorticity, frontogenesis, or vertical motion within a box centered on a relevant portion of the cyclone in the forecast. KM05 noted that sensitivities of all four chosen response functions to the initial conditions were similarly characterized as isolated structures concentrated within the lower to middle troposphere with upshear vertical tilts indicative of their potential to rapidly grow baroclinically. Similarities and differences between the results of these studies and the study presented here will be discussed in Section 3.3.

KM05 showed that for a response function representing the intensity of the cyclone at a particular forecast time, the sensitivities revealed that increases in 500 hPa vorticity of simulation in the upper-tropospheric precursor trough decreases in 500 hPa

vorticity in the upstream ridge would result in a more intense surface cyclone. The negative sensitivity to initial vorticity in the upstream ridge suggests the importance of diabatic processes such as redistribution of PV by convection in the reshaping of the upper-tropospheric trough and downstream ridge. KM05 concludes that the final forecast intensity of the cyclone would have been greater had there been less destruction of the PV associated with the upper-tropospheric trough at earlier times within the forecast. The importance of the evolution of the upper-tropospheric precursor disturbance on the forecast intensity of the cyclone in this study is described in Section 3.3.

Temperature and wind perturbations in KM05 designed to reduce forecast error at the final forecast time appeared to adhere to thermal wind-like balance, consistent with the derived initial PV perturbations. The PV perturbations made to the analysis did not result in significant changes to the structure of the tropopause at the initial time (i.e. there appeared to be little significant sensitivity to the initial structure of the tropopause). Instead, the middle-tropospheric PV perturbations, being oriented upshear within the baroclinic zone, were able to grow rapidly as the model was integrated forward becoming increasingly isotropic and superposed. This resulted in an enhanced perturbation wind field within the lower troposphere and subsequent enhancement of the lower-tropospheric perturbation thermal structure. These evolved perturbations significantly reduced the forecast error at the final forecast time, but also throughout the course of the forecast trajectory.

KM05 used a simple iterative perturbation method to generate perturbations designed to minimize forecast error, computed by scaling the sensitivity gradients by a subjectively defined scaling coefficient to produce perturbation fields of reasonable size

(i.e. roughly on the order of analysis error) that project perfectly onto the sensitivity gradients, and re-running the nonlinear forward model to establish a new basic-state trajectory before re-running the adjoint to compute new sensitivity gradients of the forecast error to the initial conditions to compute new perturbations. The present study uses similarly iteratively-composed initial perturbations except that they are optimized for minimum initial energy rather than relying on subjective scaling coefficients. As a consequence, there is additional objectivity to the defined perturbations and the introduction of constraints that affect the spatial scale of the initial perturbations. The QOIP method used to generate the iterative perturbations for this study can be found in section 2.1.4.

Based on these previous studies, the surprise snow storm is identified as an event in which large sensitivity of the forecast state to the initial conditions made the forecast especially susceptible to modulation by the perturbations to the analysis, including potential initial (analysis) errors that are capable of growing quickly, leading to significant under-forecasting of the cyclone's impact.

This study will focus on how small changes via QOIP perturbations to the initial state impact the *intensification rate* of the cyclone over a given response period. Four different perturbation structures (as outlined in section 3.4) are made to the model analysis and are addressed with the goal of understanding how arbitrarily small changes to the model analysis will reshape the synoptic- and mesoscale environment throughout the model integration in a manner which augments the time-rate-of-change of surface pressure of the cyclone. Unlike previous studies in which the sensitivity of the intensity of a cyclone is calculated at a specific forecast time, the time-rate-of-change of surface

pressure response function has not been used in previous studies and will help to elucidate the governing dynamics of mid-latitude cyclone intensification processes.

Furthermore, with the exception of KM05, most studies undertaken on this event serve as “post-mortem” diagnoses of the cyclone. Similar to KM05 however, this study seeks to understand what *could* have happened had the initial environment been slightly altered. This result speaks directly to the predictability of the cyclone, as perturbations added to the analysis that make large (small) changes during the response period indicate lower (higher) levels of intrinsic predictability.

3.5 Barotropic Preconditioning

A large percentage of baroclinic surface cyclones can be classified as “Type-B” development (Petterssen and Smebye 1971), in which baroclinic development of a surface circulation is preceded by the development and evolution of an upper-tropospheric precursor disturbance. This disturbance is typically manifest as an undulation of the dynamic tropopause, resulting in a positive potential vorticity intrusion into the troposphere. The January 2000 Surprise Snowstorm fits this definition, with surface development following the maturation of an upper-tropospheric precursor trough. An important aspect of these upper-tropospheric precursor disturbances is their capacity for growth through barotropic energy conversion (BEC); separating the flow into a mean-state and eddy-state, BEC can be defined as growth of an eddy via conversion of the mean-state kinetic energy (KE) into eddy-kinetic energy (EKE) at the expense of the mean-state shear through deformation of the eddy from an elongated structure to a more compact shape. Mak and Cai (1989) demonstrate that eddies that are locally elongated

along the axis of contraction of the mean-state, defined by the mean-state deformation field, will optimally extract energy from the mean-state flow as they deform and intensify into a compact structure, while eddies elongated along the axis of dilatation will lose energy to the mean-state flow as they are elongated. An expression for this process can be defined by the scalar product of the two vectors \mathbf{E} and \mathbf{D} , which can be described as:

$$\mathbf{E} = \{(v'^2 - u'^2), (-u' v')\}, \quad (3.1)$$

and

$$\mathbf{D} = \left(\frac{\partial U}{\partial x} - \frac{\partial V}{\partial y}\right), \left(\frac{\partial V}{\partial x} + \frac{\partial U}{\partial y}\right), \quad (3.2)$$

where u' and v' represent the eddy zonal and meridional wind components respectively, and U and V represent the mean-state wind components. The dot-product of these two vectors yields the BEC rate:

$$\mathbf{E} \cdot \mathbf{D} = \varepsilon_r = \varepsilon_x + \varepsilon_y = \left[\frac{1}{2}(v'^2 - u'^2) \left(\frac{\partial U}{\partial x} - \frac{\partial V}{\partial y}\right)\right] + \left[(-u'v') \left(\frac{\partial V}{\partial x} + \frac{\partial U}{\partial y}\right)\right]. \quad (3.3)$$

Here, \mathbf{E} represents the eddy's structure, and \mathbf{D} represents the mean-state deformation field. Within this framework, the first (ε_x) and second term (ε_y) can be viewed as the BEC rate by the stretching and shearing deformation respectively. The BEC rate is dependent upon the orientation of the perturbations to the mean-state wind field, represented by the angle between the two vectors \mathbf{E} and \mathbf{D} . Multiple previous studies (e.g., Kucharski and Thorpe 2000; Kucharski and Thorpe 2001; Rivière et al. 2003; Hoover 2015) have examined the process of barotropic growth, and have shown that perturbations to the basic-state (representing eddies relative to a mean-state defined by the basic-state) that are oriented *upshear* (e.g. against the horizontal shear of a jet) may grow through barotropic processes at the expense of the basic-state shear. A conceptual

diagram of analysis time perturbations that will likely grow through BEC via an upshear tilt relative to a jet streak can be seen in Fig 3.5 adapted from Hoover (2015).

Kucharski and Thorpe (2000) identified BEC as a significant contributor to growth of the upper-level precursor disturbance within two case-studies from the Fronts and Atlantic Storm-Track Experiment (FASTEX). They explicitly note that “... the question of the sensitivity of the cyclone development with respect to the orientation and position of the upper-level initial trough, cannot be assessed in case-studies. Therefore, a future paper addresses these issues using idealized numerical model simulations,” investigating the sensitivity issue in Kucharski and Thorpe (2001) through explicit perturbations to a zonal jet representing upper-level troughs of varying amplitude and horizontal tilt relative to the jet. Within this second study, it is shown that upshear (downshear) PV perturbations imparted upon the basic-state flow field are rotated to a barotropically negative (positive) orientation by the barotropic shear to create a geometry favorable (unfavorable) for baroclinic development. This geometry is characterized by a decreased (increased) wavelength between the trough/ridge couplet and associated increased (decreased) advection of vorticity by the thermal wind. It is further shown that in flow regimes producing positive BEC rates within perturbations, the perturbations to the flow are rotated from a positive orientation to a negative orientation and thus are favorable for baroclinic growth. The positive-to-negative barotropic tilting of flow features to produce an environment more favorable to baroclinic growth of the cyclone is defined as *barotropic preconditioning*.

While the kinds of sensitivity experiments performed by Kucharski and Thorpe (2001) in an idealized framework are diagnostically useful, these types of experiments

rely on a vastly simplified mean-state in order to do so, which may not necessarily capture much of the variability exhibited by the observed atmosphere. However, adjoint-derived sensitivity analysis is capable of estimating the sensitivity of a cyclone's forecast intensity with respect to the initial conditions in a full-physics nonlinear NWP model, allowing for the sensitivity gradient information Kucharski and Thorpe (2000) asserted was impossible to compute for case-studies beyond those calculated from idealized simulations. With the adjoint method, sensitivity is computed with respect to a real-world basic-state providing more complete, objective, dynamical insight into the phenomenon. While the adjoint's assumption of linearity may not be appropriate in highly non-linearly evolving flow, an iterative perturbation process, such as the QOIP technique described in section 2.1.4, is capable of relaxing the linearity constraint in the process.

The initial-time upper-tropospheric perturbation defined by the QOIP technique is investigated from the perspective of barotropic preconditioning as described by Kucharski and Thorpe (2000) and Kucharski and Thorpe (2001). An evaluation of the energetics will reveal that the early evolution of the upper-tropospheric QOIP in the nonlinear NWP model is dominated by growth of perturbation kinetic energy via BEC, resulting in modulation of the upper-tropospheric precursor disturbance's horizontal tilt consistent with barotropic preconditioning. The influence of upper-, middle-, and lower-tropospheric flow features on near-surface development of the cyclone will be identified with piecewise inversion of the perturbation quasi-geostrophic potential vorticity.

3.6 QOIP analysis

a) Experiment Design

Four experiments were performed for a time-rate-of-change response function R intended at augmenting the intensification rate over a forecast period consisting of two “goalpost” times between forecast hours F017 to F024 inclusive, with QOIP generated using the scheme outlined in chapter two. For two of the experiments, each iteration of the QOIP produces a perturbation introduced at the initial time designed to increase or decrease the intensification rate over the specified period by $0.15 \text{ hPa h}^{-1} = 1.05 \text{ hPa}$ over the seven-hour period. The QOIP experiment designed to increase the intensification rate is referred to as the Increased Intensification Rate (IIR) experiment. The QOIP experiment designed to decrease the intensification rate is referred to as the Decreased Intensification Rate (DIR) experiment. The QOIP for these experiments, as described in Section 2.1.3, is composed through as many iterations as the algorithm will tolerate, which depends on how linear the response to the perturbations is on each iteration. As a result, the number of perturbations in the IIR and DIR experiments can differ. The remaining two experiments are formed by reversing the sign the QOIP of these two experiments – these are referred to as the Reversed Increased Intensification Rate (RIIR) and Reversed Decreased Intensification Rate (RDIR) experiments and represent perturbations resulting from simply multiplying the IIR and DIR perturbation structures by negative one.

A benefit of the QOIP method of perturbing the analysis is that it introduces non-linearity into the otherwise linear framework of the adjoint-derived optimal perturbation method. When generating an optimal perturbation from a single run of the nonlinear forward and adjoint model, it is assumed that an optimal perturbation designed to decrease the response function is equal but opposite in sign to the optimal perturbation

designed to increase the response function, and will have an equal but opposite impact on the response function. By iteratively generating perturbations in the QOIP method, a new nonlinear forward trajectory and adjoint-derived sensitivity gradients are computed with each iteration. Due to these updates, each time a new perturbation is created and added to the previous perturbation, a divergence between the IIR and DIR perturbations occurs allowing for each iteratively generated perturbation to be unique. Due to this uniqueness in the perturbation structures, significantly different results between two experiments, such as the DIR and RIIR experiments, may occur. Examining both the QOIP experiments and their opposites is helpful for identifying the influence of nonlinearity.

Figure 3.6 shows the time-series of the average sea-level pressure in a $9^\circ \times 9^\circ$ box following the minimum sea-level pressure of the four experiments performed. It can be seen that the IIR and RIIR experiments displayed vastly different behavior during the response period between 17 and 24 hours relative to the control, illustrating the intrinsic non-linearity within the forecast state generated by those perturbations. By contrast, the departure of the DIR and RDIR experiments from the control are characterized by a high degree of linearity, yielding nearly equal-but-opposite impacts on the box-mean sea-level pressure throughout the course of the entire integration.

In the idealized model perturbation experiments of Kucharski and Thorpe (2001), it was demonstrated that while perturbations introduced to the zonal jet designed for eddy KE growth through BEC lead to increased rates of baroclinic development of the resulting cyclone, perturbations designed to diminish eddy KE through BEC *still* yielded upper-level precursor waves that underwent baroclinic growth, albeit weaker baroclinic growth. This result is similar to what is seen in Fig. 3.6, where the DIR and RIIR

experiments (which are designed to weaken the cyclone) still produce a cyclone, albeit with less intensity than in the IIR and RDIR cases. It is also noteworthy that the cyclone has the capacity to intensify in the IIR experiment to a much greater degree than it has the capacity to weaken in the DIR and RIIR experiments.

These results illustrate that it is likely not possible to barotropically precondition the atmosphere in such a manner that encourages elimination of a cyclone from the basic-state, but rather only in a manner that makes the environment less favorable for baroclinic growth. As this is the case, the process of barotropic preconditioning explored by the QOIP can not be said to be perfectly linear in the sense that initial perturbations created within the QOIP framework to intensify the cyclone do not weaken the cyclone by an equal amount when reversed in sign. The QOIP algorithm also determined that the DIR experiment lost sufficient linearity after only three iterations. It can be argued that 1) the perturbations to the weakening experiments quickly begin to behave nonlinearly; and 2) while barotropic preconditioning may be a significant contributor to intensifying the cyclone in the IIR experiment, other baroclinic and diabatic processes are likely helping to govern the intensification rates of the weakening cases, the latter of which encompasses processes that are highly nonlinear.

As this is the case, the evaluation of barotropic preconditioning will be largely restricted to the IIR and RIIR experiments, while all perturbation experiments will be considered in subsequent sections focusing on the full, baroclinic evolution of the case.

b) IIR Experiment

The IIR experiment produced an initial-time QOIP through nine iterations, having never fallen below the threshold linearity requirement prior to the final iteration (perturbed iteration nine, e.g., nine iterations subsequent to the control simulation, where the control iteration is indexed as “iteration zero,” was designated as the final iteration). This indicates that perturbations designed to increase the intensification rate of the cyclone between the 17-hr and 24-hr forecasts operated in a weakly nonlinear regime capable of producing impacts from initial-time perturbations that are accurately estimated by the adjoint-derived sensitivity gradients. The QOIP changes the time-rate-of-change of the box-average sea-level pressure between the 17-hr and 24-hr forecast times from -0.42 hPa h^{-1} to -0.80 hPa h^{-1} , drastically intensifying the cyclone between 24-40-hrs and maintaining a cyclone more intense than the control throughout the rest of the 48-hr forecast.

At the initial time, the most significant quasi-geostrophic potential vorticity (QGPV) perturbations within the upper-levels are over the western Great Lakes region of the United States. These perturbations are embedded within a flow field characterized by stretching deformation associated with a high-amplitude upper-tropospheric trough (Fig. 3.7a), and are oriented in a vertical column from roughly 400 hPa to 150 hPa (Fig. 3.7b). The majority of the BEC is performed by the stretching deformation term of Eqn. 3.1, while the contribution by the shearing deformation is small (Fig. 3.8); however, it is important to recognize that the difference between stretching and shearing deformation is relative to the orientation of the coordinate system. BEC is maximized within a layer from 400 hPa to 150 hPa, with little BEC occurring outside of this layer (Fig. 3.9) in

conjunction with the nearly vertically (barotropically) oriented column of perturbation QGPV. Thus, BEC's contribution to the evolution of the perturbations will focus on this middle-to-upper tropospheric layer. Large QGPV perturbations in the low-to-mid troposphere are slanted along isentropes in regions of strong baroclinicity, consistent with PV perturbations designed in KM05 to reduce the forecast error.

In order to establish the contribution of BEC to the perturbation KE, we employ the local energy equation from Mak and Cai (1989):

$$\frac{d\varepsilon}{dt} = -\mathbf{V} \cdot \nabla \varepsilon + G, \quad (3.4)$$

where

$$G = \mathbf{E} \cdot \mathbf{D} - 2r\varepsilon - \mathbf{v} \cdot \nabla p^{(1)}. \quad (3.5)$$

In Eqns. 3.4 and 3.5, $\varepsilon = \frac{1}{2}(v'^2 + u'^2)$ is the perturbation kinetic energy; $\mathbf{v} = (u', v')$ is the perturbation wind components; and $\mathbf{V} = (U, V)$ the basic-state wind components. Thus, for this evaluation of the energetics, the “eddy” state is defined as the QOIP perturbation as it is evolved through the nonlinear NWP model, and the “mean-state” is defined by the unperturbed (i.e., control) model state that defines the adjoint's basic-state. A non-dimensional Rayleigh friction coefficient is defined as $r = r^*LU^{-1} = 0.1$, and yields a dissipative timescale of about 10 days. The term $p^{(1)}$ can be derived from the full dynamic pressure field where $p = p^{(0)} + R_0 p^{(1)}$, in which $p^{(0)}$ represents the portion of the pressure that is in geostrophic balance and $p^{(1)}$ may be interpreted as the *ageostrophic* pressure, that is, the dynamic pressure that counteracts the divergence tendency induced by the motion. R_0 is the Rossby number U/f_0L . Expanding the term G using Eqn. 3.5, the RHS of Eqn. 3.4 contains a term representing the advection of perturbation KE by the basic-state wind field, a term representing the local effective

energy generation rate composed of BEC and an energy dissipation rate due to Rayleigh friction, and a term that measures the work done by the ageostrophic pressure.

Within this more generalized time-rate-of-change of perturbation KE framework, one can cleanly and succinctly diagnose the significance of BEC, a necessary part of the barotropic preconditioning process, by comparing the relative sizes of the BEC term to the total time-rate-of-change of perturbation KE within the system. Of note, only the first two terms in G make net contributions to the global energetics, as the advection and pressure-work terms represent a redistribution of energy already found within the system. While it is possible to show that perturbations to the upper-tropospheric disturbance are made in a manner that barotropically precondition the atmosphere for amplified baroclinic growth, objectively determining the point at which barotropic preconditioning dominates perturbation KE growth is challenging. Since BEC, baroclinic processes, and diabatic processes occur throughout the life cycle of the cyclone, defining a point within the forecast integration at which the upper-level disturbance is being significantly augmented by non-BEC processes is subjective.

Significant, positive BEC (normalized by the total KE) is noted in all four cases as beginning at the analysis time and generally increasing through the first 18 hours of the integration before beginning to steadily drop off through the duration of the simulations (Fig. 3.10a). The normalization was performed in order to be able to compare fairly simulations that achieved different numbers of iterations per the QOIP algorithm, an issue that resulted in large disparities in perturbation magnitude across the cases⁹.

⁹ It is noted that all four cases display similarly proportional BEC magnitudes when normalized by the kinetic energy at each time step. While this indicates that all four cases do attempt to, at least initially, grow by barotropic preconditioning processes, the DIR and RDIR cases are unable to take advantage of the early reservoir of barotropically generated energy (i.e., barotropic preconditioning) in a similar manner to the IIR

Perturbations introduced just upstream of the trough axis associated with the upper-tropospheric precursor to the surface cyclone are reshaped by the highly deformative basic-state flow along the trough axis, producing large BEC rates by 12-15-hrs into the simulation (non-normalized, as the magnitudes of the IIR and RIIR perturbations are similar and can therefore be compared directly; Fig. 3.11). The largest BEC rates appear in regions where perturbations oriented across the trough axis can be shaped into compact features by locally large deformation along the axis of contraction, which is likewise oriented across the trough axis.

The total time-rate-of-change of perturbation KE (dKE) can be estimated by a simple centered-difference approximation at 3-hourly intervals, with the exception of the analysis time at which dKE is computed as a forward-difference approximation. Recall that the RHS of the local energy equation (Eqn. 3.4) is comprised of an advection term, a BEC term, a frictional dissipation term and an ageostrophic pressure-work term. The Lagrangian form of the time-tendency equation therefore includes the BEC term, frictional dissipation term, and ageostrophic pressure-work term as responsible for the Lagrangian time rate of change of KE. Since the timescale of energy dissipation due to Rayleigh friction (~ 10 days) is far longer than the period under consideration, its impact on the local energy generation rate can be effectively neglected. Likewise, the pressure-work term is likely small when the flow is largely geostrophic¹⁰, as is the case for the mid-to-upper tropospheric flow in the mid-latitudes, and will be neglected as well. Under

and RIIR cases. This behavior is likely due to the propensity for non-linear processes to dominate the growth and behavior of the DIR and RDIR simulations which resulted in a relatively quick failure of the QOIP algorithm.

¹⁰ It is acknowledged that for a non-steady state geopotential height field, ageostrophic motions may be non-negligible. However, using a characteristic length scale of 1000km, the Rossby number at 350 hPa was generally on the order of 0.1-0.5 within the of the regions over which the majority of BEC was occurring. These small Rossby numbers indicate predominantly geostrophic flow and the ability to locally neglect the pressure-work term.

these simplifying assumptions, the BEC term represents the dominant source of KE in the local energy equation from a Lagrangian perspective, and when compared with observed dKE, the residual represents the influence of baroclinic and diabatic processes.

The advection term is estimated by computing the advection of perturbation KE by the basic-state wind field and removing it from the calculated dKE, and the resulting dKE is compared to the computed BEC to determine over what time period, if any, the dKE is dominated by BEC, representing a period of barotropic preconditioning. The majority of the dKE within the first 12 hours of the simulation is shown to be sourced from BEC (Fig. 3.13), with regions of dKE that are not sourced from BEC beginning to appear 9-12-hrs into the forecast, indicating that other processes have started to play larger roles in the changes to the perturbation KE. As this is the case, it can be surmised that for the IIR experiment, the barotropic preconditioning phase likely begins to lose dominance after the first 9-hrs, and becomes a significant but not dominating contributor to dKE after the first 12-hrs, the point at which the dKE generation is dominated by growth through baroclinic and associated diabatic processes.

As a consequence of the BEC that occurs during the 12-hour preconditioning period, the precursor disturbance attains characteristics making it more favorable for eventual baroclinic growth, especially during the F017 to F024 response period for which the perturbations are designed to impact the intensification rate of the cyclone. The three main consequences of the BEC on the disturbance are 1) a deepening of the perturbed trough as compared to the control, as the KE of the basic-state shear is converted into perturbation KE allowing for the growth of the disturbance; 2) a rotation of the orientation of the trough from a positive/neutral orientation within the early phases of the

development, to a more negatively tilted orientation by F012 and F015; and 3) a region of *negative* BEC is found in between and slightly to the east of the two positive BEC maxima. This region of negative BEC is collocated with a developing downstream ridge and is an indication of the local inability for perturbations in that region to be rotated negatively. Consequences one and two can be seen in Fig. 3.11a-f, in which the perturbed height contours (dark blue, solid contours) can be seen as being indicative a deeper, more negatively oriented trough as compared to the control simulation (magenta, dashed contours) as the integration progresses forward in time.

c) RIIR Experiment

The perturbation added to the RIIR experiment is the QOIP from the IIR experiment reversed in sign. The experiment resulted in a modest reduction in the intensification rate of the cyclone between 17-24-hrs, reducing the rate from $-0.42 \text{ hPa hr}^{-1}$ in the control simulation to $-0.22 \text{ hPa hr}^{-1}$, an impact roughly half of the magnitude of the impact of the QOIP in the IIR experiment. To simply draw a contrast between the RIIR experiment with a QOIP experiment explicitly designed to decrease the intensification rate, the DIR experiment is capable of achieving roughly 35% of the reduction in intensification rate that is achieved by the RIIR experiment while utilizing initial perturbations that are only roughly 10% the magnitude of the RIIR perturbation. The muted response in the RIIR experiment as compared to the IIR experiment is evidence of nonlinear impacts of the initial perturbation that reduce the response of the forecast to the QOIP when the sign is reversed, which are expressed in the DIR experiment by lowered linearity, fewer iterations, and a weakening of the cyclone of a

much smaller magnitude than the intensification of the cyclone observed in the IIR experiment. This kind of nonlinear response can be explored in the QOIP framework in a way that is not achievable using other adjoint-based techniques. Here, the RIIR experiment will be investigated for its use of barotropic preconditioning to weaken, rather than intensify, the cyclone.

Figures. 3.14 and 3.15 show the RIIR experiment BEC and dKE (evaluated in a frame of reference moving with the trough). At the initial time, the BEC rates are identical to those found in the IIR case, a result of the BEC being computed via squared values of the perturbation zonal and meridional wind field, which are identical in the reversed-sign experiment. While sources of BEC are not always in the same geographical location in the RIIR experiment as they were in the IIR experiment, the RIIR experiment displays similar characteristics to the IIR experiment through the 6-hr forecast, with the most significant differences owing to changes to the geometry of the upper-disturbance by the QOIP. By 9-hrs into the forecast, both experiments have two individual dKE maxima (Figs. 3.12d and 3.15d), located over the northern Gulf Coast and Upper Midwest of the United States, where BEC dominates the total local time-rate-of-change of KE. While both of these maxima are similar in their geometry, the southern maximum in the RIIR experiment is approximately twice the magnitude of that of the IIR experiment. Like with the IIR experiment, by 12-hrs into the forecast the southern maximum in dKE begins to displace from the BEC maximum, indicating that the preconditioning process has likely ended and other non-BEC processes are becoming significant contributors to dKE.

A region of negative BEC develops in-between BEC maxima at 9-hrs into the forecast for both the IIR and RIIR experiments. Although there are some subtle differences in the geographic location and magnitude of the BEC and dKE between the two experiments, they are qualitatively very similar. The most significant difference is that the sign of the perturbations between the two cases is reversed, resulting in the RIIR perturbations reducing the amplitude of the trough and further inhibiting the reorientation of the trough into a more negative configuration. Furthermore, unlike the IIR simulation, the lack of negative tilt aids in hindering the creation of an upstream ridge between F012 and F015, further deterring significant baroclinic growth.

3.6.1 A Note on the Linear Relationship Between the IIR and DIR Cases

Figure 3.16 shows the initial time BEC rates and QGPV perturbations at between 400 hPa and 150 hPa for the DIR experiment, whose QOIP achieved two iterations, and the QOIP for the IIR experiment that was achieved after two iterations, referred to here as IIR₂. It is notable that the two cases display largely similar perturbation structures with opposite magnitudes, indicative of the linear relationship between the QOIP of each experiment for a low number of iterations. However, it should be recognized that by definition, the QOIP of the DIR and IIR experiments will be exactly equal and opposite in magnitude after one iteration, while two iterations allows for only modest deviation between the two QOIP as only one additional perturbation is added to each QOIP computed for nonlinear trajectories that may have diverged. While the spatial structures and normalized BEC traces of the DIR and IIR₂ are largely similar to that which is seen in

the final IIR and RIIR experiments (Fig. 3.7a), the magnitude of the perturbations is approximately 25% of the IIR and RIIR experiments.

This result indicates that while the adjoint model is able to create perturbations that result in some BEC even within the DIR experiment, it is an inefficient method for weakening mid-latitude cyclones due to nonlinear interactions that sharply reduce the impact of BEC on the response function relative to what is expected from the adjoint model. This results in a QOIP that quickly falls below the chosen threshold for linearity, achieving only two iterations and producing very small perturbations relative to the IIR experiment. These findings, in conjunction with the previous results of Kucharski and Thorpe (2001) only further indicate that BEC is a phenomenon that is asymmetrically tilted towards being beneficial in increasing the intensification rate of mid-latitude cyclones while it is a less effective mechanism to decreasing the intensification rate.

3.7 QOIP Augmentation of Baroclinic Development

While the BEC diagnostic provides evidence that a barotropic preconditioning process is important in shaping the local synoptic environment for increased baroclinic growth downstream, it does not diagnose baroclinic development. For this reason, the use of a piecewise QGPV inversion technique as described in Section 2.4 is used. By using this technique, it is possible to identify explicitly the impact that a portion of the QGPV perturbation may have on the low-level height field. Although the response function used in these experiments is formulated such that it is aimed at impacting the surface pressure, for the purposes of analysis in the following section the inversion results will focus on the 900 hPa geopotential as a proxy for the surface pressure in order to avoid interpolations

to below-ground isobaric surfaces and unrealistic interpolations associated with poorly resolved near-surface layers.

Piecewise QGPV inversion is performed by defining the instantaneous control forecast state as the basic-state and the evolved QOIP as the perturbation state. The inversion is performed on a sub-domain of the global grid from 20° to 75° N and 135° to 40° W, containing the surface cyclone and the upper-tropospheric precursor disturbance. Geopotential below ground is hypsometrically interpolated from the nearest above-ground level assuming a US standard atmosphere profile, and the piecewise contribution to perturbation geopotential of the lower boundary at 1000 hPa is computed by interpolating from the 950 hPa perturbation geopotential assuming the observed vertical gradient of perturbation geopotential. This allows for the inversion of the QGPV of the interior pressure levels as well as the inversion of the effective temperature perturbation between 950 and 1000 hPa.

KM05 made note of the importance of the mid-level impact of initial PV perturbations on the baroclinic development of the cyclone. While initial-time (Fig. 3.7) perturbations were seen extending through much of the troposphere, by F012, the time at which barotropic preconditioning was determined to have largely terminated, the most substantial perturbation magnitudes in the vertical were consistent with KM05, maximizing in the mid-levels between 500 hPa and 300 hPa (not shown). Meanwhile, significant BEC is identified in the 400 hPa to 150 hPa layer (Fig. 3.9). Therefore, the perturbations were separated into five layers (seen also in table 3.1): the lower boundary temperature perturbation (1000 hPa); low-level QGPV (950 hPa to 750 hPa); mid-level QGPV (700 hPa to 450 hPa); upper-level QGPV (400 hPa to 150 hPa) and lower

stratospheric QGPV (100 hPa to 50 hPa). The mid-level QGPV is chosen to represent the contribution from mid-level PV as identified in KM05, while the upper-level QGPV is chosen to represent the contribution from the layer with the most significant BEC. In order to first identify the relative contributions of the QGPV perturbations within each of those levels, Figs. 3.17a-d shows a time-series of the total impact of the partitioned QGPV on the 900 hPa perturbation height against the observed 900 hPa perturbation height summed within boxes between 7° to 9° following the central minimum pressure of the cyclone in the control forecast.

Two immediately evident conclusions can be drawn from Figure 3.17: (1) there is a lack of direct, instantaneous influence on the low-level circulation by the upper-level perturbations; and (2) the seemingly paradoxical behavior of the surface and lower-level inverted heights versus that of the inverted mid-level heights, especially with regards to the IIR and RIIR cases. It can be seen in Fig. 3.17a that the inversion of the IIR QGPV perturbations below 700 hPa is responsible for positive height perturbations, whereas the the QGPV extending from 700 hPa to 450 hPa is largely responsible for negative height perturbations. While the latter observation is consistent with both the conceptual model of baroclinic cyclone development as well as the results from KM05, the positive height perturbations resulting from the QGPV in the lowest 300 hPa is at least somewhat surprising.

While the direct impact of the upper-level perturbations on the lower-level circulation is relatively small as compared to the lower- and mid-level perturbations, their importance in the overall development of the lower-level cyclone can not be overstated. Although the impact by the upper-level perturbations on the lower-level circulation is

minimal (Fig. 3.18), the upper-level perturbations lead to a reconfiguration of the precursor disturbance as to make it more (less) favorable for increased intensification. This is especially true for the IIR and RIIR cases, in which the trough is substantially reconfigured as compared to the DIR and RDIR cases, in which features within the trough are merely accentuated with the trough configuration largely remaining the same (e.g., an increase in the magnitude of the QGPV at the base of the trough, but no changes to the up- or downstream QGPV in a manner that would reshape or reorient the trough configuration versus the control simulation).

Due to the small magnitude of the QGPV perturbations in the DIR and RDIR cases, they will not be discussed in great detail, however some comments on their evolution will be offered in subsequent sections. The following sections will focus largely on the IIR and RIIR simulations. Additionally, as much of the impact of the perturbations in the first 12-hrs has been discussed in the sections on BEC, the discussion of baroclinic development within a QGPV framework will focus on the period deemed to be after the termination of the major BEC processes, starting at the 12-hr point in the forecast integrations.

a) IIR Experiment

Beginning at 12-hrs into the forecast integration, the IIR simulation displays positive upper- and mid-level QGPV perturbations found at the base of the trough. Recalling the BEC arguments presented in the previous section, the orientation of the upper-level trough is paramount in creating a synoptic environment favorable for baroclinic growth. The perturbations to the IIR case at F012 illustrate this (Fig. 3.19a, b),

as the IIR case displays a configuration in which the perturbations at the base of the trough has created not only a deeper wave, but one that is slightly more negatively tilted relative to the jet than the control. This change in tilt is most notable with southward extent, closer where the most substantial QGPV perturbations are located. Additionally, perturbations downstream of the trough are oriented in a manner such that a downstream ridge has begun to develop, allowing for increased positive vorticity advection (PVA) downstream and a concomitant increased baroclinic surface development. The orientation of the trough by the perturbation at F012 further illustrates the importance of the barotropic preconditioning process outlined previously.

While the upper-level QGPV perturbations modify the environment to be more favorable to baroclinic development, the mid- to lower-level QGPV perturbations evolve to exert a direct, instantaneous impact on the near-surface cyclone. A positive QGPV perturbation to the base of the mid-level trough begins to produce lowered heights at 900 hPa within the baroclinic zone directly over the developing near-surface cyclone in the southeastern United States (Fig. 3.19d). The temperature advection at 900 hPa induced by the mid-level QGPV perturbations is estimated by computing the advection by the geostrophic flow consistent with piecewise inverted mid-level QGPV perturbations. In the IIR experiment, this circulation promotes warm advection within the developing warm front and the establishment of a temperature maximum near the center of the near-surface cyclone while promoting enhanced cold air advection along the developing cold front (Fig. 3.20a), while the circulation induced from the low-level QGPV acts to reinforce these advectations, particularly those along the cold front (Fig. 3.20d).

Additionally, low-level cold air advection west of the surface cyclone center in promotes reduced static stability near the surface and enhanced static stability at mid-levels, which enhances the mid-level QGPV perturbation in the mid-level trough while reducing QGPV at low levels (Fig. 3.21). A cross-sectional view through the base of the mid-level trough and approximately perpendicular to the low-level baroclinic zone at 12-hrs (Fig. 3.21a, c) displays upward bowing isentropes underneath the mid-level positive perturbation QGPV maximum, which in conjunction with the negative temperature perturbations subsequent to the shift in the lower-level baroclinic zone helps to relax the lower-level static stability, while increasing the mid-level static stability (Fig. 3.21e). These changes allow for a large region of low-level negative perturbation QGPV to exist to the west of the shifted baroclinic zone. When inverted, this large region of negative QGPV perturbations result in a large positive height perturbation over the region (Fig. 3.22d and Fig. 3.22e). At the same time a small, diabatically generated barotropic vortex that developed as a result of convection over the Gulf of Mexico is advected over central Florida and approaches the larger-scale developing cyclone. This vortex can be seen as the baggy region within the perturbed simulation 970 m height contour over central Florida at 12-hrs.

By F017 and F024, the upper-level trough in the IIR case continues to be shaped by the perturbations in a manner that leads to a more favorable synoptic configuration for enhanced baroclinic growth. The trough is made deeper and more negatively oriented with a larger downstream ridge evident. At 17-hrs, the trough in the mid-levels is oriented similarly to the upper-levels, an (indication of the reshaping discussed previously) and is characterized by a mid-level positive QGPV perturbation found at the base of the trough

has consolidated and strengthened, resulting in a strengthened inverted perturbation lower-level circulation (Fig. 3.19b, e). This strengthened circulation acts to further shift the baroclinic zone eastward, as well as increase cold air advection west of the baroclinic zone. This process results in a strengthened negative QGPV perturbation to the west of the baroclinic zone, which when inverted produces a more significant lower-level positive height perturbation (Fig. 3.22b). Within the cross-sectional view (Fig. 3.21b, d), the mid-level positive QGPV perturbation has descended approximately 100 hPa as compared to the 12-hr forecast, while the lower-level perturbation QGPV has become even more negative owing to further reduction in low-level static stability (Fig. 3.21f) due to increased cold advection west of the baroclinic zone. The descent of the perturbation in the presence of reduced static stability aids in the penetration of the mid-level circulation to the surface. Additionally, the barotropic vortex has now been fully advected into the larger circulation, and now represents the lowest pressure in the surface cyclone, which can be seen at approximately 29° N latitude and 78° W longitude (Fig. 3.20b). As a result of a more negative QGPV perturbation to the west of the baroclinic zone, inverted lower-level height perturbations are greater than at 12-hrs with the exception of within the barotropic vortex, where the only notable inverted negative height perturbation within the cyclone is found.

By 24-hrs into the forecast, the mid-level perturbations to the trough are largely oriented identically to the upper-level trough, with a strongly negative tilt and a well-developed downstream ridge (Fig. 3.19c, f). By this point, the lower-level cyclone has deepened relative to the control and has moved further downstream. The inverted 900 hPa height perturbations resulting from the mid-level QGPV perturbation (Fig. 3.22c)

yield strong upstream (downstream) negative (positive) height perturbations, indicative of a classic baroclinic tilt. Additionally, the circulation imparted upon the low-levels by both the mid- and lower-level QGPV perturbations yields strong warm (cold) advection to the west and northwest (southwest) of the low-level cyclone (Fig. 3.21c, f). This advection helps to increase the baroclinic gradient along within the warm-frontal region, further helping to enhance baroclinic growth of the cyclone. The inverted lower-level QGPV displays further displays this enhancement, where the largest negative height perturbations resulting from the lower-level QGPV can be found along the warm front (as seen in Fig. 3.22f, where the lowest inverted perturbation heights are found along an axis stretching from the Carolina coast up through New Jersey in association with strongly positive values of perturbation QGPV as seen along the same axis in Fig. 3.19i). A final impact of the enhancement to the baroclinic gradient, a region of strong perturbation, low-level storm relative inflow can be seen just inland of and along the Carolina coast. This inflow further helps to intensify the storm by advecting positive QGPV perturbations generated along the warm-front into the core of the cyclone. This is visualized by a strong flux of positive QGPV into the center of the circulation.

b) RIIR Experiment

Opposite the IIR experiment, perturbations to the RIIR case at the 12-hr point lead to a trough that is not only weakened as compared to the control, but one that is oriented more positively than the control and lacks a notable downstream ridge and subsequent PVA. It can be seen in Fig. 3.23a-f that the location of the mid- and upper-level QGPV perturbations to the RIIR case are similar to that of the IIR case, but largely of opposite

sign. The most notable differences between the cases are seen in the mid-levels, where 1) negative QGPV perturbations at the base of the trough are more concentrated and isotropic than in the IIR simulation; and 2) a large region of positive QGPV perturbations is found downstream, a feature that is largely absent in the IIR simulation. These changes at 12-hrs indicate that the mid-level trough is not as deep as in the IIR simulation as well as the fact that a mid-level ridge is being suppressed downstream of the advancing wave. By F017 through F024, the RIIR case continues to display these characteristics, with a more positively oriented, weaker trough and lessened downstream ridge as compared to the control, opposite that of the IIR simulation. The trough also lags upstream as compared to both the control and IIR simulations, helping to further inhibit baroclinic development at the surface.

Furthermore, unlike the IIR case, in which the impacts of the lower- and mid-level QGPV perturbations on the lower-level height field develop early into the simulation, it is not until after 12-hrs that significant impacts by the QGPV perturbations from the RIIR experiment are felt. At 12-hrs, a negative low-level height perturbation due to a positive mid-level QGPV perturbations is seen over the mid-Atlantic States, being trailed by a negative QGPV perturbation upstream. These perturbations quickly expand while being advected downstream in subsequent forecast hours with the negative perturbation becoming more isotropic at the base of the trough at 17-hrs into the forecast before swinging into a highly negative orientation at the 24-hr point. This advection and reshaping/reorientation of the perturbations aids in the creation of a mid-level ridge (trough) upstream (downstream) of the developing surface cyclone. This configuration creates is highly unfavorable to baroclinic growth, as the surface cyclone is found directly

east of the upper- and mid-level trough, rather than northeast, mitigating significant upshear-tilt-with-height and results in a weakening lower-level circulation (Fig. 3.23i). This configuration also leads to strong low-level cold-advection by the mid-level circulation into the warm frontal region of the cyclone, helping to inhibit more substantial baroclinic development (Figs. 3.25a, b). The lower-level development of the cyclone that does occur can be directly attributed to the lower-level QGPV in the RIIR case, especially as the barotropic vortex is fully absorbed into the larger cyclone. It is however notable that the largest change seen to the lower-level circulation is a translation slightly to the southwest of the control forecast low position, rather than significant changes to the intensity (Fig. 3.23i). Furthermore, the configuration of the geostrophic wind by the perturbations leads to a low-level flux of QGPV *away* from the center of the cyclone.

c) DIR and RDIR Experiments

At F012, the most important factor in the comparison between the IIR (RIIR) and DIR (RDIR) simulations is the magnitude and placement of the QGPV perturbations in the mid- and upper-levels. Due to the small magnitude of the QGPV perturbations in the DIR and RDIR cases, they are not shown. However, at F012, the IIR (RIIR) and RDIR (DIR) each have positive upper- and mid-level QGPV perturbations found in similar locations at the base of the trough, albeit with the RIR and RIIR cases being characterized by perturbations of significantly higher magnitudes, resulting in higher-(lower-)amplitude, perturbed simulation upper- and mid-level pre-cursor waves. Recalling that the IIR case satisfied the linearity criterion for nine iterations as compared to the two iterations for the DIR case, the similarity in location of these perturbations indicates that

the QOIP algorithm specified that within the upper-levels, the strength of the trough was the primary factor responsible for modulating the intensification rate of the downstream cyclone during the response period. Between F017 and F024, the DIR and RDIR cases largely remain the same with respect to trough configuration, however the DIR (RDIR) case displays a slightly weaker (stronger) wave.

When inverted, the DIR and RDIR cases show little difference in their evolution as compared to the control run. The main difference between these cases and the control can be seen in the mid-levels at 24-hrs into the simulation, where QGPV perturbations are changing the magnitude of the mid-level wave. The orientation of the wave is also slightly changed poleward of these perturbations, where the DIR (RDIR) case is reconfigured into a slightly more positive (negative) orientation. With the exception of the change to the mid-levels at 24-hrs, changes to the cyclone are negligible, with low-level perturbations to the QGPV being small in magnitude and displaying little coherent structure. The lack of change is likely once again the effect of the rapid loss of linearity during the creation of and resulting small magnitude initial perturbations.

3.8 Summary and Conclusions

Four experiments were performed using a new adjoint-defined perturbation algorithm that creates and utilizes *quasi-optimal iterative perturbations* (QOIP; as outlined in section 2.1.4) to modulate the intensification rate of a moderately deepening mid-latitude cyclone. The case chosen for the experiments was the “surprise snow storm” of 24-26 January 2000 that produced unexpectedly significant snowfall across the Mid-Atlantic. The forecast challenge presented by this storm made it a good choice for

examination with an adjoint model, as much previous work done on the case indicated the importance of initial conditions on the evolution of the storm. The response function chosen for the experiment was based upon the *intensification rate* of the cyclone over the period from forecast hour 17 through forecast hour 24, a period over which the control experiment underwent the most rapid deepening.

Within the first 12 hours of the forecast integration, special attention was paid to *barotropic preconditioning* by perturbations to the mid- and upper-troposphere within the cyclone's upper-level precursor disturbance through *barotropic energy conversion*. Two of the experiments (the DIR and the RDIR cases) proportionally similar values of normalized BEC as compared to the IIR and RIIR simulations. Due to the relatively rapid degradation of linearity within the QOIP algorithm, these cases were unable to tap into the energy resulting from early-iteration BEC in a similar manner, and instead attempted to create changes to the response function via non-linear processes.

At the initial time, perturbations to the environment are maximized locally within a region of strong stretching deformation on the cyclonic shear side of a high-amplitude polar jet maximum over the northern Great Lakes region of the United States. Perturbations to the increased intensification rate (IIR) and reversed increased intensification rate (RIIR) cases showed the most BEC throughout the course of the forecast integrations, likely a result of more linear growth of the perturbations allowing for more iterations and larger initial perturbation amplitude. In each case, BEC made a substantial contribution to the overall total eddy kinetic energy (EKE) growth of the precursor disturbance, indicating its overall importance in the evolution of the early stages of the cyclone. While it is difficult to determine quantitatively the point at which

BEC becomes small relative to other processes (e.g., diabatic), the period over which BEC dominates the development of the upper wave can be referred to as a period of “barotropic preconditioning”, in which initial baroclinic growth of perturbations modifies the cyclone to enhance further baroclinic growth. In both the IIR and RIIR cases, barotropic preconditioning occurs in the first 12 hours of the simulation, and significantly augments the geometry of the upper-level trough.

The IIR simulation benefited from both positive and negative BEC within specific regions of the disturbance during the preconditioning process, allowing it to take on a more negative tilt than in the control run as well as begin to develop the downstream ridge as is seen in classic baroclinic cyclone events. Negative BEC was also oriented in a manner that it did not hinder in the phasing of the northern and southern disturbances along the basic-state upper trough. The RIIR case was unable to similarly benefit, and diverged from the IIR simulation between 9-12-hrs into the simulation. The geometry of the positive and negative BEC couplet within the RIIR simulation caused destructive interference of the northern and southern disturbances, hindered phasing, and delayed deepening. Additionally, the orientation of the BEC couplet led to a positively tilted trough orientation that was detrimental to baroclinic growth, with the perturbed simulation yielding a weaker disturbance characterized by a lack of development of the downstream ridge.

Within the decreased intensification rate (DIR) and reversed decreased intensification rate (RDIR) cases however, the perturbations suffer from a rapid drop-off in linear behavior, and therefore achieve low initial amplitude, contribute little BEC, and therefore express a negligible impact on the overall energetics of the developing upper

wave. The impact of the four experiments on the 900 hPa demonstrates that the tilt of the upper-level precursor trough at the time at which “pure” BEC terminates, 12-hrs into the simulation, shows subtle differences that have significant implications on the development of the trough at later times. The IIR case is seen to have a slightly more negatively tilted trough at 12-hrs, along with incipient downstream ridge development, a configuration beneficial to eventual downstream development of a baroclinic cyclone. Conversely, the RIIR case shows a slightly more positive tilt and a more zonal configuration downstream, a configuration detrimental to the development of a downstream baroclinic cyclone. In the DIR and RDIR cases, the trough orientations are largely unchanged as a result of a lack of appreciable barotropic preconditioning in the preceding forecast hours.

It can also be seen in Fig. 3.18a-d, that at approximately 12-hrs into the simulation, a time that corresponds to the termination of the “pure” BEC processes, a significant change to the impact on the 900 hPa height by the 700 hPa to 450 hPa QGPV occurs. Although the impact of the 700 hPa to 450 hPa QGPV is already negative in the IIR and RDIR cases, it rapidly becomes more negative starting at approximately 12-hrs into the simulation. For the DIR and RIIR cases, the impact of the 700 hPa to 450 hPa QGPV hovers around zero until approximately 12-hrs into the simulation, at which point it experiences a rapid shift towards increasing 900 hPa height perturbations that become more positive as the simulations are integrated forward in time.

As Fig. 3.5 shows that all of the experiments were characterized by deepening cyclones throughout the barotropic preconditioning process, it can be argued that barotropic preconditioning can be thought of as a mechanism by which the maximum

rates of intensification can be modulated, but the process favors intensification over weakening in this case. This is again consistent with previous work by Kucharski and Thorpe (2000; 2001) in which perturbations made to the analysis appear to only work to help *increase* the baroclinic growth of the cyclone, and at-best can delay and slightly depress baroclinic growth when oriented in the opposite direction. In this regard, it can be asserted Kucharski and Thorpe (2001) showed a similar result in an idealized framework, in which *perturbations oriented perfectly upshear of a zonal jet yielded much larger rates of intensification of a surface cyclone as compared to a control simulation, while those perturbations oriented perfectly downshear did not yield a weakening cyclone, but rather one that intensified less rapidly*. Finally, while Kucharski and Thorpe (2000) noted that an inability to calculate the sensitivity of cyclone intensity to trough orientation and position in full-physics, real-world simulations, this study has shown that adjoint-derived sensitivity gradients can provide this information and real-world case studies of barotropic preconditioning can be investigated using the QOIP technique.

After barotropic preconditioning of the precursor wave largely ceased (following the first 12-hrs of the simulation), the storm began to undergo substantial baroclinic development. This development was significantly augmented by the IIR and RIIR perturbations, while the DIR and RDIR perturbations were not able to significantly modify the evolution of the cyclone. This difference in impact was again due to the large difference in perturbation magnitudes owing to the differences in satisfying the linearity criterion specified within the algorithm creating the QOIP.

A piecewise QGPV inversion was performed in order to assess the direct impact of discrete portions of the QOIP on the development of the near-surface cyclone, with

attention paid to the cyclone at 900 hPa. In all cases, the upper-level perturbations (i.e., those from 400 hPa to 150 hPa) had relatively little direct impact on the lower-level development of the cyclone, but rather helped to reconfigure the larger-scale precursor wave in order to encourage increased (decreased) intensification rates during the response period through baroclinic processes. In the IIR and RIIR cases, this reconfiguration included significant modulation of the strength of the trough, as well as its orientation. In the DIR and RDIR, the perturbations served less in augmenting the orientation but did have some impact on trough strength.

The mid- and lower-level perturbations appeared in all four cases to be the main factors in the modulation of the intensification rate (and the evolution of the cyclone in general). As again was the case, the DIR and RDIR cases were characterized by perturbations in the mid- and lower-levels that were very small in magnitude as compared to the IIR and RIIR cases, and therefore they did not impart significant changes to the intensification rate versus the control simulation (as can be seen in the surface pressure traces in Fig. 3.5). The intensification rates of the IIR and RIIR cases however were substantially impacted by the perturbations to the initial state. Following the barotropic preconditioning period, the mid-level QGPV perturbations in both cases imparted lower-tropospheric circulations that served to reconfigure the lower-level baroclinic zone upon which the cyclone would initially develop. Furthermore, the development and consequent advection of a convectively borne diabatic vortex in the Gulf of Mexico affected the development of the cyclone. This vortex proved to be the lowest pressure in the larger-scale circulation, and by deepening this vortex and advecting it into the cyclone, the response function of the 24-hr forecast was reduced.

The intensification rate response function and QOIP method introduced in this case study are powerful tools to probe the response of a developing cyclone to initial perturbations. Furthermore, through the piecewise inversion of the QOIP perturbations, it is possible to directly identify which portions of the perturbations modulate the response function. The method of piecewise QGPV inversion, makes use of an instantaneous basic-state defined by the control simulation that allows for a direct and explicit identification of how the QOIP perturbations contribute to changes to the response function, a method that may prove useful in future perturbation-response type studies.

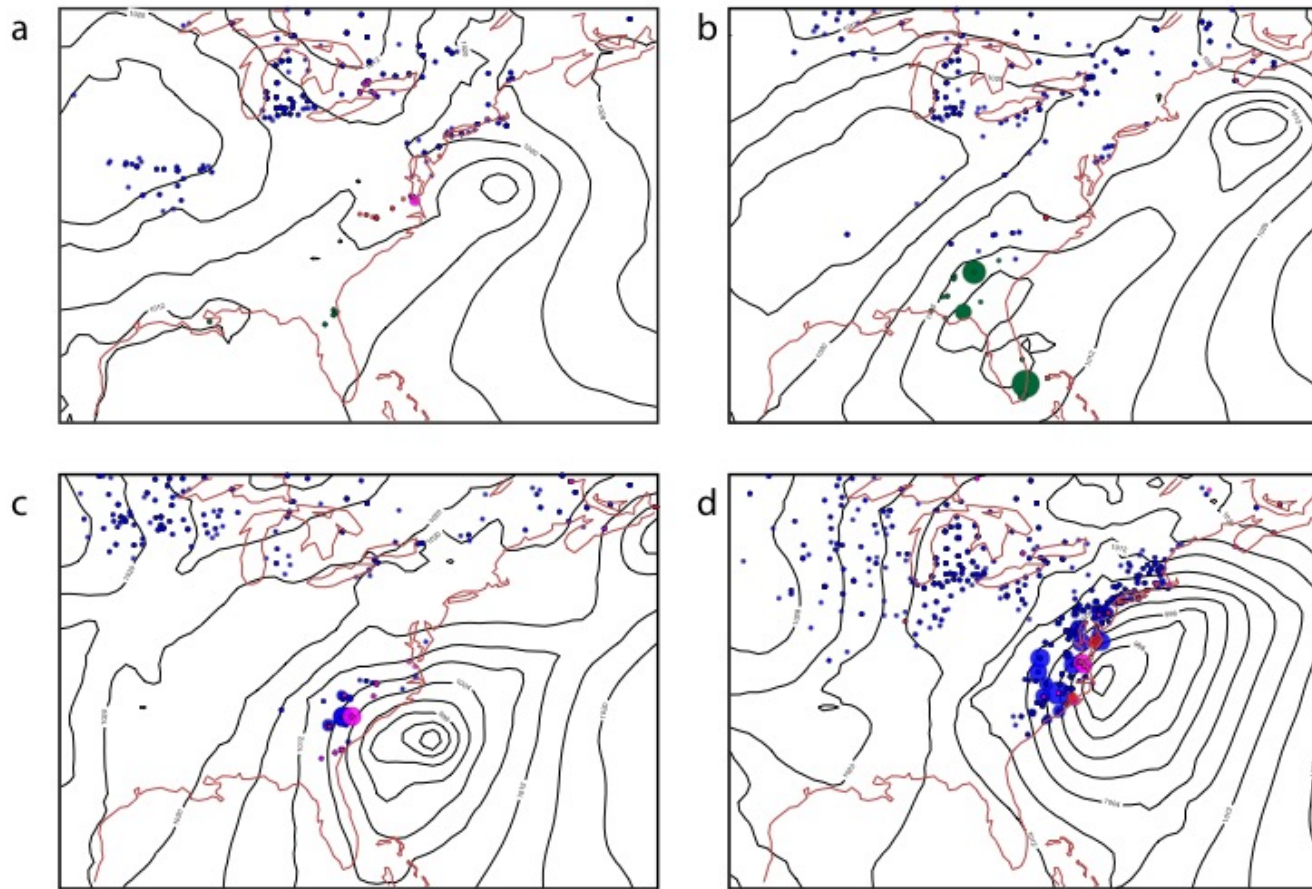


Figure 3.1. MERRA-2 analyses of surface pressure (black contours; hPa); and six-hourly snow (blue circles); mixed precipitation (magenta circles); freezing rain (red circles) and severe weather¹¹ (green circles) reports¹². Circle size indicates amount of reports at the time of the observation. valid at (a) 0000 UTC 2000 January 24; (b) 1200 UTC 2000 January 24 UTC; (c) 0000 UTC 2000 January 25 and (d) 1200 UTC 2000 January 25. Code used to generate these panels courtesy Dr. Brett Hoover.

¹¹ The United States National Weather Service (NWS) currently defines a severe thunderstorm as producing one or more of the following: hail greater than one inch; wind greater than 50 knots (25.7 m s^{-1}); and/or a tornado. Source: <http://www.spc.noaa.gov/faq/>.

¹² Storm reports courtesy of the TDL (US/Canada) network.

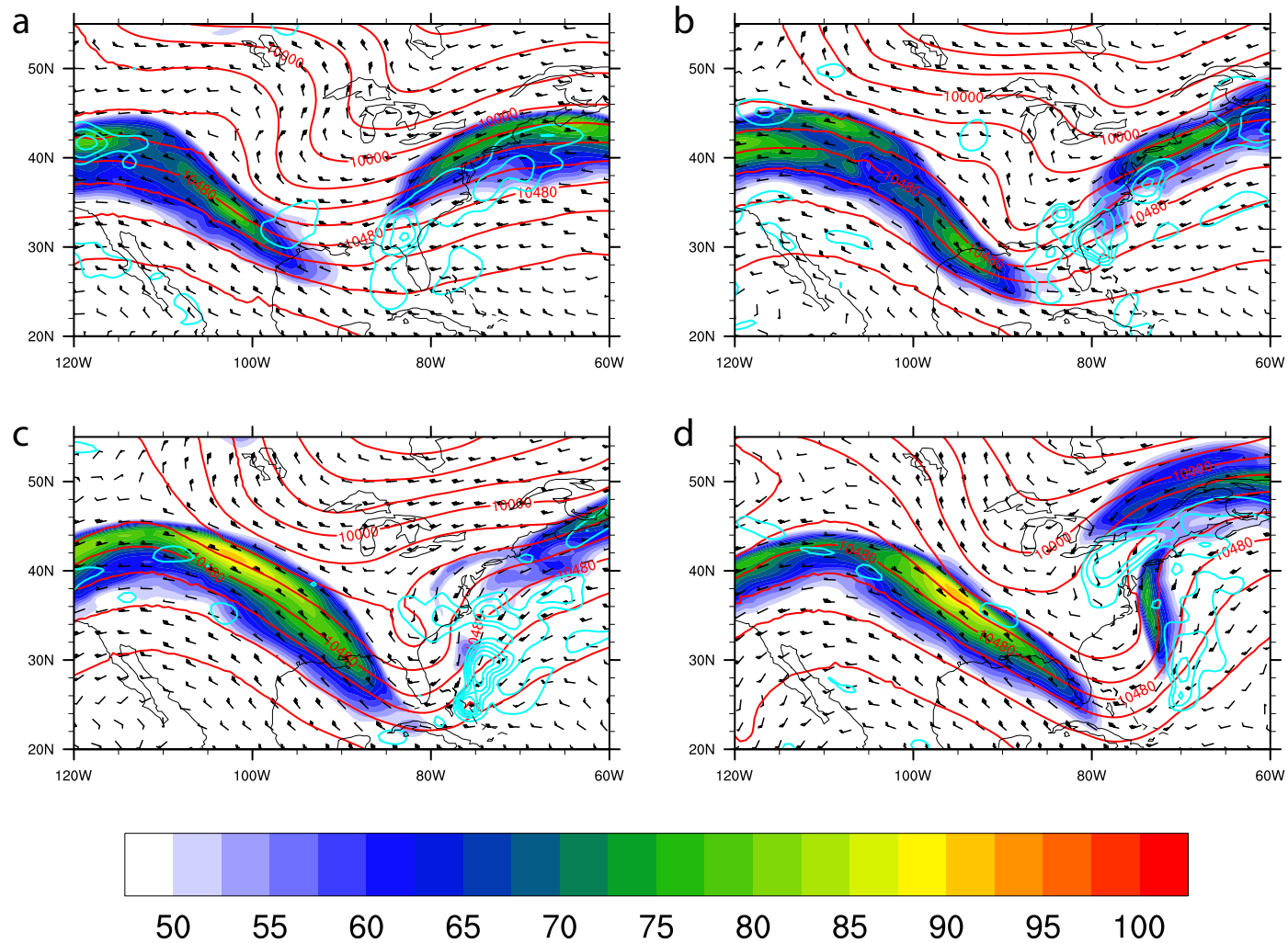


Figure 3.2. MERRA-2 analyses of the 250 hPa wind (fill and vectors; m s^{-1}); height (red contours; m) and divergence (cyan contours; s^{-1} ; contoured from 2×10^{-5} to 10×10^{-5} by 2×10^{-5}) valid at (a) 0000 UTC 24 January 2000; (b) 1200 UTC 25 January 2000; (c) 0000 UTC 25 January 2000 and (d) 1200 UTC 25 January 2000

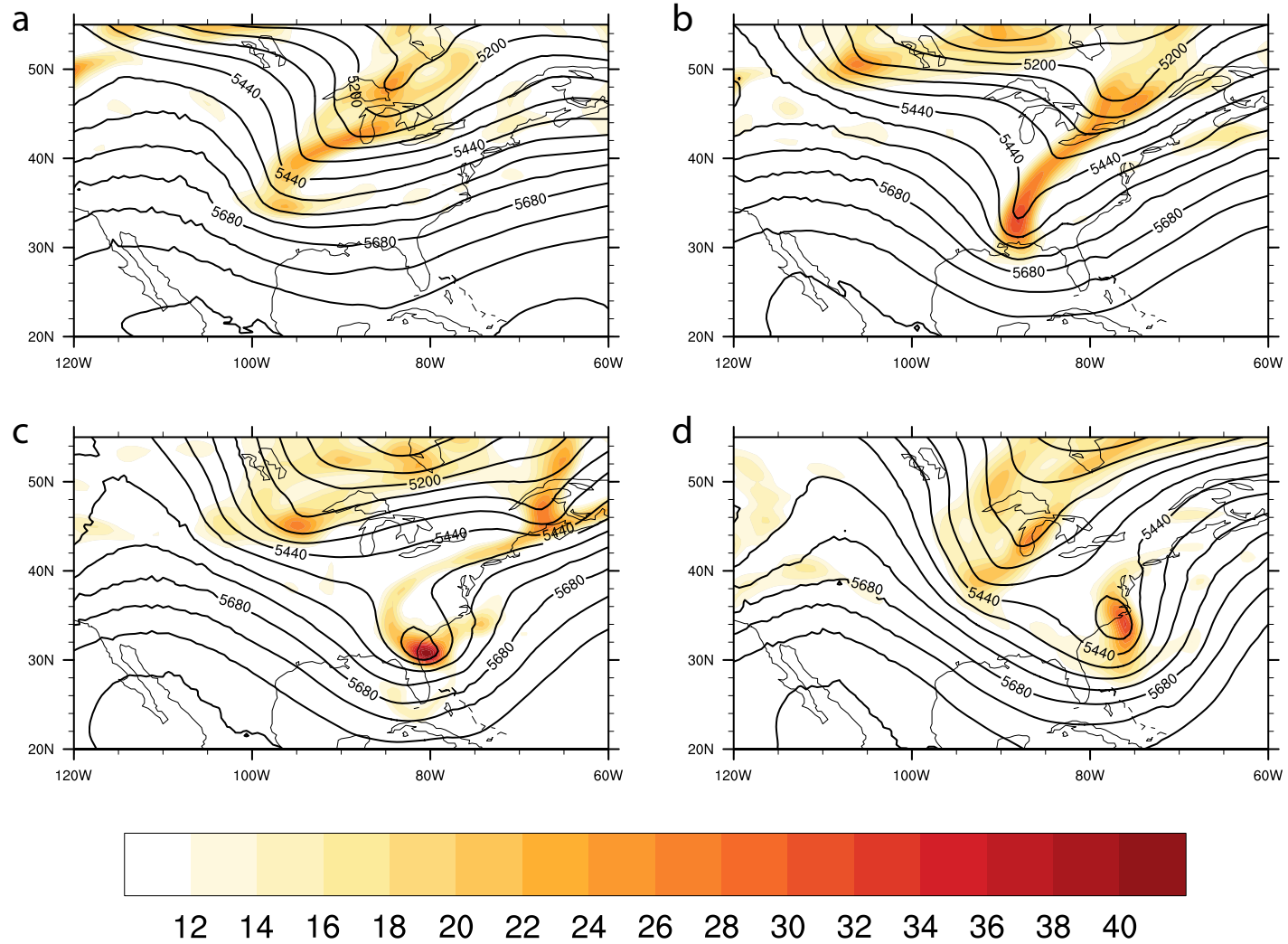


Figure 3.3. MERRA-2 analyses of the 500 hPa vorticity (fill; 10^5 s^{-1}); and height (black contours; m) valid at (a) 0000 UTC 24 January 2000; (b) 1200 UTC 25 January 2000; (c) 0000 UTC 25 January 2000 and (d) 1200 UTC 25 January 2000.

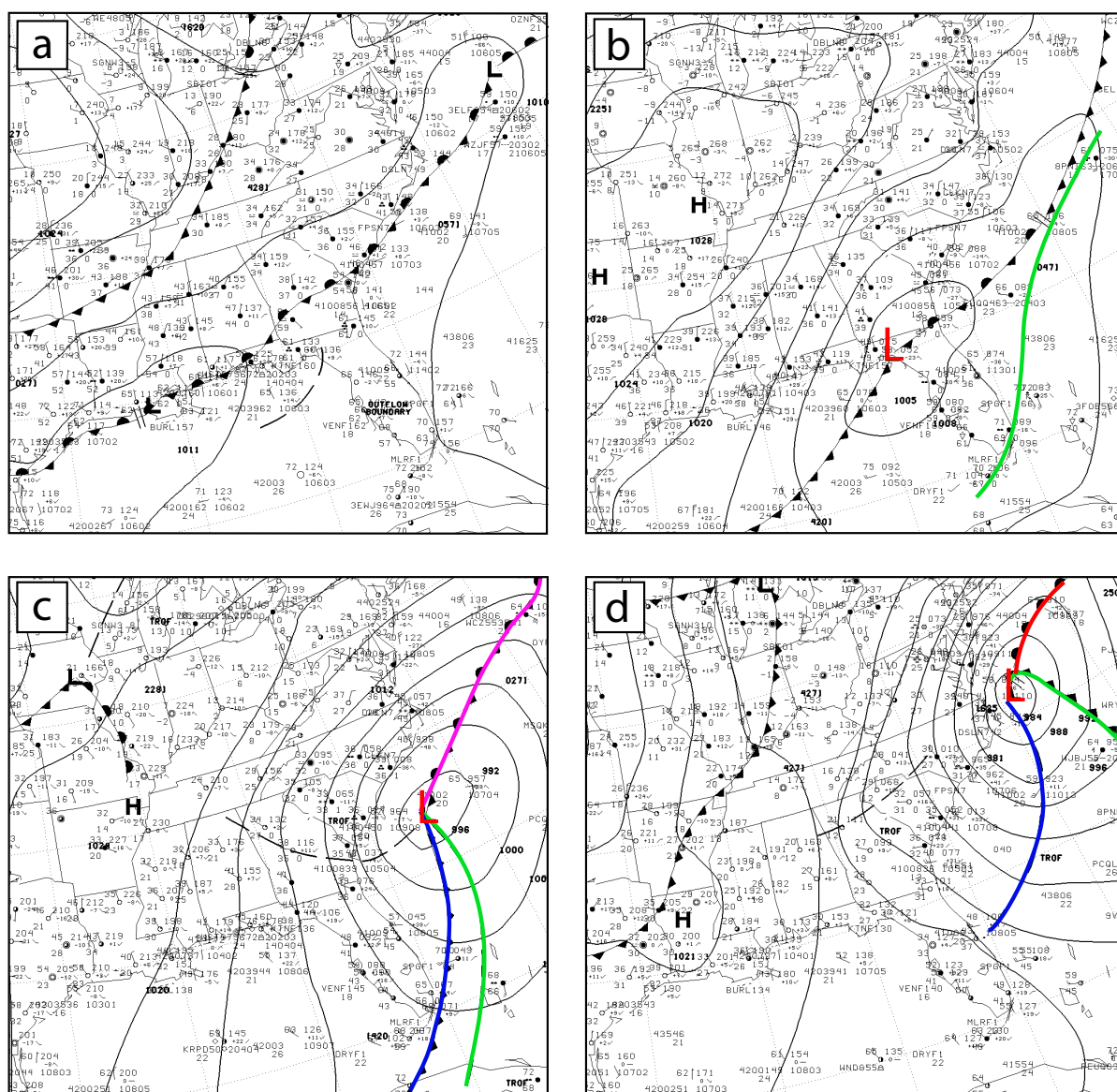


Figure 3.4. NWS subjective surface analyses¹³ valid at (a) 0000 UTC 24 January 2000; (b) 1200 UTC 25 January 2000; (c) 0000 UTC 25 January 2000 and (d) 1200 UTC 25 January 2000. The boundaries highlighted in panel (b) are the wavy remnant wind-shift baroclinic zone east of the synoptic frontal boundaries (green); (c) the wind-shift cold-front (green); the synoptic cold-front (blue); and the stationary-/warm-front (magenta); and (d) the wind-shift cold-front (green); the synoptic cold front (blue) and the warm-front (red)

¹³ Data access available at: <https://atmos.washington.edu/data/vmaproom/varchive.cgi>

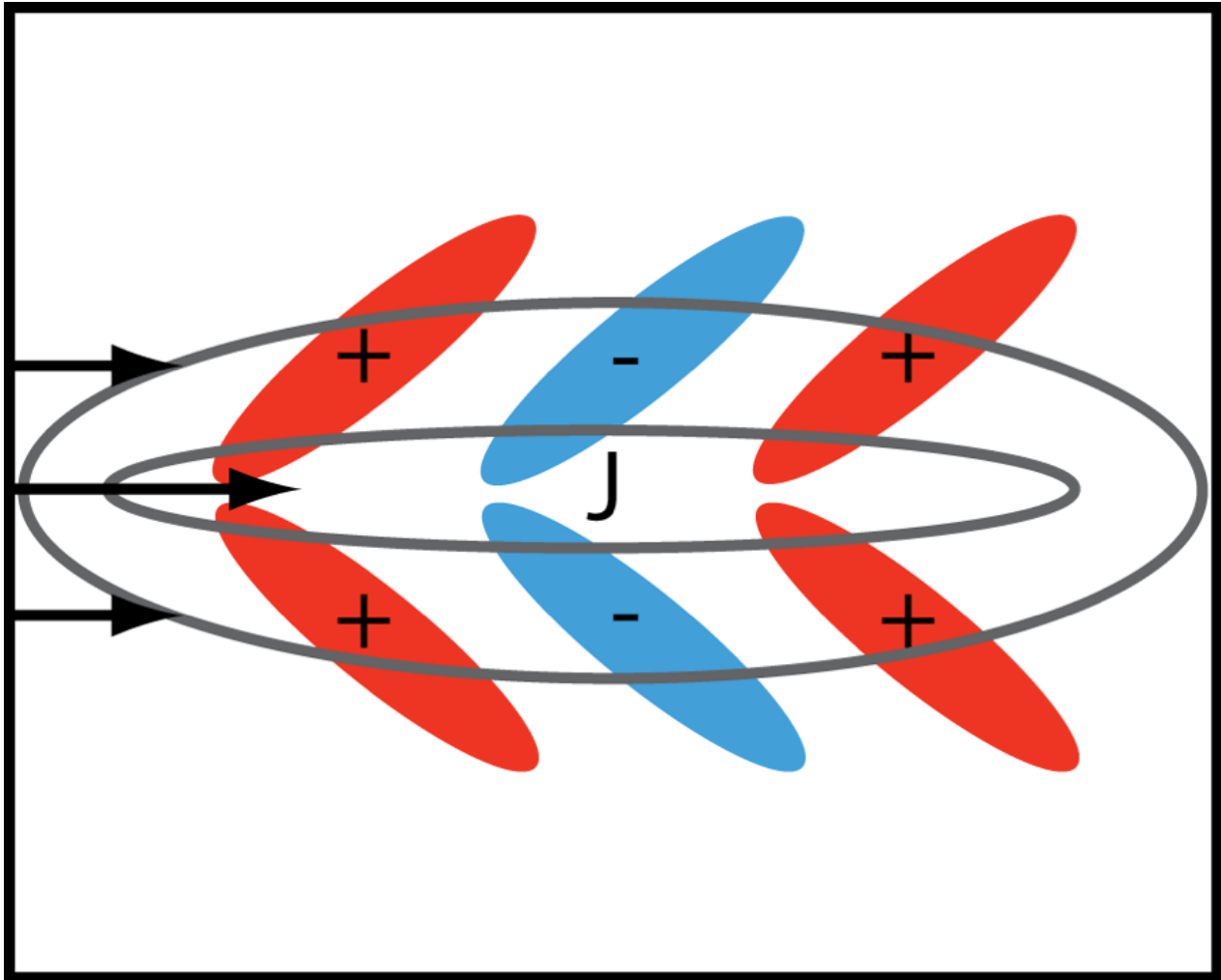


Figure 3.5. Conceptual diagram of barotropic signature in zonal wind sensitivities around a zonal jet. Gray lines are isotachs, with a “J” indicating the jet core. Vectors indicate relatively stronger zonal flow within the jet core. Sensitivity with respect to zonal flow is indicated with shaded regions representing areas of positive (red) and negative (blue) sensitivity. From Hoover (2015)

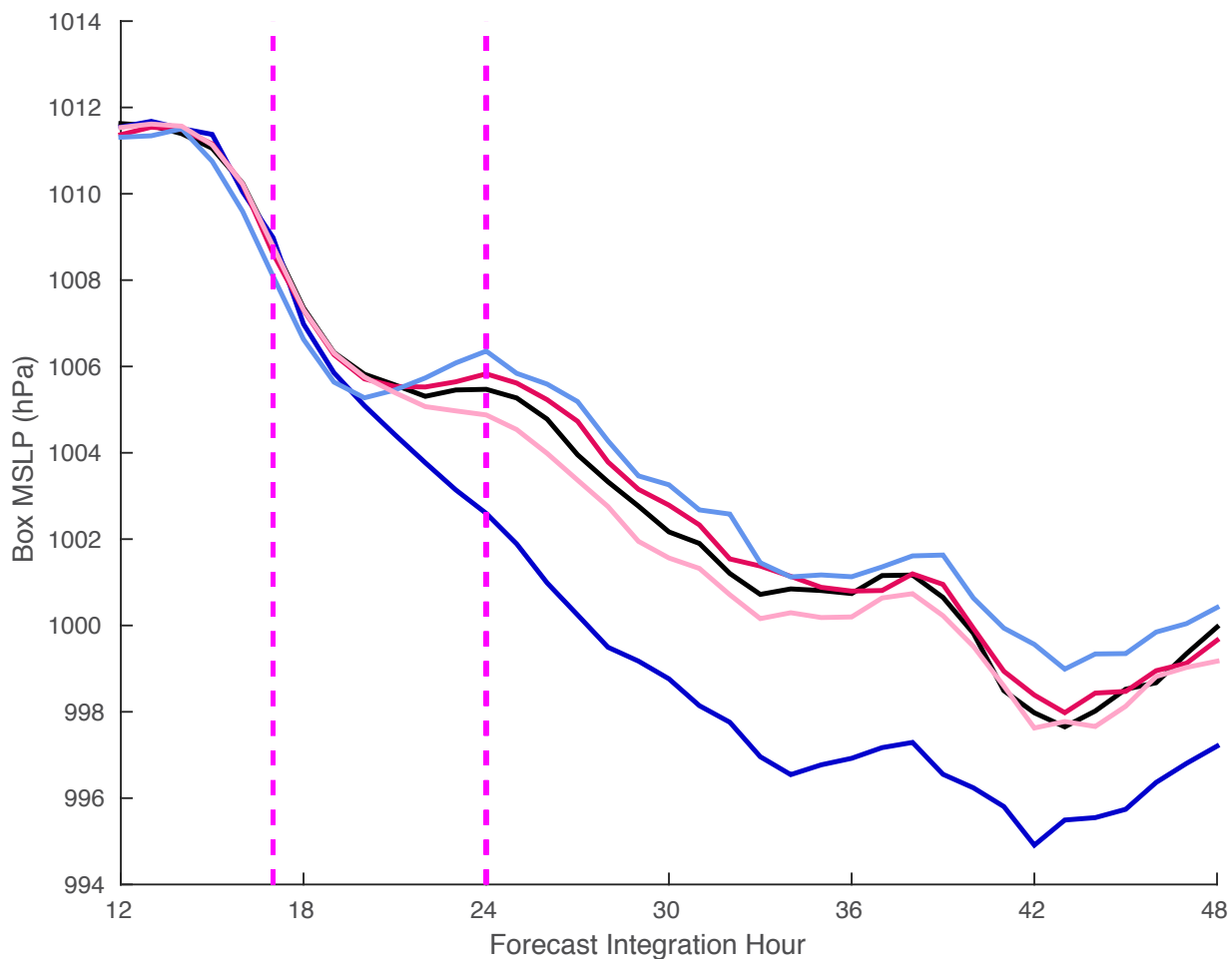


Figure 3.6. Cyclone-following time series of the 9° by 9° box-mean sea level pressure for the increased intensification rate perturbation simulation (IIR; dark blue); reversed sign intensification rate perturbation simulation (RIIR; light blue); decreased intensification rate perturbation simulation (DIR; red); and reversed sign decreased intensification rate perturbation simulation (RDIR; pink). The control simulation is seen as the black curve. The magenta, vertical bars at 17- and 24-hrs indicate the response period over which changes to the intensification rate by the QOIP to the analysis are intended.

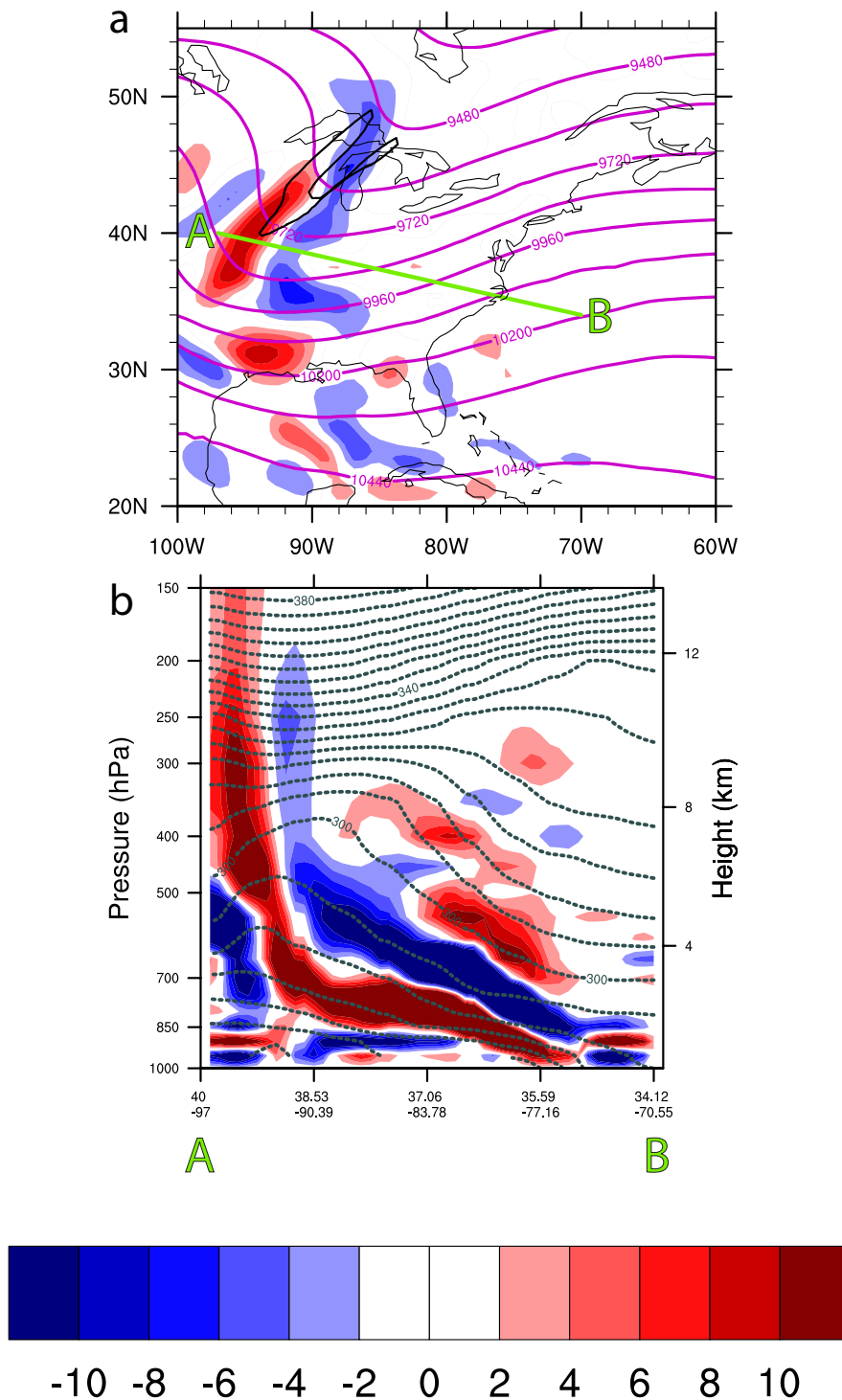


Figure 3.7. (a) Analysis time, IIR simulation upper-level layer average (400 hPa to 150 hPa) quasi-geostrophic potential vorticity (QGPV) perturbations (fill; $5 \times 10^5 \text{ s}^{-1}$); control simulation height (magenta contour; m); and stretching deformation (black contour; s^{-1}). Stretching deformation is contoured from 10^{-4} to 4×10^{-4} by 5×10^{-5} ; (b) cross-sectional view along the green line of (a) with control integrations isentropes (grey dash; K). Deformation is not plotted in (b).

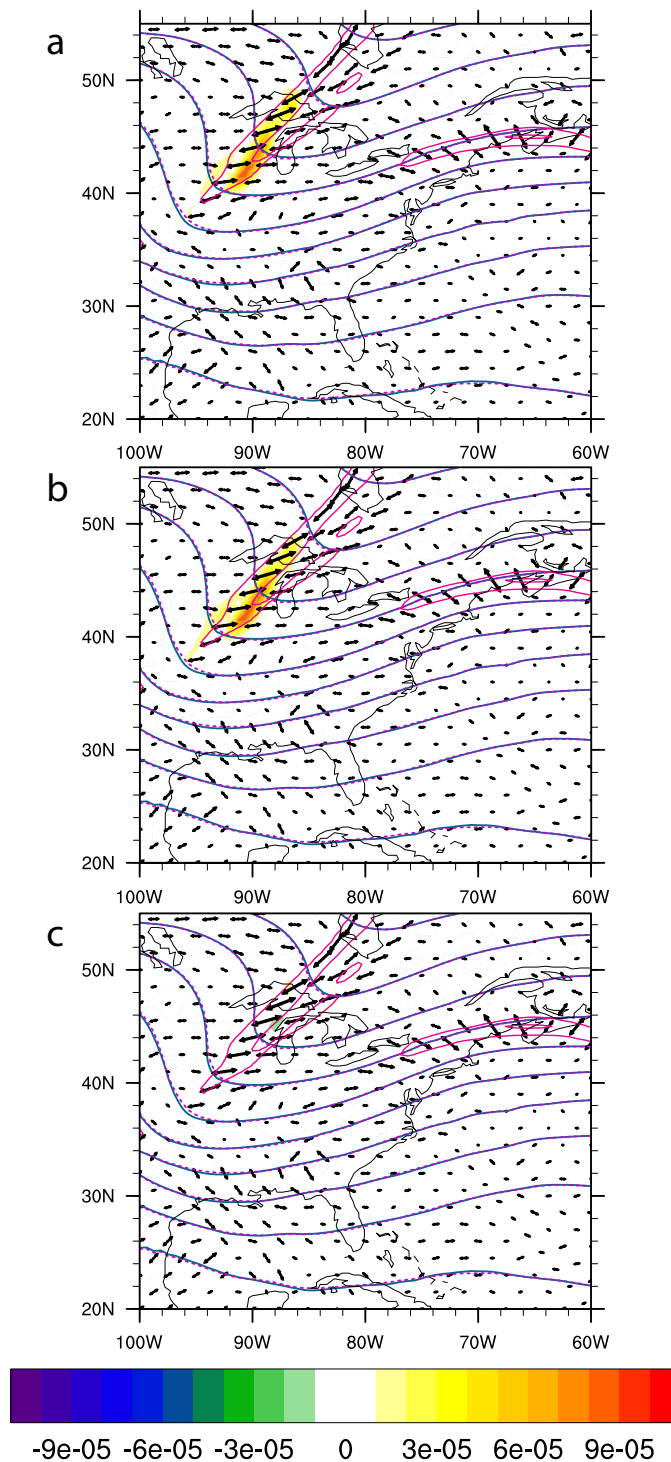


Figure 3.8. Analysis time 400 hPa to 150 hPa average barotropic energy conversion (BEC; fill; $\text{m}^2 \text{s}^{-3}$); axes of contraction (vectors; s^{-1}); control simulation height (magenta, dashed contour; m); and perturbed simulation height (dark blue, solid contour; m); and total deformation (light magenta, solid contour; s^{-1}). Heights are contoured every 120 m; deformation is contoured from 10^{-4} to 4×10^{-4} . BEC rates shown are (a) total; (b) BEC by the stretching deformation; and (c) BEC by the shearing deformation.

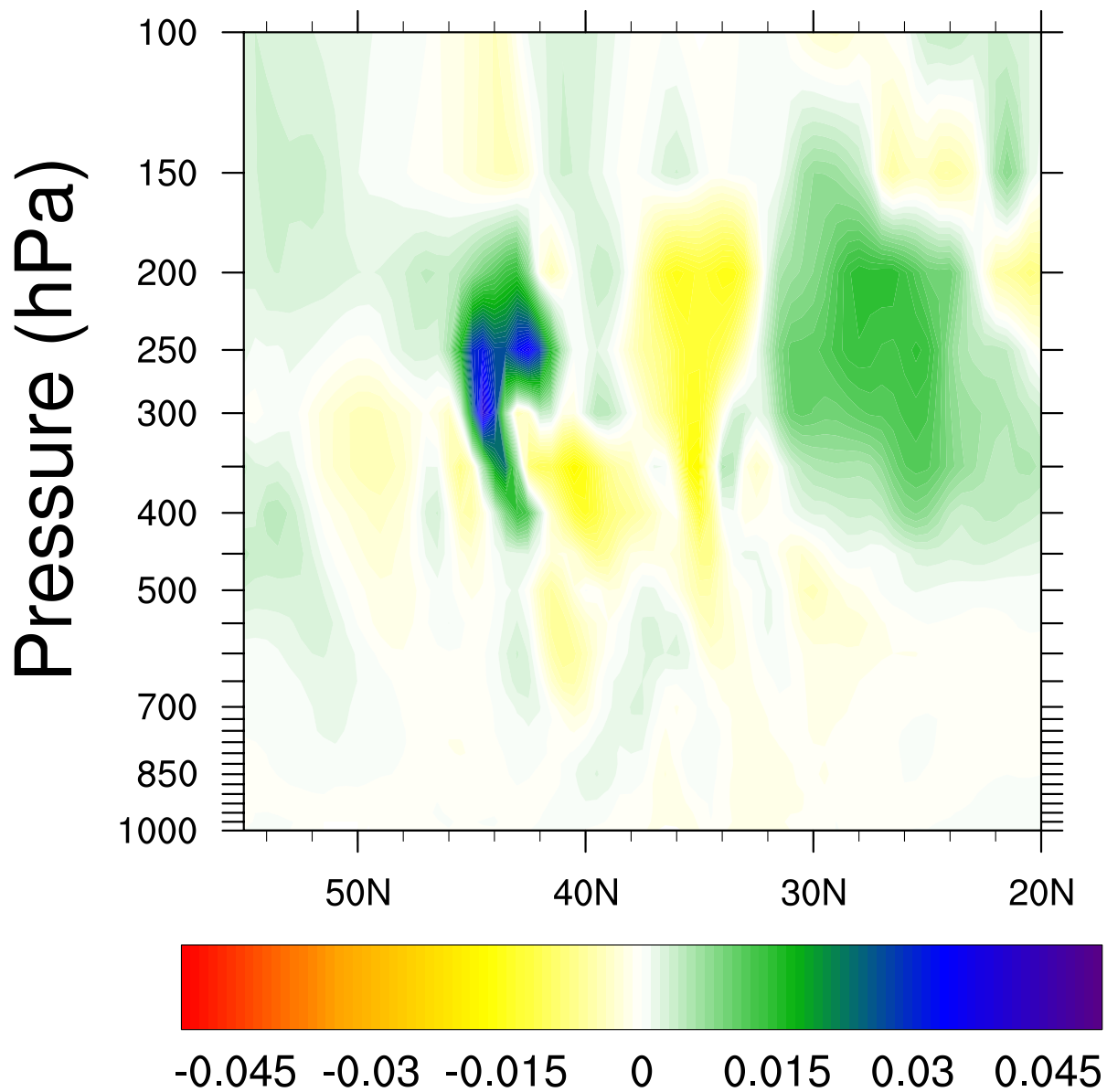


Figure 3.9. Cross section of the analysis time zonal-mean BEC from 60°W to 100°W longitude and 20°N to 55°N latitude (fill; $\text{m}^2 \text{s}^3$) for the increased intensification rate (IIR) case. Predominant BEC occurs between the 400 hPa and 150 hPa layer. The analysis time zonal-mean BEC for the RIIR case is identical to that of the IIR case, and therefore is not shown.

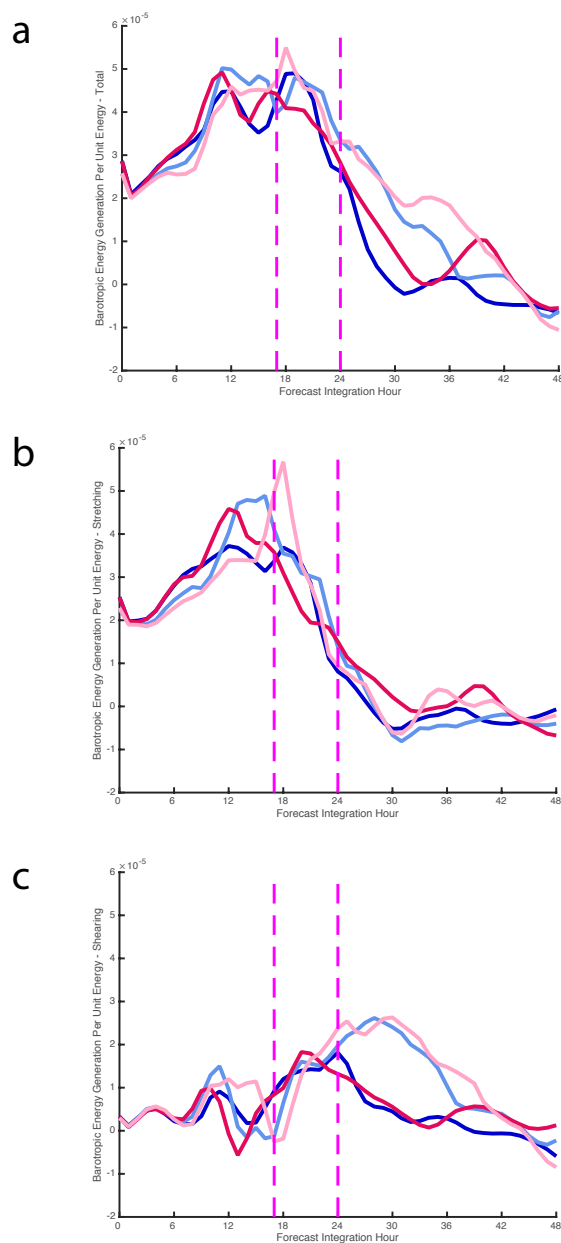


Figure 3.10. Time series of the 400 hPa to 150 hPa BEC normalized by the total KE (s^{-1}) over the course of the full, 48-hr forecast integration for the increased intensification rate perturbation simulation (IIR; dark blue); reversed sign intensification rate perturbation simulation (RIR; light blue); decreased intensification rate perturbation simulation (DIR; red); and reversed sign decreased intensification rate perturbation simulation (RDIR; pink). BEC rates in shown are (a) total; (b) BEC by the stretching deformation; and (c) BEC by the shearing deformation. The magenta, dashed vertical bars at 17- and 24-hrs indicate the response period over which changes to the intensification rate by the QOIP to the analysis are intended.

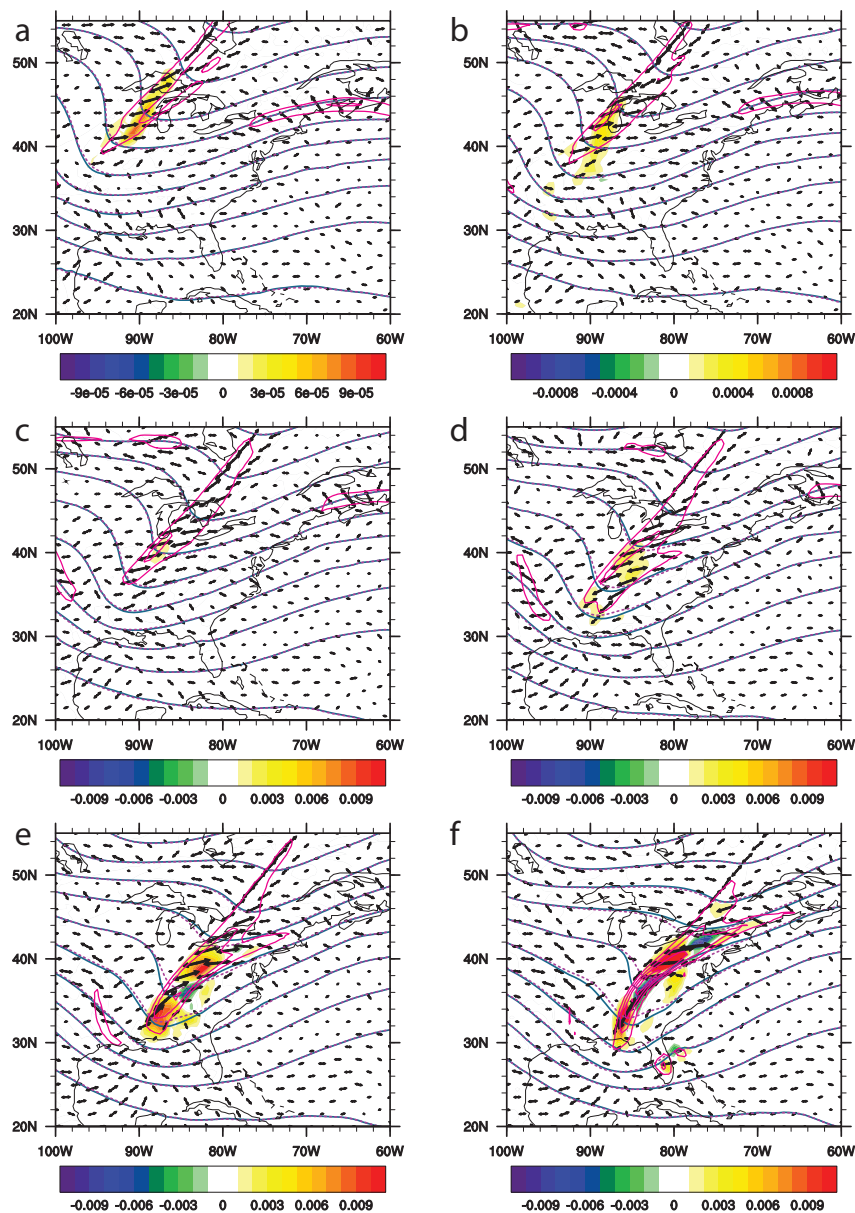


Figure 3.11. Increased intensification rate (IIR) 400 hPa to 150 hPa average BEC (fill; $\text{m}^2 \text{s}^{-3}$); axes of contraction (vectors; s^{-1}); control simulation height (magenta, dashed contour; m); perturbed simulation height (dark blue, solid contour; m); and total deformation (light magenta, solid contour; s^{-1}). Heights are contoured every 120 m; deformation is contoured from 10^{-4} to 4×10^{-4} by 5×10^{-5} . Times shown are (a) 0-hrs; (b) 3-hrs; (c) 6-hrs; (d) 9-hrs; (e) 12-hrs; and (f) 15-hrs into the simulation). Note that the color bars are not consistent across all times, as BEC increases (decreases) non-linearly.

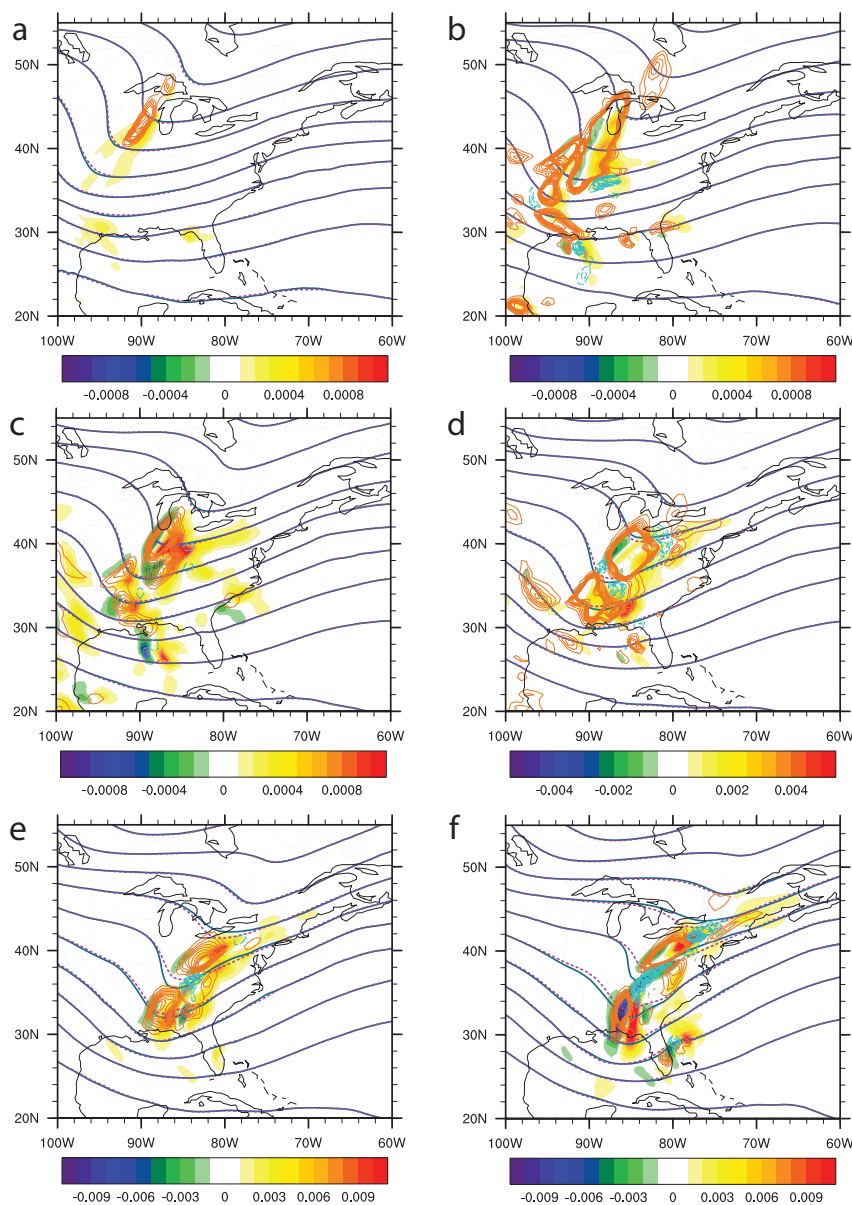


Figure 3.12. Increased intensification rate (IIR) 400 hPa to 150 hPa average local time rate of change of perturbation kinetic energy (fill; $\text{m}^2 \text{s}^3$); BEC (orange, solid contours indicate positive BEC, cyan, dashed contours indicate negative BEC; $\text{m}^2 \text{s}^3$); control simulation height (magenta, dashed contour; m); perturbed simulation height (dark blue, solid contour; m); Heights are contoured every 120 m; BEC is contoured as in Fig. 3.10. Times shown are (a) 0-hrs; (b) 3-hrs; (c) 6-hrs; (d) 9-hrs; (e) 12-hrs; and (f) 15-hrs into the simulation). Note that the color bars are not consistent across all times, as perturbation kinetic energy increases (decreases) non-linearly.

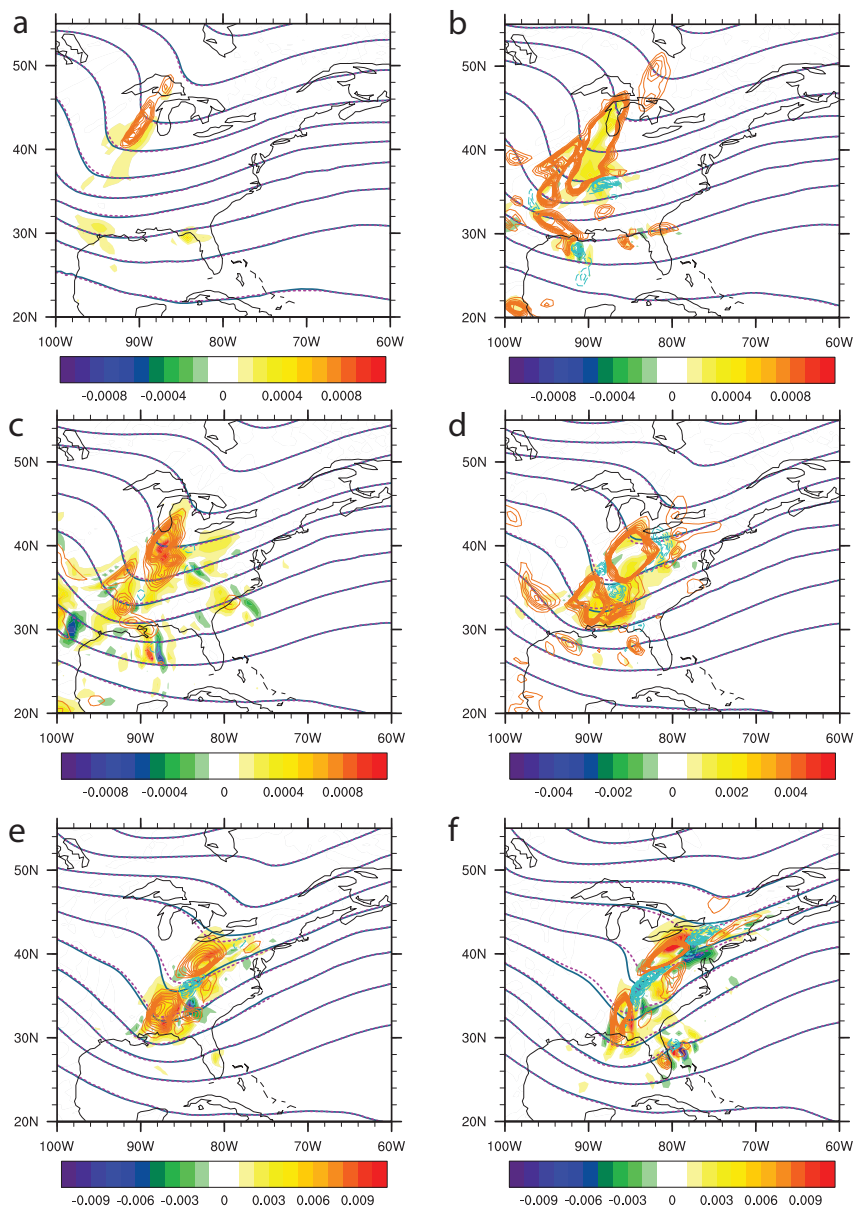


Figure 3.13. Increased intensification rate (IIR) 400 hPa to 150 hPa average local time-rate-of-change of perturbation kinetic energy (fill; $\text{m}^2 \text{s}^3$) with the component of the perturbation kinetic energy due to advection subtracted from the total; BEC (orange, solid contours indicate positive BEC, cyan, dashed contours indicate negative BEC; $\text{m}^2 \text{s}^3$); control simulation height (magenta, dashed contour; m); perturbed simulation height (dark blue, solid contour; m); Heights are contoured every 120 m; BEC is contoured as in Fig. 3.10. Times shown are (a) 0-hrs; (b) 3-hrs; (c) 6-hrs; (d) 9-hrs; (e) 12-hrs; and (f) 15-hrs into the simulation). Note that the color bars are not consistent across all times, as perturbation kinetic energy increases (decreases) non-linearly.

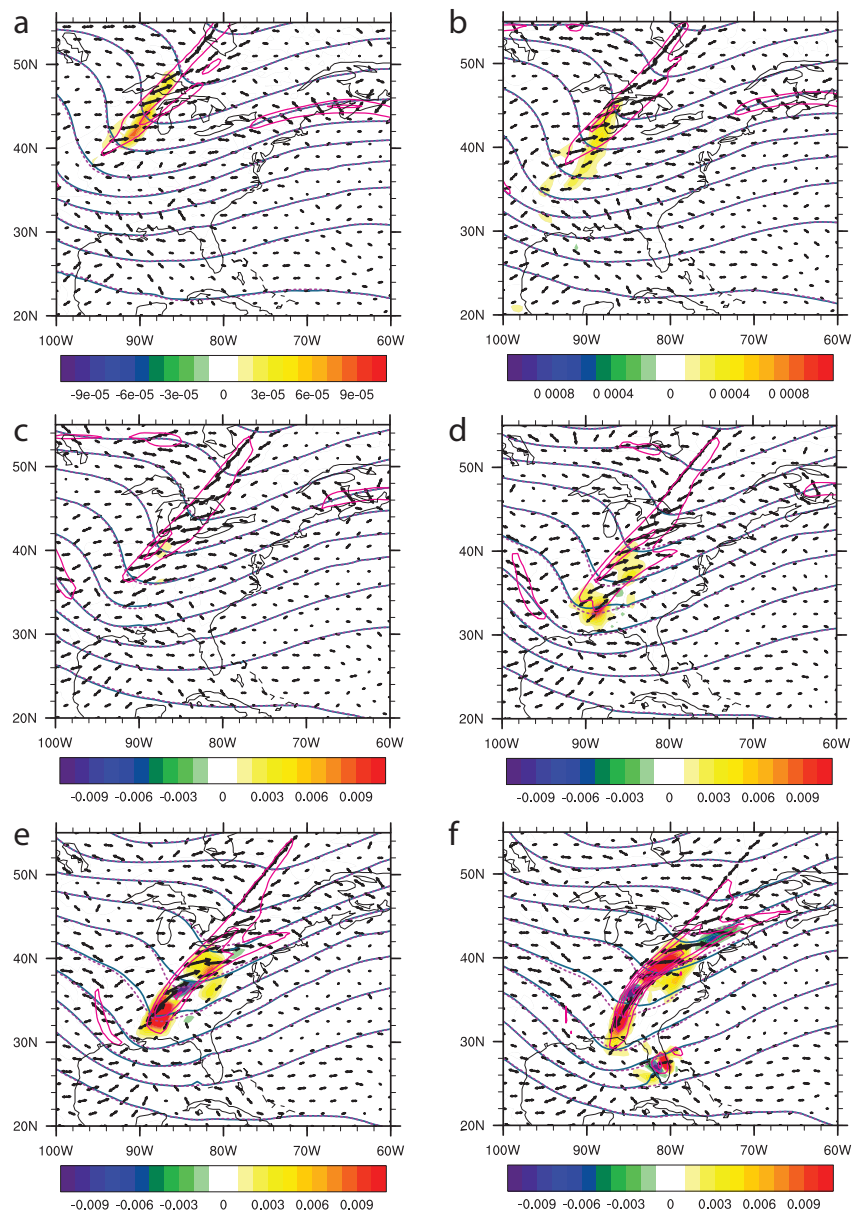


Figure 3.14. Reversed sign increased intensification rate (RIIR) 400 hPa to 150 hPa average BEC (fill; $m^2 s^3$); axes of contraction (vectors; s^{-1}); control simulation height (magenta, dashed contour; m); perturbed simulation height (dark blue, solid contour; m); and total deformation (light magenta, solid contour; s^{-1}). Heights are contoured every 120 m; deformation is contoured from 10^{-4} to 4×10^{-4} by 5×10^{-5} . Times shown are (a) 0-hrs; (b) 3-hrs; (c) 6-hrs; (d) 9-hrs; (e) 12-hrs; and (f) 15-hrs into the simulation). Note that the color bars are not consistent across all times, as BEC increases (decreases) non-linearly.

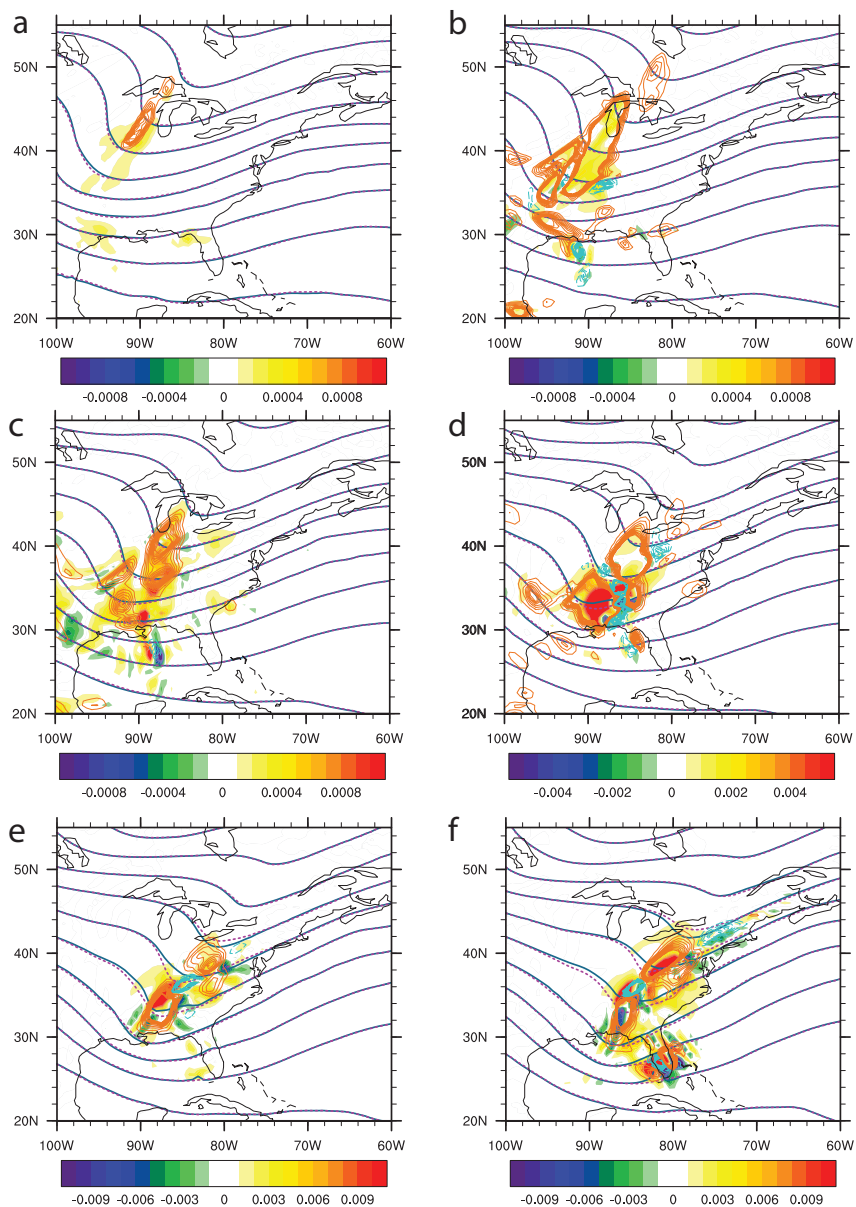


Figure 3.15. Reversed sign increased intensification rate of the RIIR experiment between 400 hPa and 150 hPa average local time-rate-of-change of perturbation kinetic energy (fill; $\text{m}^2 \text{s}^3$) with the component of the perturbation kinetic energy due to advection subtracted from the total; BEC (orange, solid contours indicate positive BEC, cyan, dashed contours indicate negative BEC; $\text{m}^2 \text{s}^3$); control simulation height (magenta, dashed contour; m); perturbed simulation height (dark blue, solid contour; m); Heights are contoured every 120 m; BEC is contoured as in Fig. 3.10. Times shown are (a) 0-hrs; (b) 3-hrs; (c) 6-hrs; (d) 9-hrs; (e) 12-hrs; and (f) 15-hrs into the simulation). Note that the color bars are not consistent across all times, as perturbation kinetic energy increases (decreases) non-linearly.

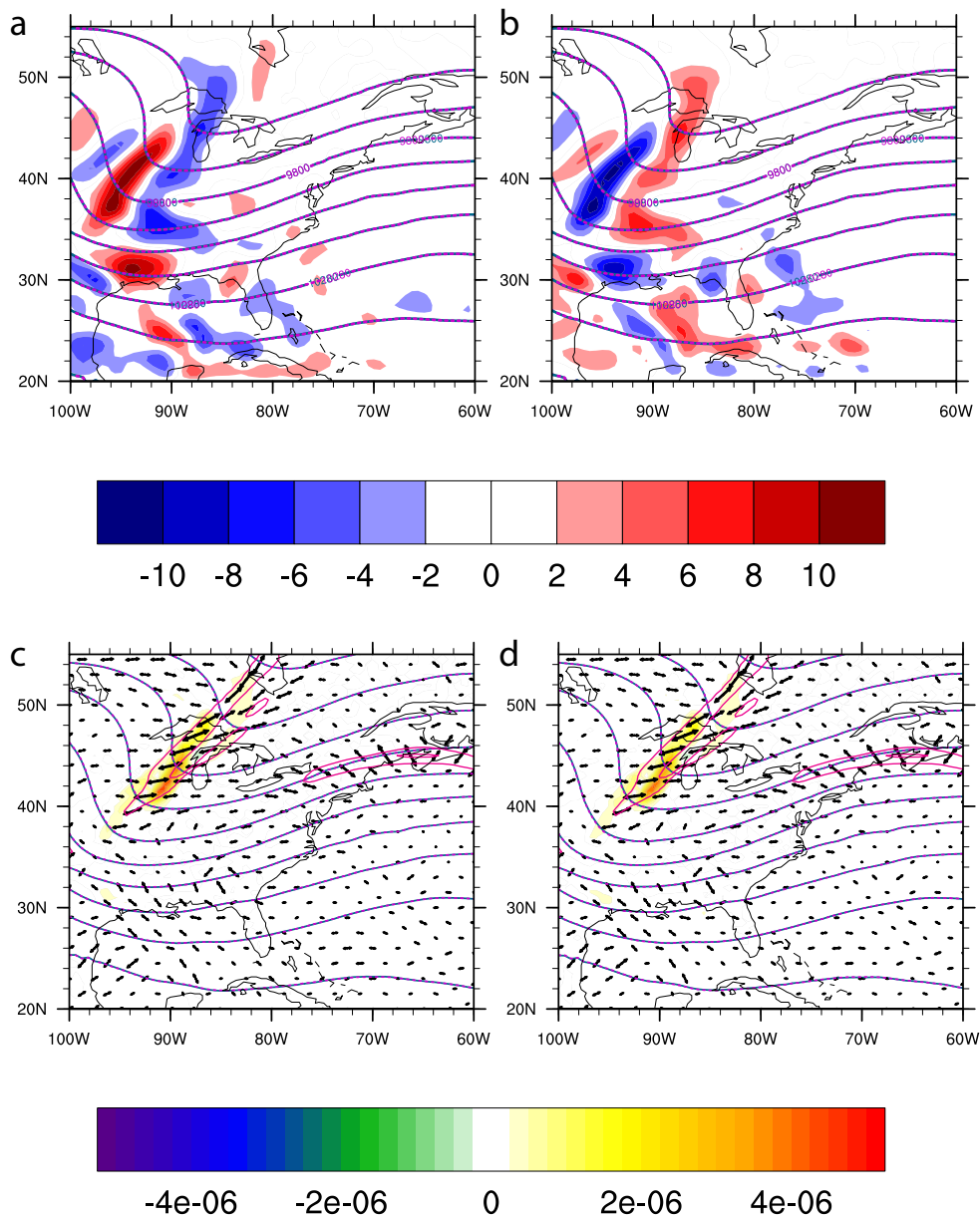


Figure 3.16. Analysis time upper-level layer average (400 hPa to 150 hPa) quasi-geostrophic potential vorticity (QGPV) perturbations (fill; $2.5 \times 10^5 \text{ s}^{-1}$); control simulation height (magenta, dashed contour; m); and perturbed simulation height (dark blue, solid contour; m) for (a) IIR simulation at iteration two; (b) DIR simulation and 400 hPa to 150 hPa average BEC (fill; $\text{m}^2 \text{ s}^3$); axes of contraction (vectors; s^{-1}); control simulation height (magenta, dashed contour; m); perturbed simulation height (dark blue, solid contour; m); and total deformation (light magenta, solid contour; s^{-1}) for (c) IIR simulation at iteration two and (d) the DIR simulation. Heights are contoured every 120m.

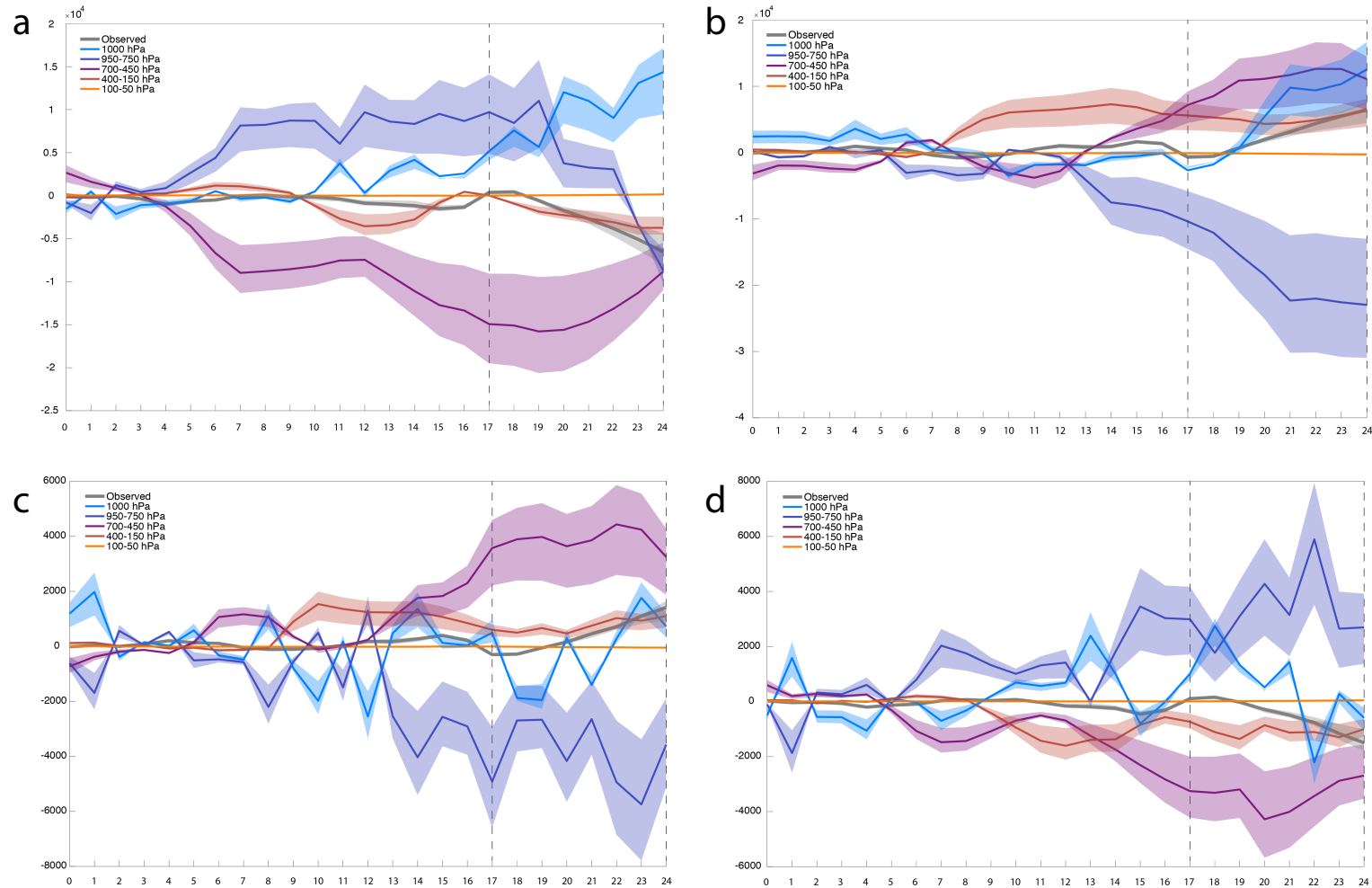


Figure 3.17. Control-simulation-cyclone-following summed 900 hPa inverted height perturbations for the (a) IIR; (b) RIIR; (c) DIR; and (d) RDIR cases. The solid lines colored as labeled represent the sum of the perturbations within a 9° by 9° box. The lines are bound within traces of summed 7° by 7° and 11° by 11° boxes. The observed contour is computed as the 900 hPa perturbation height difference between the perturbed and control simulations. The integration time is found on the x-axis with the gray, dashed lines representing the goal-post times of the response period. The summed perturbation values are found along the y-axis.

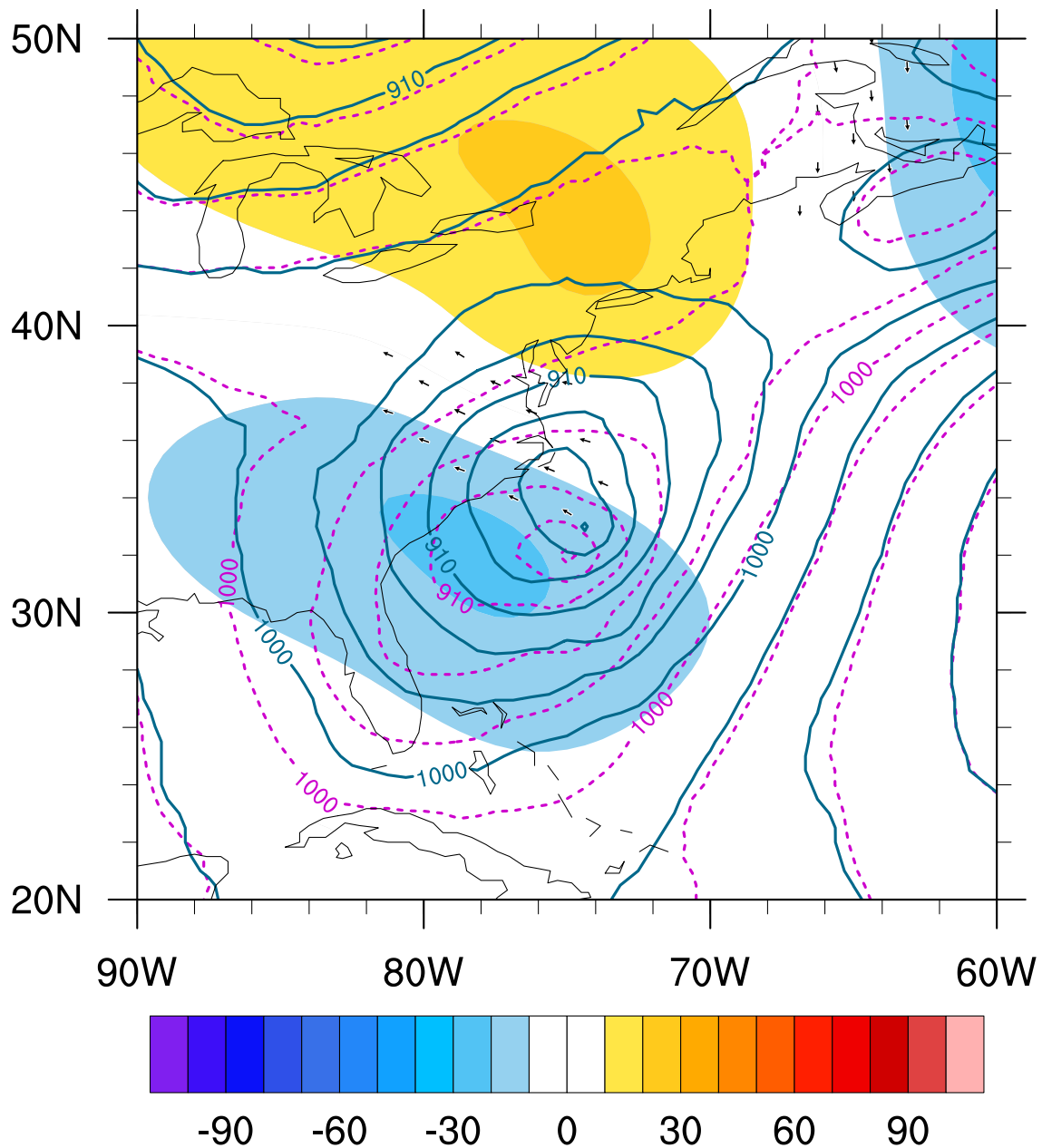


Figure 3.18. 24-hr IIR simulation upper-level (layer averaged from 400 hPa to 150 hPa) QGPV 900 hPa inverted height perturbations (fill; m); inverted wind (vectors; m s^{-1}); control simulation height (magenta, dashed contour; m); and perturbed simulation height (dark blue, solid contour; m). Even at a forecast time that features an intense lower-level circulation, the upper-level QGPV has only a minimal impact on the lower-level (i.e., 900 hPa) height field, yielding height perturbations on the order of 10 - 20 m. Wind less than 5 m s^{-1} is masked.

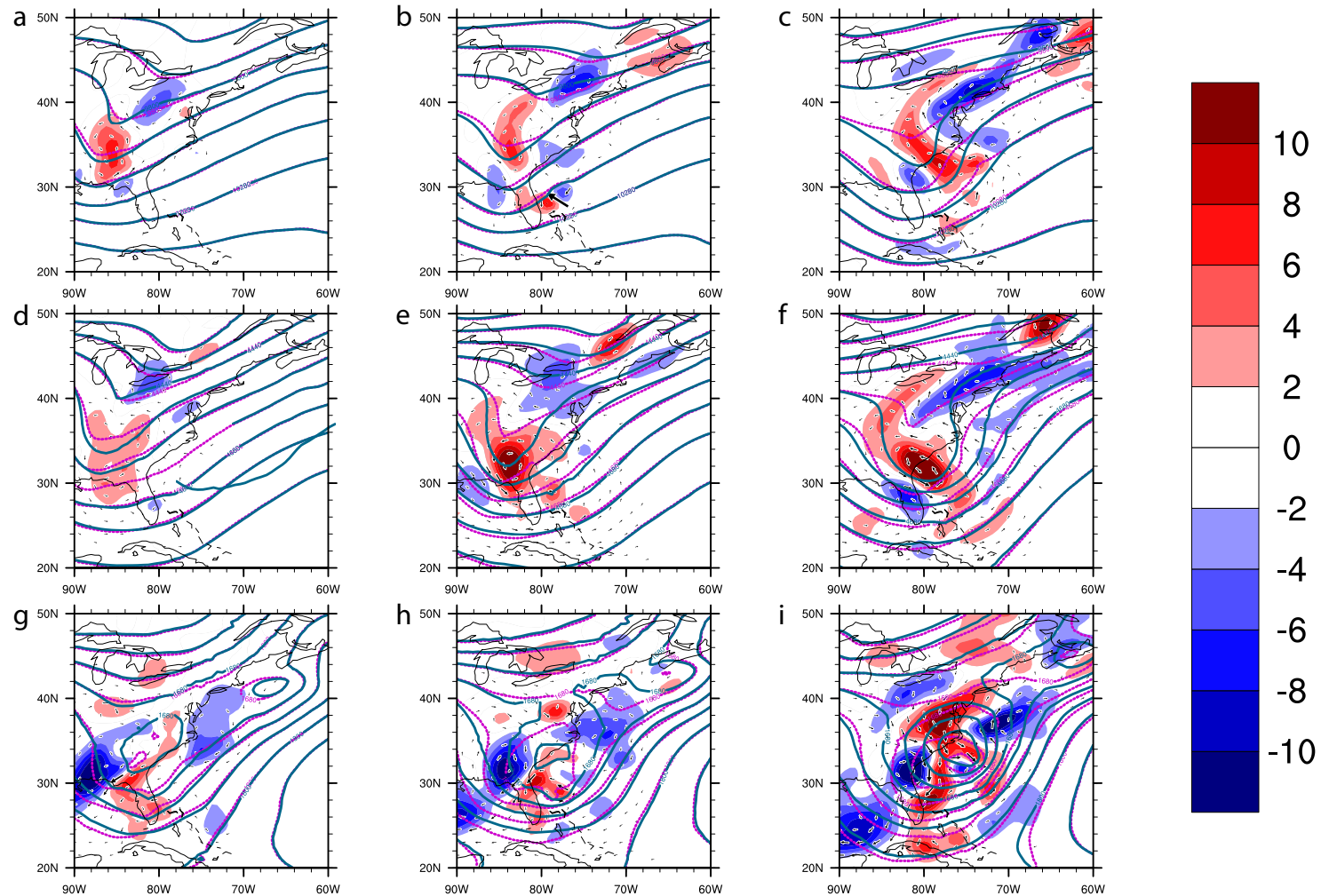


Figure 3.19. IIR simulation, layer average quasi-geostrophic potential vorticity (QGPV) perturbations (fill; 10^5 s^{-1}); inverted perturbation wind (vectors; m s^{-1}); control simulation height (magenta, dashed contour; m); and perturbed simulation height (dark blue, solid contour; m) for (a) upper-level (400 hPa to 150 hPa) at (a) 12-hrs; (b) 17-hrs; (c) 24-hrs; mid-level (700 hPa to 450 hPa) at; (d) 12-hrs; (e) 17-hrs simulations; (f) 24-hrs; and lower-level (950 hPa to 750 hPa) at (g) 12-hrs; (h) 17-hrs; and (i) 24-hrs. All quantities described are layer averaged. Wind less than 5 m s^{-1} is masked.

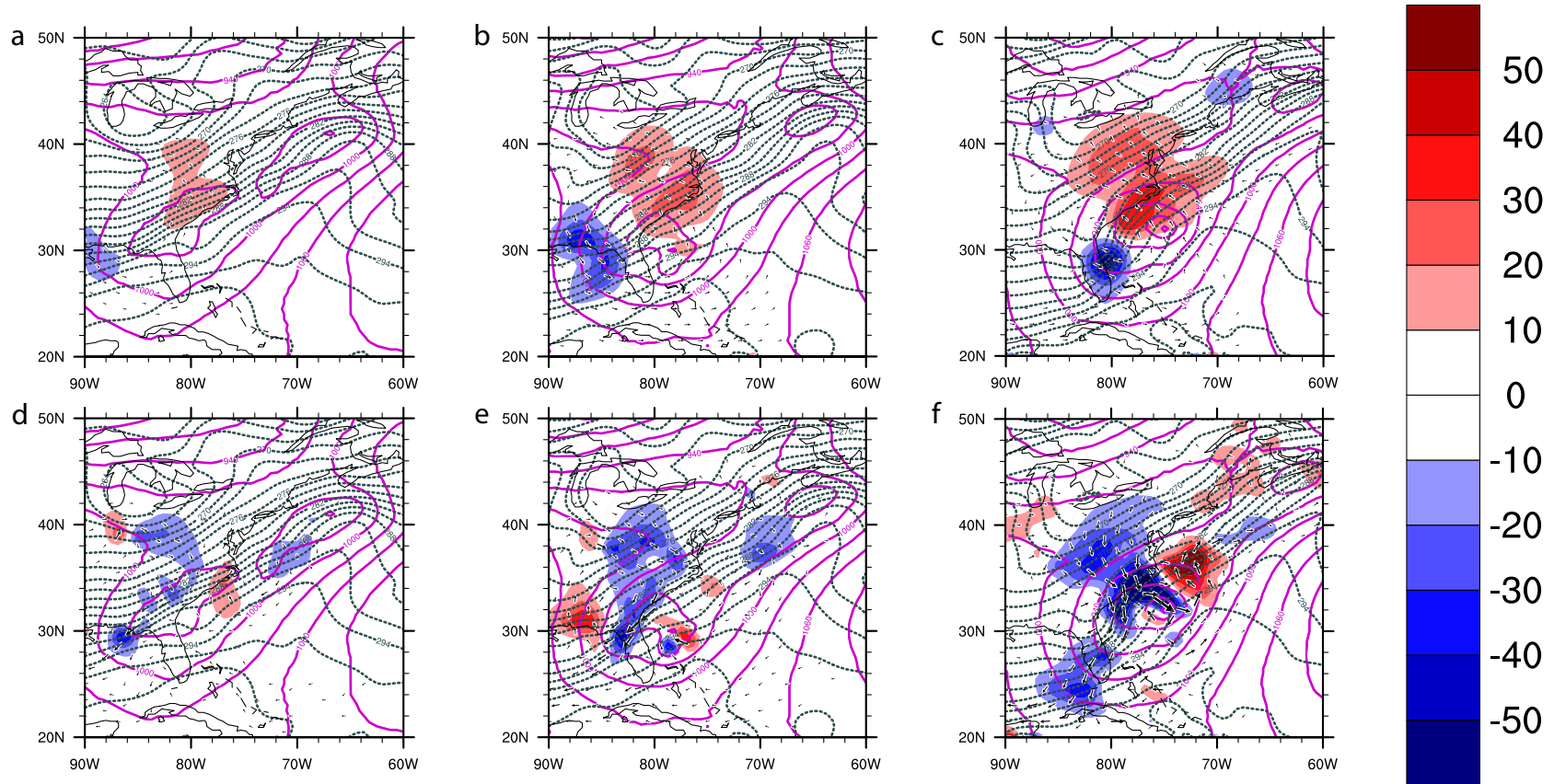


Figure 3.20. 900 hPa control simulation temperature advection by the IIR simulation inverted wind (fill; K day^{-1}); inverted wind (vectors; m s^{-1}); control simulation height (magenta, solid contour; m); and control simulation potential temperature (gray, dashed contours; K) for mid-level (700 hPa to 450 hPa layer) at (a) 12-hrs; (b) 17-hrs; (c) 24-hrs; and lower-level (950 hPa to 750 hPa) at (d) 12-hrs; (e) 17-hrs; and (f) 24-hrs. Wind less than 5 m s^{-1} is masked.

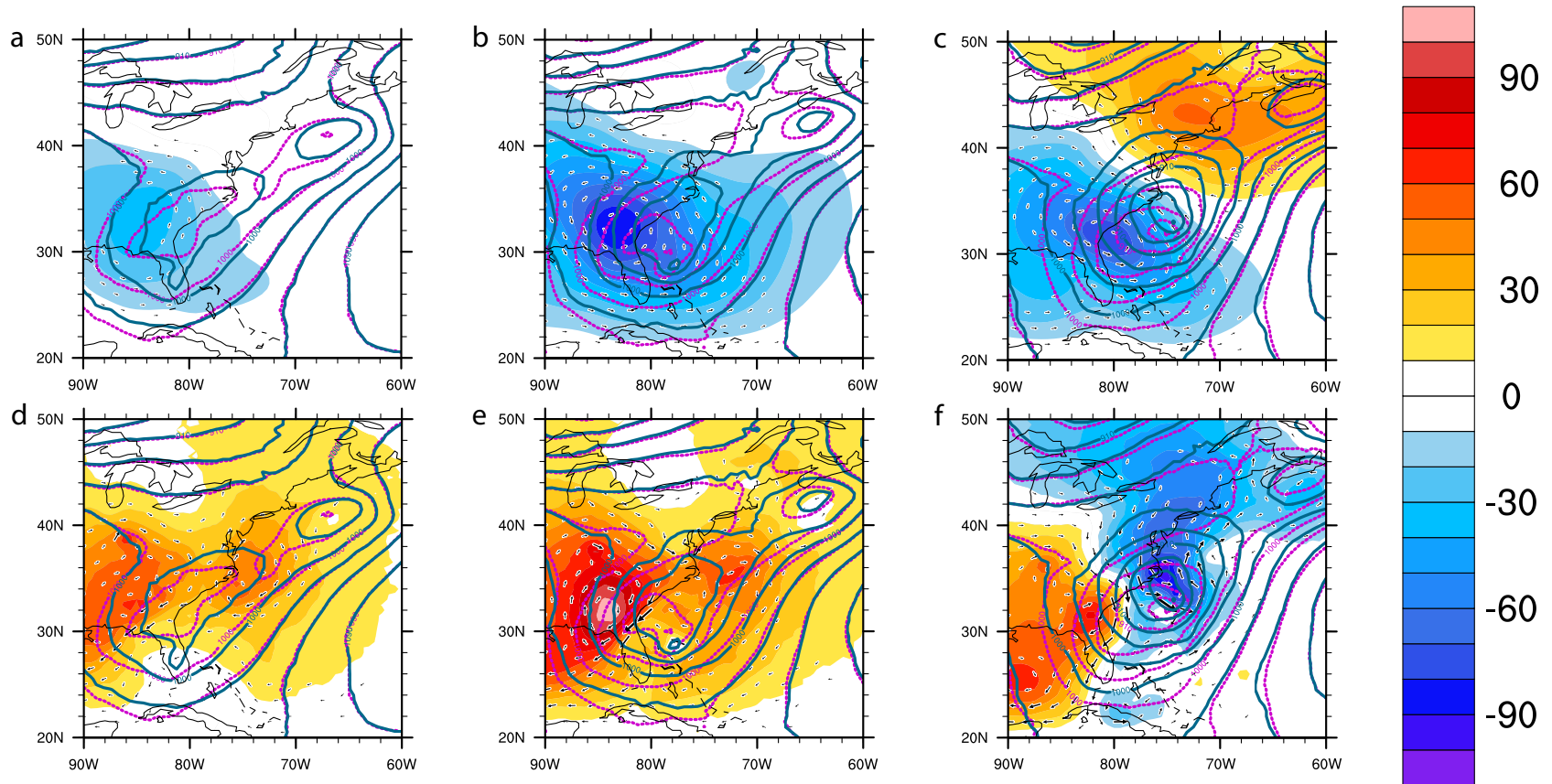


Figure 3.21. IIR simulation 900 hPa inverted height perturbations (fill; m); inverted wind (vectors; m s^{-1}); control simulation height (magenta, dashed contour; m); and perturbed simulation height (dark blue, solid contour; m) for mid-level (700 hPa to 450 hPa) at (a) 12-hrs; (b) 17-hrs; (c) 24-hrs; and lower-level (950 hPa to 750 hPa) at (d) 12-hrs; (e) 17-hrs; and (f) 24-hrs. Wind less than 5 m s^{-1} is masked.

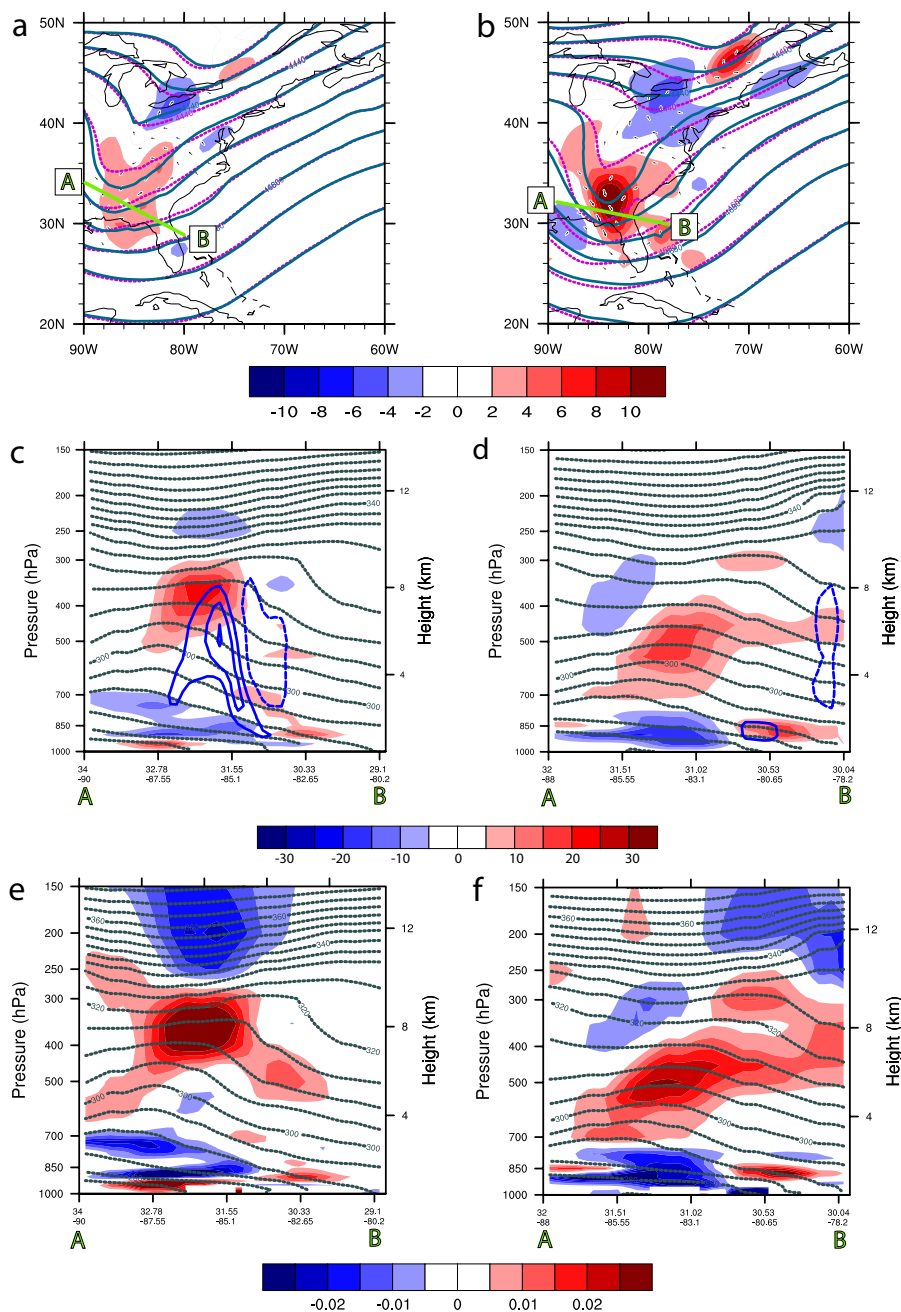


Figure 3.22. Mid-level (700 hPa to 450 hPa) layer average perturbation QGPV as in Fig. 3.20 valid at (a) 12-hrs and (b) 17-hrs; cross-sectional view of QGPV (fill; 10^5 s^{-1}); perturbed simulation potential temperature (gray, dashed contours, K) and perturbed simulation omega (blue solid contour is indicative of positive values and blue dashed contour is indicative of negative values; Pa s^{-1}) valid at (c) 12-hrs and (d) 17-hrs; and cross sectional view of static stability (fill; K Pa^{-1}); and perturbed simulation potential temperature (gray, dashed contours, K) valid at (e) 12-hrs and (f) 17-hrs. Wind less than 5 m s^{-1} is masked.

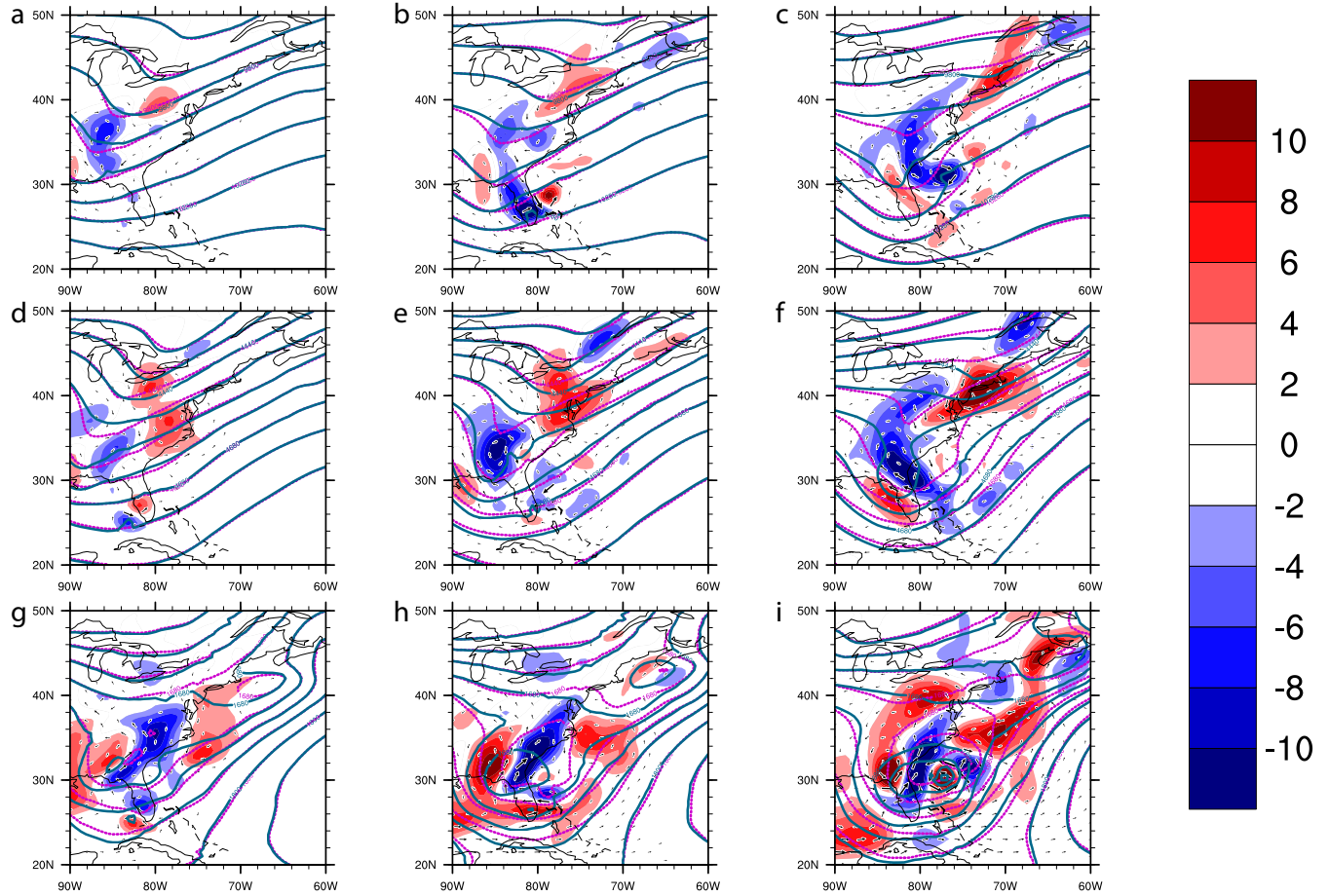


Figure 3.23. RIIR simulation, layer average quasi-geostrophic potential vorticity (QGPV) perturbations (fill; 10^5 s^{-1}); inverted perturbation wind (vectors; m s^{-1}); control simulation height (magenta, dashed contour; m); and perturbed simulation height (dark blue, solid contour; m) for (a) upper-level at (a) upper-level (400 hPa to 150 hPa) at (a) 12-hrs; (b) 17-hrs; (c) 24-hrs; mid-level (700 hPa to 450 hPa) at; (d) 12-hrs; (e) 17-hrs simulations; (f) 24-hrs; and lower-level (950 hPa to 750 hPa) at (g) 12-hrs; (h) 17-hrs; and (i) 24-hrs. All quantities described are layer averaged. Wind less than 5 m s^{-1} is masked.

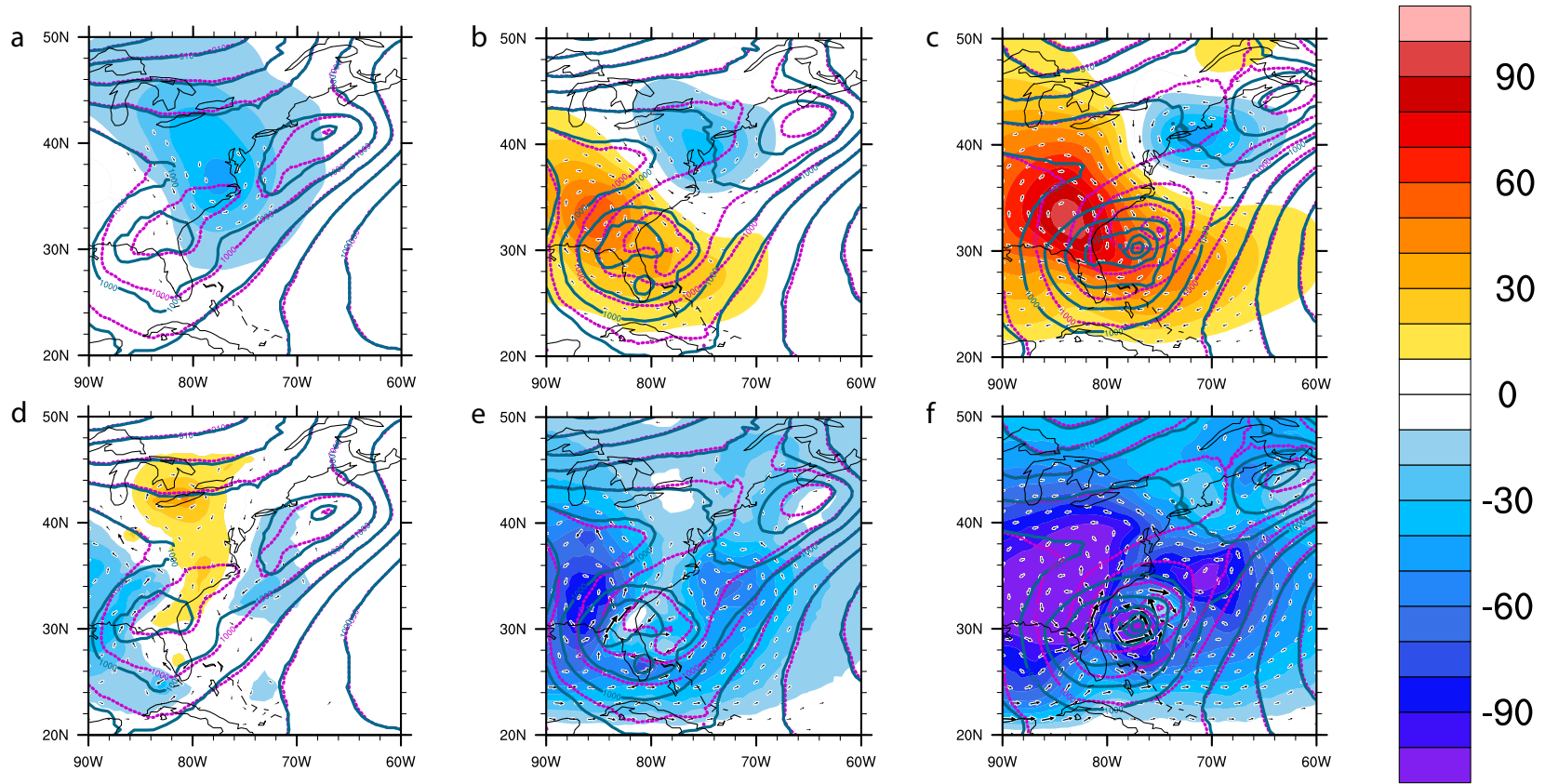


Figure 3.24. RIIR simulation 900 hPa inverted height perturbations (fill; m); inverted wind (vectors; m s^{-1}); control simulation height (magenta, dashed contour; m); and perturbed simulation height (dark blue, solid contour; m) for mid-level (700 hPa to 450 hPa) at (a) 12-hrs; (b) 17-hrs; (c) 24-hrs; and lower-level (950 hPa to 750 hPa) at (d) 12-hrs; (e) 17-hrs; and (f) 24-hrs. Wind less than 5 m s^{-1} is masked

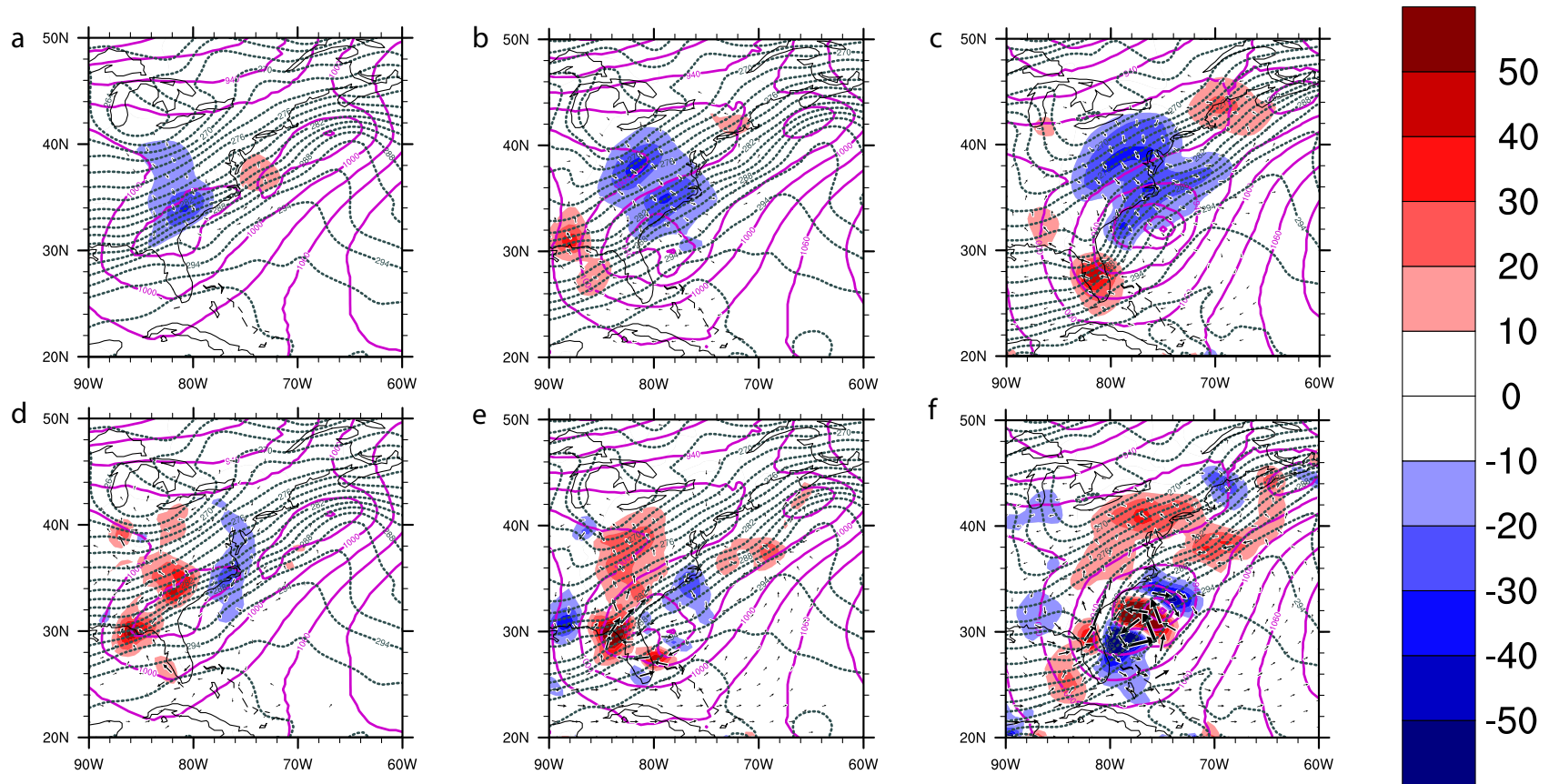


Figure 3.25. 900 hPa control simulation temperature advection by the RIIR simulation inverted wind (fill; K day^{-1}); inverted wind (vectors; m s^{-1}); control simulation height (magenta, solid contour; m); and control simulation potential temperature (gray, dashed contours; K) for mid-level (700 hPa to 450 hPa) at (a) 12-hrs; (b) 17-hrs; (c) 24-hrs; and lower-level (950 hPa to 750 hPa) at (d) 12-hrs; (e) 17-hrs; and (f) 24-hrs. Wind less than 5 m s^{-1} is masked.

Name of level	Layer Average Isobaric Levels
Surface	1000 hPa
Lower-levels	950 hPa to 750 hPa
Mid-levels	700 hPa to 450 hPa
Upper-levels	400 hPa to 150 hPa
Lower-stratosphere	100 hPa to 50 hPa

Table 3.1. Isobaric layers over which experimental quantities are averaged.

Chapter 4: A Comparison of *Quasi-Optimal Iterative Perturbation* Structure and Evolution for two Northeast Snowstorms with different Predictability

4.1 Abstract

Two case studies of East Coast snowstorms are investigated using the QOIP method to modulate the intensification rates of mid-latitude cyclones. The cases are selected to represent events with less expressed forecast uncertainty than the January 2000 “surprise snow storm” investigated in Chapter 3: (1) the March 1993 “storm of the century” and (2) a significant northeast snowstorm event on 25-28 January 2015. As the 1993 case is regarded as one characterized by high levels of predictability, it serves as a case that contrasts well with the poorly predicted January 2000 “surprise snow storm”, allowing these two cases to serve as “bookends” on a spectrum of predictability in which the 2015 case falls somewhere in the middle.

The structure and evolution of the QOIP in both cases is discussed, with allusions made to the predictability of each case therein. Two methods for the analysis of the QOIP are undertaken; (1) an examination of the QOIP energy components as calculated in Ehrendorfer (1999); and (2) a QGPV inversion, in which the QOIP QGPV is inverted to recover the balanced mass and momentum fields explicitly associated with the perturbation quantities.

It is shown that cases in which the predictability is low (high) are typically dominated by processes associated with perturbations to the thermodynamics (dry

dynamics) fields, with vertical energy profiles reflecting a domination by the perturbation available potential (kinetic) energy component. Furthermore, it is shown that contribution by the QOIP QGPV to the balanced mass and momentum fields varies significantly between those cases in which the response function is aimed at increasing the intensification rate vs. those in which it is aimed at decreasing the intensification rate.

4.2 Background

As shown in Chapter 3, the use of the *quasi-optimal iterative perturbation* (QOIP; outlined in Section 2.1.4) method is effective in modulating the intensification rate of a mid-latitude cyclone over a *response period* in the forecast by perturbing the initial simulation state variables to which the intensification rate in the forecast is sensitive, and composing perturbations through multiple iterations. The 24-26 January 2000 “surprise snow storm” (SSS; Zhang 2002; 2003; Brennan and Lackmann 2005; Kleist and Morgan 2005a) was an appropriate choice for deep examination given the low forecast skill shown by numerical weather prediction (NWP) models, and in Chapter 3 the QOIP method was applied to explore the relationship between initial model perturbations and the possible range of intensification rates of the cyclone. However, it is important to more comprehensively explore these relationships by using the QOIP method to modulate the intensification rate of mid-latitude cyclones across a range of expressed predictability in the NWP forecast.

For this reason, two additional case studies were performed and the results are compared to for the “surprise snow storm”. The two additional cases chosen for comparison are the 11-14 March 1993 “Storm of the Century” (also known as the March

1993 “Superstorm”, hereafter SOTC), a case in which NWP models showed high levels of forecast skill, and the 25-28 January 2015 northeast snow event (hereafter j15), a case that presented a forecast challenge.

It was shown in Chapter 3 that the pathway identified by the QOIP in order to increase the intensification rate of the cyclone over the response period was to create a synoptic pattern that was increasingly favorable for baroclinic growth. This was done by reconfiguring the upper-level precursor disturbance so that (1) the barotropic energy conversion rate was increased for the first 15 hours of the model integration; and (2) the precursor trough was a deeper, more barotropically negatively tilted trough as compared to the control simulation. Furthermore, this pathway left thermodynamic processes largely unchanged, further indicating the importance of the upper-level precursor in the intensification of the cyclone. In seeking a pathway that focused primarily on the dry dynamics of the system, the QOIP algorithm was able to achieve nine iterations, allowing for perturbation magnitudes to be large, resulting in a large response function change.

Conversely, the QOIP was *unsuccessful* in making significant change to the response function in the decreased intensification rate direction. The QOIP algorithm failed relatively quickly (only completing two iterations after the control simulation), resulting in small changes to the response function. This failure was due primarily to the QOIP seeking a pathway in which changes to the dry dynamics of the system were secondary to changes to the thermodynamic fields, resulting in highly non-linear behavior.

As these two results were in such stark contrast, they provide a good basis for comparison to other cases such as SOTC and j15. As both highly linear and non-linear

pathways were attempted by the QOIP, insight can be gained into (1) the methods by which intensification rates can most efficiently be modulated within the QOIP framework; and (2) the dynamical (thermodynamical) factors that are of the highest relative importance in modulating the intensification rates of cyclones across varying levels of predictability.

4.3 Synoptic Overviews

4.3.1 11-14 March 1993 “Storm of the Century”

The 11-14 March 1993 “Storm of the Century” was a particularly intense, mid-latitude cyclone of high-impact (NESIS¹⁴ scale of 12.52 – category 5; Kocin and Uccellini 2004) to significant population centers along the Eastern United States seaboard. Although the storm occurred during a time in which NWP models were far less reliable than today, multiple NWP systems performed quite well in their mid-range (e.g., 24-hr to 72-hr) forecasts of the system (Huo et al. 1995; Dickinson et al. 1997), especially with respect to the upper-level disturbance that initiated surface development. It is noted however that models struggled somewhat with the representation of diabatic effects on the development of the cyclone (Dickinson et al. 1997), an impact that will be discussed further in Section 4.3.2.

The SOTC developed a substantial surface circulation on 1200 UTC 12 March 1993 (Fig. 4.1a) when an incipient surface low moving east out of northern Mexico moved over the anomalously warm Gulf of Mexico (GOM), which was characterized by

¹⁴ The Northeast Snow Impact Scale (NESIS) is a retrospective analysis scale developed by Paul Kocin and Louis Uccellini that serves to rate northeast snow storms on a scale of one (“notable”) to five (“extreme”). The Storm of the Century is one of two blizzards that was rated as a category five, with the other occurring 6-8 January 1996. Ratings are assessed based upon a formula that takes into account areal storm coverage, snowfall amount and population impacted.

sea surface temperatures (SSTs) more than 3°C above average. As this occurred, strong cold advection north of the developing cyclone developed a strong baroclinic zone over the northwestern GOM. As the storm progressed eastward, it was further aided in its development upon interacting with a second baroclinic zone present just south of the Mississippi delta region. Both of these baroclinic gradients were enhanced by a region of broad warm advection within a southerly flow regime downstream of the cyclone intersecting the strong cold surge to the north.

In the middle- and upper-levels, two disturbances were noted west of the surface cyclone (Fig. 4.2a and 4.2b) resulting in a region of strong mid-level positive vorticity advection (PVA) downstream of the advancing troughs (Fig. 4.2a), coinciding with the location of the developing surface circulation. It is noted in Huo et al. (1995), the southeastern trough (labeled 1) was responsible for the initial development of the cyclone, while the northwestern trough (labeled 2) would deepen in response to the increased baroclinicity at the surface and become responsible for the period of explosive deepening later in the storm's lifecycle.

By 0000 UTC 13 March 1993, the influence of strong surface fluxes by the anomalously warm GOM aided in a period of rapid development, with the storm being characterized by a MSLP of 992 hPa over the northern GOM (Fig. 4.1b). A now well-defined cold-front had moved into the central GOM with a warm-frontal boundary lifting north as a result of the broad southerly flow characterizing the warm-sector. Vigorous upright convection was noted along and just ahead of the cold-front with large-scale stratiform precipitation having developed over the southeastern United States in association with the lifting warm-front. Ahead of the pre-cold-frontal squall line that had

developed, a region of strong southerly flow aided in the transport of warm, moist air toward the cyclone center, (e.g., a warm conveyor belt; Carlson 1980). This prefrontal warm conveyor-belt helped to convectively destabilize the downstream environment in a manner conducive to explosive development through the release of latent heat via both convection along the squall line as well as within the stratiform precipitation region. This warm conveyor belt also aided in increased baroclinicity along the front in association with strong cold-advection resulting from increasingly intense cyclonic flow wrapping around the back side of the developing cyclonic circulation.

In the mid-levels and upper-levels (Fig. 4.2b and 4.3b), both short-wave troughs intensified in response to the increased baroclinicity, resulting in a “dual-jet” structure (Bell and Bosart 1993) in which QG ascent increased, aiding in surface cyclogenesis. The surface cyclone also became situated in the right-entrance region of an intensifying upper-level jet streak, further aiding in its intensification. Due to the favorable synoptic positioning of the surface cyclone as well as significant diabatic forcing, the cyclone underwent a period of rapid intensification over the next 24-hr as it began to move northward along the east coast of the United States. During this period, the storm intensified approximately 30 hPa, resulting in an approximately 1.25 Bergeron bomb phase (Sanders and Gyakum 1980). During this period, the pre-frontal squall line produced 25 tornadoes over Florida, while deep, moist convection was noted well into the cyclone center.

By 1200 UTC 13 March 1993, the discrete mid-level vorticity maxima had merged into a single band and took on a negatively tilted orientation favorable for baroclinic growth (Fig. 4.2c). At the same time, the upper-level jet streak (Fig. 4.3c) that

had been situated to the northwest 12-hr earlier dug southward into the base of the trough while the jet streak that had been to the west moved northeastward, resulting in the surface cyclone now becoming situated in the left-exit and right-entrance regions (respectively) of the two jet streaks. This positioning aided in extreme baroclinic growth of the cyclone in concert with the deepening due to diabatic processes.

By 0000 UTC 14 March 1993, the storm peaked in intensity with a minimum MSLP of 966 hPa (Fig. 4.1d) before occluding and gradually beginning to fill as it continued to move to the north-northeast. Although the mid- and upper-level synoptic configurations remained highly favorable for continued baroclinic development at this time (Fig. 4.2d and 4.3b), the cyclone had moved into a more convectively stable air mass, resulting in a weakening of the pre-frontal squall line and an associated weakening in diabatic heating.

Although the cyclone had already developed a closed surface circulation by 0000 UTC 12 March 1993, it should be noted that the simulations performed in subsequent sections are initialized some 12-hr later at 1200 UTC 12 March 1993. This choice of initialization was made in order to capture the period of most rapid intensification as close to the initialization as possible, so as to maximize the efficacy of the tangent linear assumption made by use of the adjoint model. If an analysis were created 12-hr earlier in an attempt to capture the full lifecycle of the cyclone, adjoint simulations of 30-hr and 39-hr would be necessary¹⁵. Adjoint simulations of these lengths are likely to result in decreased linearity, especially with respect to a case that is heavily modulated by non-

¹⁵ Forward model integrations were performed using both the 0000 UTC and 1200 UTC 12 March 1993 analyses and resulted in nearly identical trajectories. However, as linearity with respect to the adjoint simulations back to the 1200 UTC 12 March 1993 analysis was higher than that of the simulations back to the 0000 UTC 12 March 1993 analysis, the 1200 UTC 12 March 1993 analysis was chosen for these experiments.

linear, diabatic processes (As discussed in section 2.1.1; Errico et al. 1993; Errico and Raeder 1999; Mahfouf 1999). As a result, it was necessary to use the 1200 UTC 12 March 1993 analysis time for initialization. Due to this choice, there is a period of time over which the model depicts a significantly weaker cyclone than what was observed, owing to the need for the model to “spin-up” the cyclone. The model does however ultimately simulate a cyclone that achieves a minimum MSLP that compares favorably with observations, and therefore the choice of initialization time is acceptable.

4.3.2 25-28 January 2015 Northeast Snow Event

The 25-28 January 2015 northeast snow event (j15) was a significant winter storm that caused blizzard conditions over highly populated areas in the northeastern United States. The event was characterized by a relatively low level of predictability with respect to snowfall amounts, with National Weather Service (NWS) offices as well as many private sector and broadcast meteorologists predicting snowfall amounts on the order of two feet for a region stretching from New York City to Boston in the hours preceding the event. Following the event, snowfall totals in New England generally met and exceeded forecasted values, while totals within the New York City region proved to be vastly over-forecast. Greybush et al. (2017) showed that the predictability of the snowfall for the j15 event was largely governed by errors in the position of the surface low and the associated sharp precipitation gradient to the west of the cyclone. These errors were traced back to errors in the position of the precursor 500 hPa shortwave. Forecast and verifying snowfall maps by the NWS can be found in Fig. 4.4a-c, and illustrate the significant disparity

between the forecast and verifying states as a result of the mis-forecast of the sharp precipitation gradient.

The initial disturbance that would later initiate the j15 blizzard can be traced back to strong, northern stream mid- and upper-tropospheric shortwave troughs (e.g. an “Alberta Clipper”, Hutchinson 1995) at 1200 UTC 25 January 2015 over the Upper-Midwestern United States (Fig. 4.5a and 4.6a). The shortwave trough was embedded within a large-scale wave pattern characterized by ridging (troughing) over the western (eastern) United States. At the surface, a progressive low-pressure center was found underneath the enhanced divergence associated the upper-level shortwave (Fig. 4.7a), tracking eastward along a remnant cold-/stationary-front extending from the mid-Atlantic into the central plains states. Already a well-developed cyclone, a dual-front structure extended to the south, with the lead warm-front becoming occluded by the trailing cold-front. In advance of the occluding warm front, a weak surface trough was located over Texas into Arkansas.

By 0000 UTC 26 January 2015, the surface low over the central US continued to propagate eastward along the remnant baroclinic zone (Fig. 4.7b). The surface cyclone was further aided by strong mid-level PVA (Fig. 4.5b) and enhanced divergence in association with the left-exit region of the upper-level jet streak (Fig. 4.6b), which had now broadened and strengthened to 80 m s^{-1} over the Gulf Coast. The dual-frontal structure found 12-hr earlier had by this point become a single, stationary front immediately to the south of the surface cyclone, extending further south as a cold-front (Fig. 4.7b). The surface trough previously found over Texas and Arkansas continued to propagate eastward, now found over the Gulf-Coast region. Downstream of the main

shortwave, a region of weak upper-level divergence was located just off the Carolina coast in the right-entrance region of strengthening jet-streak.

By 1200 UTC 26 January 2015, a complex surface low-pressure configuration was analyzed from surface observations (Fig. 4.7c). Off the Carolina coast, a new, well-defined surface low had quickly developed along the southward sagging remnant baroclinic zone in response to the mid- and upper-tropospheric forcing (Fig. 4.5c and Fig 4.6c) associated with the eastward moving shortwave. Associated with this new low center, the former remnant baroclinic zone now extended to the east in the form of a warm-front, with the lead surface trough that had been evident over the southern US in the previous 24-hr becoming wrapped into the circulation as a developing cold-front. To the west, the surface low began to occlude as it propagated eastward, with a long cold-frontal region extending south and west into the GOM. To the north, a weaker surface low was analyzed along a baggy surface trough, with a trailing cold front to its southwest beginning to occlude a stationary front that extended to its south and intersected the main surface low.

At 500 hPa, a weak, negatively tilted northern-stream disturbance was now noted over the Midwest, with its trough axis intersecting the main southern-stream shortwave which was beginning to rotate into a more negative configuration as well (Fig. 4.5c). At 250 hPa, the downstream jet-streak noted 12-hr earlier had shifted to east of the Canadian Maritimes, with the 80 ms^{-1} western shortwave extending from the northern GOM eastward across central and northern Florida into the western Atlantic (Fig. 4.6c). Strong divergence was now located in the left-exit region of this jet-streak, aiding in a period of rapid intensification of the surface low.

At 0000 UTC 27 January 2015, the mid- and upper-level disturbances began to take on a strongly negative tilt (Fig. 4.5d and Fig. 4.6d), resulting in a configuration highly favorable for baroclinic growth of the surface cyclone. As a result of this, the main surface circulation was now associated with the northward moving coastal low that had developed in response to the southern-stream disturbance east of the Carolinas. Greybush et al. (2017) notes that the Global Ensemble Prediction System (GEFS) initialized at 1200 UTC 26 January 2015 displayed a relatively large spread in the predicted track of the center of circulation of the cyclone as well as a correspondingly large spread in the track of the 25.4-mm precipitation contour, even with a 24-hr lead-time. The spread in these two metrics was highly indicative of an overall lack of predictability even at short forecast lead times. Over the previous 12 h, the surface low had consolidated and intensified by 12 hPa to a minimum central pressure of 992 hPa off the coast of New Jersey (Fig. 4.7d).

During the period between 0000 UTC 27 January 2015 and 1200 UTC 27 January 2015, the mid-level trough developed into a strong, closed low at 500 hPa, aiding in the continued rapid deepening of the surface cyclone. At the same time, the upper-level jet took on a “dual-jet” structure (Fig. 4.6e), aiding further in the development of the surface low via enhanced QG ascent. Diabatic heating from precipitation also aided in the now explosive development of the cyclone, with strong latent heat release helping to intensify the cyclone 17 hPa in 12-hr to a minimum central pressure analyzed at 975 hPa (Fig. 4.7e). Over this same time, the surface low moved just east of Cape Cod, resulting in the heaviest (in many cases record-breaking) snowfall being recorded over a corridor stretching from Long Island to Maine. Multiple bands of intense snowfall formed within

a region of intense deformation, with hourly snowfall rates between 3-4 inches noted within that same corridor. A radar image (courtesy NWS OKX) can be seen in Fig. 4.8, which displays intense, banded regions of snowfall. Between 1800 UTC 27 January 2015 and 1200 UTC 28 January 2015, the upper-level low began to fill (Fig. 4.5f and Fig. 4.6f), leading to a gradual weakening of the surface low and eventual decay of the surface cyclone (Fig. 4.7f).

4.4 QOIP Analysis

4.4.1 Comments on Linearity and “Forecast Elasticity”

The QOIP method relies fundamentally upon the tangent-linear approximation for each individual iteration, requiring that the observed change in the response function due to the incremental initial condition perturbation be accurately estimated by the adjoint model within a pre-specified threshold (see Section 2.1.4). One can quantify both the overall linearity that a particular case displays as well as (assuming that the perturbations that are computed adequately and span the appropriate portion of the phase space of solutions) make assertions about that case’s intrinsic predictability by assessing the change in the response function upon each iteration. Those cases in which analysis-time QOIP have a large (small) impact upon the response function can be regarded as those cases that may suffer from intrinsically low (high) levels of predictability with respect to that response function, as small changes to the analysis (such as observation error) may quickly push the forecast integration away from a control state. Upon the final iteration as determined by the QOIP algorithm (i.e., the point at which the algorithm fails in returning a response within acceptable thresholds, or the maximum allowable number of iterations

has been reached), one can define the total overall change in the response function as what will be termed as the “forecast elasticity” (FE) for that case. “Forecast elasticity” is defined as the total change in the response function that can be achieved by the QOIP methodology (within the specified thresholds of linearity and maximum allowable iterations). Cases that exhibit large (small) FE are those that display large (small) changes to the response function. In this way, FE can be defined as the “spread” within an ensemble of deterministic model solutions with respect to a single, predefined response function.

FE depends on the linear behavior exhibited by perturbations imposed upon the analysis for a particular case. Typically, a case that has large (small) FE is one in which the QOIP at each individual iteration behave highly linearly (non-linearly). As the QOIP algorithm defines within its inner-loop a threshold level of linearity that must be satisfied in order to proceed to the next iteration, those cases in which the perturbations behave linearly (non-linearly) at each step will succeed (fail) in moving to the next iteration. Successive, linear (non-linear) iterations will allow (fail to allow) for the magnitude of the perturbations to increase upon each step, therefore necessitating a large (small) change to the response function. A larger (smaller) change to the response function will result in a larger (smaller) total FE. In this regard, the FE also may suggest some of the processes that are responsible for the changes to the response function, as large (small) FE is likely a result of perturbations to the kinematic (thermodynamic, microphysical) fields, which will behave in a more (less) linear fashion. This is due in part to the linear approximation used in creating the QOIP that define the FE. While the QOIP method is designed such that it allows for non-linear information contained within the control

trajectory to be considered within a by-definition linear framework, each individual iteration within the QOIP algorithm still must attain a threshold of linearity. As this is the case, QOIP iterations in which perturbations that have a larger impact on the “dry dynamics” fields (i.e., perturbations to the wind resulting in perturbations to kinetic energy) dominate will likely attain a higher level of linearity than iterations in which perturbations to the thermodynamics fields dominate. Within the iterations in which thermodynamics fields (e.g., fields characterized by perturbations to the available potential energy) dominate, it is more likely that highly non-linear physical processes (e.g., precipitation processes) will be resolved by additionally highly non-linear parameterization schemes. In tandem, these factors lead to QOIP iterations that fall short of the linearity threshold and terminate the QOIP algorithm.

Paradoxically however, large FE may also imply a high degree of non-linear behavior when comparing the final, composed QOIP that are intended to make changes to the response function in opposite directions (e.g., the response functions are identical but of opposite sign). For a case that behaves with complete linearity, identically structured but opposite signed perturbations that are imposed upon identical sensitivity structures will yield responses that are identical in magnitude but opposite in sign. While a case may display high FE in a particular direction (i.e., a positively signed intended response), implying a high degree of linearity upon each iteration, if the case displays less FE in the opposite direction, it can be asserted that the linear response to perturbations to the analysis for that case are skewed in a particular direction, and the case itself can be regarded as non-linear. An example of this can be found in Fig. 4.9, in which the response to the QOIP by the Surprise Snow Storm (SSS) are skewed towards the

increased intensification response function, as indicated by the greater number of QOIP iterations achieved in the increased intensification rate simulations versus the decreased intensification rate simulations. Furthermore, it is evident in Fig. 4.9 that simply reversing the sign of the positive (negative) QOIP (as opposed to generating independent positive and negative QOIP per the QOIP algorithm) does not result in perfectly opposite responses. This lends further credence to the skewing of the response towards the increased intensification, and the case's overall, intrinsic non-linearity. The QOIP method is capable of exploring these non-linearities between positive and negative responses to initial perturbations because of the way in which the nonlinear trajectory is updated with each incremental change to the initial conditions.

While perhaps most useful as a tool to discern the linearity of a particular case both at each iteration and overall, FE also may imply limits to a particular case's (practical) forecast predictability. A case in which there is a high (low) level of FE is likely to be highly unpredictable (predictable), as the response function can (cannot) be modified easily from the control forecast by the inclusion of small perturbations to the analysis. This case exhibits a high level of FE in the direction of larger rates of intensification (Fig. 4.10a), in which the QOIP are able to push the forecast away from the control trajectory towards an increased intensification rate over the response period. Conversely, as discussed in section 4.3.1, SOTC is a case in which there was a high level of predictability. Figure 4.10b shows that the QOIP have little to no impact on the response function, with the positive and negatively signed QOIP remaining nearly identical to the control trajectory throughout the entire forecast integration. Fig. 4.10c shows that j15 falls in between the SSS and SOTC cases with respect to FE, with overall

change to the response function larger than the SOTC case, but smaller than the SSS case. This is consistent with a case in which modulation of the response function is characterized by processes dominated by neither kinematic nor thermodynamic/microphysical processes, but rather a fairly even distribution of the two. This will be further discussed in section 4.3.4.

FE also speaks to the preferred “direction” of the change to the response function. Recalling Fig. 4.9, it can be seen that the decreased intensification rate experiments (DIR and RIIR) lie close to the control trajectory, whereas the increased intensification rate experiments (IIR and RDIR) are substantially different than the control. This shows that 1) the control simulation cannot be made significantly less intense than it already is by the inclusion of QOIP at the analysis; and 2) shows that small errors in the initial conditions could result in a cyclone that was much weaker than was actually realized, as small changes to the analysis could have resulted in a significantly more intense storm. Conversely, Fig. 4.10b shows that the SOTC displayed no significant preference in either the increased or decreased intensification rate direction. The j15 (Fig. 4.10c) case is characterized by a little preference in either the increased or decreased intensification rate direction, with the control typically falling almost exactly in between the four simulations. To this end, for a given response function a forecaster may use FE to better understand an array of possible outcomes based on the potential for initial analysis errors to project onto the QOIP. In this way, FE can be regarded as similar to an ensemble of NWP solutions for a particular response function, and may represent an “envelope of predictability” that likely contains the final verifying state.

4.4.2 Vertical Perturbation Energy Profiles

When attempting to diagnose the synoptic and mesoscale evolution of QOIP the FE may complicate analysis. In cases that lack significant forecast elasticity (i.e., SOTC), drawing specific conclusions based upon the evaluation of discrete perturbation structures is difficult given the evolved perturbations' relatively small magnitudes. Therefore, in order to draw broader conclusions about the evolution of the perturbations, one can make use of integrated vertical profiles of the perturbation energy components – kinetic, available potential, elastic, and latent heat energy. In employing this method, it is possible to understand not only the investments that the QOIP makes to the initial state in attempting to create a change to the response function, but also to draw conclusions about the linear (non-linear) behavior shown by that case.

Vertical perturbation profiles are calculated by computing the perturbation energy attributable to kinetic, available potential, elastic, and latent heat energy components (as calculated using the moist energy norm found in Section 2.1.3; Ehrendorfer et al. 1999). The perturbation energy is calculated and averaged over the full, global domain and is normalized by the average of the total energy (i.e., the sum of the components; Figs. 4.12a-j – 4.17a-j) at each hybrid-sigma model level, a list of which can be found in Table 4.1. The energy components are calculated for the three cases at the analysis time, the 6-hr forecast, 12-hr forecast, and the forecast at the beginning and ending goalpost times for their respective response periods.

The intensifying QOIP for the SSS case displays characteristics at the analysis time (Fig. 4.11a, b) that are markedly different from the other two cases, with initial energy dominated largely by available potential and kinetic energy below the tropopause

(Fig. 4.12a, seen at approximately hybrid-sigma coordinate level 44; approximately 250 hPa), with available potential energy composing the vast majority of the attributable perturbation energy. Above the tropopause, the available potential and kinetic energy components immediately reverse, with the kinetic energy comprising the largest percentage of the total energy, though in the non-normalized profiles it can be seen that the total energy of the perturbations sharply reduces to near zero at these levels (Fig. 4.12b). Conversely, in the SOTC (Fig. 4.13a-j and Fig. 4.16a-j) and j15 (Fig. 4.14a-j and Fig. 4.15a-j) cases the perturbation energy in the lowest model levels is dominated by kinetic energy before switching to being dominated by available potential energy throughout much of the lower and middle troposphere. Non-negligible amounts of latent heat energy are also found in the lowest levels for the SOTC and j15 cases, with relative maxima in magnitude found approximately halfway between the surface and the top of the boundary layer found at approximately model level 60.

As the perturbations evolve in the nonlinear forecast, the perturbation energy components in all cases remain largely dominated by kinetic and available potential energy perturbations. In each of the three cases however, the contributions of these energy components to the total perturbation energy, shown by the normalized profiles, quickly reverse relative to the analysis time, with perturbation kinetic energy growth dominating in layers initialized predominantly with perturbation available potential energy, and vice versa. This trend is most notable within the troposphere, but is also noted to a lesser degree in the lower stratosphere. The SSS intensifying QOIP, which behaved the most linearly of all experiments and achieved the most iterations by satisfying linearity thresholds, is shown to have perturbation kinetic energy comprise

greater than half of the total energy from the surface to model top within the first 12-hrs of the simulation, with a maximum of 90% kinetic energy found near the tropopause as soon as 6-hrs into the simulation. This is largely consistent with the analysis done in Sections 3.4 and 3.5, in which the upper-level precursor disturbance is most heavily modulated by the perturbations, as compared to the lower-levels.

The SOTC and j15 cases however are similar in their perturbation energy profiles (SOTC-IIR (-DIR) Figs. 4.13 (4.15); and j15-IIR (-DIR) to Fig. 4.14 (4.16)), and both display vastly different characteristics than SSS. Within the boundary layer, the perturbation energy for both cases is composed primarily of available potential energy before reversing back to a majority kinetic energy contribution through much of the middle and upper troposphere, while available potential energy becomes the dominant perturbation energy in the lower troposphere, creating a substantially different profile by the time of the response period than was observed in SSS. Additionally, both cases show a relatively large component of latent heat energy maximizing at the top of the boundary layer that was not observed in SSS.

As the increased intensification rate QOIP for SOTC and j15 displayed a quick drop-off in linearity within the QOIP algorithm, it stands to reason that the comparatively higher nonlinearity of the perturbation growth in these cases may be related to the evolution of the vertical distribution of the perturbation energy types. The vertical profiles of perturbation energy for the SSS-DIR case can be seen in Fig. 4.17a-j. The SSS-DIR case was similarly characterized by a rapid drop-off in linearity, only achieving two iterations per the QOIP algorithm. At the initial time, the SSS-DIR perturbations are qualitatively very similar to those of the IIR case, but as the forecast is integrated forward

in time, the profile takes on characteristics more similar to the SOTC and j15 cases, with a large majority of the perturbation energy in the lowest levels being attributed to the available potential energy component, as well as a latent heat energy component very similar to the SOTC and j15 cases. Noting that the j15-DIR case displayed slightly more linear behavior than the j15-IIR case, this is further consistent with the linearity hypothesis.

The non-linearity seen in the SOTC, j15 and SSS-DIR cases, and conversely the linearity seen in the SSS-IIR case, seems somehow related to the evolution of the kinetic versus available potential energy in the perturbation energy profiles, where highly nonlinear cases appear to develop a dominant available potential energy component at low levels, while linear cases appear to develop a dominant kinetic energy component. This is consistent with a hypothesis that perturbations that are largely kinematic in nature will concentrate on modifying the synoptic-scale pattern, and are likely to evolve using the model's dynamical core¹⁶, while perturbations that are largely thermodynamic will result in changes to quantities such as relative humidity and will adjust the activation (de-activation) of the precipitation parameterization schemes within the model, and create potentially large changes to highly non-linear sub-grid scale processes. These different pathways for perturbations to affect the forecast state may have drastically different characteristics with regard to the linearity of their development, which could be expressed by the QOIP method as larger or smaller FE.

Within the GEOS-5, a simple parameterization as outlined in Errico et al. (1994) is employed for large-scale precipitation, with the relaxed Arakawa-Schubert (RAS)

¹⁶ The GEOS-5 employs the Finite Volume Cubed-Sphere (FV3) dynamical core (Lin and Rood 1997; Lin 2004).

scheme used for convection (Arakawa and Schubert 1971; Holdaway et al. 2013). Both of these parameterization schemes employ (amongst other conditions) relative humidity as a switch to trigger their activation (de-activation). By changing the temperature and moisture fields, the relative humidity fields will also be changed, resulting in changes to the parameterized precipitation distributions. Precipitation processes themselves are small scale and highly non-linear, and therefore introduce non-linearity into the forecast integration. In perturbing the simulations in a manner that largely impacts the precipitation fields, it can be expected that only minimal impact by the QOIP will be seen, as perturbations of this kind are not likely to achieve the threshold linearity required to enter multiple outer loops and generate large QOIP over several iterations.

4.4.3 Barotropic Preconditioning

Unlike the SSS case, the SOTC and j15 cases displayed did not display any evidence of barotropic preconditioning by the QOIP. Figs. 4.18a-c and 4.19a-c show the zonal mean barotropic energy conversion (BEC) at the analysis time and total barotropic energy conversion (normalized by the total kinetic energy at each forecast time step) respectively for each of the three cases. The BEC traces are computed between 600 hPa to 150 hPa for the SOTC case and 400 hPa to 150 hPa for the j15 case. These layers are chosen as they encapsulate the largest magnitudes of BEC within the zonal mean BEC plots.

Figure 4.18b shows that BEC within the SOTC case is negligible in the zonal mean, likely symptomatic of the small magnitude of the perturbations. This is further expressed in Fig. 4.19b, where normalized BEC values are near zero throughout the

integration. Although there is a slight build-up of BEC in the first 9-hrs of the simulation, it is quickly exhausted prior to the response period. For the j15 case, owing to its slightly larger-in-magnitude perturbations, Figs. 4.18c and 4.19c display more robust BEC in the zonal mean and normalized time-series. Even considering the slightly larger magnitude of initial-time BEC in j15 versus SOTC, there is still no evidence for barotropic preconditioning, as there is no substantial build-up of BEC per unit kinetic energy prior to the response period, and therefore no eventual exhaustion of BEC during and after the response period, as is observed in the SSS case.

4.4.4 QGPV Analysis

As was performed in section 3.5, perturbation QGPV was calculated and inverted for both the SOTC and j15 cases. Identical to the SSS analysis, the QGPV was inverted in a piecewise fashion over layers found at 1000 hPa and between 950 hPa and 750 hPa; 700 hPa and 450 hPa; 400 hPa and 150 hPa; and 100 hPa and 50 hPa. Within this discussion, “surface”, “lower-levels”, “mid-levels” and “upper-levels” will refer to the 1000 hPa, 950hPa to 750 hPa, 700 hPa to 450 hPa and 400 hPa to 150 hPa layers respectively. As the impact of the 100 hPa to 50 hPa layer was negligible, it will be neglected for discussion.

a) 11-13 March 1993 “Storm of the Century”

Noting once again that the QOIP were largely ineffectual in modulating the intensification rate of SOTC, only a brief discussion of the QGPV will be undertaken. For the first 12 hours of the forecast, QGPV perturbations at all levels are minimal and result

in virtually no inverted height perturbations in the lower-levels. Beyond 12-hrs, the majority of the QGPV perturbations at all levels are heavily governed by diabatic effects of large-scale precipitation associated with the developing surface cyclone. This is evident in both the IIR and DIR cases between 12-hrs and 27-hrs, with the latter representing the second goalpost time of the response period; since the intensifying QOIP (IIR) and weakening QOIP (DIR) are largely similar in structure, the SOTC-IIR experiment will be focused on for brevity. Within the 12-27-hr forecast period, kinematic perturbations are minimal at all levels, while QGPV perturbations nearly perfectly coincide with areas of large-scale precipitation perturbations (Fig. 4.20), with upper-tropospheric QGPV perturbations of alternating sign appearing along fronts of the cyclone anti-correlated with regions of enhanced or depressed precipitation, physically consistent with the impact of diabatic erosion of upper-tropospheric PV. This result demonstrates, as was hypothesized in Section 4.3.2, that the first-order impact that highly non-linear precipitation processes have on the evolution of the perturbations can be expressed through the QOIP as low FE.

When compared to the SSS case, these results indicated that the QOIP acted to impact the intensification rate of the cyclone through a fundamentally different approach. Within the SSS experiments, QGPV perturbations reshape the upper-level precursor disturbance in order to create an environment more conducive for large-scale baroclinic growth of a cyclone. These perturbations to the synoptic pattern influence the development of the cyclone through growth, predominantly, of the kinetic energy component of the perturbation at all levels, and evolve in a highly linear manner as discussed in Section 3.1.2. Although there are perturbations to the atmosphere that result

in diabatic perturbations to the QGPV fields in the SSS cases, this augmentation plays a relatively small role in the development of the perturbed cyclone. Conversely, the QOIP for SOTC-IIR appears to focus on augmenting the cyclone's intensification rate through changes to sub-grid scale precipitation processes, an approach that leads to growth mainly of the available potential energy component of the perturbation in the lower-troposphere, a rapid decay in linearity, and an overall lack of change to the response function due to failure to produce many iterations that meet the threshold linearity criteria of the QOIP algorithm.

b) 25-28 January 2015 Northeast Snow Event

Recalling the box-mean pressure trace for j15 (Fig. 4.10c), it can be seen that the method that is used by the QOIP to increase the intensification rate of j15 is *slightly* different than that which is used for SSS. In the SSS cases, the intensity of the cyclone at the first goalpost time is essentially identical for all cases, with the majority of the change to the intensification rate due to significant changes to the intensity at the final goalpost time. Unlike SSS however, the intensification rate of j15 is increased (decreased) by generally creating a marginally weakened (strengthened) cyclone at the first goalpost time, with a (comparatively) more robust strengthening (weakening) of the cyclone at the final goalpost time. This can be further seen in Fig. 4.11, the difference between the perturbed and control simulation box-mean pressure traces. Considering the mathematical formulation of the response function, either method for changing the intensification rate is equally valid.

It is apparent that the majority of the FE displayed by j15 (Fig. 411) is expressed after the second goalpost time, where the largest deviation from the control forecast is noted. While the QOIP algorithm terminated after two (four) iterations for the IIR (DIR) experiments, indicating that the each individual outer-loop iteration within the QOIP algorithm quickly displayed highly non-linear behavior, the response of the cyclone's intensity to increased and decreased intensification was roughly equal in magnitude. As this is the case, it can be surmised that the FE of the response of the forecast to the QOIP for is roughly the same in both the intensifying and weakening directions, given that the control trajectory lies very close to the center of these experiments. Furthermore, it is noteworthy that the IIR and RDIR (DIR and RIIR) yield relatively similar box-mean pressure traces, even given the difference in QOIP iterations. This is a similar result as shown in Chapter 3 for the SSS case, in which the RIIR QOIP, one that was computed by the sum of nine iterations of individual optimal perturbations, yielded a similar perturbed forecast trajectory as the DIR case, which only achieved two iterations. This indicates that a limit on the total impact that the perturbations can have on increasing or decreasing the response function, as QOIP that are the result of a larger number of iterations, and therefore have a larger magnitude (thus theoretically yielding a larger response), yield the same magnitude of change to the response function as those that result from fewer iterations.

Unlike the SSS and SOTC cases which in which the QGPV perturbations were dominated by kinematic and thermodynamical processes respectively, the j15 case is characterized by a combination of the two types of processes. At 16-hrs into the simulation, it can be seen for the IIR simulations in Fig. 4.21c and Fig 4.21e and for the

DIR simulations in Fig. 4.21d and 4.21f that within the mid- and lower-levels, the cases are characterized by relative vorticity dominated (e.g., QGPV that is augmented via changes to the kinematics fields vs. that which is augmented by changes to the stratification) positive (for the IIR case) and negative (for the DIR case) QGPV perturbation rounding the base of the synoptic trough located over Florida. These QGPV perturbations are found slightly upstream of the developing surface circulation, and in the mid-levels are associated with a slight intensifying (weakening) of the synoptic wave in order to enhance (suppress) baroclinic development. Two additional regions of perturbation QGPV are located upstream of the kinematic QGPV perturbation in the lower- and mid-levels, just off the Carolina coast and further to the northeast off the New Jersey coast. These regions of QGPV perturbations are diabatically generated, as they are associated with perturbation large-scale precipitation (Fig. 4.22).

Within the IIR simulation, the mid- and lower-level diabatically generated QGPV perturbations can be seen in dipole patterns, and are anti-correlated to dipoles in the perturbation precipitation field, as was observed in the SOTC-IIR case. It is likely that this is representative of a geographic shift in the QGPV perturbations in those levels rather than generation of “new” QGPV. In the upper-levels however (Fig 4.21a and Fig. 4.21d), these perturbations are not characterized by dipole patterns, but rather can be seen as largely negative in the IIR case and largely positive in the DIR case. For the IIR case, this is representative of the diabatic destruction of the upper-level QGPV in order to aid in the development of both an upper-level anticyclone and the development of a slight downstream ridge.

Within the lower-levels of the DIR simulation, there is largely a reversal in the sign of the perturbations versus the IIR simulation, indicative of reasonably high linearity within the lower-levels between the cases. The configuration of the perturbation QGPV in the mid-levels however is more complex than a simple reversal in the sign of the perturbations. As to be expected, the QGPV perturbations dominated by kinematic processes largely behave linearly, as can be seen by the *negative* QGPV perturbation over Florida rounding the base of the mid-level trough. Downstream however, the diabatically generated positive QGPV perturbation is not found to be characteristic of a dipole pattern, unlike the IIR simulation. As can be seen in Fig. 4.22b, there is a highly negative region of large-scale perturbation precipitation in this region, rather than the dipole seen in the IIR simulation. This indicates that there is a region of strong drying within the perturbation simulation rather than a shift in the precipitation field. This is a highly non-linear response, as the positive and negatively signed perturbations (e.g., the IIR and DIR simulations; Fig. 4.22a and Fig. 4.22b) show significantly different results in similar geographic areas. In the upper-levels, there is once again a relatively linear response, with largely positive QGPV perturbations associated with the reduced large-scale precipitation.

By 21-hrs into the simulation, the trends found at 16-hrs within the IIR simulation largely continue. In the upper-levels (Fig. 4.23a), strong diabatic QGPV destruction continues, further aiding in the development of the surface cyclone. Additionally, the region of mid-level kinematically dominated QGPV having propagated downstream and merged with the diabatically generated QGPV dipole (seen off the Carolina coast in Fig. 4.23c), aiding to help deepen the trough upstream of the developing surface circulation.

In the upper-levels (Fig. 4.23a), strong diabatic QGPV destruction continues, further aiding in the development of the surface cyclone. Within the lower-levels, a dipole in QGPV perturbation is present, and associated with a slight southward shift in the center of the circulation.

Within the DIR simulation (Fig. 4.23b, d, and f), a fairly convoluted configuration at all levels can be seen. Within the mid-levels, several dipoles in QGPV perturbations can now be seen, and are associated with both the merging of the kinematically generated QGPV perturbations as well as several regions of large-scale precipitation perturbations. Unlike 5-hrs earlier in which the upper-level perturbation QGPV is largely diabatic in nature, it appears that much of the highest magnitude positive perturbation QGPV that is found over the Carolinas is now kinematic in nature, perhaps associated with the generation of westward shift in the surface cyclone, which is now comprised of multiple height minima. It also appears that much of the perturbation QGPV is vertically stacked rather than tilted as is the case in the IIR simulation. This is also likely aiding in the satisfaction of the response function, as it indicates that the lower-level circulation began to exist in a relatively steady state in which intensity changes were minimal as compared to during the response period. This assertion is also seen in Fig. 4.10c in which the DIR cyclone failed to continue deepening past approximately 18-hrs into the simulation.

Considering both the configuration and relatively high degree of linearity between the experiments, it is unsurprising that the perturbation QGPV yields nearly opposite responses between the IIR and DIR (RIIR and RDIR) simulations at 900 hPa for each of the piecewise inversions. Fig. 4.24a-d show a time-series of the contribution of the piecewise QGPV within each layer to the 900 hPa geopotential height perturbations for

each of the four experiments. The degree of similarity between the IIR and RDIR (DIR and RIIR) is high, further indicating the response to the perturbations is highly linear and that the perturbations are limited at a certain point in their ability to further change the response function.

Throughout the majority of the increased (decreased) intensification rate experiments, it can be seen in the time-series that the surface and upper-level QGPV perturbations act to weaken (intensify) the cyclone at 900 hPa, while the lower- and mid-level QGPV perturbations act to intensify (weaken) the cyclone at 900 hPa. At the initial goalpost time, the observed height perturbation at 900 hPa (as well as at the surface as seen in Fig. 4.10c) is positive (negative), as the surface and upper-level QGPV perturbations dominate the lower- and mid-level perturbations. This can be seen in Fig. 4.25a-d (j15-IIR; RDIR not shown due to its similarity to the IIR simulation), in which the positive height perturbations by the surface and upper-level QGPV are 1) largely greater in magnitude than those by the lower- and mid-level perturbations; and 2) act to mute the lower-magnitude lower- and mid-level height perturbations in regions of overlap. As this is the case, the total inversion is dominated by a dipole in height perturbations, with a lower-magnitude region of negative height perturbations found in the southwest corner of the response box and a higher-magnitude, larger region of positive height perturbations in the northeast corner of the response box.

By 21 hours into the simulation (Fig. 4.24a and 4.26e) the observed 900 hPa height perturbations have become negative, indicating that the cyclone has undergone a period of increased intensification rate over the response period. While the sign of the perturbation 900 hPa height field due to the upper-, mid-, lower-level and surface

perturbations remains constant throughout the intensification period, it appears that it is the surface QGPV perturbations that controls the intensification rate during the response period. This is achieved by surface perturbations acting to mitigate the impact of positive 900 hPa height perturbations by the upper-level QGPV. Although the height perturbations due to the surface QGPV remain positive at this time, the impact by the surface on the box-mean 900 hPa heights is reduced to near-zero. In this way, the surface perturbations act to counteract the (increasing in magnitude) positive perturbation height tendency due to the upper-level perturbations, thus lessening their impact and allowing the lower- and mid-level perturbations to become the driving influence upon the intensification rate over the response period. It should also be noted that over the response period, the mid-level perturbations experience a steady increase in magnitude resulting in increasingly large negative 900 hPa height perturbations. While the response period is also characterized by lower-level height perturbations that are also responsible for negative 900 hPa height perturbations, the magnitude of those height perturbations decreases rapidly beginning at 20 hours, mitigating a potentially larger impact on the response function. Furthermore, although large positive perturbations to the 900 hPa height can be seen in Fig. 4.26a at 21-hrs, they are outside of the response function box and thus have no *direct* impact on the calculation of the response function.

In conjunction with the increased importance of the surface perturbations, it is apparent that the lower- and mid-level impact on the 900 hPa height perturbations inside the response function box is large, and contributes to the lowered perturbation heights at the final goalpost time. Furthermore, while the upper-level perturbations do appear to create significant positive height perturbations within the box at the final time, that

impact is largely muted by the negative perturbation heights due to the lower- and mid-level QGPV perturbations at the same time.

Given the linearity between the increased and decreased intensification rate experiments, it is expected that the decreased intensification rate responses of the 900 hPa perturbation height to the partitioned QGPV would be opposite the increased intensification rate simulations. It can be seen that the observed 900 hPa perturbation height field is lower at the first goalpost time and higher at the second goalpost time, with the mid- and upper-level QGPV perturbations largely acting perfectly opposite both one another and also opposite of their behavior in the increased intensification rate experiments. In the decreased intensification rate experiments, however, it appears that it is the lower-level QGPV perturbations and not the surface QGPV perturbations that modulate the overall perturbation height tendency during the response period. Furthermore, unlike the intensifying experiments, in which a tight perturbation pressure gradient develops at 900 hPa due to the perturbations QGPV, the weakening experiments largely lack this feature.

4.5 Summary and Conclusions

Two cases, the 11-13 January 1993 “Storm of the Century” (SOTC) and the 25-28 January 2015 Northeast Snow event (j15) were analyzed using the method described in Chapter 3 aimed at increasing or decreasing the intensification rate of a mid-latitude cyclone over a specified period within the respective simulations. The cases were selected given both their qualitative and quantitative levels of predictability as a means by which to compare cases with levels of predictive skill both significantly and

marginally higher than that of the 24-26 January 2000 “Surprise Snow Storm” (SSS) discussed in Chapter 3.

The SOTC simulations displayed only marginal levels of forecast elasticity (FE), indicating that that case was not susceptible to significant modulation of the response function by the QOIP method. This indicates the highly predictable nature of the case, as perturbations numerically formulated to have a specified impact upon the simulations fail to do so. The behavior of these perturbations indicates that analysis uncertainty with similar structure would have little impact upon the outcome of the forecast state, allowing for a highly predictable forecast. Paradoxically, the inability to calculate QOIP that were successful in creating a large change in the response function was likely due to the dependence upon small-scale, non-linear diabatic processes that helped to both increase the intensity of the cyclone but mitigate the linear behavior of the perturbations within the inner-loop of the QOIP algorithm. Additionally, as a result of the lack of impact that the perturbations have on the case, SOTC displayed virtually no barotropic preconditioning, a mechanism that appeared to dictate the evolution of the SSS case described in Chapter 3.

The j15 case displayed a moderate FE based on the QOIP method. The changes to the response function resulted in a period of modest change to the rate of intensification over the response period in the intensifying experiment that was manifest as a slight weakening (strengthening) of the cyclone at the first goalpost and a more robust strengthening (weakening) of the cyclone at the final goalpost. This result was relatively consistent with that of the SSS case in Chapter 3, in which the majority of the change to the response function was also found at the second goalpost time. Unlike the SSS case,

the FE was not strongly skewed, with the control forecast falling nearly perfectly in between the increased and decreased intensification rate experiments. In this way, the case behaved relatively linearly, as the final, composed QOIP resulted in largely symmetric responses about the control forecast. Finally, there appears to be an intrinsic limit on the amount of response function by the perturbations within the j15 case. Both the IIR (DIR) and RDIR (RIIR) simulations displayed nearly identical responses to the QOIP, even given the fact that the magnitude of the IIR (RIIR) perturbations were smaller than the DIR (RDIR) perturbations owing to a more rapid failure of the QOIP algorithm due to non-linear behavior by the individual, inner-loop iterations.

As the QOIP were successful in creating a change to the response function, diagnosis of the behavior of the QGPV perturbations through a piecewise QGPV inversion technique was performed. It was shown that the intensification rates within intensifying experiments (IIR and RDIR) were largely dictated by the surface QGPV perturbations, which showed the greatest fluctuation in the resulting inverted 900 hPa height perturbations over the length of the integrations. The IIR and RDIR cases also displayed inverted height perturbations that aided in the development of a near surface perturbation pressure gradient and resulted in perturbations ageostrophic convergence inward towards the cyclone center.

Conversely, the weakening experiments (DIR and RIIR) displayed a large modulation by the lower-level QGPV perturbations, which dominated the perturbation height field over the course of the integration.

Finally, it was shown that vertical profiles of the contribution to perturbation energy by kinetic, available potential, elastic, and latent heat components varied

significantly between the highly linear case (SSS-IIR) and the other, less-linearly behaving cases. The SSS-IIR case was characterized by a dominance of the kinetic energy component and developed a “top-down” structure, consistent with “Type-B” (Petterssen and Smebye 1971) mid-latitude cyclogenesis, through barotropic preconditioning of the upper-tropospheric precursor disturbance. Additionally, normalized thermodynamic perturbation energy (available potential and latent heat components) was smaller than perturbations to kinetic energy in the SSS-IIR case. Conversely, the remaining cases (SSS-DIR, and SOTC and j15 for either the IIR or DIR experiments) displayed less linear behavior, and were characterized by a lower- to mid-level dominance by the available potential energy perturbations. This configuration indicated a “bottom-up” evolution of the perturbations as the integration proceeded forward in time, and illustrated the importance of small-scale, diabatic processes in the QOIP attempting to make changes to the response function primarily through modification of precipitation. As these small-scale diabatic processes are generally high non-linear, the QOIP algorithm stopped outer loops relatively early (as compared to SSS-IIR) due to relatively high non-linearity within the inner-loop of the QOIP algorithm.

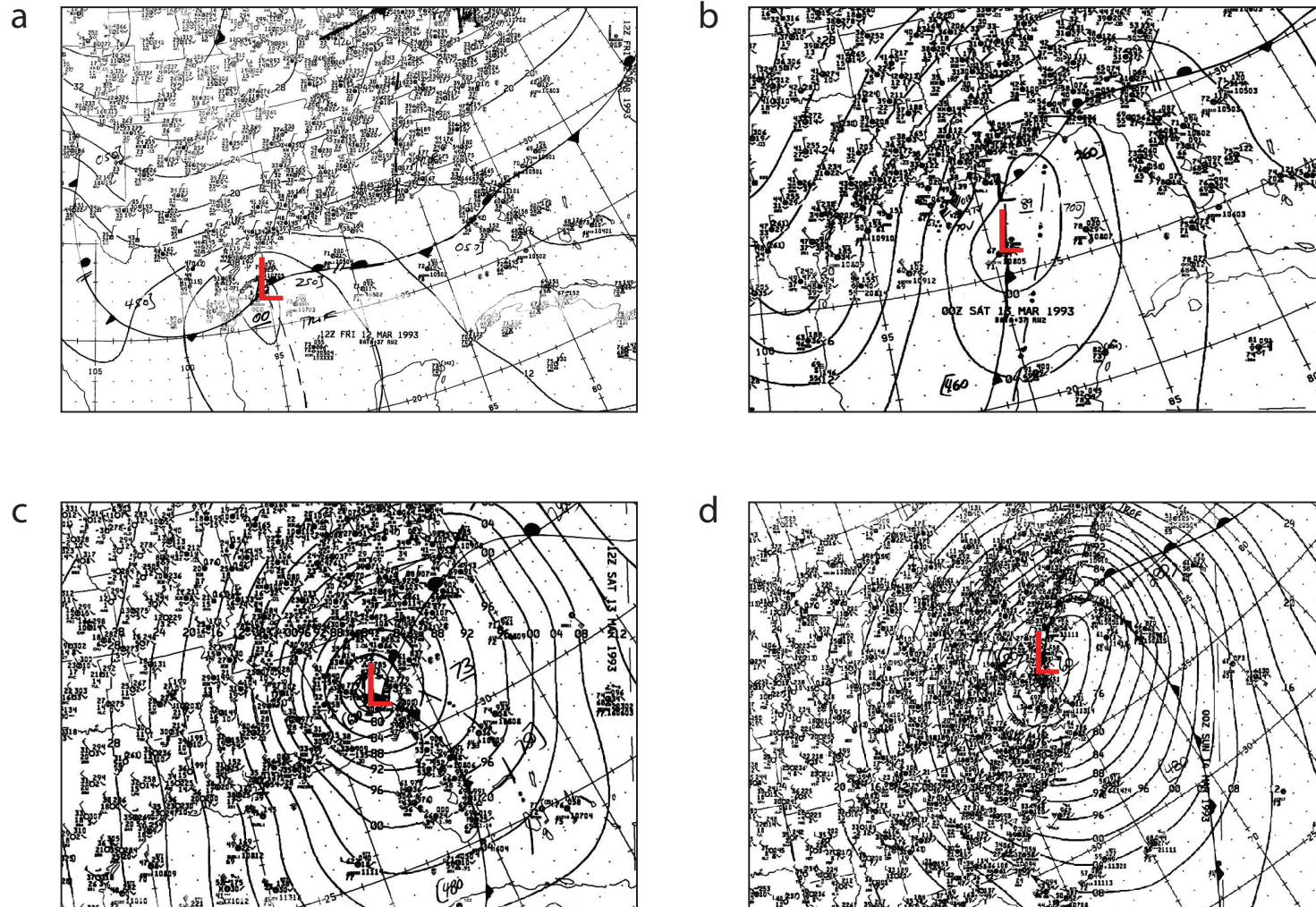


Figure 4.1. NWS subjective surface analyses¹⁷ valid at (a) 1200 UTC 12 March 1993, (b) 0000 UTC 13 March 1993, (c) 1200 UTC 13 March 1993, and (d) 0000 UTC 14 March 1993

¹⁷ Surface analyses courtesy David Roth, NOAA Weather Prediction Center.

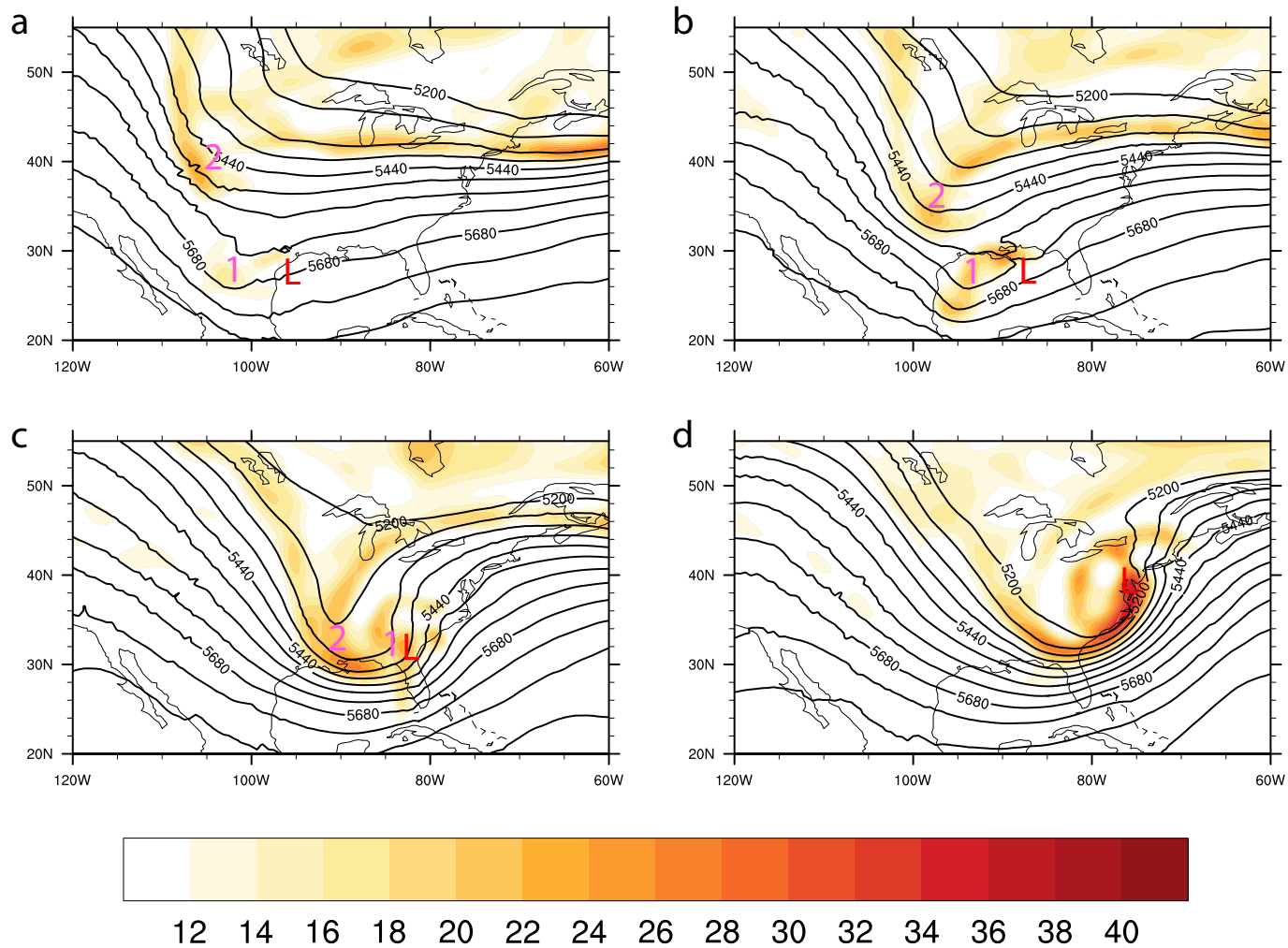


Figure 4.2. MERRA-2 analyses of the 500 hPa vorticity (fill; 10^5 s^{-1}); and height (black contours; m) valid at (a) 1200 UTC 12 March 1993, (b) 0000 UTC 13 March 1993, (c) 1200 UTC 13 March 1993, and (d) 0000 UTC 14 March 1993. The “northwestern” trough is denoted by the magenta number 1; the southeastern trough is denoted by the magenta number 2; and the location of the surface low is denoted with the red L.

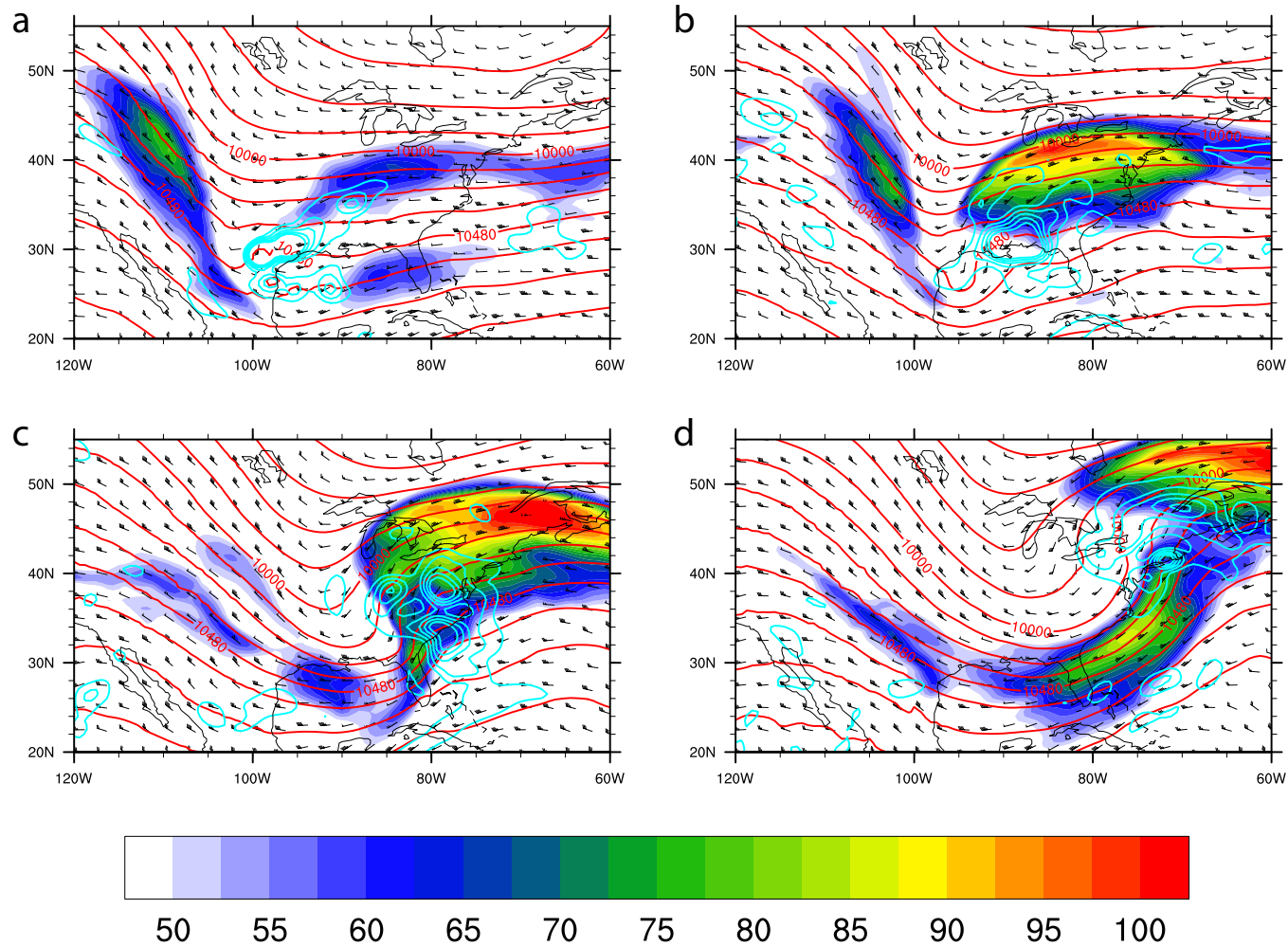


Figure 4.3. MERRA-2 analyses of the 250 hPa wind (fill and vectors; m s^{-1}); height (red contours; m) and divergence (cyan contours; s^{-1} ; contoured from 2×10^{-5} to 10×10^{-5} by 2×10^{-5}) valid at (a) 1200 UTC 12 March 1993, (b) 0000 UTC 13 March 1993, (c) 1200 UTC 13 March 1993, and (d) 0000 UTC 14 March 1993.

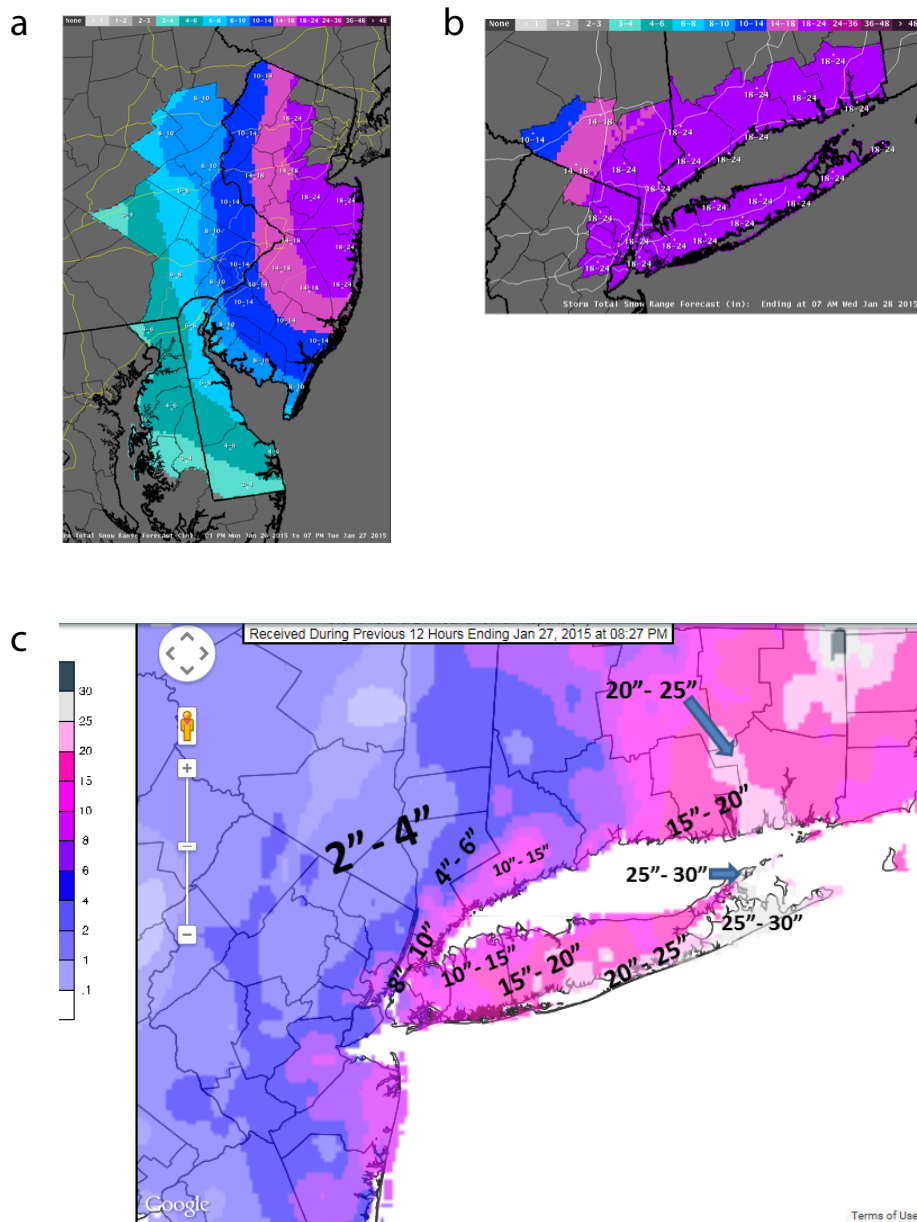


Figure 4.4. Snow forecast maps as issued by the National Weather Service (NWS) offices in (a) Philadelphia/Mt. Holly; and (b) New York City/Upton issued mid-morning January 25. Verifying snow totals can be seen in panel (c) and display a significant disparity from forecasted totals, especially over inland regions.

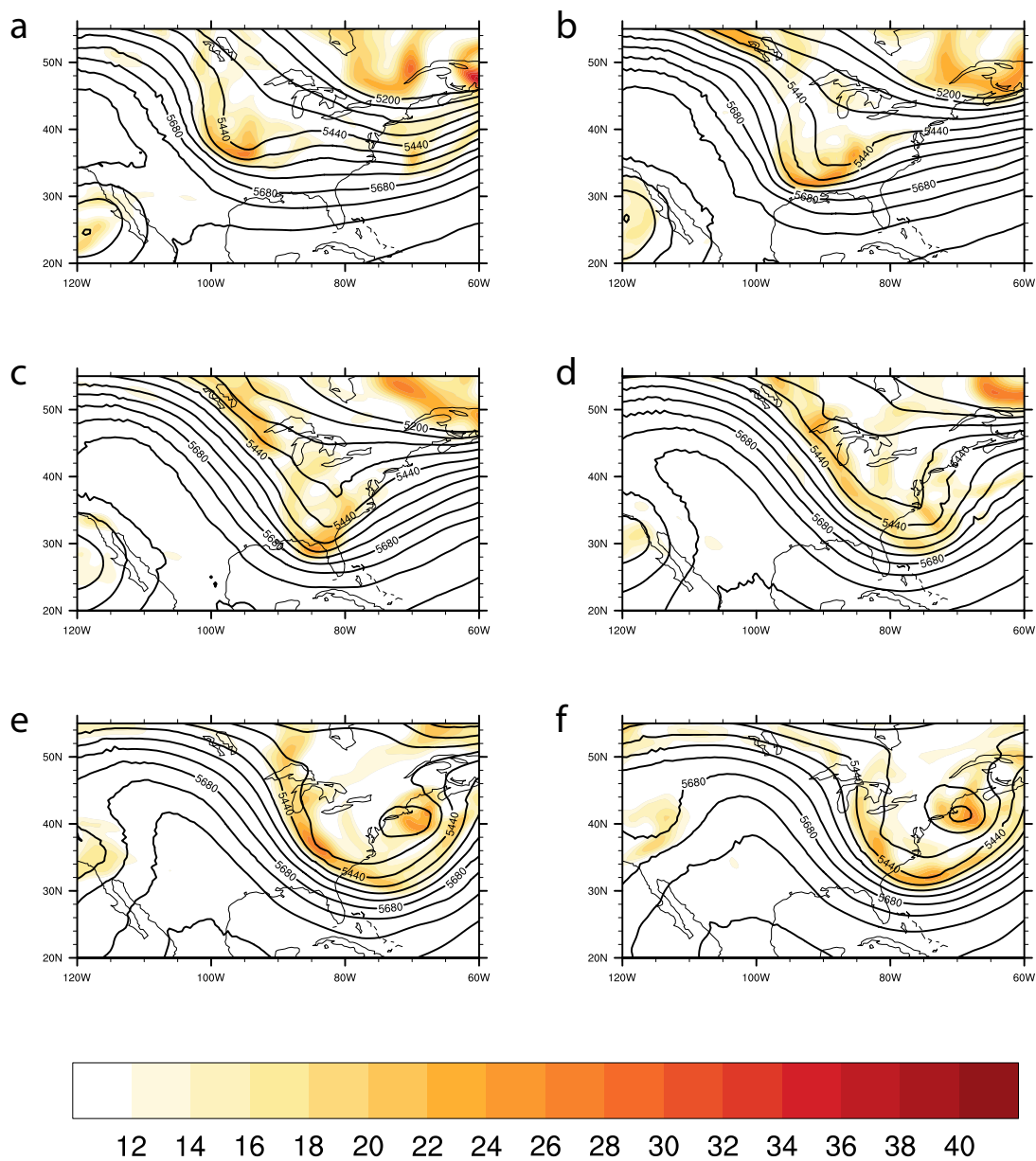


Figure 4.5. MERRA-2 analyses of the 500 hPa vorticity (fill; 10^5 s^{-1}); and height (black contours; m) valid at (a) 1200 UTC 25 January 2015; (b) 0000 UTC 26 January 2015; (c) 1200 UTC 26 January 2015; (d) 0000 UTC 27 January 2015; (e) 1200 UTC 27 January 2015 and (f) 0000 UTC 28 January 2015.

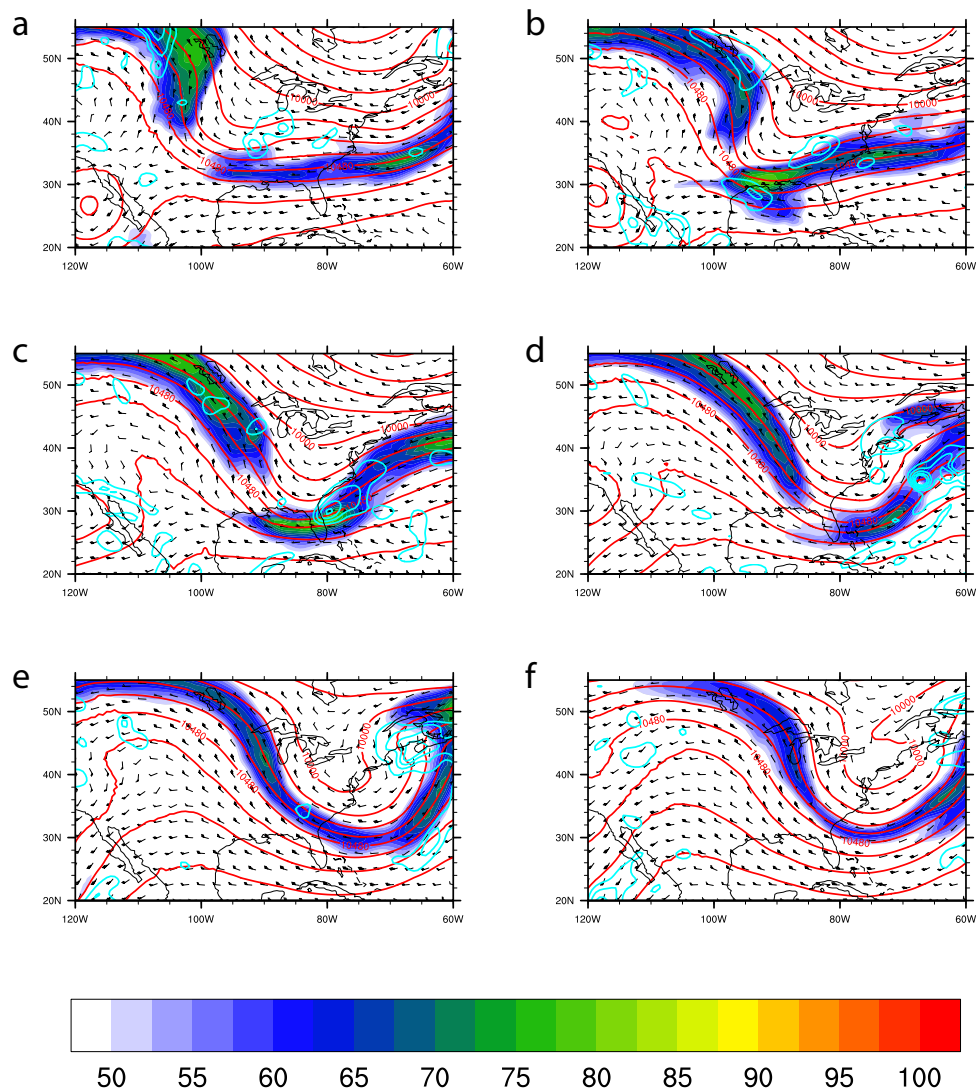


Figure 4.6. MERRA-2 analyses of the 250 hPa wind (fill and vectors; m s^{-1}); height (red contours; m) and divergence (cyan contours; s^{-1} ; contoured from 2×10^{-5} to 10×10^{-5} by 2×10^{-5}) valid at (a) 1200 UTC 25 January 2015; (b) 0000 UTC 26 January 2015; (c) 1200 UTC 26 January 2015; (d) 0000 UTC 27 January 2015; (e) 1200 UTC 27 January 2015 and (f) 0000 UTC 28 January 2015.

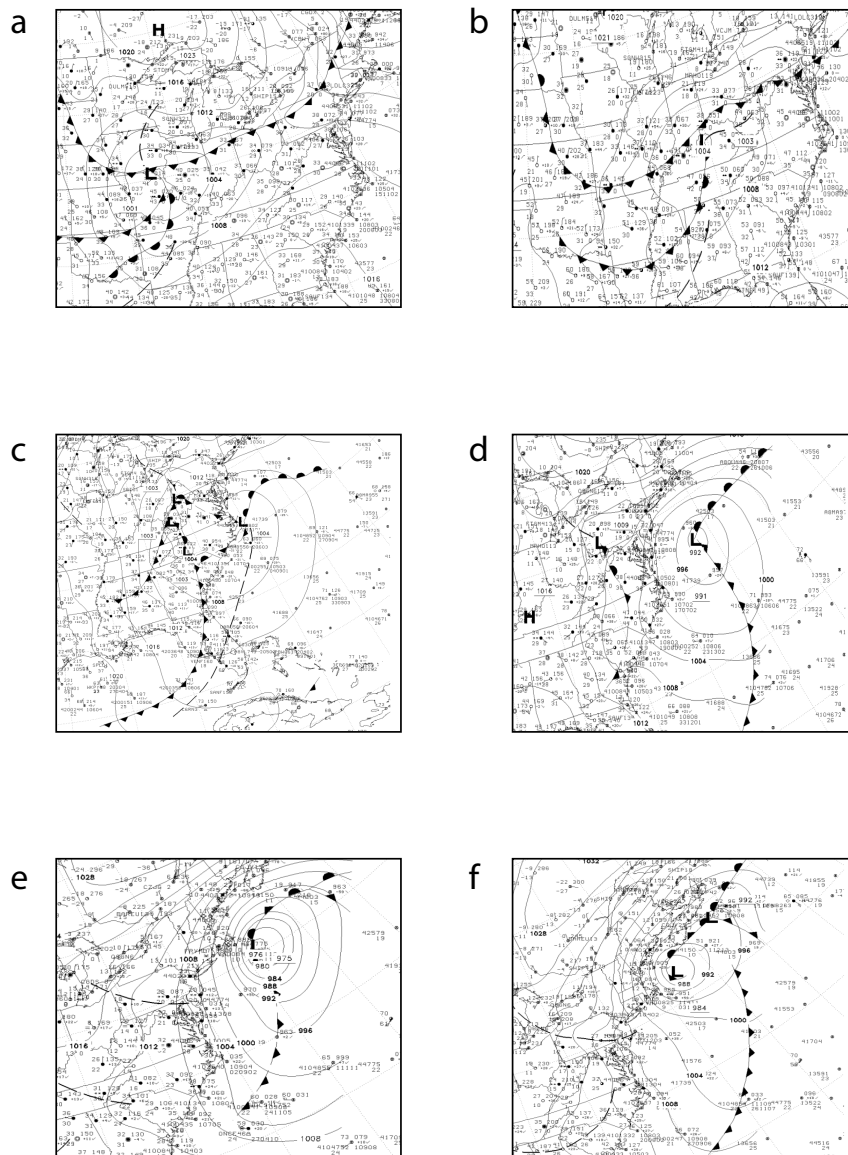


Figure 4.7. NWS subjective surface analyses¹⁸ valid at (a) 1200 UTC 25 January 2015; (b) 0000 UTC 26 January 2015; (c) 1200 UTC 26 January 2015; (d) 0000 UTC 27 January 2015; (e) 1200 UTC 27 January 2015 and (f) 0000 UTC 28 January 2015.

¹⁸ Data access available at: <https://atmos.washington.edu/data/vmaproom/varchive.cgi>

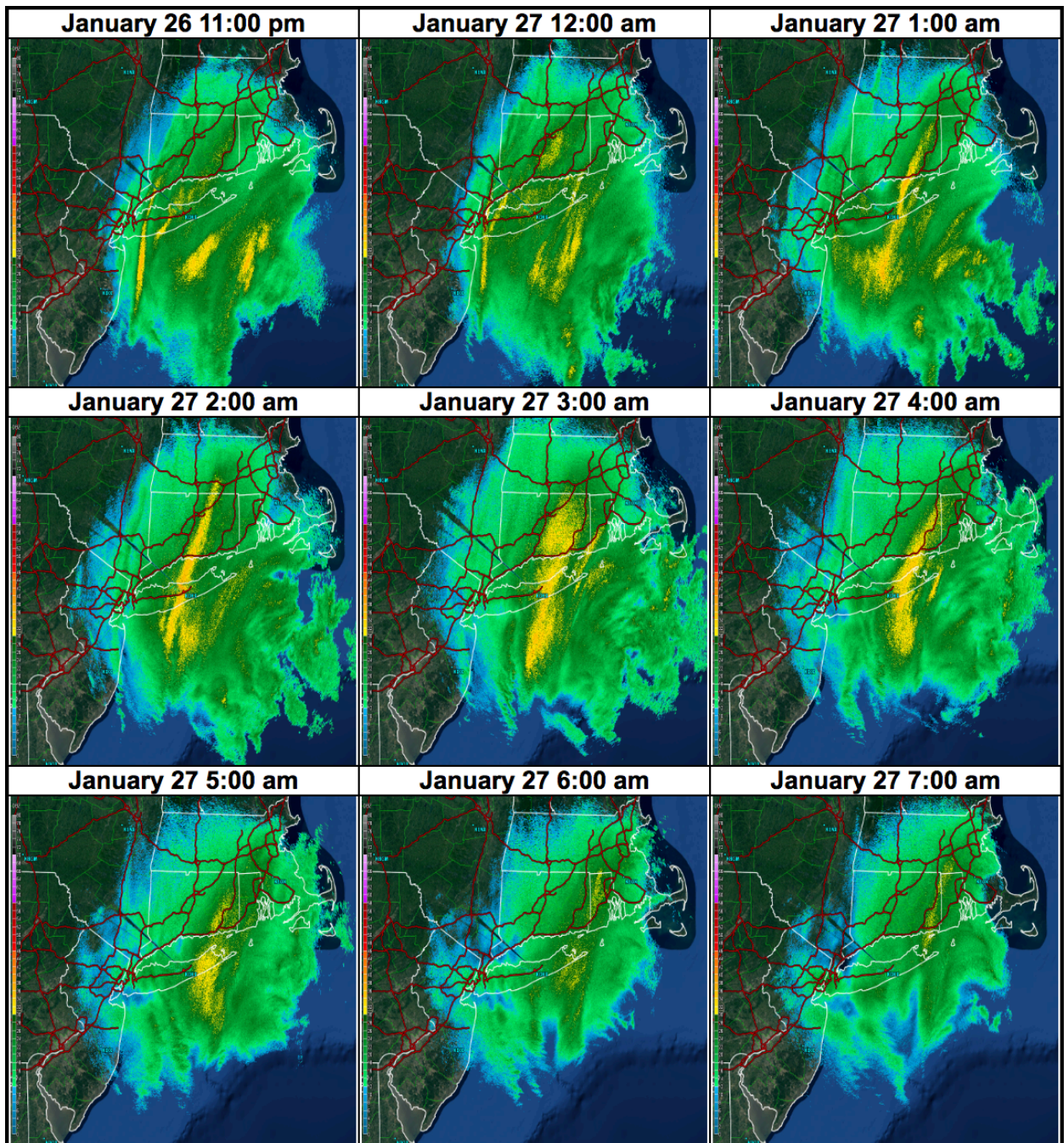


Figure 4.8. WSR-88d¹⁹ base reflectivity valid at the specified (Eastern Standard) times. Banded precipitation structures are found within regions of deformation.

¹⁹ Images courtesy NWS OKX: https://www.weather.gov/okx/Blizzard_01262715

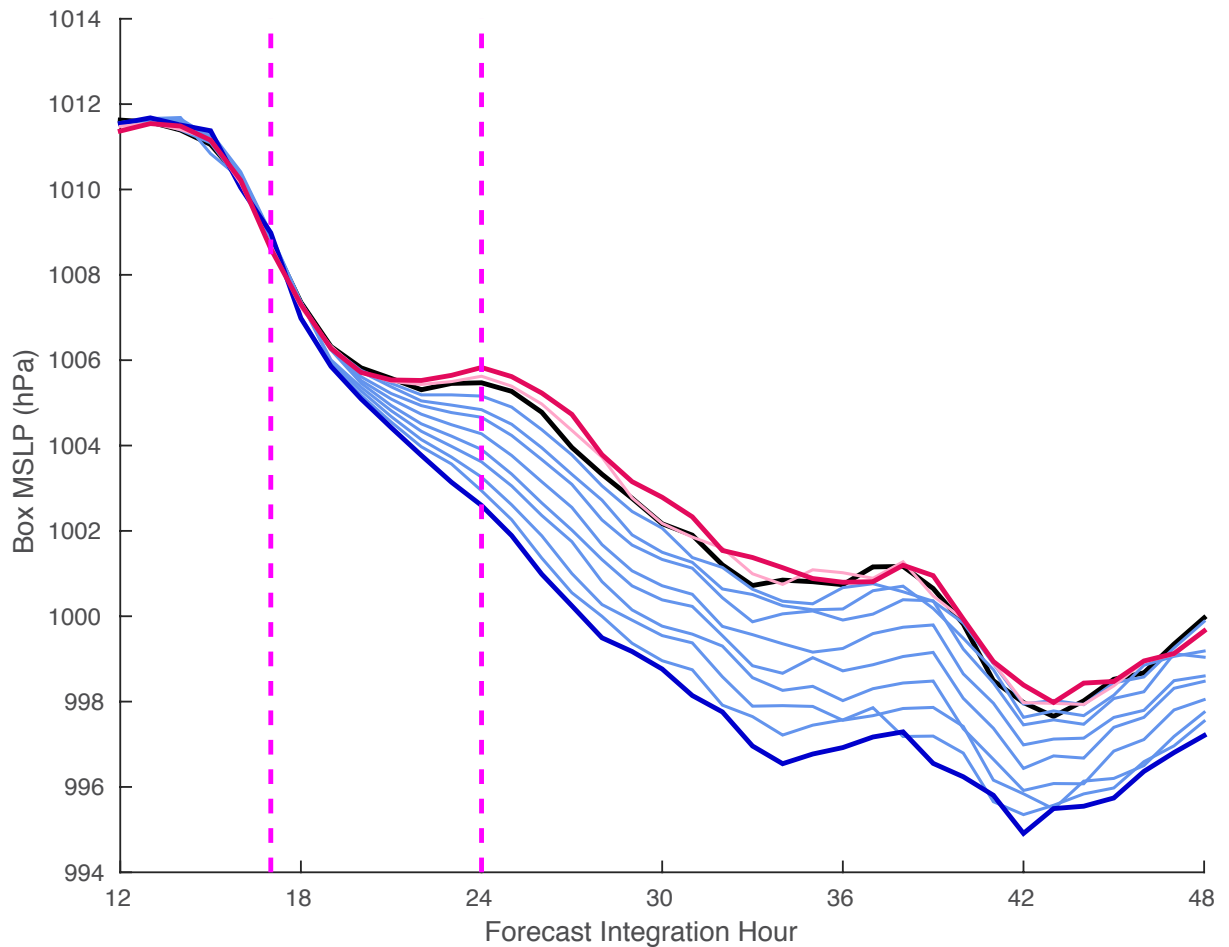


Figure 4.9. Cyclone-following time series of the 9° by 9° box-mean sea level pressure for the increased intensification rate perturbation simulation (Final IIR denoted by dark blue line; individual IIR iterations denoted by the light blue lines); decreased intensification rate perturbation simulation (Final DIR denoted by dark red line; individual IIR iterations denoted by the pink line). The control simulation is seen as the black curve. The magenta, vertical bars at 17- and 24-hrs indicate the response period over which changes to the intensification rate by the QOIP to the analysis are intended.

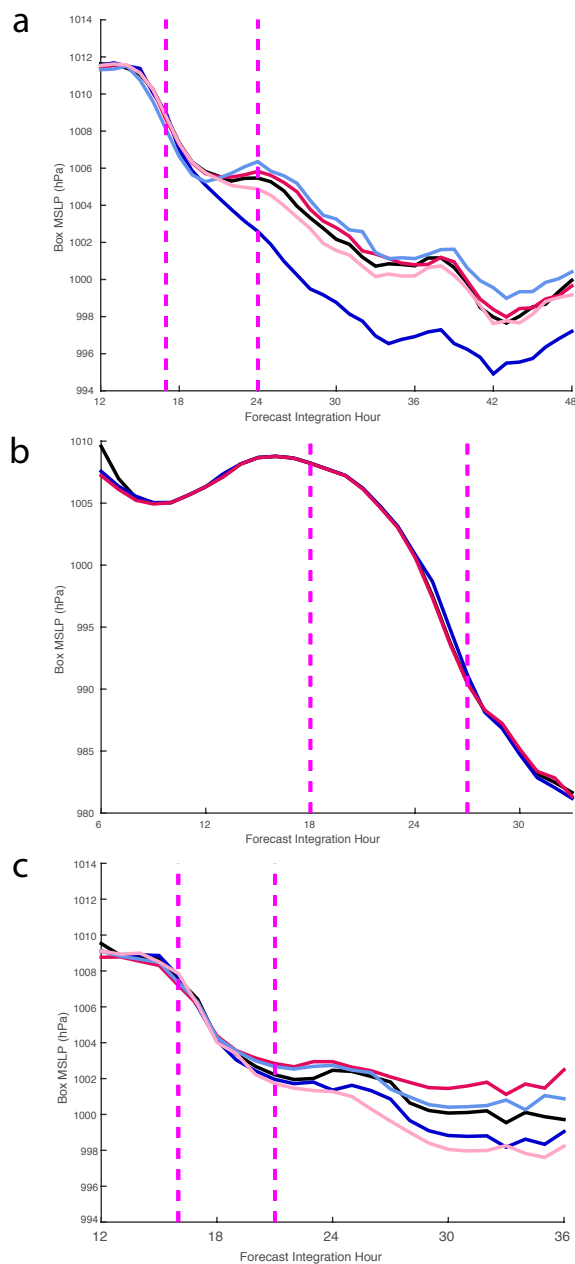


Figure 4.10. Cyclone-following time series of the 9° by 9° box-mean sea level pressure for the increased intensification rate perturbation simulation (IIR; dark blue); reversed sign intensification rate perturbation simulation (RIIR; light blue); decreased intensification rate perturbation simulation (DIR; red); and reversed sign decreased intensification rate perturbation simulation (RDIR; pink). The control simulation is seen as the black curve. The magenta, vertical bars indicate the response period over which changes to the intensification rate by the QOIP to the analysis are intended. The cases plotted are seen as (a) SSS; (b) SOTC; and (c) j15 simulations.

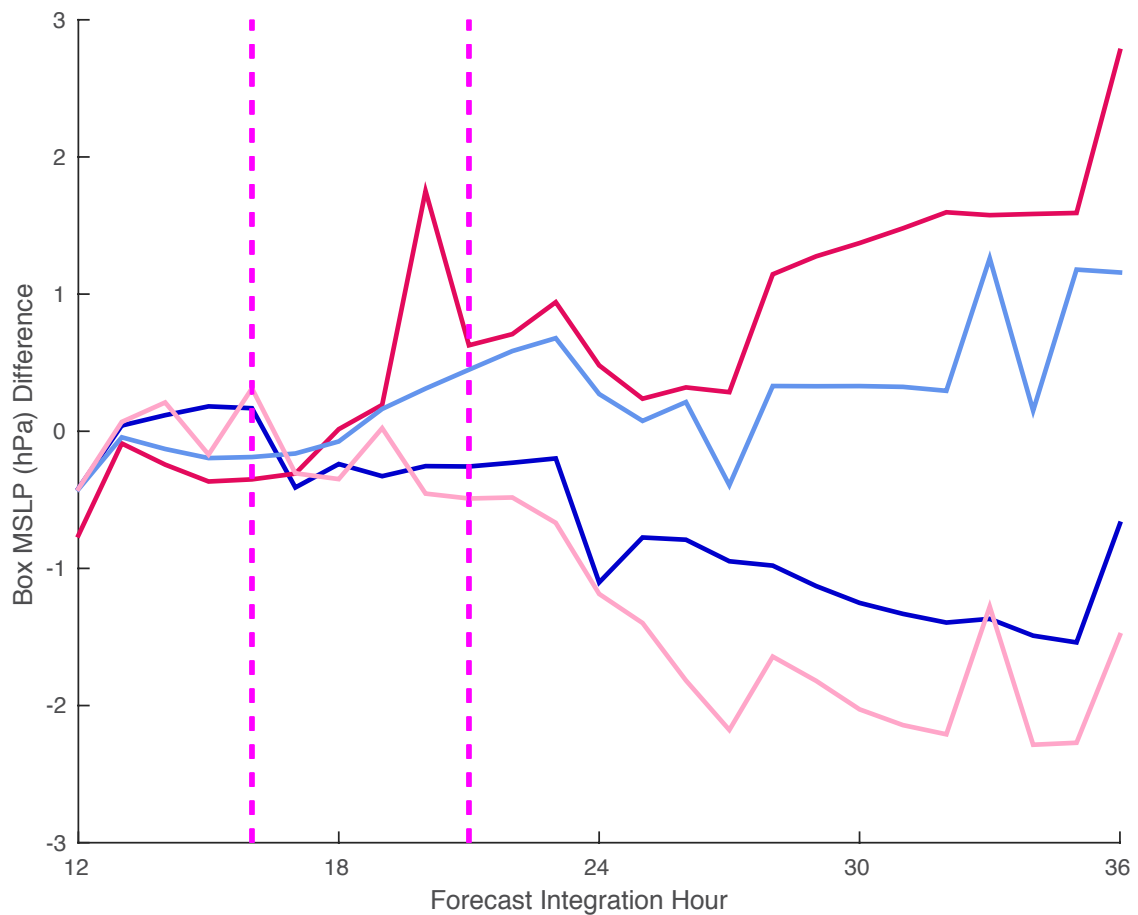


Figure 4.11. j15 simulation cyclone-following time series of the 9° by 9° box-mean sea level pressure difference between the control simulation and the increased intensification rate perturbation simulation (IIR; dark blue); reversed sign intensification rate perturbation simulation (RIIR; light blue); decreased intensification rate perturbation simulation (DIR; red); and reversed sign decreased intensification rate perturbation simulation (RDIR; pink). The magenta, vertical bars indicate the response period over which changes to the intensification rate by the QOIP to the analysis are intended.

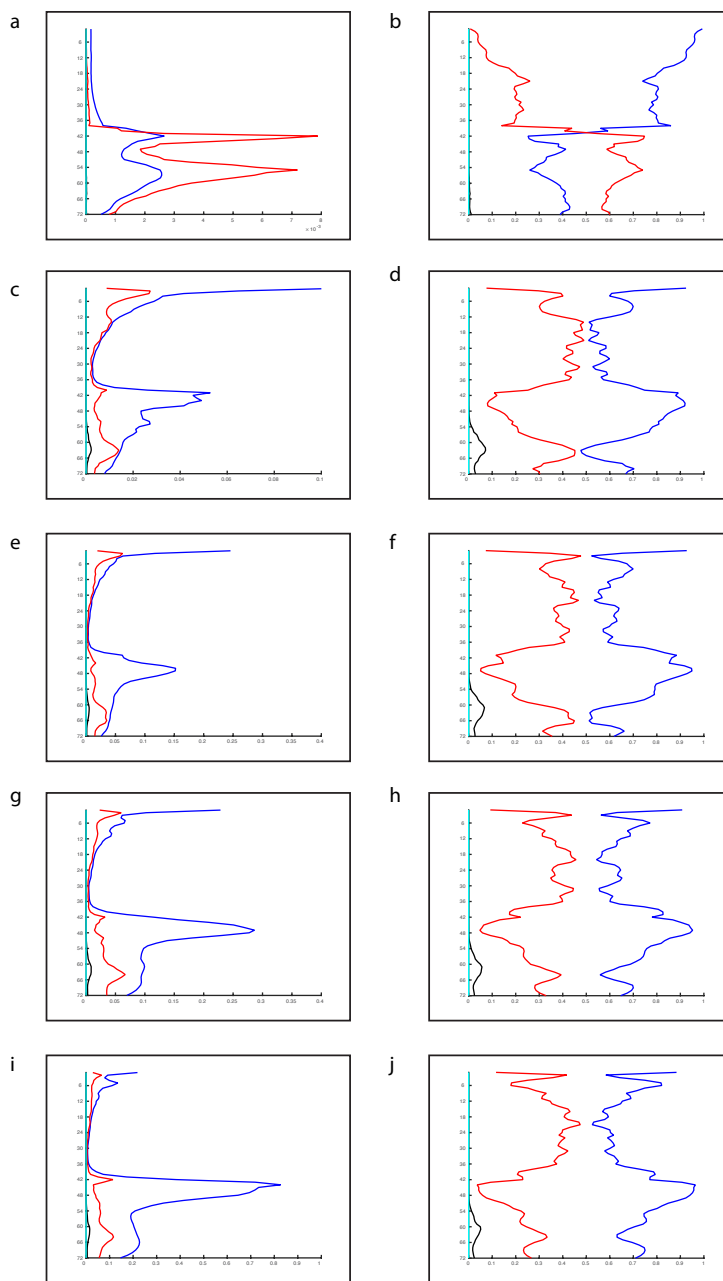


Figure 4.12. Non-normalized vertical perturbation profiles for the SSS-IIR case valid at (a) F000; (c) F006; (e) F012; (g) F017 – beginning of the response period; (i) F024 – end of response period. Vertical perturbation profiles normalized by the sum of the total energy (e.g., the sum of the components) valid at (b) F000; (d) F006; (f) F012; (h) F017 – beginning of the response period; (j) F024 – end of response period. The components of the energy are colored as blue – kinetic energy; red – available potential energy; black – elastic energy; cyan – moist energy. Energy components are computed by taking the mean of the component values on every level.

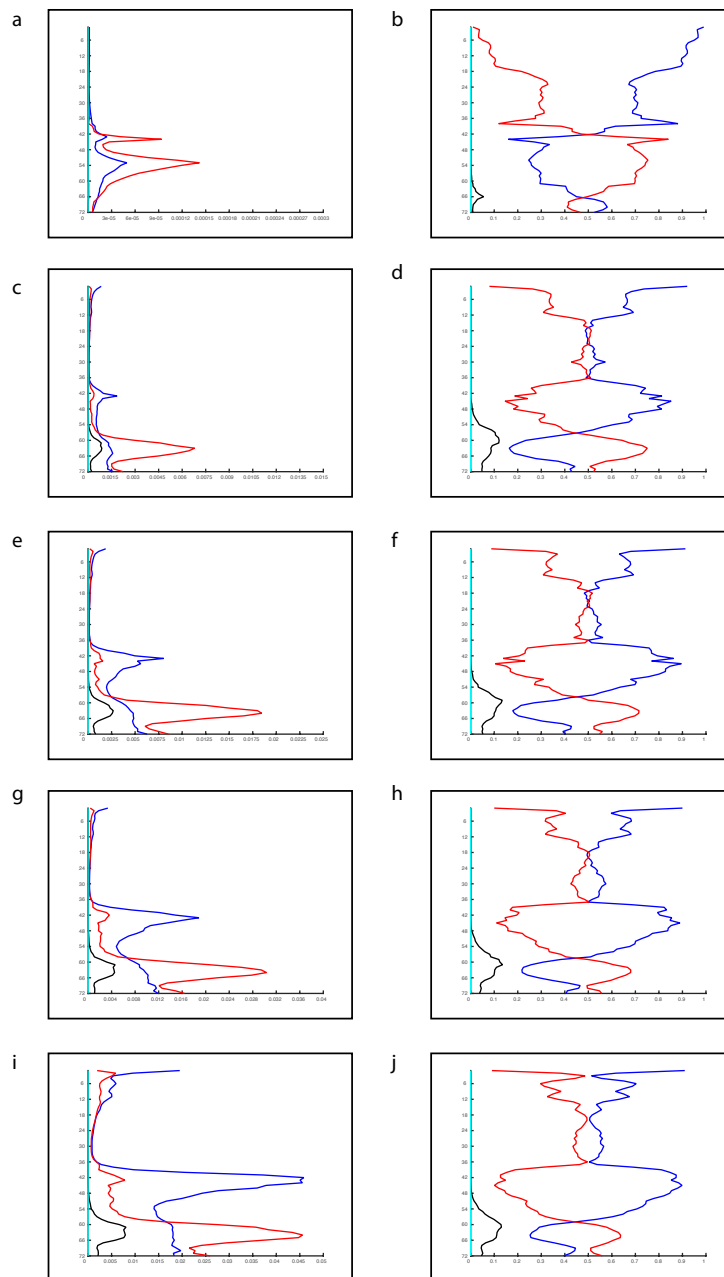


Figure 4.13. Non-normalized vertical perturbation profiles for the SOTC-IIR case valid at (a) F000; (c) F006; (e) F012; (g) F017 – beginning of the response period; (i) F024 – end of response period. Vertical perturbation profiles normalized by the sum of the total energy (e.g., the sum of the components) valid at (b) F000; (d) F006; (f) F012; (h) F018 – beginning of the response period; (j) F027 – end of response period. The components of the energy are colored as blue – kinetic energy; red – available potential energy; black – elastic energy; cyan – moist energy. Energy components are computed by taking the mean of the component values on every level.

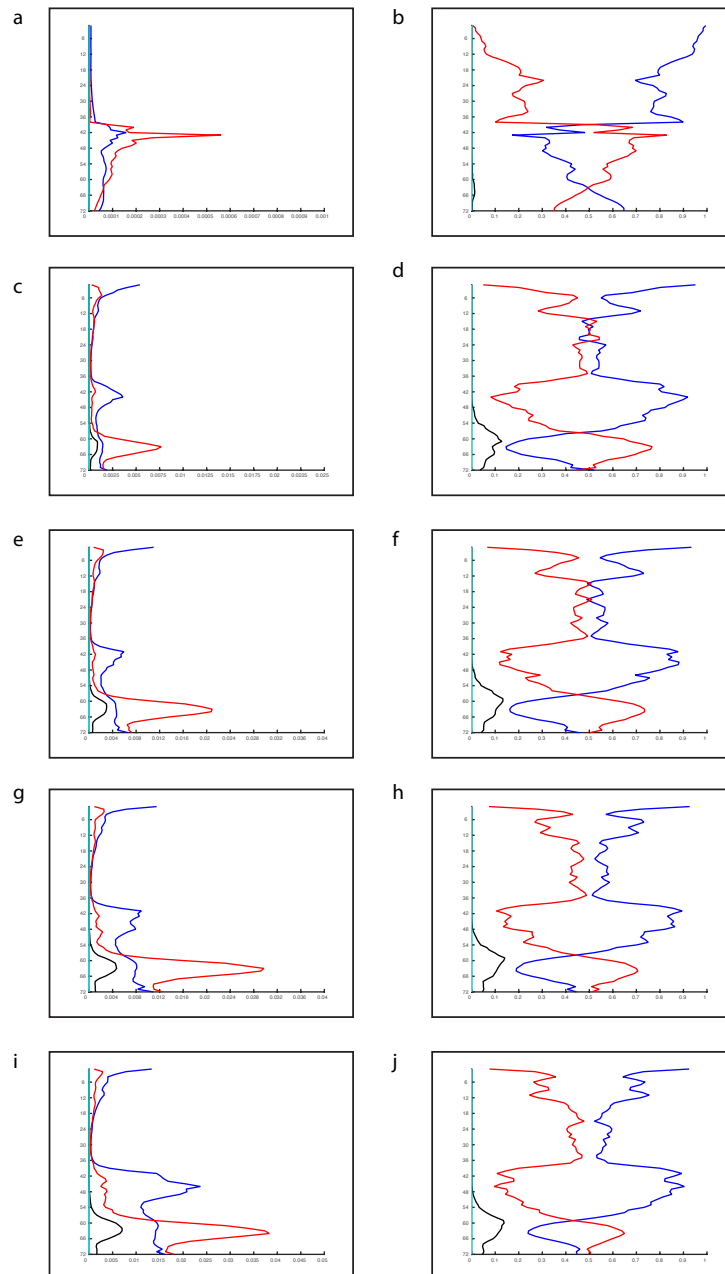


Figure 4.14. Non-normalized vertical perturbation profiles for the j15-IIR case valid at (a) F000; (c) F006; (e) F012; (g) F016 – beginning of the response period; (i) F021 – end of response period. Vertical perturbation profiles normalized by the sum of the total energy (e.g., the sum of the components) valid at (b) F000; (d) F006; (f) F012; (h) F017 – beginning of the response period; (j) F024 – end of response period. The components of the energy are colored as blue – kinetic energy; red – available potential energy; black – elastic energy; cyan – moist energy. Energy components are computed by taking the mean of the component values on every level.

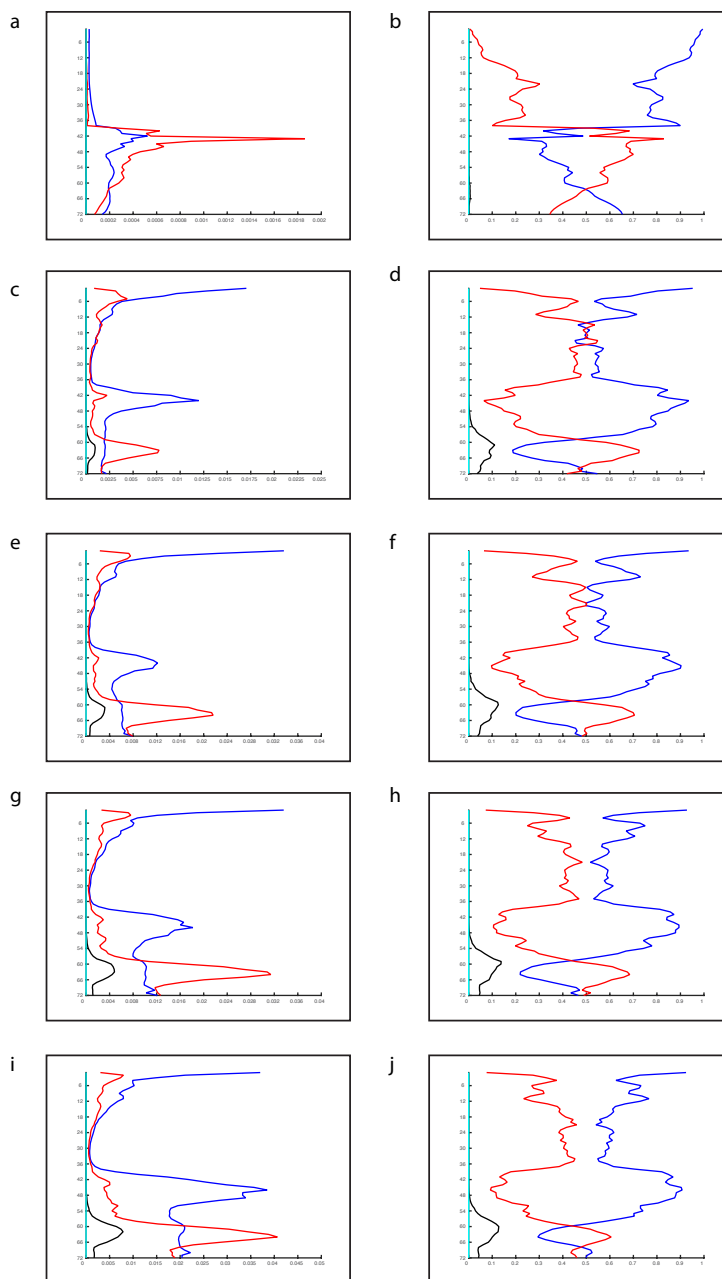


Figure 4.15. Non-normalized vertical perturbation profiles for the j15-DIR case valid at (a) F000; (c) F006; (e) F012; (g) F016 – beginning of the response period; (i) F021 – end of response period. Vertical perturbation profiles normalized by the sum of the total energy (e.g., the sum of the components) valid at (b) F000; (d) F006; (f) F012; (h) F017 – beginning of the response period; (j) F024 – end of response period. The components of the energy are colored as blue – kinetic energy; red – available potential energy; black – elastic energy; cyan – moist energy. Energy components are computed by taking the mean of the component values on every level.

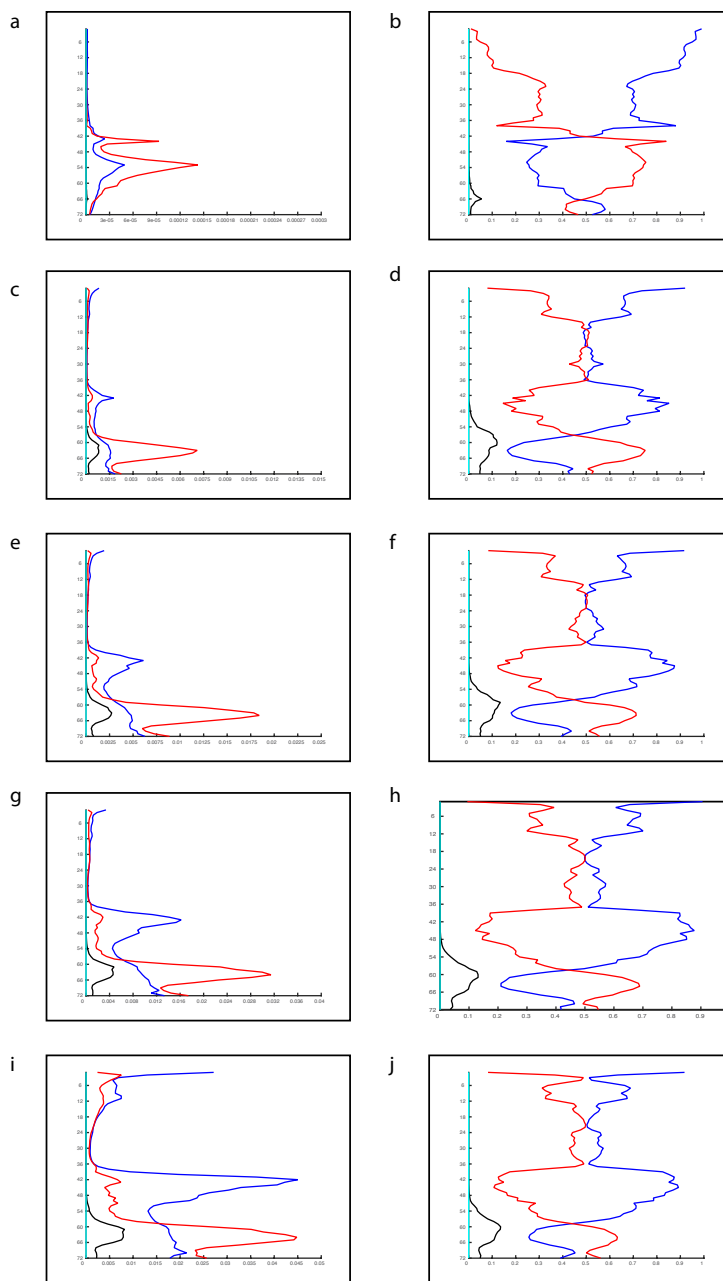


Figure 4.16. Non-normalized vertical perturbation profiles for the SOTC-DIR case valid at (a) F000; (c) F006; (e) F012; (g) F018 – beginning of the response period; (i) F027 – end of response period. Vertical perturbation profiles normalized by the sum of the total energy (e.g., the sum of the components) valid at (b) F000; (d) F006; (f) F012; (h) F017 – beginning of the response period; (j) F024 – end of response period. The components of the energy are colored as blue – kinetic energy; red – available potential energy; black – elastic energy; cyan – moist energy. Energy components are computed by taking the mean of the component values on every level.

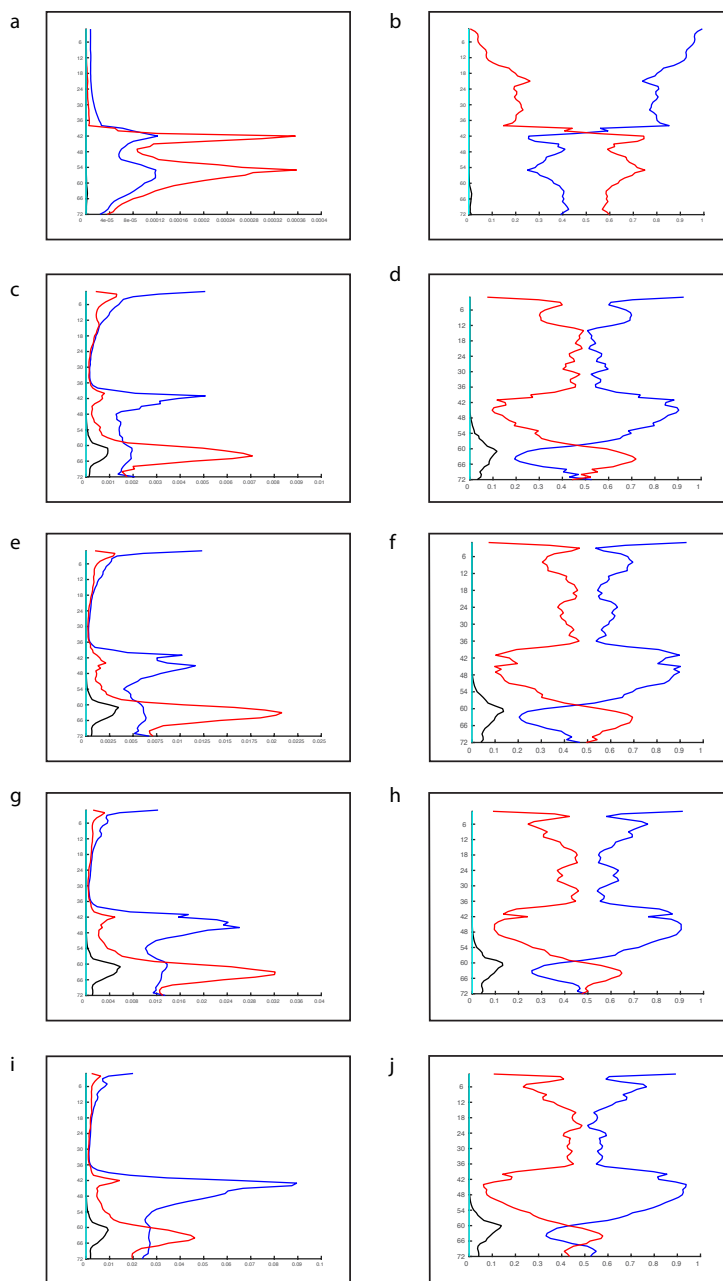


Figure 4.17. Non-normalized vertical perturbation profiles for the SSS-DIR case valid at (a) F000; (c) F006; (e) F012; (g) F017 – beginning of the response period; (i) F024 – end of response period. Vertical perturbation profiles normalized by the sum of the total energy (e.g., the sum of the components) valid at (b) F000; (d) F006; (f) F012; (h) F017 – beginning of the response period; (j) F024 – end of response period. The components of the energy are colored as blue – kinetic energy; red – available potential energy; black – elastic energy; cyan – moist energy. Energy components are computed by taking the mean of the component values on every level.

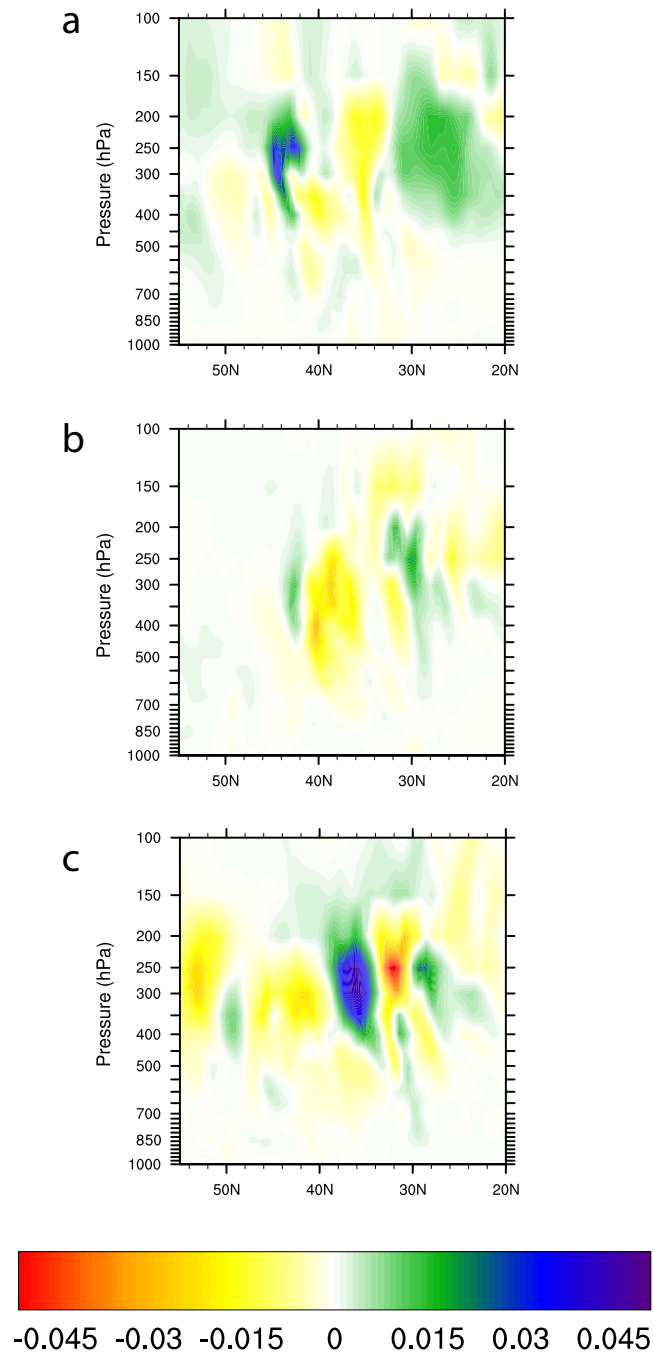


Figure 4.18. Cross section of the analysis time zonal-mean BEC from 60°W to 100°W longitude and 20°N to 55°N latitude (fill; $\text{m}^2 \text{s}^{-3}$) for the (a) SSS-IIR; and (b) SOTC-IIR and (c) j15-IIR. Initial time BEC rates for IIR and RIIR (DIR and RDIR) are similar, and therefore not shown.

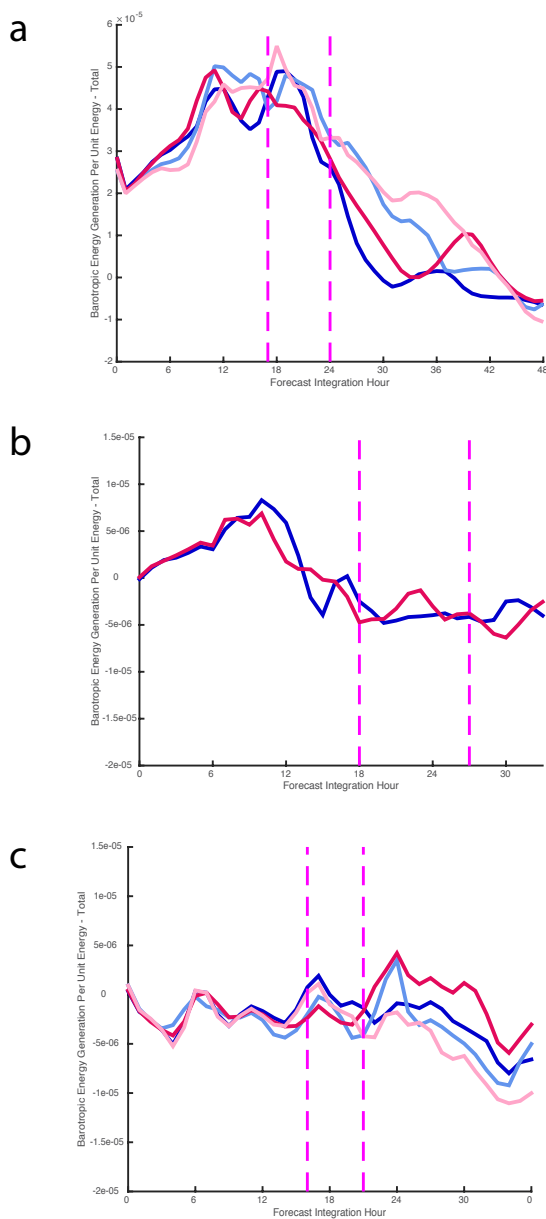


Figure 4.19. Time series of BEC normalized by the total kinetic energy (s^{-1}) over the course of the forecast integrations for the reversed sign intensification rate perturbation simulation (IIR; dark blue); reversed sign intensification rate perturbation simulation (RIR; light blue); decreased intensification rate perturbation simulation (DIR; red); and reversed sign decreased intensification rate perturbation simulation (RDIR; pink). BEC rates in shown are (a) SSS (calculated and summed over a 400 hPa to 150 hPa layer); (b) SOTC (calculated and summed over a 600 hPa to 150 hPa layer); and (c) j15 (calculated and summed over a 400 hPa to 150 hPa layer). The magenta, dashed vertical bars indicate the response period over which changes to the intensification rate by the QOIP to the analysis are intended. Note that SOTC failed the linearity test within the QOIP algorithm after the first iteration for each case, resulting in only one iteration for both the IIR and DIR simulations. Therefore, no additional RIIR and DIIR simulations were performed.

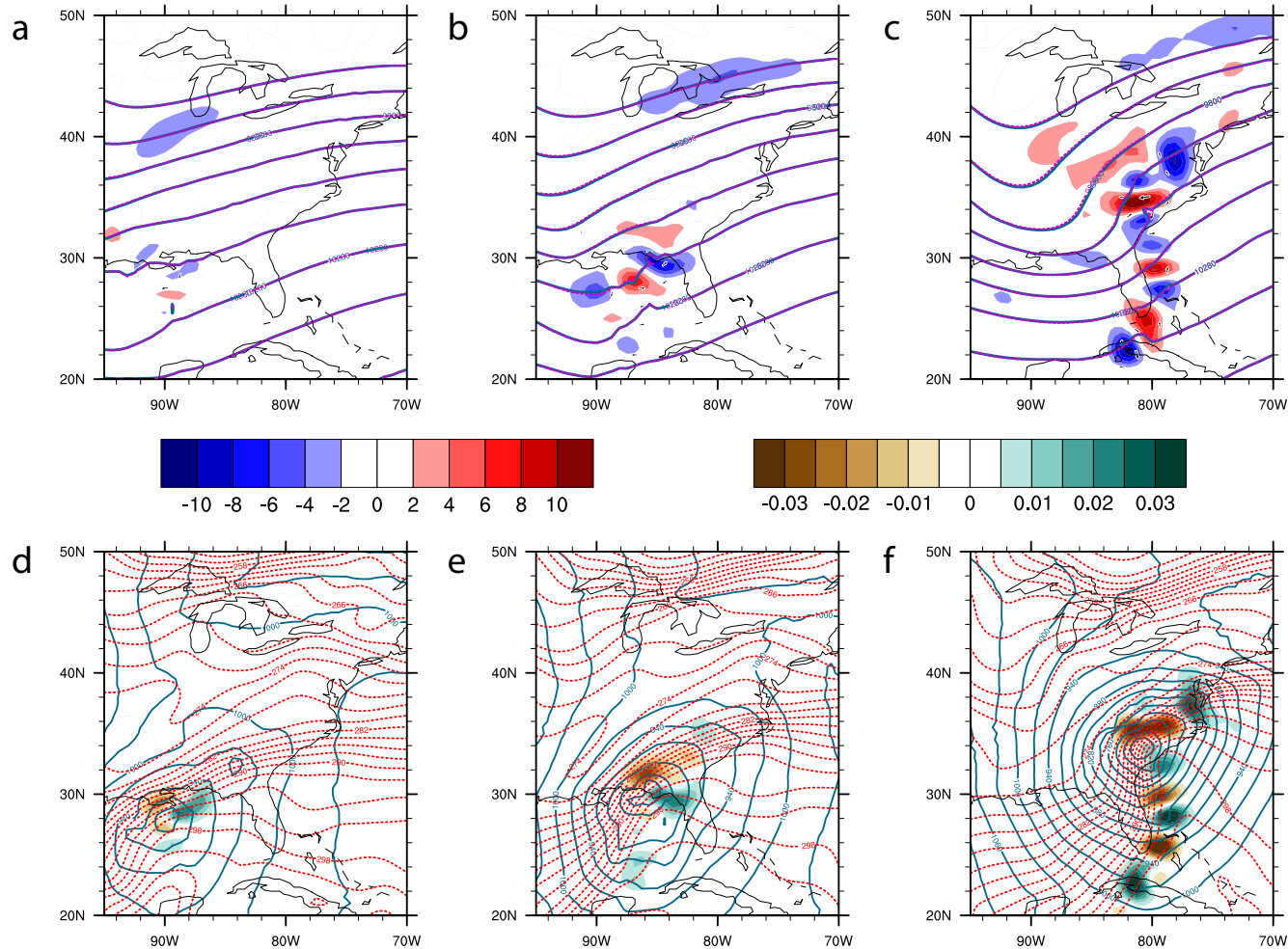


Figure 4.20. SOTC-IIR upper level QGPV perturbations (red to blue fill; 10^5 s^{-1}); control simulation height (magenta, dashed contour; m); perturbed simulation height (dark blue, solid contour; m); and inverted geostrophic wind (vectors; m s^{-1}); valid at (a) F012; (b) F18; and (c) F27 and large-scale precipitation perturbations (brown to green fill; in hr^{-1}); control simulation height (dark green solid contours, dashed contour; m); and control simulation theta (red, dashed contour; m) valid at (d) F012; (e) F18; and (f) F27. QGPV perturbations are largely coincident with large-scale precipitation perturbations, indicating the important on diabatic effects on the QGPV perturbations. Wind less than 5 m s^{-1} is masked.

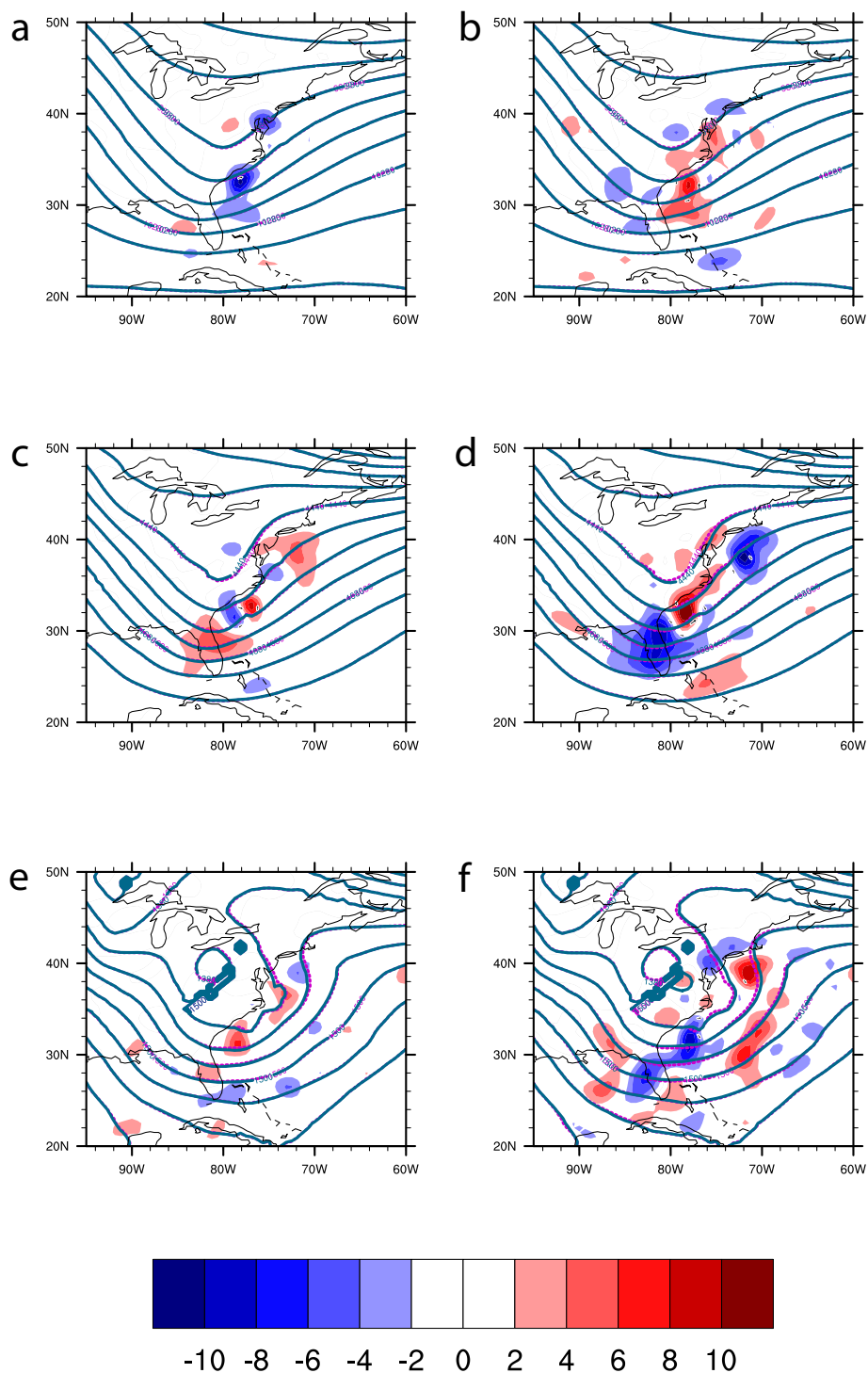


Figure 4.21. j15 layer averaged QGPV perturbations (fill; 10^5 s^{-1}); control simulation height (magenta, dashed contour; m); perturbed simulation height (dark blue, solid contour; m); and inverted geostrophic wind (vectors; m s^{-1}); valid at 16 hours into the simulation for (left) the IIR experiment, and (right) the RIIR experiment, for (top) the upper-troposphere, (middle) the middle-troposphere, and (bottom) the lower-troposphere. Note that lower-tropospheric contours in panels (c) and (f) intersect high terrain. Wind less than 5 m s^{-1} is masked.

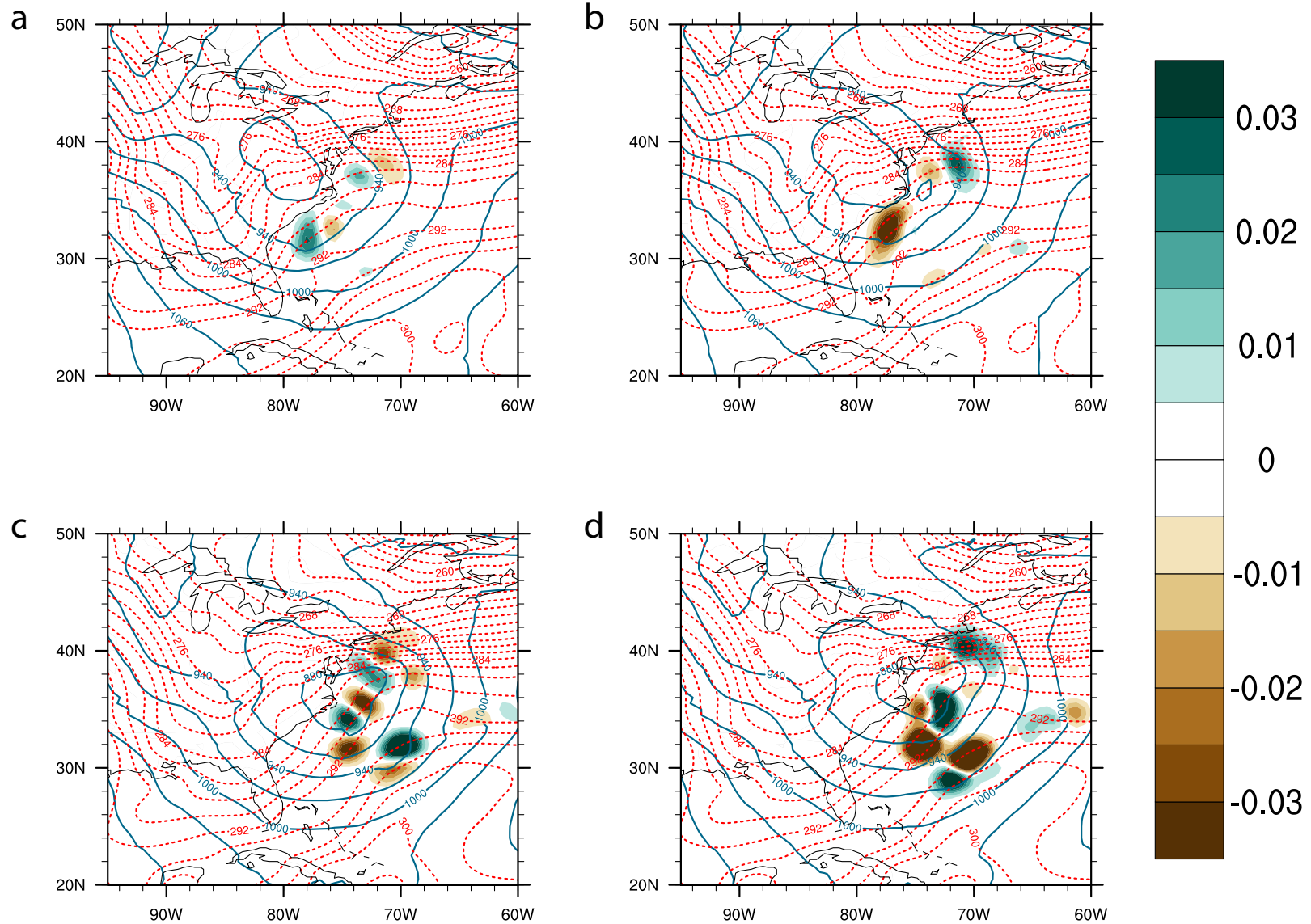


Figure 4.22. j15 large-scale (fill; in hr^{-1}); control simulation height (magenta, dashed contour; m); and perturbed simulation height (dark blue, solid contour; m) precipitation perturbations valid for (a) F016 – IIR; (b) F016 – DIR; (c) F021 – IIR; (d) F021 – DIR.

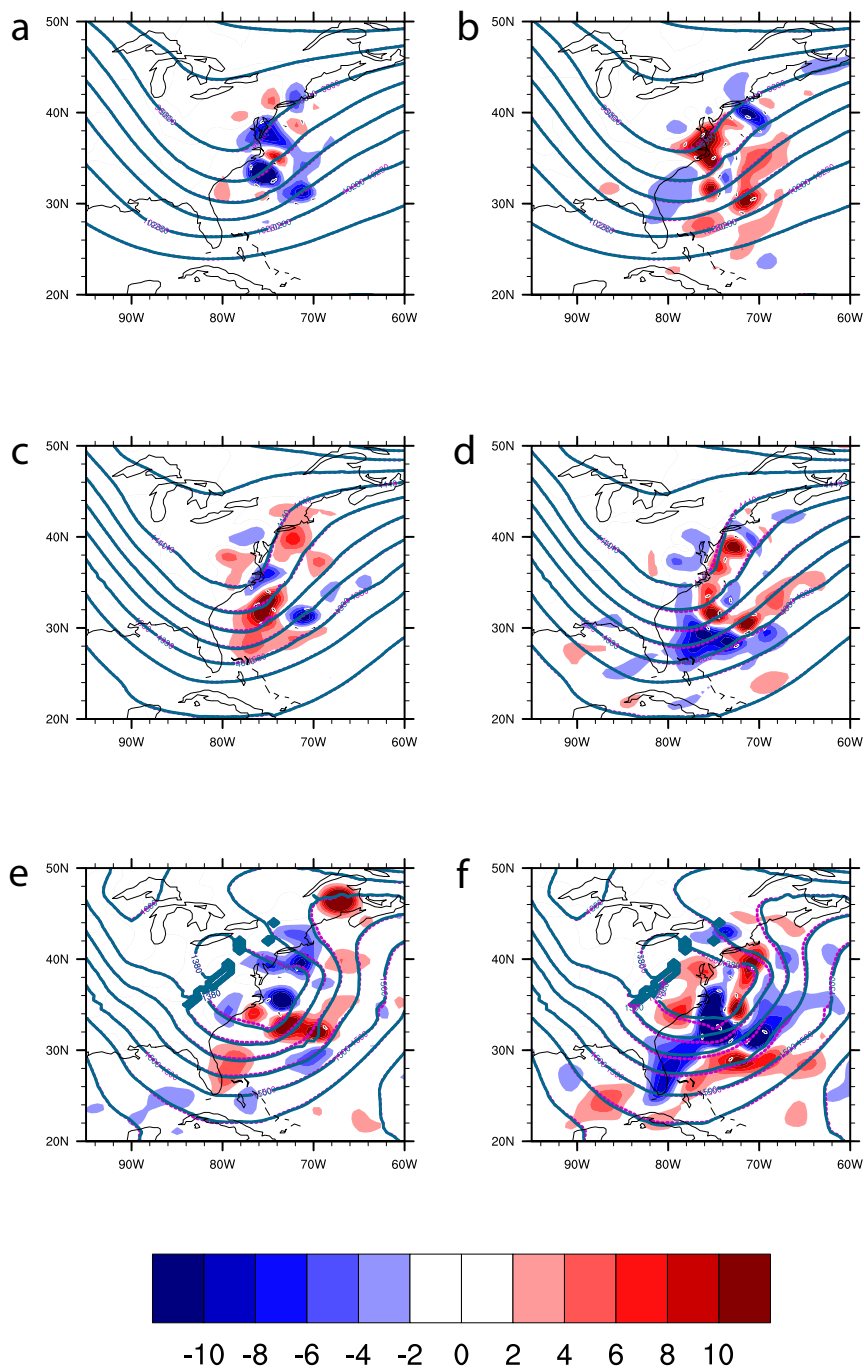


Figure 4.23. j15 layer averaged QGPV perturbations (fill; 10^5 s^{-1}); control simulation height (magenta, dashed contour; m); perturbed simulation height (dark blue, solid contour; m); and inverted geostrophic wind (vectors; m s^{-1}); valid at 21 hours into the simulation for (left) the IIR experiment, and (right) the RIIR experiment, for (top) the upper-troposphere, (middle) the middle-troposphere, and (bottom) the lower-troposphere. Note that lower-tropospheric contours in panels (c) and (f) intersect high terrain. Wind less than 5 m s^{-1} is masked.

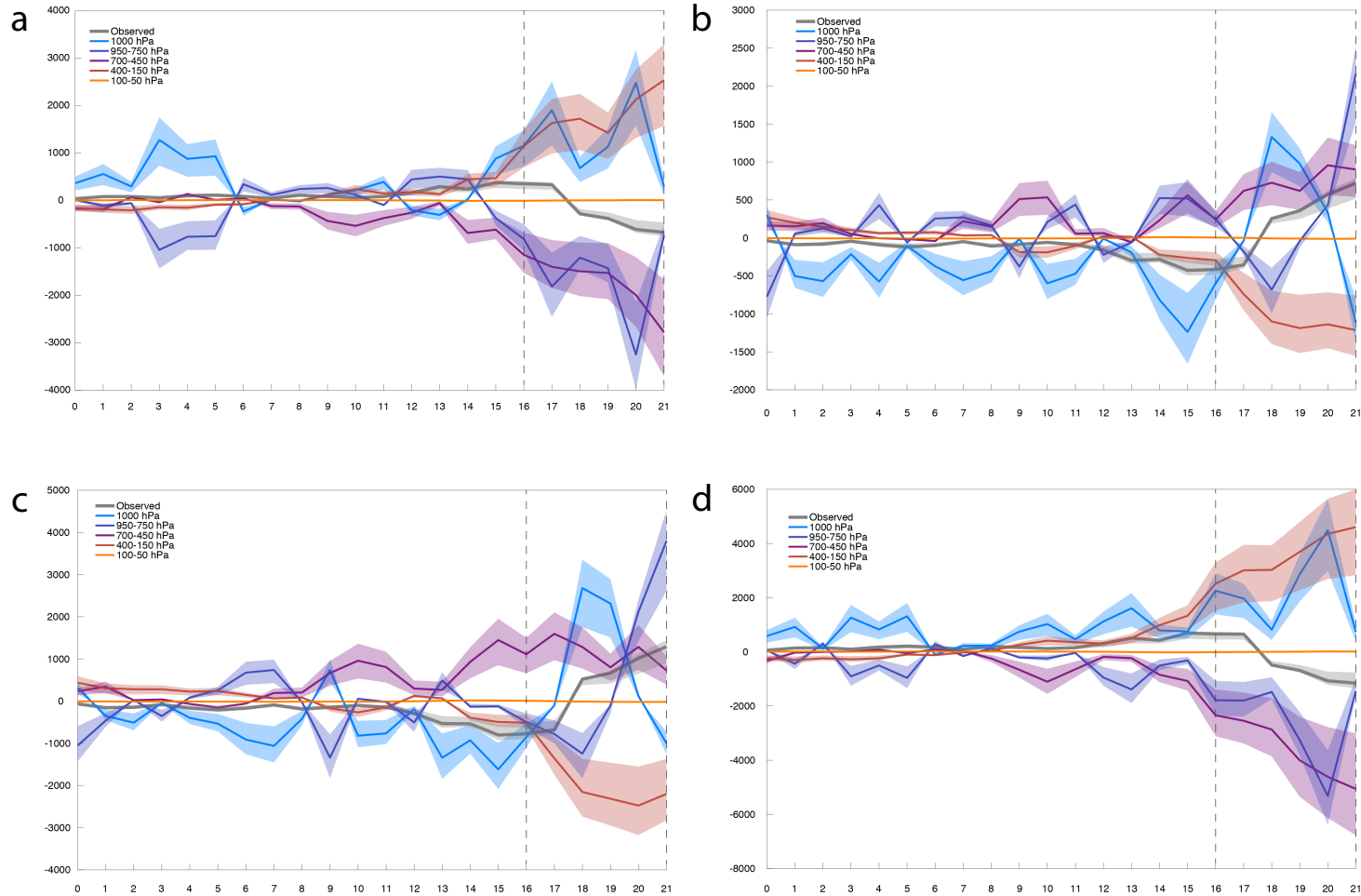


Figure 4.24: j15 control-simulation-cyclone-following summed 900 hPa inverted height perturbations for the (a) IIR; (b) RIIR; (c) DIR; and (d) RDIR cases. The solid lines colored as labeled represent the sum of the perturbations within a 9° by 9° box. The lines are bound within traces of summed 7° by 7° and 11° by 11° boxes. The observed contour is computed as the 900 hPa perturbation height difference between the perturbed and control simulations. The integration time is found on the abscissa with the gray, dashed lines representing the goal-post times of the response period. The summed perturbation values are found along the ordinate.

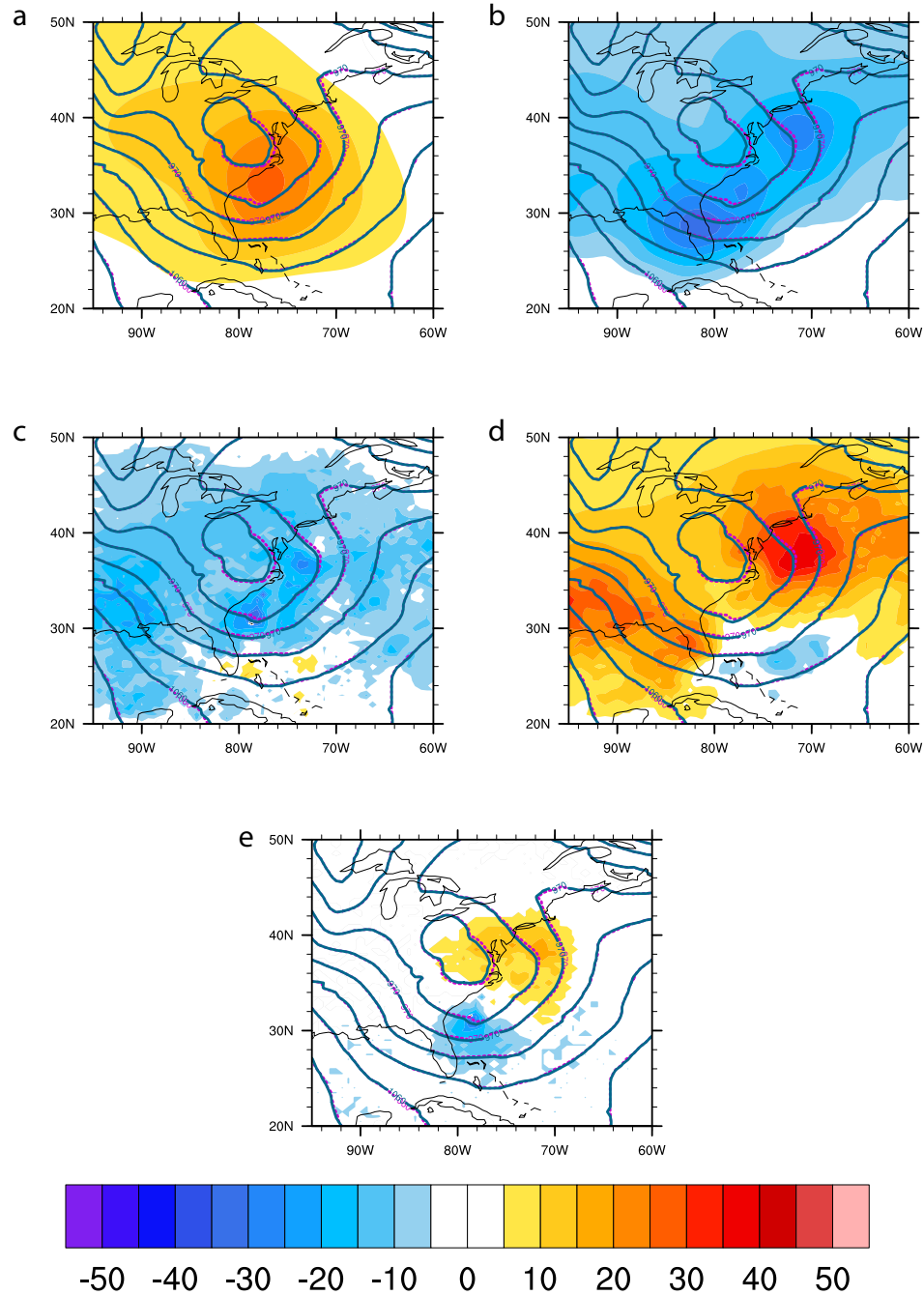


Figure 4.25. j15 – IIR piecewise 16-hr 900 hPa inverted height perturbations (fill; m); inverted wind (vectors; m s^{-1}); control simulation height (magenta, dashed contour; m); and perturbed simulation height (dark blue, solid contour; m) for (a) upper-level; (b) mid-level; (c) lower-level; (d) surface QGPV; and (e) total inversions. Wind less than 5 m s^{-1} is masked.

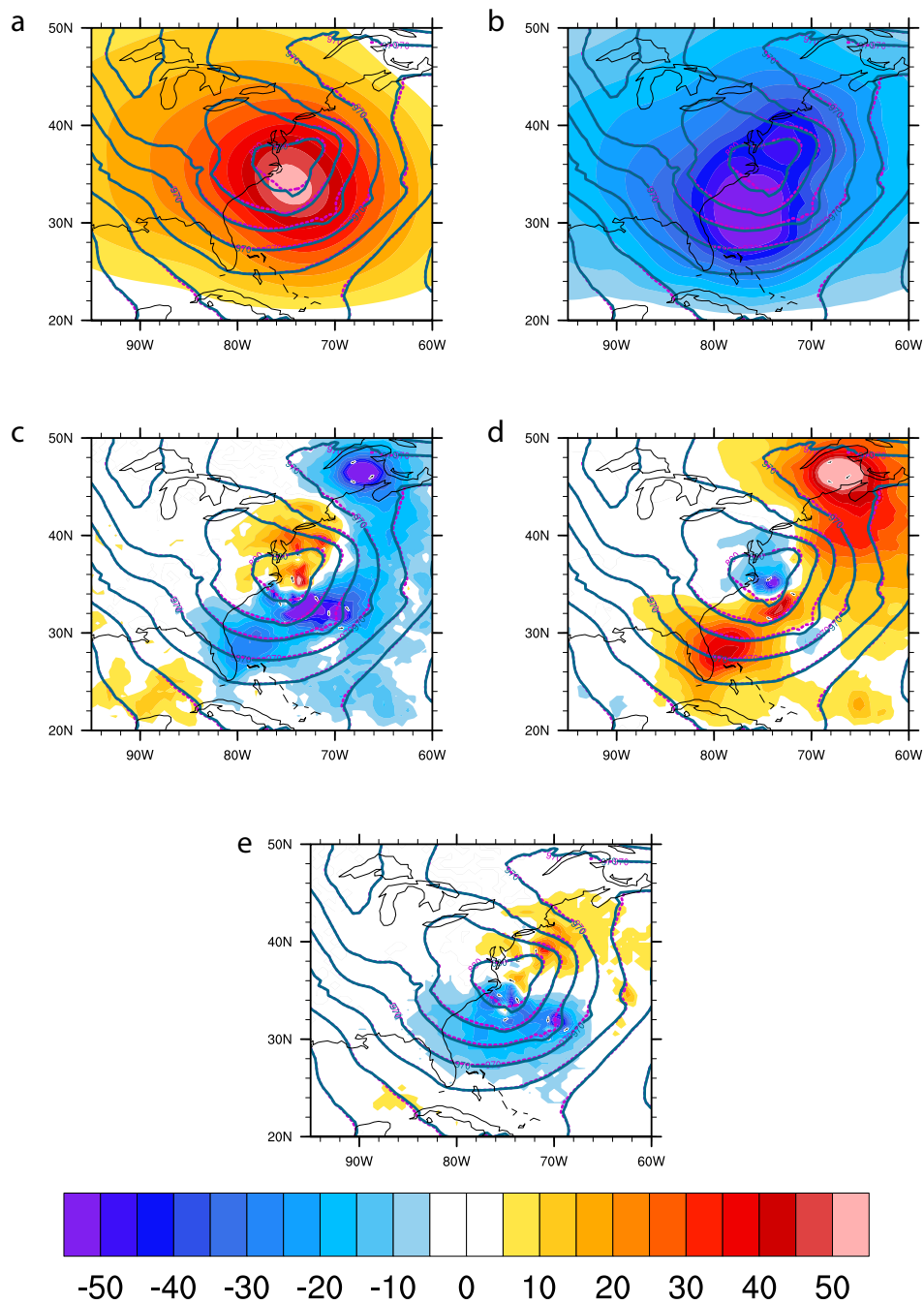


Figure 4.26. j15 – IIR piecewise 21-hr 900 hPa inverted height perturbations (fill; m); inverted wind (vectors; m s⁻¹); control simulation height (magenta, dashed contour; m); and perturbed simulation height (dark blue, solid contour; m) for (a) upper-level; (b) mid-level; (c) lower-level; (d) surface QGPV; and (e) total inversions. Wind less than 5 m s⁻¹ is masked.

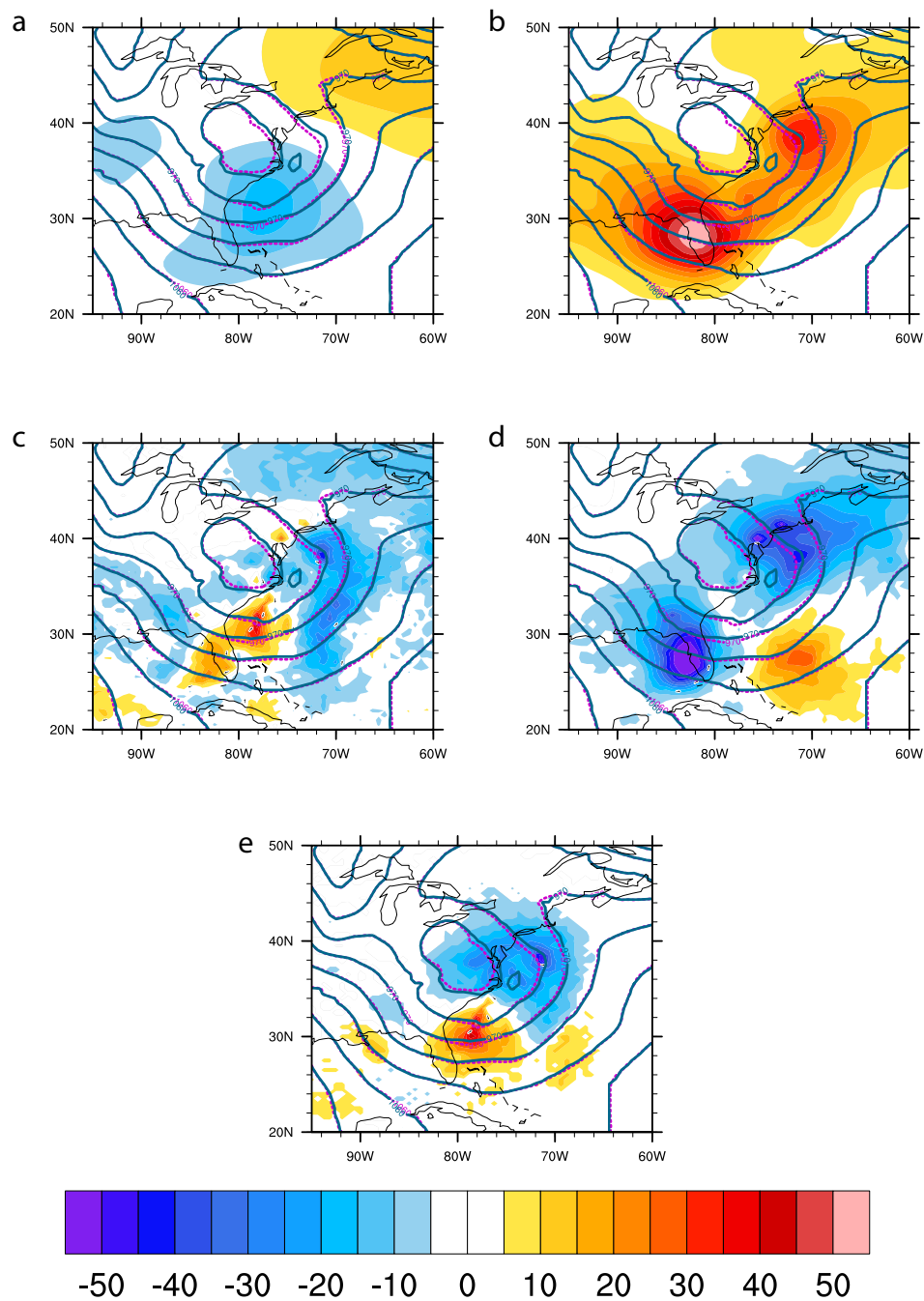


Figure 4.27. j15 – DIR piecewise 16-hr 900 hPa inverted height perturbations (fill; m); inverted wind (vectors; m s^{-1}); control simulation height (magenta, dashed contour; m); and perturbed simulation height (dark blue, solid contour; m) for (a) upper-level; (b) mid-level; (c) lower-level; (d) surface QGPV; and (e) total inversions. Wind less than 5 m s^{-1} is masked.

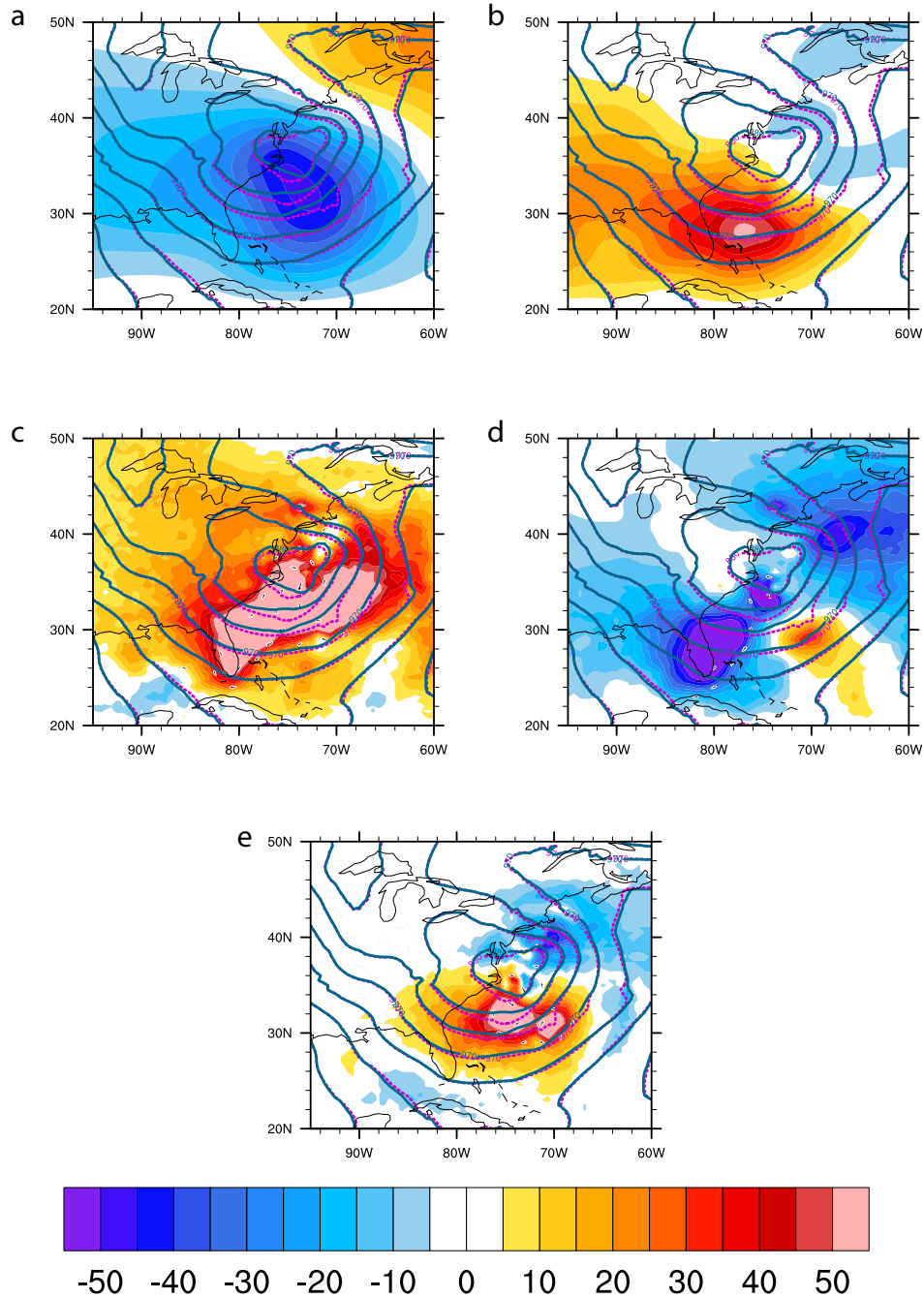


Figure 4.28. j15 – DIR piecewise 21-hr 900 hPa inverted height perturbations (fill; m); inverted geostrophic wind (vectors; m s^{-1}); control simulation height (magenta, dashed contour; m); and perturbed simulation height (dark blue, solid contour; m) for (a) upper-level; (b) mid-level; (c) lower-level; (d) surface QGPV; and (e) total inversions. Wind less than 5 m s^{-1} is masked.

Chapter 5: Conclusions and Directions for Future Work

5.1 Background

Rapidly-intensifying mid-latitude cyclones are a meteorological phenomenon of great consequence to the eastern seaboard of the United States. While not exclusive to this region, the large population centers along the eastern US coast amplify the societal impacts of the strong wind, heavy precipitation, flooding and significant coastal erosion attendant to this class of cyclones. Amongst the biggest challenges for meteorologists tasked with forecasting these high-impact events are the accurate prediction of rapid-intensification phase, a period within the cyclone's lifecycle in which the largest impacts are often felt.

Although a multitude of sensitivity studies have been previously performed in order to better understand the governing dynamics of rapidly-intensifying mid-latitude cyclones, these studies have either been performed such that they assess subjectively-based sensitivities such as sensitivity to model parameterization (e.g., Mullen and Baumhefner 1988; Mailhot and Chouinard 1989) or employ an adjoint- or ensemble-based sensitivity approach in which the response function used identifies cyclone intensity at a static point in time within the life-cycle of the simulated cyclone (e.g., Doyle et al. 2014; Chu et al. 2016). This study has sought to identify the governing dynamics of mid-latitude cyclone intensification rates by: 1) identifying a new response function that objectively and explicitly assesses the sensitivity of the time-rate-of-change of cyclone intensity; 2) devise a method for the relaxation of the tangent-linear assumption that is used in adjoint-derived sensitivity calculations so as to minimize the impact of changes to the intensification rate due to small-scale, non-linear processes; and 3) understand how these perturbations impact the predictability of an event.

5.2 Introduction of New Methodologies

5.2.1 A Time-Rate-of-Change of Surface Pressure Response Function

In order to assess the governing dynamics that modulate the intensification rates of mid-latitude cyclones, it was necessary to formulate a response function that would create objective, adjoint-derived sensitivity gradients for the intensification rate of a mid-latitude cyclone. Following the framework of Hoover (2015), a response function that describes the instantaneous intensity of a cyclone was selected as the average perturbation pressure within a box surrounding a cyclone at the lowest (hybrid-sigma) model level, described in Section 2.1.2 (eqn. 2.4). Unlike response functions that define the intensity at a single model grid-point (e.g., Langland et al. 1995; Ancell and Hakim 2007) or define intensity using average vorticity in a box (e.g., Kleist and Morgan 2005a), the lowest model level perturbation pressure response function is advantageous in that it represents the intensity of the cyclone while remaining largely insensitive to both small shifts in the location of the minimum in (lowest model level) perturbation pressure or small interactions between adjacent vortices. This response function also removes the ambiguity found in kinetic energy based response functions, in which it can be difficult to ascertain whether the response to initial-time perturbations is due to actual cyclone intensity changes or simply changes to nearby geopotential gradients.

While the above response function(s) are useful, they lack the time component necessary to make direct assertions about the intensification *rate* versus the intensity at a given point in the forecast trajectory. In order to do this, a response function that measures the time-rate-of-change in cyclone intensity was devised. As the sensitivity

gradients are explicitly linear in nature, it is possible to perform a simple temporal centered-difference approximation of the sensitivity of intensity of the cyclone at two static points in time within the forecast trajectory. In order to do this, a non-linear, forward trajectory was defined, and the adjoint run backwards in time at two “goalpost” times that encapsulated a period of intensification (termed the “response period”). The temporal finite-difference of the two sensitivity gradients was then calculated, as described in Section 2.1.2 (eqns. 2.5 and 2.6). The resulting sensitivity gradient is one that objectively and explicitly describes how small changes to the analysis-state will impact the intensification rate of the cyclone during the response period.

5.2.2 “Perturbation-Response” and the QOIP

While calculating the sensitivity of the intensification rate of a cyclone is useful, it yields information pertaining to the *hypothetical* change to the response function given perturbations that project onto the initial-time sensitivity gradients. Therefore, one can create perturbations to the initial-state and quantitatively measure their (non-)linear response. Within this “perturbation-response” framework, it is possible to gain significant insight into both the governing dynamics of the phenomenon in question, as well as assess the overall linearity of the system being investigated.

As any *optimal* perturbation that is created based upon adjoint-derived sensitivity gradients is implicitly constrained by the tangent-linear assumption, they can only modulate the response function within highly linear regimes. In order to circumvent this problem, an iterative method for the calculation of perturbations was devised. This method, known as the *quasi-optimal iterative perturbation* (QOIP) method, allows for the

calculation of perturbations using a multiple loop mechanism similar in spirit to that which is used in incremental four-dimensional variational data assimilation (4DVAR; Tremolet 2007). QOIP structures that are aimed at making a prescribed change to the response function are computed as the sum of small, optimally derived perturbations (as in Section 2.1.3) that are calculated based upon an iterative algorithm described in Section 2.1.4. Unlike effectively “single-loop” (optimal or subjective) perturbations in which non-linear processes tend to mute the total response, the formulation of QOIP structures are able to create a greater change to the response function by making small, incremental changes with multiple updates to the nonlinear trajectory and re-calculation of adjoint-derived sensitivity gradients, rather than attempting to make one large change from one set of sensitivity gradients computed along one nonlinear trajectory. The QOIP method, in conjunction with the “perturbation-response” framework, has proven tremendously useful in understanding the governing dynamics that modulate changes to the intensification rate of mid-latitude cyclones, a phenomenon that is known to rely heavily on small-scale, non-linear interactions (Anthes et al. 1983; Uccellini 1990). Additionally, the QOIP method allows for insight into the predictability of changes to the intensification rate, as the ability for large (small) changes to the response function by the QOIP is indicative of lower (higher) levels of predictability.

5.2.3 Piecewise Inversion of QOIP Quasi-Geostrophic Potential Vorticity

Though the analysis of perturbation structures is useful in the investigation of the governing dynamics of meteorological phenomena in and of itself, this type of analysis does not necessarily lend itself to a complete understanding of the full, three-dimensional

evolution of the system being investigated. Furthermore, it is often advantageous to analyze the evolution of the system in question through the lens of a conserved, dynamical variable such as potential vorticity (PV). The question of cyclogenesis and cyclone evolution is especially well-suited to be viewed through this lens, making the use of PV within this investigation especially appropriate. Although there are two main formulations for PV, the *quasi-geostrophic* potential vorticity (QGPV) formulation is chosen for this study. Although QGPV suffers from some shortcomings as compared to the Ertel's PV (EPV) formulation, particularly within regions characterized by higher Rossby number flows, it is appealing in its simplicity and correlates well with EPV when compared side-by-side.

Given a three-dimensional distribution of QGPV, as well as a set of boundary conditions specified along the lateral and top and bottom boundaries, one can invert the QGPV to recover the associated balanced mass and momentum fields. Furthermore, as first shown in Emanuel and Davis (1991), it is possible to perform a *piecewise* QGPV inversion (e.g., Hakim et al. 1996; Morgan 1999; Korner and Martin (2000)). While past studies (e.g., Breeden and Martin 2018) have defined the perturbation QGPV as a deviation from a time-mean state, this study introduces the inversion of the QGPV calculated from the QOIP itself, with the mean-state defined by the instantaneous QGPV of the control forecast. By performing a piecewise inversion of the QOIP, it is possible to gain an understanding of the *exact* contributions made by the QOIP to the balanced fields, an aspect largely missing within the traditional diagnosis of sensitivity or perturbation structures.

5.3 Summary of Results

As laid out in Section 1.4, the main motivation for this investigation can be summarized by four fundamental research questions (*RQ1-RQ4*) relating to the modulation of the intensification rate of mid-latitude cyclones within an adjoint-derived “perturbation-response” framework, as well as implications on predictability. In order to test the new methodologies laid out in Section 5.2, three case studies were performed on cyclones that (subjectively) displayed a range in predictability in order to compare and contrast the character of the QOIP as well the resulting response.

It was successfully shown in Chapters 3 and 4 that the QOIP that were computed based upon the adjoint-derived sensitivity of the time-rate-of-change of cyclone intensity was successfully able to modulate the intensification rate of two of the three cyclones that were studied (satisfying *RQ2*). The largest changes to the intensification rate were achieved by the QOIP that were projected onto the analysis state for the “Surprise Snow Storm”, while a moderate response to the QOIP was noted for the late January 2015 northeast snow event. Both of these cases were characterized by a lack of predictability, with the former suffering from historically low levels of predictability. Conversely, the March 1993 “Storm of the Century”, a case that displayed remarkably high levels of predictability, was largely unchanged by an analysis-time QOIP.

It was shown that the character of the QOIP that impacts both the increase and decrease in intensification rate over the response period for all cases was largely flow dependent, with the cases that displayed more susceptibility to modulation by the QOIP being those in which the QOIP focused mainly on making changes to the momentum fields rather than the thermodynamic fields. This result is unsurprising, given that

changes to the thermodynamics fields typically result in a more non-linear response given the highly non-linear nature of precipitation processes strongly affected by perturbations to the thermodynamic fields, as well as the parameterized physics found within the GEOS-5 model used to represent them. Within the surprise snow storm case, the largest changes to the intensification rate were resultant from the reshaping of the upper-level precursor trough that helped initiate the surface cyclone, whereas the QOIP for the storm of the century case ultimately modulated the large-scale precipitation fields and resulted in virtually no change to the response function (satisfying RQI).

Those cases that suffered from a lower-level of predictability were also characterized by a larger impact by the QOIP. This is unsurprising, as a case that is highly susceptible to large modulation by small changes to the initial state is more likely to be unpredictable, as any observational uncertainty that is protected onto the analysis state may have a large impact on forecast uncertainty at a later time in the forecast. This impact, termed in Section 4.4.1 as the Forecast Elasticity (FE), presents a linearity paradox with significant implications on the relationship between the increased and decreased intensification rate QOIP. In order for the QOIP to achieve a large impact, it is necessary that the incremental changes to the QOIP that are created upon each iteration within the QOIP algorithm must meet a certain linearity criterion (as specified in Section 2.1.4). While this implies that each individual iteration must behave linearly, it can be seen in the surprise snow storm case that the impact on the response function is heavily skewed towards an increased intensification rate. This skewedness is attributed to the fact that the QOIP are formulated so that the incremental changes made by changing the new “control” trajectory iteration accounts for the non-linearity that results from changes to

the basic-state trajectory, which ultimately results in an asymmetric QOIP response. This implies that the dynamical system itself is non-linear, as a highly linear system would have a symmetric response about the control simulation (satisfying *RQ3* and *RQ4*). This is to be expected, as in changing the new trajectory in order to account for the intrinsic non-linearity, the forecast is pushed further away from the initial control forecast with each iteration, thus reducing the likelihood for a symmetric response to the perturbations with each additional iteration.

In order for the system to achieve high levels of linearity, the QOIP aimed at increasing and decreasing the intensification rates must be identical in magnitude and spatial distribution, but opposite in sign. This was largely the case within the January 2015 and Storm of the Century cases, which displayed little skewedness towards either the increased or decreased intensification rate directions. It is however noteworthy, that neither of these two cases achieved even half of the total iterations in either the increased or decreased intensification rate directions that the increased intensification rate surprise snow storm case achieved, indicating that each individual iteration within these two cases generally behaved less linearly than the individual iterations in the increased intensification rate surprise snow storm case. It can therefore be asserted that the linearity of a system as a whole, rather than that of any one individual QOIP iteration, has larger implications on the predictability of an event.

5.3.1. Broader Context

Within a larger scope, much of the work done herein fits within the current available literature on the deepening processes of mid-latitude cyclones. Similar to what

was shown with respect to sensitivity (which given the proportionality between the QOIP and adjoint-derived sensitivity can be looked at as relatively equivalent) of cyclone intensity by Kleist and Morgan (2005a) as well as Doyle et al. (2014), QOIP structures that were prescribed in order to increase the rate of intensification of the cyclone 1) grew rapidly during over the course of the non-linear integration; 2) appeared to reshape the mid- and upper-level pre-cursor disturbance in a manner that promoted baroclinic development; and 3) were initially oriented (vertically) upshear before being tilted downshear while converting background-state kinetic energy to eddy kinetic energy for growth of the cyclone. Doyle et al. (2014) further describes the relatively small impact on the modulation of cyclone intensity by initial time moisture perturbations, a finding that is further affirmed within this study. In these ways, it can be argued that many of the same processes that impact the intensity at a static point in the forecast trajectory have an impact upon the intensification rate.

Unlike the above described results however, which largely agree with the current literature pertaining to sensitivity studies of cyclone intensification, the results shown in section 3.5 pertaining to the idea of “barotropic preconditioning” appear to be largely contradictory to the currently accepted paradigm. While it is well understood that barotropic energy conversion (BEC) is a process that may have a large impact on the development and evolution of upper-level precursor disturbances that initiate surface cyclone development, Kucharski and Thorpe (2000; 2001) state explicitly that it is impossible to simulate these processes outside of the framework of idealized numerical simulations. It is shown in section 3.5 however that using the QOIP method it *is* possible to impose perturbations onto the analysis state of a real-world case study in a manner that

shows the propensity for “barotropic preconditioning” of the upper-level precursor disturbance in a manner that enhances later development of a surface cyclone.

Where the work performed herein largely differs from work performed previously is within the comparison between the QOIP prescribed in order to increase versus decrease the intensification rates of mid-latitude cyclones. Much of the current literature available today appears to focus solely upon increased intensification of these type of events, but does little to elucidate the processes that may be responsible for a decrease in intensification rate. It is shown within this work that 1) the response between perturbations prescribed to increase the intensification rate and those prescribed to decrease the intensification rate is largely non-linear (as described in section 5.3); and 2) the character of the perturbations prescribed to increase the intensification rate may be completely different than those prescribed to decrease the intensification rate (e.g., Surprise Snow Storm IIR QOIP largely augmented the dry, kinetic energy fields vs. the DIR QOIP augmenting the largely thermodynamically impacted available potential energy fields). This information may be useful in further studies and perhaps even to operational forecasters, as performing perturbation or sensitivity energy diagnostics may indicate the propensity for a system to realize greater (lesser) intensification rates than that which is represented within a forecast trajectory.

5.4 Future Directions for Research

5.4.1 Standardized Uncertainty Anomalies

While the method for the calculation of standardized uncertainty anomalies (SUA) is described in Section 2.3.1, it was not explicitly applied in this dissertation. It is

important however to touch upon this diagnostic in order to lay the groundwork for future efforts. When used in conjunction with dynamical sensitivity analysis, SUA is a useful tool in gaining insight into the predictability of a particular event with respect to a particular response function. Figs. 5.1a,b through 5.4a,b show the 500 hPa stream function²⁰ SUA as well as the single-loop, 500 hPa sensitivity of *static* cyclone intensity to the 500 hPa stream function (e.g., $\frac{\partial R_p}{\partial \psi_{500}}$; $R_p = \frac{\sum_{i,j \in D} p_s}{\sum_{i,j \in D} 1}$) for both the surprise snow storm and the storm of the century respectively, at both the analysis time and 36-hrs into the forecast. The 36-hr sensitivity is calculated by defining a control, non-linear simulation at 60-hrs, and running the adjoint backwards in time 24-hrs, resulting in the sensitivity of the 60-hr forecast state to the 36-hr forecast state. A schematic diagram of this process can be seen in Fig. 5.5.

By comparing the spatial distribution of the SUA with the sensitivity structures, it can be asserted that cases characterized by significant overlap of the two quantities will be those cases that suffer from issues of predictability. Keeping in mind that the SUA is intended to represent the *intrinsic uncertainty*²¹ within the atmosphere, it is the growth of this uncertainty that represents where the perturbations will have the largest impact on the forecast trajectory. Within regions where there is significant overlap, it can be surmised that variability within the atmosphere will project onto the sensitivity, resulting in

²⁰ The selection of stream function as a variable for investigation is merely used as an example. This type of diagnosis can be performed for any state or derived variable to which sensitivity of the response function can be calculated. In this instance, 500 hPa height is preferable, however sensitivity to height is not easily calculated, and therefore stream function is used as an analog.

²¹ It is noted that two different modeling systems are employed when comparing the SUA with the sensitivity gradients. This was necessary due to the lack of access to GEOS-5 ensemble data and/or GFS adjoint sensitivity data. As this is the case, the SUA is meant strictly to represent the *intrinsic uncertainty* within the atmosphere, and discounts any impact on the SUA by model formulation (e.g., physical parameterizations, dynamical core, etc.).

potentially large changes to the response function and a drop-off in predictability of the aspect of the forecast represented by the response function.

As is evident in Fig. 5.1a, b, there is significant overlap between the analysis time SUA and the sensitivity to the stream function, indicating that the system will likely be relatively unpredictable. Conversely, Figs. 5.2a, b; 5.3a, b and 5.4a, b, show that there is little overlap between the two quantities, indicating that at and beyond 36-hrs into the evolution of the surprise snow storm, as well as throughout the life cycle of the storm of the century, predictability will be high. Noting that multiple studies have remarked both on the importance of initial conditions on the predictability of the *Surprise Snow Storm*, as well as the high level of predictability noted for the *Storm of the Century*, it appears that these metrics, when used in concert, may offer some level of *a priori* insight into the predictability of an event.

5.4.2 QOIP Piecewise Tendency Diagnosis

As the overarching purpose of this study is to determine the character of QOIP to the initial state that modulate the intensification rate – a time dependent field – a natural follow-on is to employ the use of a *piecewise tendency diagnosis* (PTD) as in Hakim et al. (1996) and Nielsen-Gammon and Lefèvre (1996). By employing PTD, an extension of traditional QGPV inversion, the local QGPV can be inverted such that one can directly ascertain the contributions of distinct dynamical processes (i.e., large-scale wave-wave interactions, downstream development, baroclinic amplification, horizontal and vertical deformation and small-scale vortex interactions) to the *time tendency* of the geopotential height field. By employing this technique within the framework laid out within this study,

it is possible to take the results shown herein a step further. Within this study, the QOIP QGPV was inverted at discrete times and conclusions drawn from the evolution of the inverted fields over time. PTD however allows for direct attributions to dynamical processes with respect to the intended response function, the time-rate-of-change of surface pressure (geopotential height). Unlike the static inversion (whose utility is shown within this dissertation), PTD will help to elucidate the mechanisms that may lead to changes to the QGPV field that may ultimately impact the response function, unlike the current method which simply diagnoses changes to the response functions based upon what is assumed to be a static QGPV field.

5.4.3 Investigation of Tropical Cyclone Rapid Intensification Using the QOIP

As the QOIP employs a relaxation of the tangent-linear assumption, it is perhaps a tool that could be used in investigating the intensification rates (specifically the rapid intensification) of tropical cyclones. It is well understood that tropical cyclones behavior is heavily modulated by convection, a highly non-linear process. As this is the case, the use of traditional adjoint-derived dynamical sensitivity analysis is suboptimal when studying the intensification of tropical cyclones. By employing the perturbation-response and QOIP framework, as well as the time-rate-of-change response function, it is conceivable that some linearity concerns pertaining to the dynamical sensitivity analysis of tropical cyclones will be mitigated.

5.4.4 Sensitivity to Potential Vorticity

While Morgan (2018) derived the sensitivity to potential vorticity (PV) within the shallow water system, there has to-date been no adjoint-based derivation of the sensitivity to either isentropic (Ertel) PV or quasi-geostrophic PV, either of which would be more relevant to the complex, three dimensional flow of the real atmosphere. As it is a conserved, dynamical variable that can be inverted to obtain the balanced component of the winds and temperatures associated with it (e.g. Hoskins et al. 1985, Davis and Emanuel 1992), the sensitivity to PV would be an invaluable tool in the synoptician's toolkit. Prior studies have attempted to resolve some semblance of the sensitivity of the forecast to PV by examining the response of the forecast to PV perturbations subjectively defined by intuition (e.g. McTaggart-Cowan et al. 2001), or additionally informed by the location of leading singular vectors (Røsting et al. 2003), or by performing the computationally expensive process of fully mapping the sensitivity to PV by perturbing each grid point of the model individually in the nonlinear model framework and avoiding the adjoint entirely (Beare et al. 2006). Some success in computing the sensitivity to PV has been obtained through analytical solutions using the adjoint of the operator that relates PV to the balanced state itself, but has to-date only been applied in a simplified model framework (Arbogast 2006).

While optimal perturbations computed from adjoint-derived sensitivity gradients can only be created for model-state variables or other variables for which the sensitivity can be analytically derived from the sensitivity with respect to model-state variables, such as vorticity and divergence (Kleist and Morgan 2005a), when model-state variables are perturbed it is possible to obtain the resulting perturbations to derived variables such

as PV by simply applying the operator that computes PV from model-state variables. These PV perturbations therefore represent the PV perturbations that are induced from optimal perturbation of the model-state variables. While these PV perturbations are computed from an optimal model-state variable perturbation and are diagnostically useful for evaluation of the optimal perturbation and its evolution (Kleist and Morgan 2005b, Doyle et al. 2014), these perturbations do not represent “sensitivity to PV” in any analytical sense. Presumably they are *consistent* with the sensitivity to PV, but the sensitivity gradient itself is still an unknown, and conflating these perturbations with the sensitivity to PV is erroneous.

Recalling Section 2.1.3, an optimal perturbation to the model-state vector (\mathbf{x}'_0) can be expressed as:

$$\mathbf{x}'_0 = \lambda \mathbf{W}^{-1} \frac{\partial R}{\partial \mathbf{x}_0}, \quad (5.1)$$

where the optimal perturbation to \mathbf{x}'_0 is directly informed by the sensitivity gradient $\frac{\partial R}{\partial \mathbf{x}_0}$.

Note that all variables share the same Lagrange multiplier, λ but the weighting is based on a subjectively chosen norm that can vary for each component of the model-state vector. Therefore, it is conceivable that, if the norm weighting for PV were known, it may be possible to obtain the sensitivity to PV by simply rearranging the terms Eqn. 5.1 and solving for the sensitivity gradient. As the (optimal) perturbation vector \mathbf{x}'_0 , the Lagrange multiplier λ , and the weighting matrix \mathbf{W}^{-1} are all calculated explicitly, it should be possible to obtain the sensitivity to any particular derived variable (a) as:

$$\frac{W_a a'_0}{\lambda} = \frac{\partial R}{\partial a_0}, \quad (5.2)$$

where W_a is the weighting for variable a . By analogy, the sensitivity to the quasi-geostrophic PV (QGPV) at the initial time (q_0) should therefore be:

$$\frac{\partial R}{\partial q_0} = \frac{1}{\lambda} \mathbf{W}_q \mathbf{q}'_0. \quad (5.3)$$

Unlike the QGPV perturbation computed from optimally computed model-state variable perturbations (as discussed in section 2.1.3), which is *presumably informed* by the sensitivity to QGPV, it is conceivable that the algebraic manipulation of Eqn. 5.1 (with respect to q_0) would yield an *exact sensitivity* to QGPV as shown in Eqn. 5.3. In doing so, it would be possible to perform adjoint-derived sensitivity analysis with respect to a conserved, dynamical variable.

In order to obtain this solution, the appropriate weighting matrix \mathbf{W}_q must be identified. The norm used for weighting is subjective and specific to an intended purpose; in the optimal perturbation experiments presented, \mathbf{W} represents a weighting norm intended to translate model-state variable perturbations into an equivalent amount of energy and perturbations are optimized to utilize the minimum amount of initial perturbation energy. For the model-state perturbation \mathbf{x}'_0 , the calculation of energy may be generalized as

$$\varepsilon = \frac{1}{2} \langle \mathbf{x}'_0, \mathbf{W} \mathbf{x}'_0 \rangle. \quad (5.4)$$

and analogously, the energy norm for a QGPV perturbation is defined as:

$$\varepsilon = \frac{1}{2} \langle q'_0, \mathbf{W}_q q'_0 \rangle. \quad (5.5)$$

Therefore, in order to find \mathbf{W}_q , some expression of energy is necessary that can be expressed through eqn. 5.5.

First, consider the barotropic, 2-dimensional, non-divergent, inviscid case on an f -plane where the relevant PV is the relative vorticity. In that case, one can construct

optimal perturbations to the wind components u and v given sensitivity gradients $\frac{\partial R}{\partial u}$ and $\frac{\partial R}{\partial v}$ and subject to a norm for kinetic energy, in which case \mathbf{W} in eqn. 5.4 contains values of 1 for the u and v components. In searching for the appropriate norm weighting for vorticity, eqn. 5.5 may be expressed as:

$$\varepsilon = \frac{1}{2} \langle \zeta'_0, \mathbf{W}_\zeta \zeta'_0 \rangle. \quad (5.6)$$

It is known that the perturbation energy associated with a vorticity perturbation can be expressed as function of the product of the vorticity perturbation and the streamfunction perturbation (Pedlosky 1987):

$$\varepsilon = -\frac{1}{2} \langle \zeta'_0, \psi'_0 \rangle, \quad (5.7)$$

Further, the streamfunction can be derived from the inverse Laplacian of the vorticity, so the energy can be computed as:

$$\varepsilon = -\frac{1}{2} \langle \zeta'_0, \nabla^{-2} \zeta'_0 \rangle. \quad (5.8)$$

It therefore follows from equating the right hand side of eqn. 5.6 and eqn. 5.8 that $\mathbf{W}_\zeta = -\nabla^{-2}$, the inversion operator. As a consequence, the sensitivity to vorticity must be:

$$\frac{\partial R}{\partial \zeta_0} = \frac{1}{\lambda} \mathbf{W}_\zeta \zeta'_0 = \frac{-1}{\lambda} \nabla^{-2} \zeta'_0. \quad (5.9)$$

This solution for the sensitivity with respect to vorticity in eqn. 5.9 must be identical to the analytical solution for the sensitivity with respect to vorticity identified by Kleist and Morgan (2005a), since the sensitivity is the same irrespective of the chosen norm weighting. Recognizing that $\mathbf{W}_u = \mathbf{W}_v = 1$ for the energy norm weighting, the optimal perturbation to u and v is directly proportional to the sensitivity with respect to u and v , respectively:

$$u'_0 = \lambda \frac{\partial R}{\partial u}; \quad v'_0 = \lambda \frac{\partial R}{\partial v}. \quad (5.10)$$

Since it is known from the definition of vorticity that $\zeta'_0 = \frac{\partial}{\partial x}(v'_0) - \frac{\partial}{\partial y}(u'_0)$, we can substitute the equivalent expressions for the u and v perturbations from eqn. 5.10 into the definition of the vorticity perturbation and insert that expression into eqn. 5.9:

$$\frac{\partial R}{\partial \zeta_0} = \frac{-1}{\lambda} \nabla^{-2} \zeta'_0 = \frac{-1}{\lambda} \nabla^{-2} \left(\frac{\partial}{\partial x}(v'_0) - \frac{\partial}{\partial y}(u'_0) \right) = \frac{-1}{\lambda} \nabla^{-2} \left(\frac{\partial}{\partial x} \left(\lambda \frac{\partial R}{\partial v} \right) - \frac{\partial}{\partial y} \left(\lambda \frac{\partial R}{\partial u} \right) \right), \quad (5.11)$$

which simplifies to:

$$\frac{\partial R}{\partial \zeta_0} = -\nabla^{-2} \left(\frac{\partial}{\partial x} \left(\frac{\partial R}{\partial v} \right) - \frac{\partial}{\partial y} \left(\frac{\partial R}{\partial u} \right) \right), \quad (5.12)$$

which is the exact analytical solution to $\frac{\partial R}{\partial \zeta}$ found in Kleist and Morgan (2005a). This solution verifies that, provided the appropriate norm weighting can be identified, the sensitivity with respect to a derived variable can be obtained as a function of the optimal perturbations of the model-state variables that were computed using the same norm. This indicates that it may not be necessary to find the analytical solution for the sensitivity of derived variables if the other terms in eqn. 5.3 are known. Since the weighting norm is a subjective choice, this technique becomes a flexible and powerful method by which to calculate the sensitivity to derived variables.

It follows that when considering QGPV perturbation q'_0 , the energy of the QGPV can be expressed as:

$$\varepsilon = -\frac{1}{2} \langle q'_0, \varphi'_0 \rangle = -\frac{1}{2} \langle q'_0, \nabla^{-2} q'_0 \rangle = \frac{1}{2} \langle q'_0, W_q q'_0 \rangle, \quad (5.13)$$

where φ'_0 is the initial time perturbation geopotential height perturbation (Pedlosky 1987). Therefore, it is expected that the sensitivity to QGPV is computed as:

$$\frac{\partial R}{\partial q_0} = \frac{1}{\lambda} W_q q'_0 = \frac{-1}{\lambda} \nabla^{-2} q'_0. \quad (5.14)$$

The computation of sensitivity to QGPV is predicated on the assumptions that the Lagrange multiplier λ is identically the same for each variable, including derived variables, and that the appropriate weighting norm W has been found. Beyond the very simplified test shown here using the relative vorticity as the relevant PV, further testing is necessary to evaluate these assumptions. The sensitivity to PV in the shallow water system has been analytically derived in Morgan (2018), and successful testing of this methodology in the shallow water system would constitute greater evidence of the applicability of this method to more complex systems.

Beyond the diagnostic applications of the sensitivity to QGPV as a measure of the sensitivity of the forecast to a conserved variable, the sensitivity to QGPV could have other, far-reaching application. Just as the QGPV can be inverted to recover the balanced winds and temperatures associated with the QGPV, knowing the sensitivity with respect to QGPV may allow for the computation of the sensitivity with respect to the *balanced components* of the wind and temperature. Hoover (2015) was able to use sensitivity with respect to vorticity to compute the sensitivity with respect to *non-divergent* wind, recognizing that the divergent component of the wind carries no vorticity. In a similar way, knowledge of the sensitivity with respect to QGPV may help compute the sensitivity with respect to the balanced wind and temperatures, recognizing that the unbalanced component of the winds and temperatures carries no QGPV.

Being able to separate the sensitivity to wind and temperatures into their balanced wind/temperature and unbalanced wind/temperature components has great potential in data assimilation. In 4-dimensional variational data assimilation, the analysis state is perturbed based on sensitivity gradient information in order to minimize the distance

between the model-state and observations within a short time-window, often 6-12 hours. In analysis, a *balanced* state is sought that represents the best guess as to the current state of the atmosphere, but the sensitivity gradients that drive the minimization of the cost-function are computed on a timeframe that is often well beneath the timeframe of the geostrophic adjustment process, which means that much of the sensitivity that is computed represents sensitivity to *unbalanced* initial perturbation; within the 6-12 hour timeframe of the observation window, unbalanced initial perturbations may have a significant impact on the cost-function and therefore may represent significant portions of the sensitivity, and the implications of this issue are currently unknown. Restricting the sensitivity gradients to their *balanced* components may significantly change the minimization process and resulting analysis even if the same observations are assimilated. The application of sensitivity to balanced model-state variables on data assimilation and other atmospheric science issues represents a new direction for adjoint-based research.

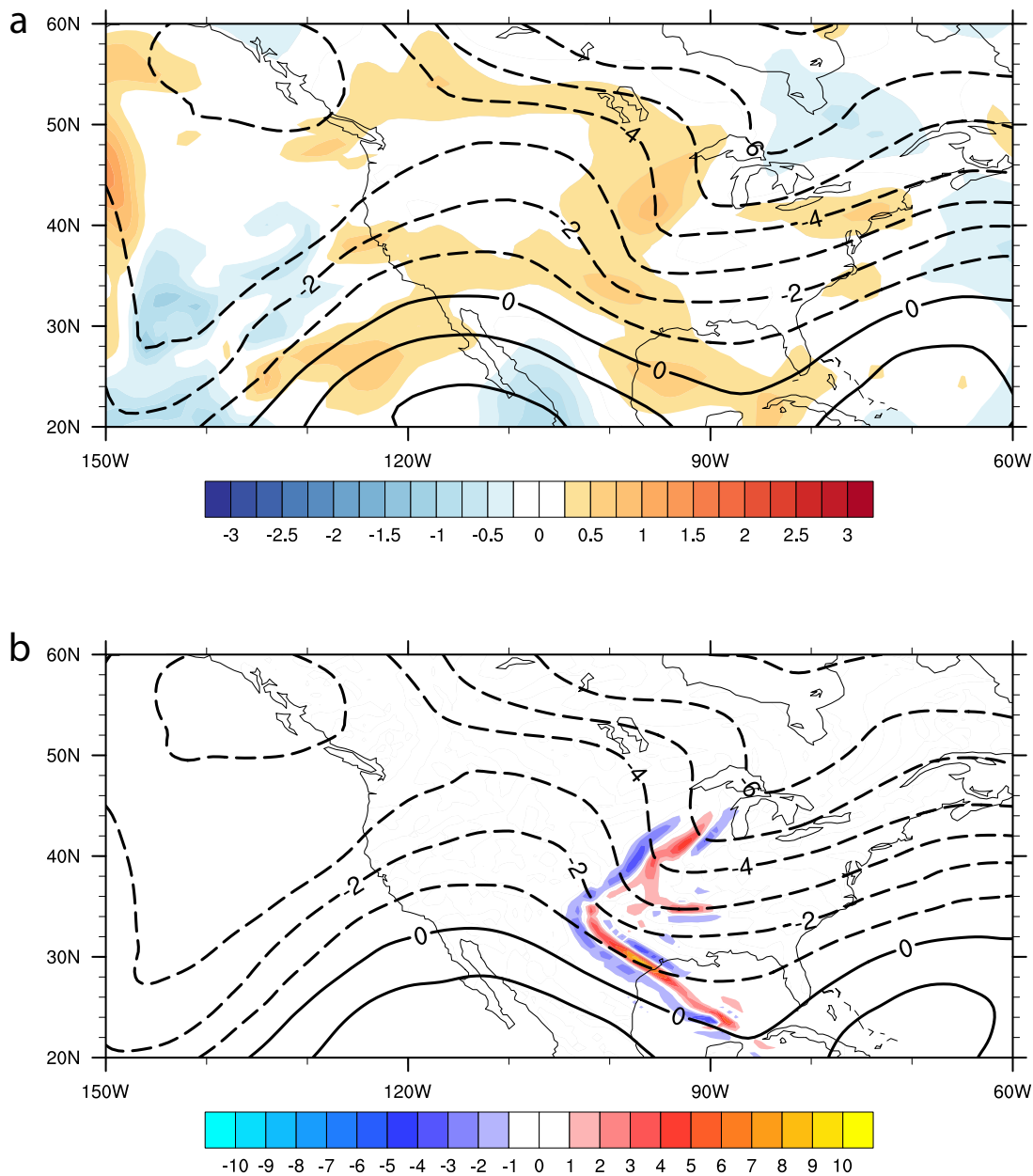


Figure 5.1. 500 hPa (a) GEFS stream function standardized uncertainty anomaly (fill; $\text{m}^2 \text{s}$) and mean stream function (contour; $10^{-7} \text{m}^2 \text{s}$); and (b) 24-hr sensitivity of cyclone intensity into the forecast to the analysis time 500 hPa stream function (fill; 10^8Pa s m^{-2}) and the deterministic GEOS-5 500 hPa stream function (contour; $10^{-7} \text{m}^2 \text{s}$), valid 2000 January 24 0000 UTC. Significant overlap between *positive* SUA and *non-zero* sensitivity indicates anomalously low levels of predictability are likely with respect to the intensity of the cyclone 24-hrs into the forecast. When assessing overlap between the two quantities, it is only the magnitude of the sensitivity that need be considered.

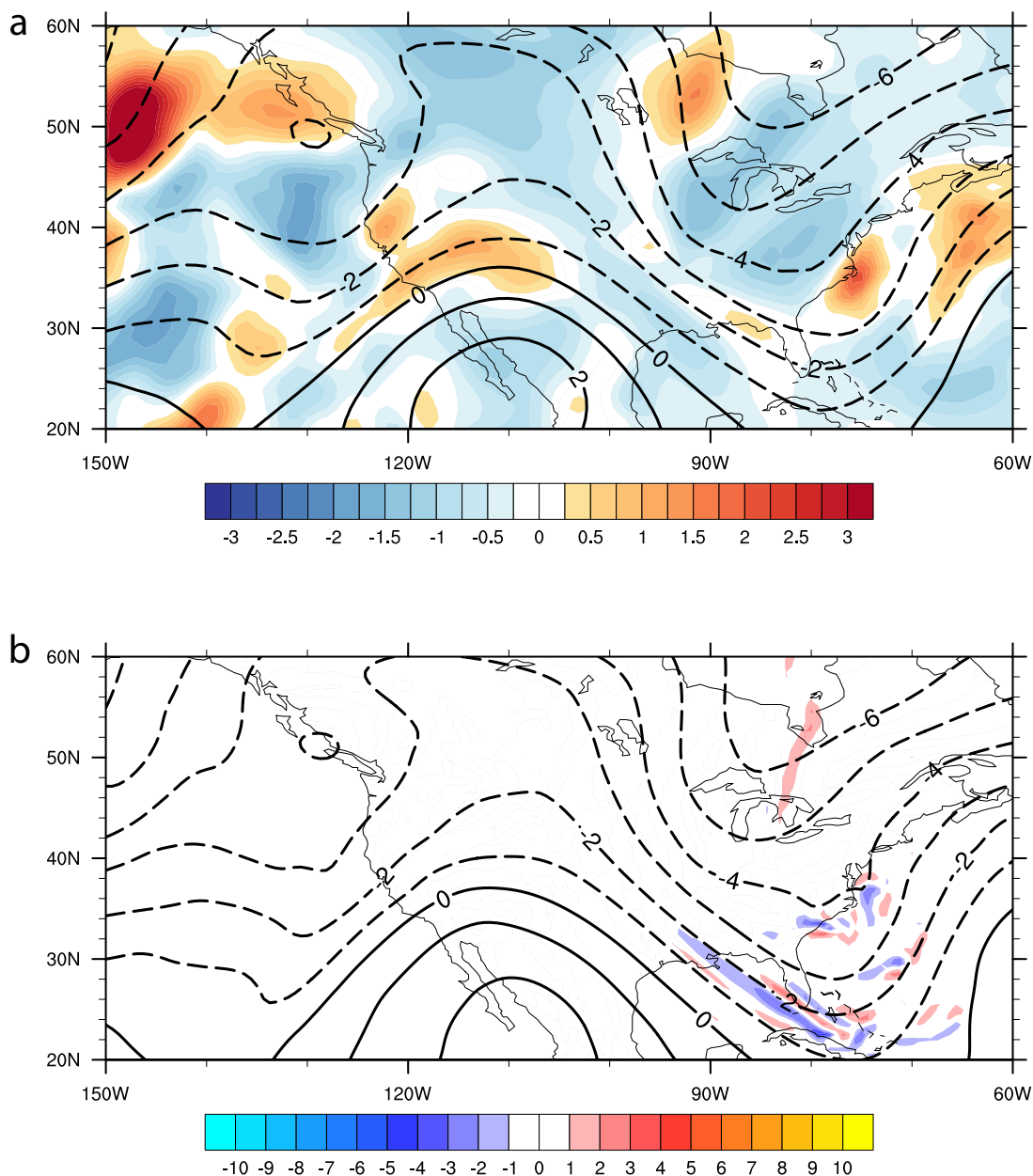


Figure 5.2. 500 hPa (a) GEFS stream function standardized uncertainty anomaly (fill; $\text{m}^2 \text{s}$) and mean stream function (contour; $10^{-7} \text{m}^2 \text{s}$); and (b) 60-hr sensitivity of cyclone intensity into the forecast to the 36-hr forecast state 500 hPa stream function (fill; 10^8Pa s m^{-2}) and the deterministic GEOS-5 500 hPa stream function (contour; $10^{-7} \text{m}^2 \text{s}$), valid 2000 January 25 1200 UTC. Lessened overlap between *positive* SUA and *non-zero* sensitivity as compared to 36-hrs previous indicates higher levels of predictability are likely with respect to the intensity of the cyclone 60-hrs into the forecast. When assessing overlap between the two quantities, it is only the magnitude of the sensitivity that need be considered.

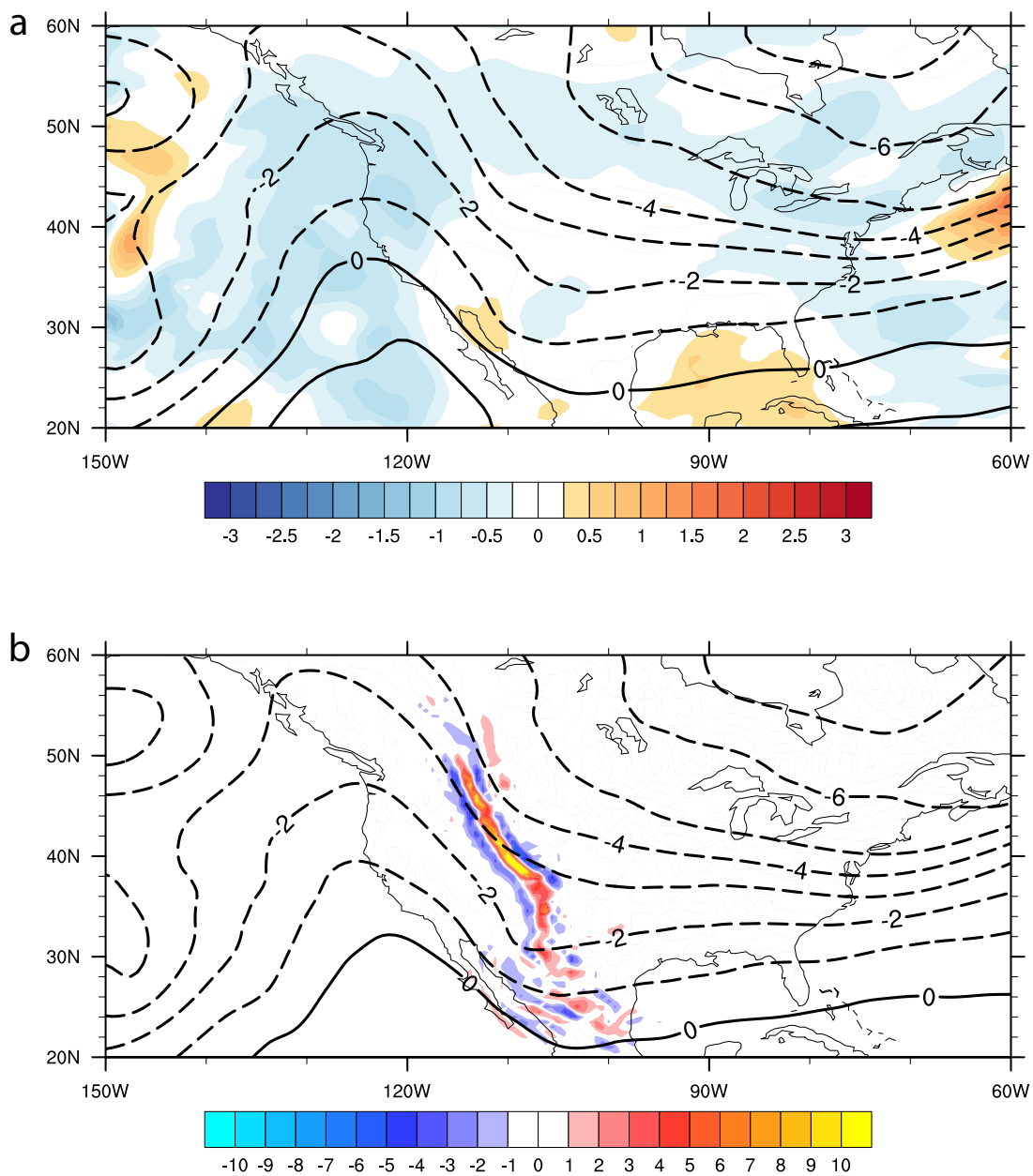


Figure 5.3. 500 hPa (a) GEFS stream function standardized uncertainty anomaly (fill; $\text{m}^2 \text{s}$) and mean stream function (contour; $10^{-7} \text{m}^2 \text{s}$); and (b) 24-hr sensitivity of cyclone intensity into the forecast to the analysis time 500 hPa stream function (fill; 10^8Pa s m^{-2}) and the deterministic GEOS-5 500 hPa stream function (contour; $10^{-7} \text{m}^2 \text{s}$), valid 1993 March 0000 UTC. Negligible overlap between *positive* SUA and *non-zero* sensitivity indicates anomalously high levels of predictability are likely with respect to the intensity of the cyclone 24-hrs into the forecast. When assessing overlap between the two quantities, it is only the magnitude of the sensitivity that need be considered.

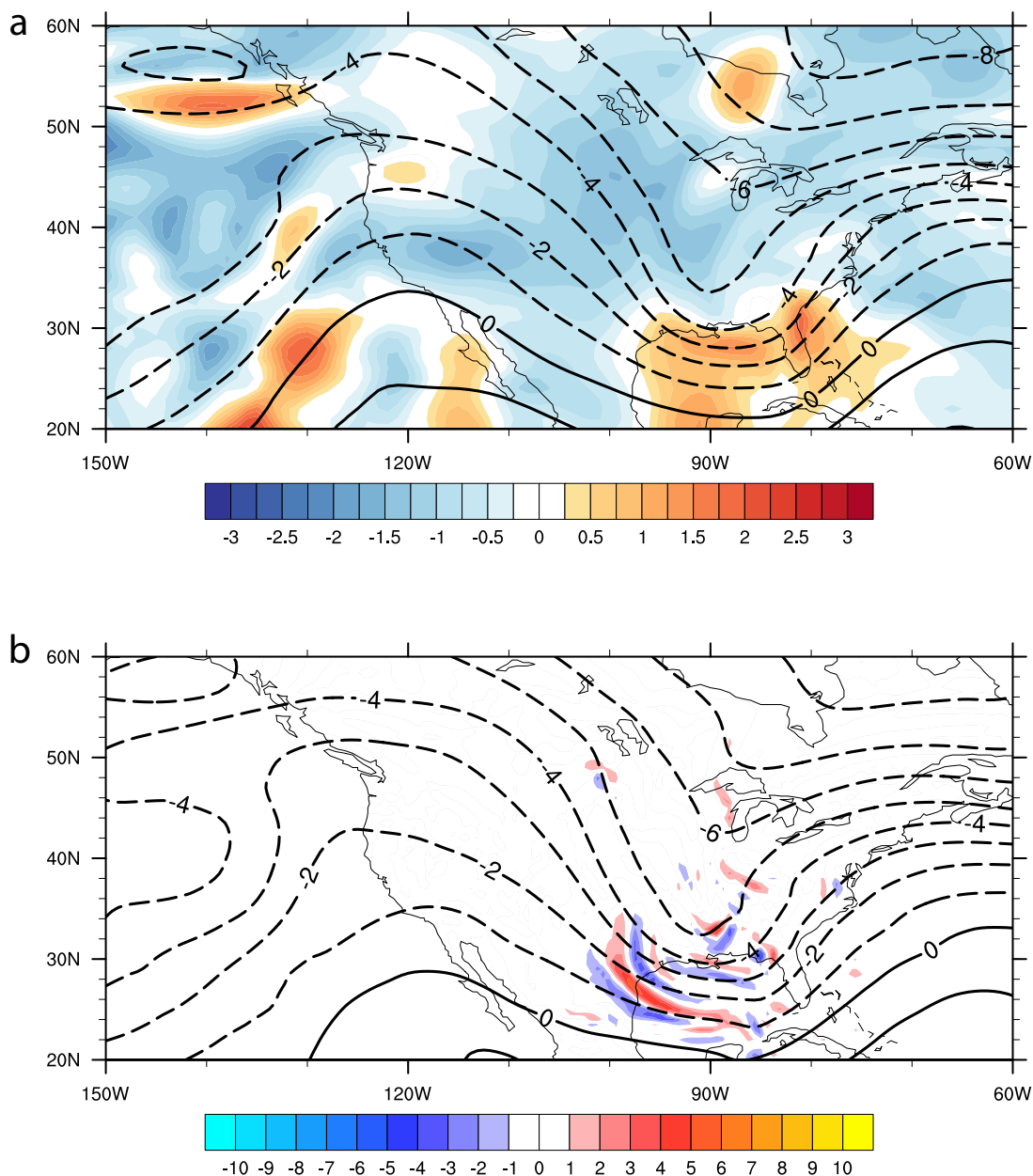


Figure 5.4. 500 hPa (a) GEFS stream function standardized uncertainty anomaly (fill; $\text{m}^2 \text{s}$) and mean stream function (contour; $10^{-7} \text{m}^2 \text{s}$); and (b) 60-hr sensitivity of cyclone intensity into the forecast to the 36-hr forecast state 500 hPa stream function (fill; 10^8Pa s m^{-2}) and the deterministic GEOS-5 500 hPa stream function (contour; $10^{-7} \text{m}^2 \text{s}$), valid 1993 March 12 1200 UTC. Non-negligible overlap between *positive* SUA and *non-zero* sensitivity indicates a small but non-negligible level of unpredictability for the 60-hr forecast of intensity. When assessing overlap between the two quantities, it is only the magnitude of the sensitivity that need be considered.

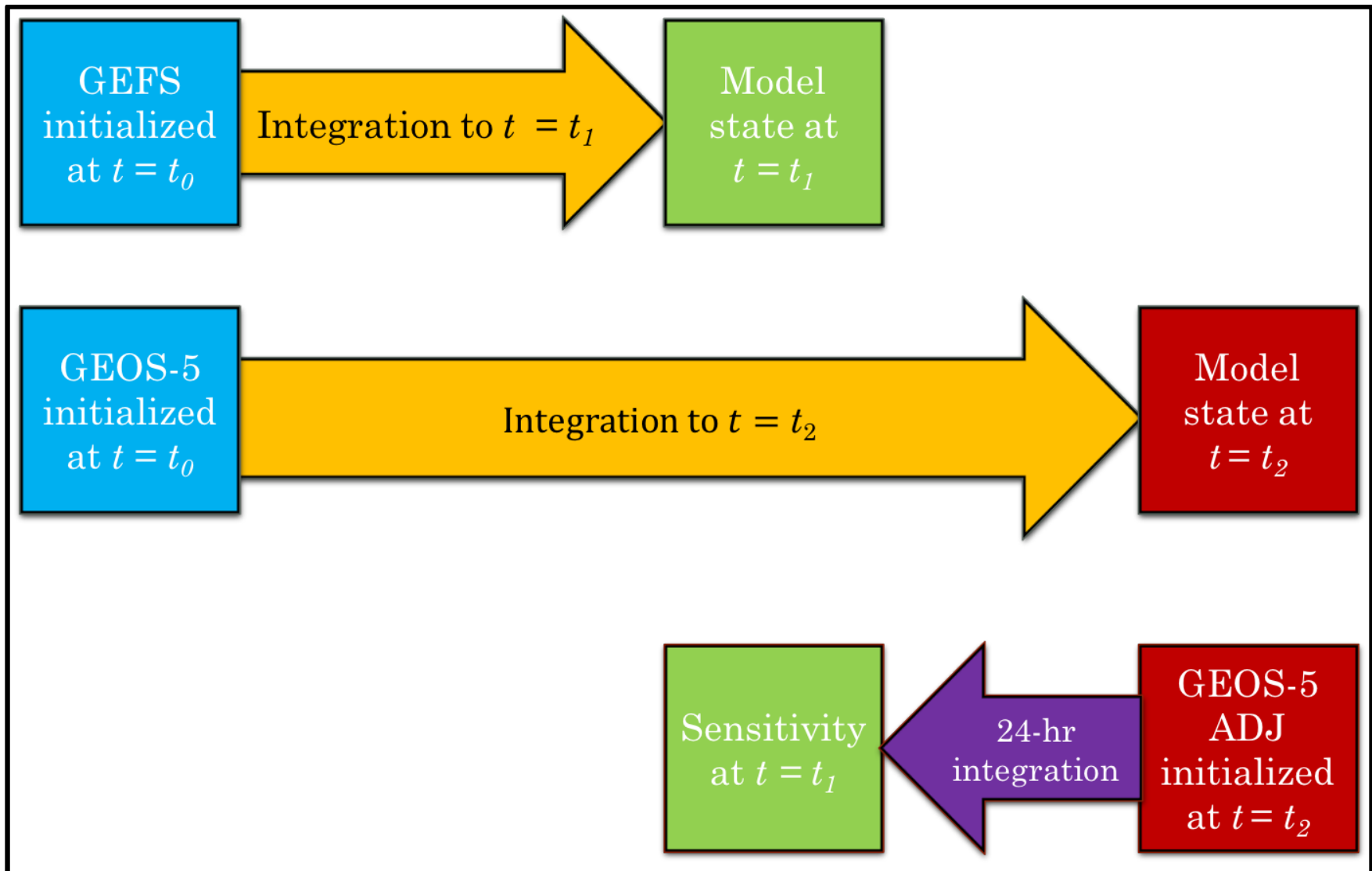


Figure 5.5. A schematic diagram indicating how equivalently timed SUA and forecast-state sensitivity gradients are calculated. The GEFS and GEOS-5 are initialized at the same analysis time, with the GEOS-5 integrated 24-hrs longer than the GEFS integration. The GEOS-5 adjoint is then integrated backwards in time 24-hrs, resulting in SUA and sensitivity gradients valid at equivalent times.

Chapter 6: References

- Ancell, B., and G. J. Hakim, 2007: Comparing adjoint- and ensemble-based sensitivity analysis with applications to observation targeting. *Mon. Wea. Rev.*, **135**, 4117-4134.
- Anthes, R. A., 1983: Regional models of the atmosphere in middle latitudes. *Mon. Wea. Rev.*, **111**, 1306–1335.
- Arakawa, A., and W. H. Schubert, 1974: Interaction of a cumulus cloud ensemble with the large-scale environment, Part I. *J. Atmos. Sci.*, **31**, 674–701
- Arbogast, P., 1998: Sensitivity to potential vorticity. *Quart. J. Roy. Meteor. Soc.*, **124**, 1605–1615.
- Atlas, R., 1987: The role of oceanic fluxes and initial data in the numerical prediction of an intense coastal cyclone. *Dyn. Atmos. Oceans*, **10**, 359–388
- Bassill, N. P., 2015: An analysis of the operational GFS simplified Arakawa Schubert parameterization within a WRF framework: A Hurricane Sandy (2012) long-term track forecast perspective. *J. Geophys. Res.*, **120**, 379-398.
- Beare, R. J., A. J. Thorpe, and A. A. White, 2003: The predictability of extratropical cyclones: Nonlinear sensitivity to localized potential-vorticity perturbations. *Quarterly Journal of the Royal Meteorological Society*, **129**, 219-237
- Bell, G.D. and L.F. Bosart, 1993: A Case Study Diagnosis of the Formation of an Upper-Level Cutoff Cyclonic Circulation over the Eastern United States. *Mon. Wea. Rev.*, **121**, 1635–1655
- Bjerknes, J., 1919: On the structure of moving cyclones. *Geofys. Publ.*, **1**, 1–8
- Bjerknes, J., and E. Palmén, 1937: Investigations of selected European cyclones by means of serial ascents. *Geofys. Publ.*, **12**, 1–62.
- Bjerknes, J., and H. Solberg, 1922: Life cycle of cyclones and the polar front theory of atmospheric circulation. *Geofys. Publ.*, **3** (1), 1–18.
- Bjerknes, J., and J. Holmboe, 1944: On the theory of cyclones. *J. Meteor.*, **1**, 1–22.
- Bjerknes, J., 1937: Theorie der aussertropischen Zyklonenbildung. *Meteor. Z.*, **54**, 462–466.
- Blessing, S., R. J. Greatbatch, K. Fraedrich, and F. Lunkeit, 2008: Interpreting the atmospheric circulation trend during the last half of the twentieth century: Application of an adjoint model. *J. Climate*, **21**, 4629-4646.

- Boettcher, M. and M. Wernli, 2011: Life Cycle Study of a Diabatic Rossby Wave as a Precursor to Rapid Cyclogenesis in the North Atlantic—Dynamics and Forecast Performance. *Mon. Wea. Rev.*, **139**, 1861–1878.
- Bosart L.F., 1999: Observed Cyclone Life Cycles. In: Shapiro M.A., Grønås S. (eds) *The Life Cycles of Extratropical Cyclones*. Amer. Meteor. Soc., Boston, MA
- Bosart, L. F., 1970: Mid-tropospheric frontogenesis. *Quart. J. Roy. Meteor. Soc.*, **96**, 442–471.
- Bosart, L. F., 1981: The Presidents' Day snowstorm of 18–19 February 1979: A subsynoptic-scale event. *Mon. Wea. Rev.*, **109**, 1542–1566.
- Breeden, M. and J. E. Martin, 2018: Diagnosing the initiation of an extreme north Pacific jet retraction using piecewise tendency diagnosis. *Quart. J. Roy. Meteor. Soc.*, **144**
- Brennan, M. J., and G. M. Lackmann, 2005: The influence of incipient latent heat release on the precipitation distribution of the 24–25 January 2000 U.S. East Coast cyclone. *Mon. Wea. Rev.*, **133**, 1913–1937.
- Bretherton, F. P. 1966: Baroclinic instability and the short wavelength cut-off in terms of potential vorticity. *Quart. J. Roy. Meteor. Soc.* **92** (393), 335–345
- Brown, B. R., and G. J. Hakim, 2015: Sensitivity of intensifying Atlantic hurricanes to vortex structure. *Quart. J. Roy. Meteor. Soc.*, **141**, 2358–2551.
- Carlson, T., 1980: Airflow through mid-latitude cyclones and the comma cloud pattern. *Mon. Wea. Rev.*, **108**, 1498–1509.
- Chen, J. H., M. S. Peng, C. A. Reynolds, and C. C. Wu, 2009: Interpretation of tropical cyclone forecast sensitivity from the singular vector perspective. *J. Atmos. Sci.*, **66**, 3383–3400.
- Chen, S.-J., and L. Dell'Osso, 1987: A numerical case study of east Asian coastal cyclogenesis. *Mon. Wea. Rev.*, **115**, 477–487.
- Chen, S.-J., Kuo, Y.-H., Zhang, P.-Z., Bai, Q.-F., 1992: Climatology of explosive cyclones off the East Asian coast. *Mon. Wea. Rev.*, **120**, 3029–3035.
- Chu, K., and Z. Yi, 2016: Adjoint sensitivity study on idealized explosive cyclogenesis. *Journal of Meteorological Research*, **30**, 547–558

- Courtier P, Thépaut JN, Hollingsworth A, 1994: A strategy for operational implementation of 4D-VAR, using an incremental approach. *Quart. J. Roy. Meteor. Soc.*, **120**(519):1367-1387.
- Davies, H.C., C. Schär, and H. Wernli, 1991: The palette of fronts and cyclones within a baroclinic wave development. *J. Atmos. Sci.*, **48**, 1666–1689.
- Davis, C. A., 1992a: Piecewise potential vorticity inversion. *J. Atmos. Sci.*, **49**, 1397–1411.
- Davis, C.A., Emanuel, K.A., 1991: Potential vorticity diagnostics of cyclogenesis. *Mon. Wea. Rev.*, **119**, 1929–1953.
- Dickinson, M. J., L. F. Bosart, W. E. Bracken, G. J. Hakim, D. M. Schultz, M. A. Bedrick, and K. R. Tyle, 1997: The March 1993 Superstorm cyclogenesis: Incipient phase synoptic- and convective-scale flow interaction and model performance. *Mon. Wea. Rev.*, **125**, 3041–3072.
- Dirks, R. A., J. P. Kuettner, and J. A. Moore, 1988: Genesis of Atlantic Lows Experiment (GALE): An Overview. *Bull. Amer. Meteor. Soc.*, **69**, 148–160.
- Doyle, J. D., C. A. Reynolds, C. Amerault, and J. Moskaitis, 2012: Adjoint sensitivity and predictability of tropical cyclogenesis. *J. Atmos. Sci.*, **69**, 3535-3557.
- Du, J., 2007: Uncertainty and ensemble forecasting. *Science and Technology Infusion Climate Bulletin*, NOAA/NWS Science and Technology Infusion Lecture Series, 42 pp.
- Eady, E.T., 1949: Long Waves and Cyclone Waves. *Tellus*, **1**, 33-52.
- Ehrendorfer, M., R. Errico, and K. Raeder, 1999: Singular-vector perturbation growth in a primitive equation model with moist physics. *J. Atmos. Sci.*, **56**, 1627–1648.
- Emanuel, K. A., M. Fantini, and A. J. Thorpe, 1987: Baroclinic instability in an environment of small stability to slantwise moist convection. Part I: Two-dimensional models. *J. Atmos. Sci.*, **44**, 1559 –1573.
- Errico, R. M., 1997: What is an adjoint model? *Bull. Amer. Meteor. Soc.*, **78**, 2577-2591.
- Errico, R. M., and K. D. Raeder, 1999: An examination of the accuracy of the linearization of a mesoscale model with moist physics. *Quart. J. Roy. Meteor. Soc.*, **125**, 169-195.
- Errico, R. M., and T. Vukicevic, and K. Raeder, 1993b: Examination of the accuracy of a tangent linear model. *Tellus*, **45A**, 462–497.

- Ertel, H., 1942: Ein Neuer hydrodynamischer Wirbelsatz. *Meteor. Z.*, **59**, 271–281.
- Farrell, B. F., 1985: Transient growth of damped baroclinic waves. *J. Atmos. Sci.*, **42**, 2718–2727.
- Farrell, B. F., 1982a: The initial growth of disturbances in a baroclinic flow. *J. Atmos. Sci.*, **39**, 1663–1686.
- Farrell, B.F., and P. J. Ioannou, 1996: Generalized stability theory part I: autonomous operators. *J. Atmos. Sci.* **53** 2025–2040.
- Fehlmann, R., and H.C. Davies, 1998: Role of salient PV-elements in an event of frontal wave cyclogenesis. *Quart. J. Roy. Meteor. Soc.*, **124**, 1–22.
- Fehlmann, R., and H. C. Davies, 1997: Misforecasts of synoptic systems: diagnosis via PV retrodiction. *Mon. Wea. Rev.*, **125**, 2247–2264.
- Godske, C. L., T. Bergeron, J. Bjerknes, and R. C. Bundgaard, 1957: *Dynamic Meteorology and Weather Forecasting*. Amer. Meteor. Soc., 800 pp.
- Greybush, S. J., S. Saslo, and R. Grumm, 2017: Assessing the ensemble predictability of precipitation forecasts for the January 2015 and 2016 East Coast winter storms. *Wea. Forecasting*, **32**, 1057–1078
- Gyakum, J. R., 1983a: On the evolution of the QE II storm. I: Synoptic aspects. *Mon. Wea. Rev.*, **111**, 1137–1155.
- Gyakum, J. R., 1983b: On the evolution of the QE II storm. II: Dynamic and thermodynamic structure. *Mon. Wea. Rev.*, **111**, 1156–1173.
- Hadlock, R. and C. W. Kreitzberg 1988: The Experiment on Rapidly Intensifying cyclones over the Atlantic (ERICA) Field Study: Objectives and Plans. *Bull. Amer. Meteor. Soc.*, **69**, 1309–1320.
- Hakim, G., L. Bosart, and D. Keyser, 1996: The Ohio Valley wave-merger cyclogenesis event of 25–26 January 1978. Part II: Diagnosis using quasigeostrophic potential vorticity inversion. *Mon. Wea. Rev.*, **124**, 2176–2205.
- Hamill, T. M., G. T. Bates, J. S. Whitaker, D. R. Murray, M. Fiorino, T. J. Galarneau Jr., Y. Zhu, and W. Lapenta, 2013: NOAA's second-generation global medium-range ensemble reforecast dataset. *Bull. Amer. Meteor. Soc.*, **94**, 1553–1565.
- Hamill, T. M., J. S. Whitaker, D. T. Kleist, M. Fiorino, and S.G. Benjamin, 2011: Predictions of 2010's tropical cyclones using the GFS and ensemble-based data assimilation methods. *Mon. Wea. Rev.*, **139**, 3243–3247.

- Heckley, W. A., and B. J. Hoskins, 1982: Baroclinic waves and frontogenesis in a non-uniform potential vorticity semi-geostrophic model. *J. Atmos. Sci.*, **39**, 1999–2016.
- Heo, K., Y. Seo, K. Ha, K. Park, J. Kim, J. Choi, K. Jun, and J. Jeong, 2015: Development mechanisms of an explosive cyclone over East Sea on 3–4 April 2012. *Dyn. Atmos. Oceans* **70**, 30–46.
- Holdaway, D., and R. Errico, 2014: Using Jacobian sensitivities to assess a linearization of the relaxed Arakawa–Schubert convection scheme. *Quart. J. Roy. Meteor. Soc.*, **140**, 1319–1332.
- Holdaway, D., R. Errico, R. Gelaro, and J.G. Kim and R. Mahajan, 2015: A Linearized Prognostic Cloud Scheme in NASA’s Goddard Earth Observing System Data Assimilation Tools. *Mon. Wea. Rev.*, **143**, 4198–4219.
- Hoover, B. T., 2009: Comments on “Interaction of Typhoon Shanshan (2006) with the mid-latitude trough from both adjoint-derived sensitivity steering vector and potential vorticity perspectives”. *Mon. Wea. Rev.*, **137**, 4420–4424.
- Hoover, B. T., 2010: Dynamical Sensitivity Analysis of Tropical Cyclone Steering and Genesis Using an Adjoint Model. Ph.D. Dissertation, University of Wisconsin - Madison, 128 pp.
- Hoover, B. T., 2015: Identifying a barotropic growth mechanism in East Pacific tropical cyclogenesis using adjoint-derived sensitivity gradients. *J. Atmos. Sci.*, **72**, 1215–1234.
- Hoover, B. T., and M. C. Morgan, 2011: Dynamical sensitivity analysis of tropical cyclone steering using an adjoint model. *Mon. Wea. Rev.*, **139**, 2761–2775.
- Hoskins, B. J. 1976: Baroclinic waves and frontogenesis. Part I: Introduction and Eady waves. *Quart. J. Roy. Meteor. Soc.* **102**, 103–122.
- Hoskins, B. J., and N. V. West, 1979: Baroclinic waves and frontogenesis. Part II: Uniform potential vorticity jet flows—Cold and warm fronts. *J. Atmos. Sci.*, **36**, 1663–1680.
- Hoskins, B. J., M.E. McIntyre and A. W. Robertson, 1985: On the use and significance of isentropic potential vorticity maps. *Quart. J. Roy. Meteor. Soc.* **111** (470), 877–946.
- Hoskins, B. J., M. McIntyre, and A. W. Robertson, 1985: On the use and significance of isentropic potential vorticity maps. *Quart. J. Roy. Meteor. Soc.*, **111**, 877–946.

- Huo, Z., D. Zhang, J. R. Gyakum, and A. Staniforth, 1995: A diagnostic analysis of the Superstorm of March 1993. *Mon. Wea. Rev.*, **123**, 1740–1761.
- Huo, Z., D. L. Zhang, and J. R. Gyakum, 1999: Interaction of potential vorticity anomalies in extratropical cyclogenesis: Part I: static piecewise inversion. *Mon. Wea. Rev.*, **127**, 2546–2561.
- J.D. Doyle, C. Amerault, C.A. Reynolds, P.A. Reinecke, 2014: Initial condition sensitivity and predictability of a severe extratropical cyclone using a moist adjoint *Mon. Wea. Rev.*, **142** (1) (2014), pp. 320-342
- Kim, H. M., M. C. Morgan, and R. E. Morss, 2004: Evolution of analysis error and adjoint-based sensitivities: Implications for adaptive observations. *J. Atmos. Sci.*, **61**, 795–812,
- Kim, H. M., S.-M. Kim, and B.-J. Jung, 2011: Real-time adaptive observation guidance using singular vectors for Typhoon Jangmi (2009) in T-PARC 2008. *Wea. Forecasting*, **26**, 634–649
- Kleist, D. T., and M. C. Morgan, 2005a: Interpretation of the structure and evolution of adjoint-derived forecast sensitivity gradients. *Mon. Wea. Rev.*, **133**, 466-484.
- Kleist, D. T., and M. C. Morgan, 2005b: Application of adjoint-derived forecast sensitivities to the 24-25 January 2000 U.S. east coast snowstorm. *Mon. Wea. Rev.*, **133**, 3148-3175.
- Klinker, E., F. Rabier, and R. Gelaro, 1998: Estimation of key analysis errors using the adjoint technique. *Quart. J. Roy. Meteor. Soc.*, **124**, 1909–1933.
- Kocin, P. J. and L. W. Uccellini, 2004: A Snowfall Impact Scale Derived From Northeast Storm Snowfall Distributions. *Bull. Amer. Meteor. Soc.*, **85**, 177-194
- Kocin, P.J., and L. W. Uccellini, 1990: Snowstorms along the Northeastern Coast of the United States: 1955 to 1985. *Amer. Meteor. Soc.*, 280 pp
- Korner, S. O., and J. E. Martin, 2000: Piecewise frontogenesis from a potential vorticity perspective: Methodology and a case study. *Mon. Wea. Rev.*, **128**, 1266-1288
- Kucharski, F. and A. J. Thorpe, 2000: Upper-level barotropic growth as a precursor to cyclogenesis during FASTEX. *Quart. J. Roy. Meteor. Soc.*, **126**, 3219–3232
- Kucharski, F. and A. J. Thorpe, 2001: The influence of transient upper-level barotropic growth on the development of baroclinic waves. *Quart. J. Roy. Meteor. Soc.*, **127**, 835–844

- Kuo, H-L., R. J. Reed, and Y. Liu, 1996: The ERICA IOP5 storm: Mesoscale cyclogenesis and precipitation parameterization. *Mon. Wea. Rev.* **124**:1409–1434.
- Kuo, Y. H., R. J. Reed, and S. Low-Nam, 1990: Effects of surface energy fluxes during the early development and rapid intensification stages of seven explosive cyclones in the Western Atlantic. *Mon. Wea. Rev.*, **119**, 457-476
- Kuo, Y. H., M. A. Shapiro, and E. G Donall, 1991: The interaction between baroclinic and diabatic processes in a numerical simulation of a rapidly intensifying extratropical marine cyclone. *Mon. Wea. Rev.* **119**, 368–384
- Langland, R. H., and R. M. Errico, 1996: Comments on “Use of an Adjoint Model for Finding Triggers for Alpine Lee Cyclogenesis”. *Mon. Wea. Rev.*, **124**, 757-760.
- Langland, R. H., R. L. Elsberry, and R. M. Errico, 1995: Evaluation of physical processes in an idealized extratropical cyclone using adjoint sensitivity. *Quart. J. Roy. Meteor. Soc.*, **121**, 1349-1386.
- Lin, S.-J., 2004: A “vertically Lagrangian” finite-volume dynamical core for global models, *Mon. Wea. Rev.*, **132**, 2293–2307
- Lin, S.-J., R. Rood, 1996: Multidimensional flux form semi-Lagrangian transport schemes, *Mon. Wea. Rev.*, **124**, 2046–2070
- Lock, A. P., A. R. Brown, M. R. Bush, G. M. Martin, and R. N. B. Smith, 2000: A new boundary layer mixing scheme. Part I: Scheme description and single column model tests. *Mon. Wea. Rev.*, **128**, 3187–3199.
- Louis, J.F., M. Tiedtke and J.F. Geleyn, 1982: A short history of the PBL parameterization at ECMWF. Workshop on Boundary Layer Parameterization, 25-27 Nov. 1981, ECMWF, Reading.
- Ludwig, P., J.G. Pinto, M. Reyers and S.L. Gray, 2014: The role of anomalous SST and surface fluxes over the southeastern North Atlantic in the explosive development of windstorm Xynthia. *Quart. J. Roy. Meteor. Soc.*, **140**: 1729–1741.
- Mailhot, J. and C. Chouinard, 1989: Numerical Forecasts of Explosive Winter Storms: Sensitivity Experiments with a Meso- α scale Model. *Mon. Wea. Rev.*, **117**, 1311–1343.
- Mak, M., and M. Cai, 1989: Local barotropic instability. *J. Atmos. Sci.*, **46**, 3289–3311
- Martin, J. E., 2006: *Mid-latitude Atmospheric Dynamics: A First Course*. John Wiley and Sons, 336 pp.

- McGrath-Spangler, E. L., and A. M. Molod. 2014: "Comparison of GEOS-5 AGCM planetary boundary layer depths computed with various definitions." *Atmos. Chem. Phys.*, **14** (13), 6717-6727
- McTaggart-Cowan, R., J. R. Gyakum, and M. K. Yau, 2001: Sensitivity testing of extratropical transitions using potential vorticity inversions to modify initial conditions: Hurricane Earl case study. *Monthly Weather Review*, **129**, 1617-1636
- McTaggart-Cowan, R., J. R. Gyakum, and M. K. Yau, 2004: The impact of tropical remnants on extratropical cyclogenesis: Case study of Hurricanes Danielle and Earl (1998). *Mon. Wea. Rev.*, **132**, 1933–1951
- Miller, J. E., 1946: Cyclogenesis in the Atlantic coastal region of the United States. *J. Meteor.*, **3**, 31–44.
- Morgan, M.C., 2018: On the Dynamics of Adjustment in the f-Plane Shallow Water Adjoint System. *J. Atmos. Sci.*, **75**, 1571–1585
- Morgan, M.C., 1999: Using piecewise potential vorticity inversion to diagnose frontogenesis. Part I: A partitioning of the Q vector applied to diagnosing surface frontogenesis and vertical motion. *Mon. Wea. Rev.*, **127**, 2796–2821.
- Mullen S. L. and D.P. Baumhefner, 1988: Sensitivity of Numerical Simulations of Explosive Oceanic Cyclogenesis to Changes in Physical Parameterizations. *Mon. Wea. Rev.*, **116**, 2289–2329.
- Nielsen-Gammon, J. W. and R. J. Lefèvre, 1996: Piecewise Tendency Diagnosis of Dynamical Processes Governing the Development of an Upper-Tropospheric Mobile Trough. *J. Atmos. Sci.*, **53**, 3120–3142.
- Orlanski, I. and J. P. Sheldon., 1995: Stages in the energetics of baroclinic systems. *Tellus*, **47A**: 605–628.
- Pang, H., and Fu, G., 2017: Case study of potential vorticity tower in three explosive cyclones over Eastern Asia. *J. Atmos. Sci.*, **74**: 1445–1454
- Park, S. K., and K. K. Droegemeier, 2000: Sensitivity analysis of a 3D convective storm: Implications for variational data assimilation and forecast error. *Mon. Wea. Rev.*, **128**, 140-159.
- Parrish, D. F., R. J. Purser, E. Rogers, and Y. Lin, 1996: The regional 3D-variational analysis for the eta model. Preprints, *11th Conf. on Numerical Weather Prediction*, Norfolk, VA, Amer. Meteor. Soc., 454–455.
- Pedlosky, J, 1987. *Geophysical Fluid Dynamics*, 2nd Edition. Springer-Verlag, New York, 710 pp.

- Peng, M. S., and C. A. Reynolds, 2006: Sensitivity of tropical cyclone forecasts as revealed by singular vectors. *J. Atmos. Sci.*, **63**, 2508-2528.
- Petterssen, S. and Smebye, S. J. 1971: On the development of extratropical cyclones. *Quart. J. Roy. Meteor. Soc.*, **97**, 457-482
- Petterssen, S., 1956: *Weather Analysis and Forecasting*. Vol. I, 2d ed. McGraw Hill, 428 pp.
- Putman, W. M., S-J Lin 2007: Finite-volume transport on various cubed-sphere grids. *J. Comput. Phys.* **227** 55-78
- R.S. Lindzen and B. Farrell, 1980: A simple approximate result for the maximum growth rate of baroclinic instabilities. *J. Atmos. Sci.*, **37**, 1648-1654
- Rabier, E. Klinker, P. Courtier, and A. Hollingsworth, 1996: Sensitivity of forecast errors to initial conditions. *Quart. J. Roy. Meteor. Soc.*, **122**, 121-150.
- Ratnam, J. V. and K. K. Kumar, 2005: Sensitivity of the simulated monsoons of 1987 and 1988 to convective parameterization schemes in the MM5. *J. Climate*, **18**, 2724-2743.
- Reed, R. J., and F. Sanders, 1953: An investigation of the development of a mid-tropospheric frontal zone and its associated vorticity field. *J. Meteor.*, **10**, 338-349.
- Reed, R. J., and M.D. Albright, 1986: A case study of explosive cyclogenesis in the Eastern Pacific. *Mon. Wea. Rev.*, **112**, 2297-2319.
- Reynolds, C. A., M. S. Peng, and J. H. Chen, 2009: Recurving tropical cyclones: Singular vector sensitivity and downstream impacts. *Mon. Wea. Rev.*, **137**, 1320-1337
- Rienecker, M. M., and Coauthors, 2011: MERRA: NASA's Modern-Era Retrospective Analysis for Research and Applications. *J. Climate*, **24**, 3624-3648
- Rivière, G., B. L. Hua, and P. Klein, 2003: Perturbation growth in terms of barotropic alignment properties. *Quart. J. Roy. Meteor. Soc.*, **129**, 2613-2635
- Roebber, P. J., 1984: Statistical analysis and updated climatology of explosive cyclones. *Mon. Wea. Rev.*, **112**, 1577-1589.
- Rogers, E., and L. F. Bosart, 1986: An investigation of explosively deepening oceanic cyclones. *Mon. Wea. Rev.*, **114**, 702-718.

- Rossby, C. G., 1940: Planetary flow patterns in the atmosphere. *Quart. J. Roy. Meteor. Soc.*, **66**, 68–87.
- Rossby, C.-G., 1939: Relation between variations in the intensity of the zonal circulation of the atmosphere and the displacements of the semipermanent centers of action. *J. Mar. Res.*, **2**, 38–55.
- Rossby, C.-G., and R. H. Weightman, 1926: Application of the polarfront theory to series of American weather maps. *Mon. Wea. Rev.*, **54**, 485-496
- Røsting, B., J. E. Kristjansson, and J. Sunde, 2003: The sensitivity of numerical simulations to initial modifications of potential vorticity – a case-study. *Quarterly Journal of the Royal Meteorological Society*, **129**, 2697-2718
- Sanders, F. and J. R. Gyakum, 1980: Synoptic-Dynamic Climatology of the “Bomb”. *Mon. Wea. Rev.*, **108**, 1589–1606.
- Sanders, F., 1955: An investigation of the structure and dynamics of an intense surface frontal zone. *J. Meteorol.*, **12**, 542–552
- Sanders, F., 1986: Explosive cyclogenesis in the west-central North Atlantic Ocean, 1981–84. Part I: Composite structure and mean behavior. *Mon. Wea. Rev.*, **114**, 1781–1794
- Sanders, F., 1986: Frontogenesis and symmetric stability in a major New England snowstorm. *Mon. Wea. Rev.*, **114**, 1847–1862.
- Schultz, D.M., Keyser D., Bosart L.F., 1998: The effect of large-scale flow on low-level frontal structure and evolution in mid-latitude cyclones. *Mon. Wea. Rev.*, **126**, 1767–1791
- Selz, T., and G. C. Craig, 2015: Upscale error growth in a high-resolution simulation of a summertime weather event over Europe. *Mon. Wea. Rev.*, **143**, 813-827
- Shapiro, M. A., 1970: On the applicability of the geostrophic approximation to upper-level frontal-scale motions. *J. Atmos. Sci.*, **27**, 408–420.
- Shapiro, M. A., and D. Keyser, 1990: Fronts, jet streams and the tropopause. *Extratropical Cyclones, The Erik Palmén Memorial Volume*, C. W. Newton and E. O. Holopainen, Eds., Amer. Meteor. Soc., 167–191.
- Simmons, A. J. and B.J. Hoskins, 1980: “Barotropic influence on the growth and decay of nonlinear baroclinic waves,” *J. Atmos. Sci.* **37**, 1679–1684.

- Uccellini, L.W., 1990: Processes contributing to the rapid development of extratropical cyclones. In: Newton, C.W., Holopainen, E.O. (Eds.), *Extratropical Cyclones, The Erik Palmén Memorial Volume*. Amer. Meteor. Soc., pp. 81–105.
- Wang C. and J.C. Rogers, 2001: A composite study of explosive cyclogenesis in different sectors of the North Atlantic. Part I: Cyclone structure and evolution. *Mon. Wea. Rev.*, **129**, 1481–1499.
- Wei, M., Z. Toth, R. Wobus, and Y. Zhu, 2008: Initial perturbations based on the ensemble transform (ET) technique in the NCEP global operational forecast system. *Tellus*, **60A**, 62–79.
- Wernli, H., R. Fehlmann, and D. Lüthi, 1998: The effect of barotropic shear on upper-level induced cyclogenesis: Semigeostrophic and primitive equation numerical simulations. *J. Atmos. Sci.*, **55**, 2080–2094.
- Y. Tremolet. Incremental 4D-Var Convergence Study. Tech. Memo. **469**, ECMWF, July 2005.
- Zhang, F., C. Snyder, and R. Rotunno, 2002: Mesoscale predictability of the "surprise" snowstorm of 24-25 January 2000. *Mon. Wea. Rev.*, **130**, 1617-1632.
- Zhang, F., C. Snyder, and R. Rotunno, 2003: Effects of moist convection on mesoscale predictability. *J. Atmos. Sci.*, **60**, 1173-1185.
- Zhang, F., N. Bei, R. Rotunno, C. Snyder, and C. Epifanio, 2007: Mesoscale predictability of moist baroclinic waves: Convection-permitting experiments and multistage error growth dynamics. *J. Atmos. Sci.*, **64**, 3579–3594.
- Zou, X., F. Vandenberghe, M. Pondecà, and Y.-H. Kuo, 1997: Introduction to adjoint techniques and the MM5 adjoint modeling system. NCAR Technical Note, NCAR/TN-435+STR, 117 pp.
- Zupanski, D., M. Zupanski, D. F., Parrish, G. J. DiMego, and E. Rogers, 2002: Fine-resolution 4DVAR data assimilation for the Great Plains tornado outbreak of 3 May 1999. *Wea. Forecasting*, **17**, 506–525.